

ISSN 2071-4726  
2071-0305

# Инженерно-строительный журнал

НАУЧНОЕ ИЗДАНИЕ

№3(87) 2019







**ПОЛИТЕХ**  
Санкт-Петербургский  
политехнический университет  
Петра Великого

**Инженерно-строительный институт**  
**Центр дополнительных профессиональных программ**  
195251, г. Санкт-Петербург, Политехническая ул., 29,  
тел/факс: 552-94-60, [www.stroikursi.spbstu.ru](http://www.stroikursi.spbstu.ru),  
[stroikursi@mail.ru](mailto:stroikursi@mail.ru)

**Приглашает специалистов организаций, вступающих в СРО,  
на курсы повышения квалификации (72 часа)**

Код	Наименование программы	Виды работ*
<b>Курсы по строительству</b>		
<b>БС-01-04</b>	«Безопасность и качество выполнения общестроительных работ»	п.1,2, 3, 5, 6, 7, 9, 10, 11, 12, 13, 14
<b>БС-01</b>	«Безопасность и качество выполнения геодезических, подготовительных и земляных работ, устройства оснований и фундаментов»	1,2,3,5
<b>БС-02</b>	«Безопасность и качество возведения бетонных и железобетонных конструкций»	6,7
<b>БС-03</b>	«Безопасность и качество возведения металлических, каменных и деревянных конструкций»	9,10,11
<b>БС-04</b>	«Безопасность и качество выполнения фасадных работ, устройства кровель, защиты строительных конструкций, трубопроводов и оборудования»	12,13,14
<b>БС-05</b>	«Безопасность и качество устройства инженерных сетей и систем»	15,16,17,18,19
<b>БС-06</b>	«Безопасность и качество устройства электрических сетей и линий связи»	20,21
<b>БС-08</b>	«Безопасность и качество выполнения монтажных и пусконаладочных работ»	23,24
<b>БС-12</b>	«Безопасность и качество устройства мостов, эстакад и путепроводов»	29
<b>БС-13</b>	«Безопасность и качество выполнения гидротехнических, водолазных работ»	30
<b>БС-14</b>	«Безопасность и качество устройства промышленных печей и дымовых труб»	31
<b>БС-15</b>	«Осуществление строительного контроля»	32
<b>БС-16</b>	«Организация строительства, реконструкции и капитального ремонта. Выполнение функций технического заказчика и генерального подрядчика»	33
<b>Курсы по проектированию</b>		
<b>БП-01</b>	«Разработка схемы планировочной организации земельного участка, архитектурных решений, мероприятий по обеспечению доступа маломобильных групп населения»	1,2,11
<b>БП-02</b>	«Разработка конструктивных и объемно-планировочных решений зданий и сооружений»	3
<b>БП-03</b>	«Проектирование внутренних сетей инженерно-технического обеспечения»	4
<b>БП-04</b>	«Проектирование наружных сетей инженерно-технического обеспечения»	5
<b>БП-05</b>	«Разработка технологических решений при проектировании зданий и сооружений»	6
<b>БП-06</b>	«Разработка специальных разделов проектной документации»	7
<b>БП-07</b>	«Разработка проектов организации строительства»	8
<b>БП-08</b>	«Проектные решения по охране окружающей среды»	9
<b>БП-09</b>	«Проектные решения по обеспечению пожарной безопасности»	10
<b>БП-10</b>	«Обследование строительных конструкций и грунтов основания зданий и сооружений»	12
<b>БП-11</b>	«Организация проектных работ. Выполнение функций генерального проектировщика»	13
<b>Э-01</b>	«Проведение энергетических обследований с целью повышения энергетической эффективности и энергосбережения»	
<b>Курсы по инженерным изысканиям</b>		
<b>И-01</b>	«Инженерно-геодезические изыскания в строительстве»	1
<b>И-02</b>	«Инженерно-геологические изыскания в строительстве»	2,5
<b>И-03</b>	«Инженерно-гидрометеорологические изыскания в строительстве»	3
<b>И-04</b>	«Инженерно-экологические изыскания в строительстве»	4
<b>И-05</b>	«Организация работ по инженерным изысканиям»	7

\*(согласно приказам Минрегионразвития РФ N 624 от 30 декабря 2009 г.)

**По окончании курса слушателю выдается удостоверение о краткосрочном повышении  
квалификации установленного образца (72 ак. часа)**

Для регистрации на курс необходимо выслать заявку на участие, и копию диплома об образовании по телефону/факсу: 8(812) 552-94-60, 535-79-92, , e-mail: [stroikursi@mail.ru](mailto:stroikursi@mail.ru).

**Инженерно-строительный журнал**

НАУЧНОЕ ИЗДАНИЕ

ISSN 2071-4726, 2071-0305

Свидетельство о государственной регистрации: ПИ №ФС77-38070, выдано Роскомнадзором

Специализированный научный журнал. Выходит с 09.2008.

Включен в Перечень ведущих периодических изданий ВАК РФ

Периодичность: 8 раз в год

**Учредитель и издатель:**

Санкт-Петербургский политехнический университет Петра Великого

**Адрес редакции:**

195251, СПб, ул. Политехническая, д. 29, Гидрокорпус-2, ауд. 245

**Главный редактор:**

Екатерина Александровна Линник

**Научный редактор:**

Николай Иванович Ватин

**Выпускающий редактор:**

Ксения Дмитриевна Борщева

**Литературный редактор:**

Крупина Анастасия

**Редакционная коллегия:**

д.ф.-м.н., доцент Р.А. Абдикаримов;  
 д.т.н., проф. В.В. Бабков;  
 к.т.н., проф. А.И. Боровков;  
 д.т.н., проф. Н.И. Ватин;  
 PhD, проф. М. Вельжкович;  
 к.т.н., М.Р. Гарифуллин;  
 д.т.н., проф. Э.К. Завадскас;  
 д.ф.-м.н., проф. М.Н. Кирсанов;  
 D.Sc., проф. М. Кнежевич;  
 д.т.н., проф. В.В. Лалин;  
 д.т.н., проф. Б.Е. Мельников;  
 д.т.н., академик М.М. Мирсаидов;  
 д.т.н., проф. Ф. Неправишта;  
 д.т.н., проф. Р.Б. Орлович;  
 Dr. Sc. Ing., professor  
 Л. Пакрастиньш;  
 Dr.-Ing. Habil., professor  
 Х. Пастернак;  
 д.т.н., проф. А.В. Перельмутер;  
 д.т.н., проф. М.Р. Петриченко;  
 д.т.н., проф. В.В. Сергеев;  
 д.ф.-м.н., проф. М.Х. Стрелец;  
 д.т.н., проф. О.В. Тараканов;  
 д.т.н., проф. Б.Б. Телтаев;  
 д.т.н., проф. В.И. Травуш;  
 д.т.н., проф. Д. Унгерман;  
 д.т.н., проф. С.В. Федосов

Дата выхода: 05.07.2019

**Содержание**

Кафя М.А., Ник-Хуш К. Параметры распределительного клапана в жёстком стальном каркасе при циклическом нагружении	3
Брянцев А.А., Абсиметов В.Э., Лалин В.В. Влияние отверстий на деформативность стенки сварной гофрированной балки	18
Лу Ч., Чао Г. Несущая способность крепёжной стальной трубы строительных лесов	35
Ислам С. Легкие бетоны с крупным керамическим заполнителем	46
Ванг Х., Хе Я., Пан Ю., Ю Г. Механические свойства магнево-калий-фосфатного цемента	59
Лалин В.В., Рыбаков В.А., Дьяков С.Ф., Кудинов В.В., Орлова Е.С. Полусдвиговая теория В.И. Сливкера в задачах устойчивости тонкостенных стержней	66
Кантаржи И.Г., Железняк М.И., Аншаков А.С. Численное моделирование нелинейных гидродинамических процессов береговой зоны	80
Коянкин А.А., Митасов В.М., Деордиев С.В. Совместность деформирования пустотной плиты с ригелем	93
Козлов Д.В., Гебрехивот А.А. Эффективность цифровых моделей рельефа и моделей Нэша в прогнозировании стока	103
Базаров Д.Р., Мавлянова Д.А. Численные исследования длинноволновых процессов в бьефах гидроузлов и водохранилищ	123

© ФГАОУ ВО СПбПУ, 2019

© Иллюстрация на обложке: Илья Смагин

**Контакты:**

E-mail: mce@spbstu.ru

Web: <http://www.engstroy.spbstu.ru>

*Magazine of Civil Engineering*

SCHOLAR JOURNAL

ISSN 2071-4726, 2071-0305

Peer-reviewed scientific journal

Start date: 2008/09

8 issues per year

**Publisher:**Peter the Great St. Petersburg  
Polytechnic University**Indexing:**Scopus, Russian Science Citation  
Index (WoS), Compendex, DOAJ,  
EBSCO, Google Academia, Index  
Copernicus, ProQuest, Ulrich's Serials  
Analysis System**Corresponding address:**245 Hydro Building, 29  
Polytechnicheskaya st., Saint-  
Petersburg, 195251, Russia**Editor-in-chief:**

Ekaterina A. Linnik

**Science editor:**

Nikolay I. Vatin

**Technical editor:**

Ksenia D. Borshcheva

**Editorial board:**

R.A. Abdikarimov, D.Sc., associate  
professor  
V.V. Babkov, D.Sc., professor  
A.I. Borovkov, PhD, professor  
M. Veljkovic, PhD, professor  
M. Garifullin, PhD, postdoctorant  
E.K. Zavadskas, D.Sc., professor  
M.N. Kirsanov, D.Sc., professor  
M. Knezevic, D.Sc., professor  
V.V. Lalin, D.Sc., professor  
B.E. Melnikov, D.Sc., professor  
M.M. Mirsaidov, D.Sc., professor  
F. Nepravishta, D.Sc., professor  
R.B. Orlovich, D.Sc., professor  
L. Pakrastinsh, Dr.Sc.Ing., professor  
H. Pasternak, Dr.-Ing.habil.,  
professor  
A.V. Perelmuter, D.Sc., professor  
M.R. Petrichenko, D.Sc., professor  
V.V. Sergeev, D.Sc., professor  
M.Kh. Strelets, D.Sc., professor  
O.V. Tarakanov, D.Sc., professor  
B.B. Teltayev, D.Sc., professor  
V.I. Travush, D.Sc., professor  
S.V. Fedosov, D.Sc., professor

Date of issue: 05.07.2019

## Contents

Kafi, M.A., Nik-Hoosh, K. Geometry of steel slit dampers in a braced steel frame under cyclic loading	3
Bryantsev, A.A., Absimetov, V.E., Lalin, V.V. The effect of perforations on the deformability of welded beam with corrugated webs	18
Lu, Z., Chao, G. Bearing capacity of fastener steel tube full hall scaffolds	35
Islam, S. Aggregate concrete factor ( $\lambda$ ) for burnt clay brick aggregate concrete	46
Wang, H., He, Y., Pan, Y., Yu, G. Mechanical properties of magnesium potassium phosphate cement	59
Lalin, V.V., Rybakov, V.A., Diakov, S.F., Kudinov, V.V., Orlova, E.S. The semi-shear theory of V.I. Slivker for the stability problems of thin-walled bars	66
Kantardgi, I.G., Zheleznyak, M.I., Anshakov, A.S. Numerical modeling of nonlinear hydrodynamics of the coastal areas	80
Koyankin, A.A., Mitasov, V.M., Deordiev, S.V. The compatibility of deformation of the hollow-core slab with beams	93
Kozlov, D.V., Ghebrehiwot, A.A. Efficacy of digital elevation and Nash models in runoff forecast	103
Bazarov, D.R., Mavlyanova, D.A. Numerical studies of long-wave processes in the reaches of hydrosystems and reservoirs	123

© Peter the Great St. Petersburg Polytechnic University. All rights reserved.

© Illustration – Ilya Smagin

E-mail: [mce@spbstu.ru](mailto:mce@spbstu.ru)Web: <http://www.engstroy.spbstu.ru/eng/index.html>





DOI: 10.18720/MCE.87.1

## The geometric shape effect of steel slit dampers in their behavior

**M.A. Kafi\*, K.Nik-Hoosh**

*Semnan University, Semnan, Iran*

\* E-mail: [mkafi@semnan.ac.ir](mailto:mkafi@semnan.ac.ir)

**Keywords:** yield damper; cyclic loading; flexural behavior; shear behavior; dissipated energy

**Abstract.** Dampers are excellent for improving the performance of steel structures and protecting them against earthquakes. The Steel Slit Damper (SSD) is a type of damper designed to be replaced after being damaged under a strong earthquake. Aiming to investigate the effects of the number of blade rows and optimize the length-to-width ratio of blades, seven specimens of identical thickness with one or two rows of blades and three length-to-width ratios were tested and subjected to static cyclic loading. Different parameters, including the force capacity, displacement capacity, effective stiffness, dissipated energy, ductility, and damage indices, were calculated from the experimental results and compared. The results indicate the evident advantage of dampers with two rows of blades in terms of the force capacity, effective stiffness, and absorbed energy, as the highest force capacities corresponding to the two groups exhibited a 61.6 % difference. Furthermore, given the advantage of dampers with two rows of blades and based on the observations, an optimal blade length-to-width ratio ( $h/b$ ) of 1.58 is recommended to prevent buckling.

### 1. Introduction

In recent decades, the use of energy dissipation systems experienced rapid growth in construction. Such systems can be generally categorized into active, passive, semi-active, and hybrid groups. Among the said dampers, the passive damper does not require an external source of energy. Unlike common methods of designing earthquake-resistant structures that absorb most of the seismic energy by yielding at certain points (typically at the ends of beams and columns in the moment frame system), in passive control systems, the energy is dissipated by certain devices known as seismic dampers. These systems offer several advantages, including (1) absorbing non-elastic deformations – thus allowing for a considerable reduction of damages to the main structure; (2) reducing the lateral structural displacements that, for its part, limits the damage to non-structural components, and (3) facility of inspection, repair, and replacement without requiring the evacuation of the building [1]. As shown in Figure 1 several Steel Slit Dampers (SSDs) – including the ADAS [2], TADAS [3], and the double X-shaped [4] – have been proposed as passive control systems.

Chan et al. [5] introduced the SSD for the first time in a study on the effect of slits in three different configurations. In their study on these dampers, Teruna et al. [6] showed that slits with convex edges prevent low cycle fatigue and are far more stable under cyclic loading. In another study, the effect of the slit was investigated against variable height, concluding that a configuration with thinner blades in the middle and thicker ones on the sides improves energy dissipation to some extent under cyclic loading [7]. The effect of different slits shapes (blades or bands with variable cross-section) was also investigated, showing that dumbbell-shaped, gradually-narrowing blades offer a better earthquake performance [8]. A study on this type of damper addressed dampers with variable cross-section and (fixed) large thickness. Given the large thickness of their bands, such dampers are resistant to buckling. The said study investigated the optimal aspect ratio for damper blades [9].

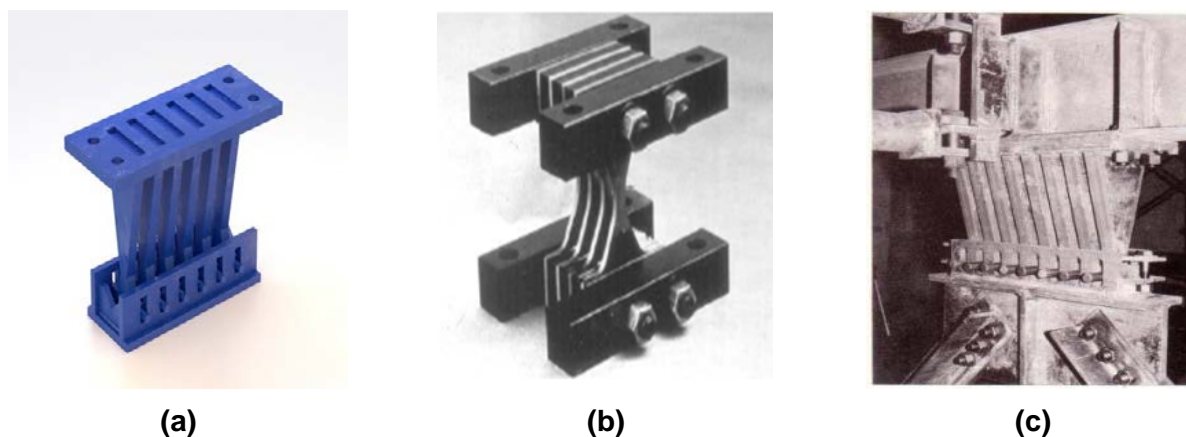
---

Kafi, M.A., Nik-Hoosh, K. The geometric shape effect of steel slit dampers in their behavior. Magazine of Civil Engineering. 2019. 87(3). Pp. 3–17. DOI: 10.18720/MCE.87.1.

Кафя М.А., Ник-Хуш К. Влияние геометрической формы распределительных клапанов на их характеристики // Инженерно-строительный журнал. 2019. № 3(87). С. 3–17. DOI: 10.18720/MCE.87.1.

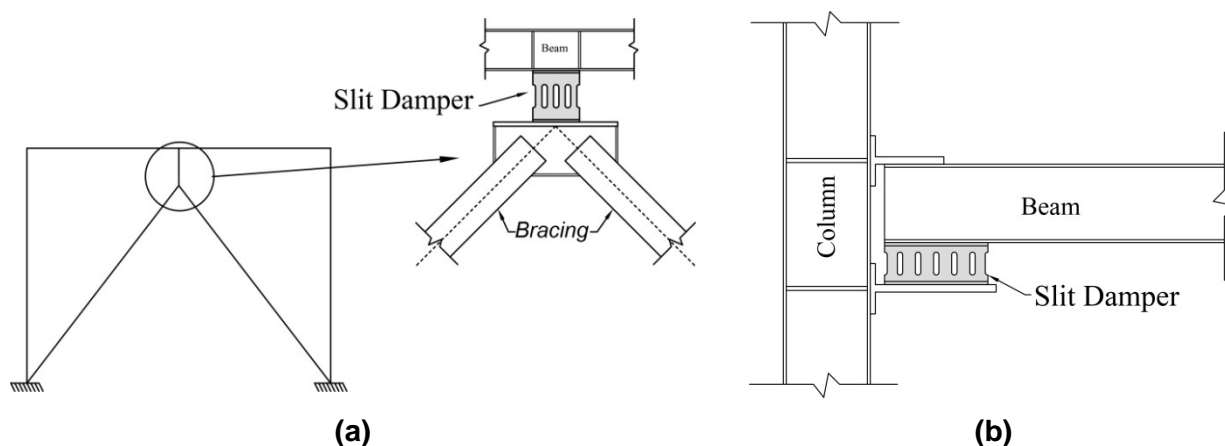


This open access article is licensed under CC BY 4.0 (<https://creativecommons.org/licenses/by/4.0/>)



**Figure 1. a) TADAS damper b) double X-shaped damper c) TDAS damper.**

This type of damper is employed in both bracing (Figure 2a) and beam-to-column (Figure 2b) connections. These dampers are placed in the frame such a way that reach to yield strength due to shear, bending or axial force. In order to dissipate energy, it is necessary to consider how to embed them in a frame to undergo deformation due to the relative displacement of the floor which caused by the lateral load; otherwise, they will not function and dissipate energy properly.



**Figure 2. Different uses of the SSD a) Integration into bracing connection and b) Integration into beam-to-column connection.**

Lin et al. [10] developed a buckling-restrained damper with a replaceable, composite, steel – concrete shear plate protection. Twelve specimens were tested in order to investigate effective design parameters such as the type of steel, the number of internal panels, etc. on the seismic behavior of dampers. Furthermore, relations were suggested to estimate the elastic stiffness and the ultimate strength of the dampers. Xu et al. [11] investigated four types of shear panel dampers by cyclic tests using a new type of low-yield-strength steel (BLY160) to study the seismic behavior. Chaofeng et al. [12] developed a model of the hysteretic mechanical characteristics of low-yield-strength shear panel dampers under extreme plastic deformation and verified it using other models and experimentally testing the dampers. In another study, the authors addressed low-cycle fatigue in small shear panel dampers made of low-yield-strength steel under monotonic and cyclic loading [13]. They also investigated the possibility of predicting the performance of shear panel dampers using finite-element software, claiming this approach to be useful as regards this type of damper [14]. Chen et al. [15] made an attempt at the numerical simulation of large deformations in Shear Panel Dampers (SPD) by the Smoothed-Particle Hydrodynamics (SPH) method. Shen et al. [16] analytically investigated the seismic behavior of concentrically braced frames with and without brace buckling. Given the dependence of the performance of Steel Shear Panel Dampers (SSPD) on the stiffener arrangement and the type of steel, Deng et al. [17] addressed the optimization of the shapes of these dampers aiming to improve their low-cycle fatigue performance. Moreover, in a study, the authors proposed a method for designing buckling plates in buckling-restrained SPDs by examining five test dampers, evaluating their experimental results using ABAQUS. Bazzaz et al. [18] proposed and evaluated the new bracing system using nonlinear software. Andalib et al. [19] experimentally investigated three types of steel rings and their ductility in bracing frames they also performed a finite element study using ANSYS software. Latour et al. [20] made an attempt at the experimental and numerical investigation of two types of friction dampers in beam-to-column metallic connections that can limit structural damages inflicted by severe seismic conditions. Their experimental and numerical results verified the effectiveness of this type of damper, offering a considerable improvement in design requirements. Zeynali



et al. [21] used lead rubber damper which was constructed with steel core and rubber plates in chevron concentrically braced frames and studied their behavior experimentally and numerically.

Qu et al. [22] studied a new type of seismic dampers with replaceable U-shaped metal plates. Their study involved seven experimental specimens, reporting that all specimens exhibited stable hysteretic performance and excellent capacity for energy dissipation. Furthermore, replacing the damaged U-shaped metal plates led to favorable results under consecutive loading. Furthermore, relations were presented to estimate the yield strength and the ultimate strength of the dampers. Sahoo et al. [23] carried out an experimental investigation of the shear-and-flexural metallic yielding dampers under cyclic loading. The tested dampers included two types of plates that yielded under shear or flexural loading. The plate dimensions varied in this study and covered different parameters including the load-bearing capacity, energy dissipation, and ductility. Furthermore, a numerical study was carried out, delineating a design process.

According to previous studies, in the present study, focusing on steel slit dampers, the effect of geometric characteristics and blade arrangement, and the relative dimensions of gaps with constant cross-section and fixed thickness on cyclic behavior and hysteresis curves are studied. According to the results of experimental tests on 7 specimens, the effect of the different dimensions on the shear force, ductility, absorbed energy and etc. the most suitable arrangement of the slits and the optimal ratio of geometric dimensions for the dampers are suggested. The most prominent feature of this research is the installation and testing of dampers inside the braced frame in order to approach the behavior of the dampers to the actual conditions and to observe the effect of the frame on their behavior. Also, in this study, with the aim of using a large range of geometrical dimensions of the damper section, beam girder was used to construct dampers.

## 2. Method

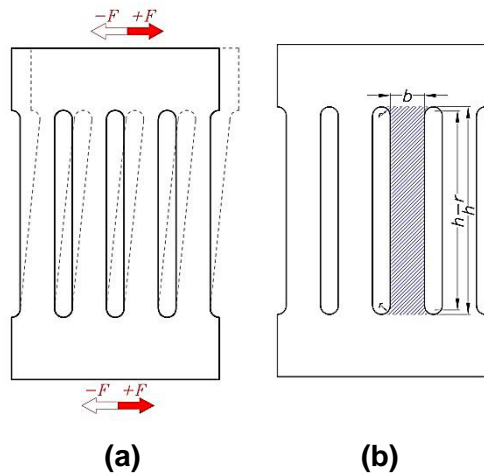
In order to investigate the behavior of slit dampers in braced steel frame under cyclic loading, an experimental method was used. In this section, firstly existing equations for calculation of elastic stiffness, yield force, and yield displacement were presented for slit dampers, and then the specification of experimental specimens were introduced.

### 2.1. Analytical Relations

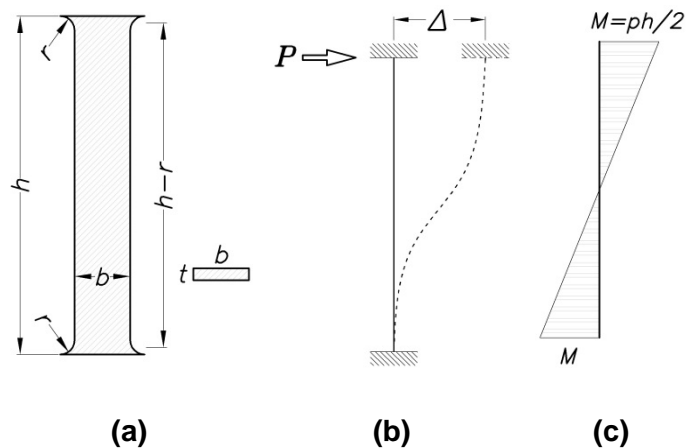
Relations are presented in this section for elastic stiffness, force, and the yield displacement of the damper based on the principles of solid mechanics. These relations can be used to design dampers in proportion to the seismic demands.

#### 2.1.1. Elastic Stiffness

Figures 3 and 4 illustrate the behavior of a blade using an equivalent fixed-end beam. The simplified behavior is relevant when the stiffness of the blade is much lower than that of the supports, which considerably simplifies the calculations.



**Figure 3. Schematic view of damper mechanism**  
a) The mode of deflection of SSD  
b) Blade selected.



**Figure 4. Blade equivalent to a fixed-end beam**  
a) Blade  
b) Blade deformation under lateral loading  
c) Moment diagram.

In dampers with one row of blades, the geometry suggests that this simplified behavior is usable. However, it can be shown for dampers with two rows of blades, that the condition is only satisfied when the  $h/b$  ratio (Figure 4) is enough larger than the  $2r/c$  (where  $r$  is the curvature radius at the end of the blades and  $2r$  is the free distance between two blades and  $c$  is the distance between two rows in dampers with two rows of blades).

Given the large value of  $h/b$  ratio, shear deformation has a significant contribution to the total deformation, which must be taken into account. With the above discussions, the elastic stiffness of a blade can be calculated using Eq. (1).

$$k_1 = \frac{Etb^3}{h^3(1+3b^2/h^2)}, \quad (1)$$

where  $E$  represents the elastic modulus of the damper steel, and the parameters corresponding to the geometry of the damper are presented in Figure 4.

The relation ignores the small curvature at the end of the blade, therefore if  $r$  is smaller than  $h$ , it is best to replace  $h$  with  $h-r$  when using Eq. (1) to improve the accuracy of results. Knowing the stiffness of a single blade, and given the uniformity across all blades, the elastic stiffness can be calculated for dampers with  $n$  blades in a single row and  $2n$  blades in two rows (two rows of blades in  $n$  columns) by using Eq. (2) and Eq. (3) respectively.

$$k = nk_1; \quad (2)$$

$$k = \frac{nk_1}{2}. \quad (3)$$

As explained above  $2r$  is the free distance between the two blades. Assuming that the damper is similar to a frame, the blades have the role of the columns and middle elements have the role of the beams. Given that, the cross-section of the beams and its columns is rectangular with a constant width  $t$  (the thickness of the damper), it is obvious that  $h/b$  indicates the stiffness of the blades and  $2r/c$  represents the softness of the middle elements. If the beams are not hard enough, the plastic hinge is formed in the middle element instead of the blade, which contradicts the initial assumptions so it must be noted that the  $h/b$  ratio is more than 4.2 times the  $2r/c$ , which satisfies the conditions necessary for using the above relations.

### 2.1.2. Yield Force and Displacement

Assuming the dominance of flexural behavior and formation of plastic hinges at both ends of each blade and by referring to the moment diagram in Figure 4, the yield force of a one- or two-row damper with  $n$  blade columns under bending can be formulated according to Eq. (4).

$$P_{yb} = \frac{nb^2tf_y}{3h}, \quad (4)$$

where  $f_y$  is the yield strength of the damper steel. For dampers with two rows of blades, in case  $c$  is enough larger than  $b$ , the blade yields at both ends, and Eq. (4) remains relevant for calculating the yield force.

Knowing the yield force from Eq. (4) and elastic stiffness from Eqs. 2 or 3, yield displacement can be calculated from Eq. (5).

$$\Delta_y = \frac{P_y}{k}. \quad (5)$$

In case the shape factor of a rectangular cross-section ( $Z/S = 1.5$  where  $Z$  is plastic section modulus and  $S$  is elastic section modulus for rectangular section) is used, Eq. (6) can be obtained from Eq. (5) to estimate the plastic force of one- or two-row damper with  $n$  blade columns.

$$P_p = \frac{nb^2tf_y}{2h}. \quad (6)$$

Under the dominance of the shear behavior, the yield force of one- or two-row damper with  $n$  blade columns for a rectangular cross-section is obtained from Eq. (7).

$$P_{ys} = \frac{2nbt f_y}{3\sqrt{3}}. \quad (7)$$

Depending on the type of the dominant behavior, the yield force and the maximum apparent force of the dampers can be obtained analytically from the following relations [5].

$$P_y = \min \left\{ n \frac{f_y tb^2}{3h}, n \frac{2f_y tb}{3\sqrt{3}} \right\}, \quad P_u = \min \left\{ n \frac{f_u tb^2}{3h}, n \frac{2f_u tb}{3\sqrt{3}} \right\}. \quad (8)$$



As it was mentioned earlier, the first term in the Eq. (8) was obtained assuming the yield of the damper under bending, whereas in the second term the damper is assumed to yield under shear. In Eq. (8)  $f_u$  is the maximum stress. The factor  $2/3$  in the second term of the above equations responds to the fact that the ratio of the average to maximum shear stresses is  $2/3$  when the  $b/h$  ratio is less than 1 in the elastic range.

### 2.1.3. Slit Damper Analysis Mechanism

The second moment of area  $I$  is calculated from the prismatic geometry of the blades [5].

$$I = tb^3/12. \quad (9)$$

When the moment is large enough, the bending moment at the end of the blades brings the farthest fibers to the yield stress. As a result, plastic hinges form at both ends by rotation  $\theta_p$ . For geometrical beams, the full plastic moment  $M_p$  is obtained using the following relation:

$$M_p = f_y \frac{tb^2}{4}. \quad (10)$$

The ultimate damper force can be calculated based on the failure mechanism when the entire ultimate moment of the beam is used up in a plastic hinge. Based on conservation of energy, and assuming full elastic-plastic behavior for the materials, the following equation is obtained.

$$P_y \delta_p = 2nM_p \theta_p. \quad (11)$$

Using the geometrical relations of Figure 5 the plastic displacement that the damper can withstand can be expressed in terms of plastic rotation as follows [5]:

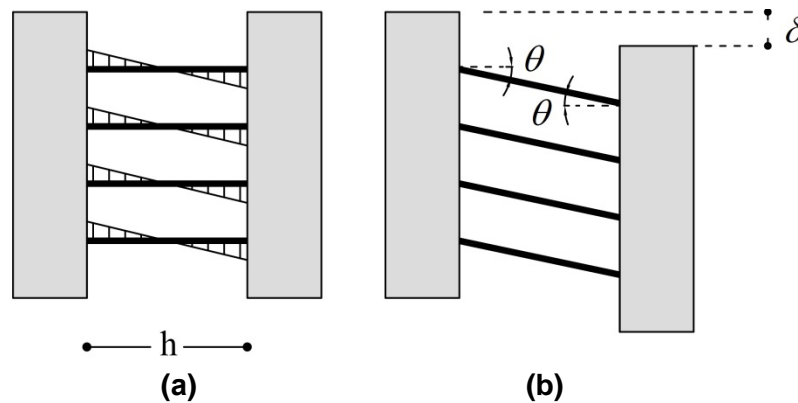


Figure 5. a) Bending moment in the single-row damper; b) the deformed single-row damper.

$$\delta_p = h \tan \theta_p. \quad (12)$$

For small rotations where  $\tan \theta_p \approx \theta_p$  Eq. (12) can be rewritten as follows:

$$\delta_p = h \theta_p. \quad (13)$$

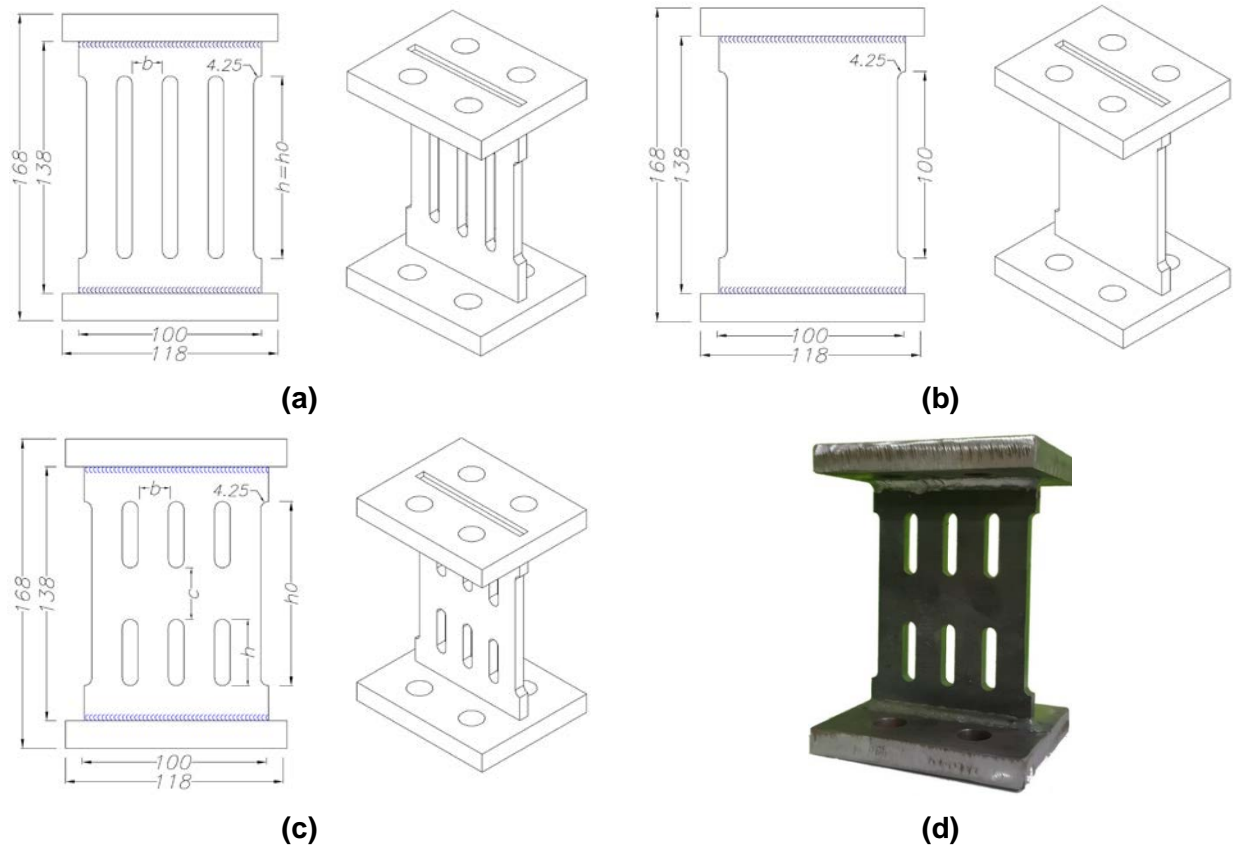
By replacing Eqs. 10 and 13, Eq. (11) can be rewritten as follows:

$$P_y = \frac{2nM_p}{h} = \frac{nf_y tb^2}{2h}. \quad (14)$$

In order to investigate the behavior of slit dampers in braced steel frame under cyclic loading, an experimental method was used.

## 2.2. Specimen Details

In order to achieve the study objectives (investigate the geometric characteristics and blade arrangement, observe the effect of the frame on SDD's behavior) seven experimental specimens were made and tested. Three simple slit specimens with a single row of four uniform blades, three specimens with four uniform blades in two rows, and a no-slit one – the reference – were tested. The blade height ( $h$ ) was assumed as the variable whereas the thickness ( $t$ ) and width ( $b$ ) of the blades were fixed. Accordingly, besides investigating the rows of dampers, the dimensionless  $h/b$  ratio of the blades was also discussed as the main variable of the parametric study. Figure 6 illustrates the details of the slits and the dimensions of the specimens DFF, DSSH, DSDH and also a real specimen of DSDH before the test. The geometrical parameters illustrated in Figure 6 are presented in Tables 1 and 2 for specimens with one and two rows of slits, respectively.



**Figure 6. The geometry and parameters determining the specifications of the specimens (all sizes are in mm) a) DSSH b) DFF c) DSDH d) DSDH before the test.**

**Table 1. The geometrical specifications (mm) of the specimens with one row of blades.**

Specimen	$h/b$	$h_0 = h$	$b$	$t$
DSSH1	4.85	80	16.5	8
DSSH2	5.45	90	16.5	8
DSSH3	6.06	100	16.5	8

**Table 2. The geometrical specifications (mm) of the specimens with two rows of blades.**

Specimen	$h/b$	$c$	$h$	$h_0$	$b$	$t$
DSDH1	1.28	28	21	80	16.5	8
DSDH2	1.58	28	26	90	16.5	8
DSDH3	1.88	28	31	100	16.5	8

### 2.3. Material Specifications

Table 3 presents the mechanical specifications of the steel used to make a prism specimen with 2.7 in 6 mm<sup>2</sup> rectangular cross-section obtained by standard tensile testing [24]. St 37 steel plate is in DIN 17100 standard.

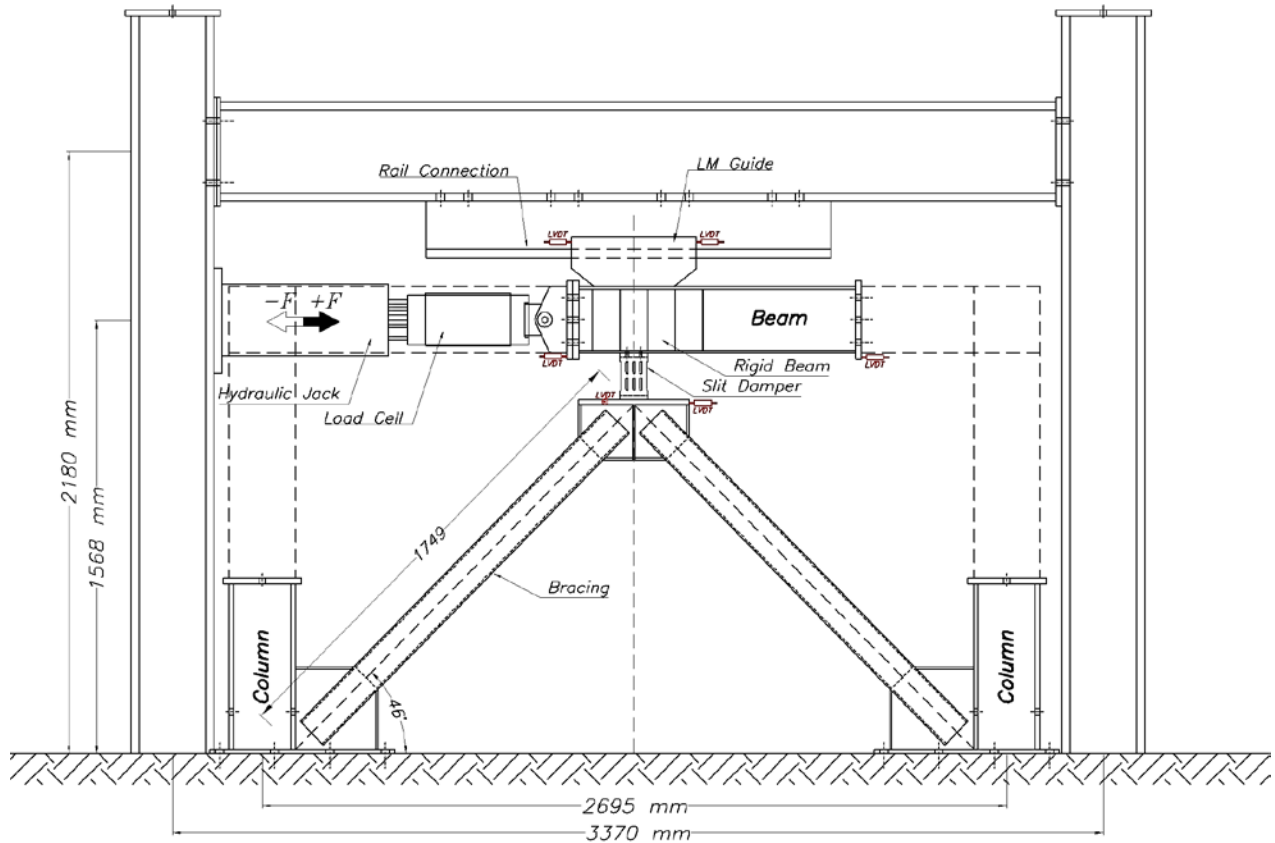
**Table 3. Steel Properties.**

Specimen	Maximum strain	Ultimate strength N/mm <sup>2</sup>	Yield strength N/mm <sup>2</sup>
St 37	0.4	434	250

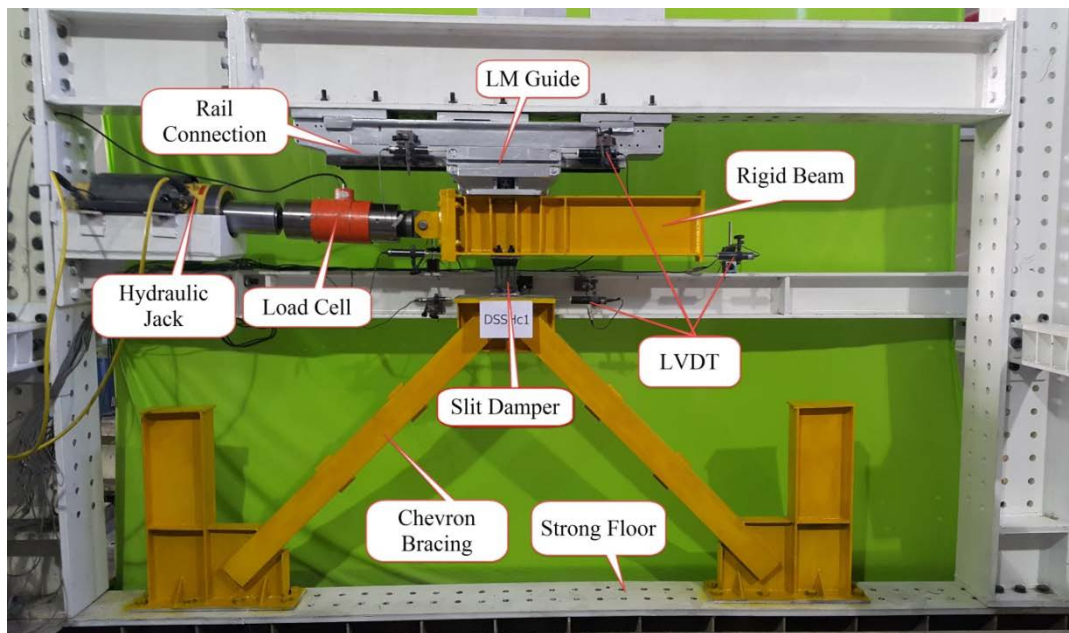
### 2.4. The Arrangement and Laboratory Equipment

In order to establish real conditions and investigate the behavior of the damper inside the frame, the specimens were installed on a chevron brace (Figures 7 and 8). As a general rule in the design of the frame and braces, these elements were calculated so that the frame and braces remain in the elastic behavior zone when the damper is in the plastic zone under cyclic loading. Accordingly, the maximum force capacity of the dampers, which was related to the DFF specimen, was calculated and with the obtained capacity, the structural calculations and frame elements including the beam, column, braid and connection sheets were done. The specimens were attached to the braces at the bottom and to the rigid beam at the top and then tested. To prevent the rotation of the rigid beam (simulating a rigid ceiling) and the displacement of the loading jack and the rigid beam in a linear path, and to restrict their out-of-plane movements, the rigid beam was connected to a Linear Motion Guide (LMguide) at the top. Furthermore, given that the beam-column connection is a hinge, the connection was removed by simulating the equivalent frame behavior.





**Figure 7. Test layout design for cyclic loading.**



**Figure 8. Test layout system and the installations.**

A hydraulic jack with 100 ton capacity in tension and 200 ton in compression was used to test the specimens. Furthermore, a 100-ton tension/compression load cell was employed to measure the force exerted on the specimen. Four 4 cm LVDT units were used to record the specimen displacements. Moreover, three LVDT units were also placed on the brace plates to investigate in-plane and off-plane movements. The test layout and the equipment are illustrated in Figures 7 and 8. Furthermore, Figure 9 shows the LMguide layout and the exact location of the LVDT units.

The specimens were subjected to static, cyclic loading according to the test plan. The loading process was displacement controlled. An incremental loading history based on the ATC-24 protocol [25] was used to apply the said loading cycle. Figure 10 illustrates the loading protocol applied to the specimen. In this protocol, each displacement is applied to the specimen three times back and forth, continuing until it is destroyed.



Figure 9. The LMguide and the location of the LVDT units.

## 2.5. Test Plan and Layout

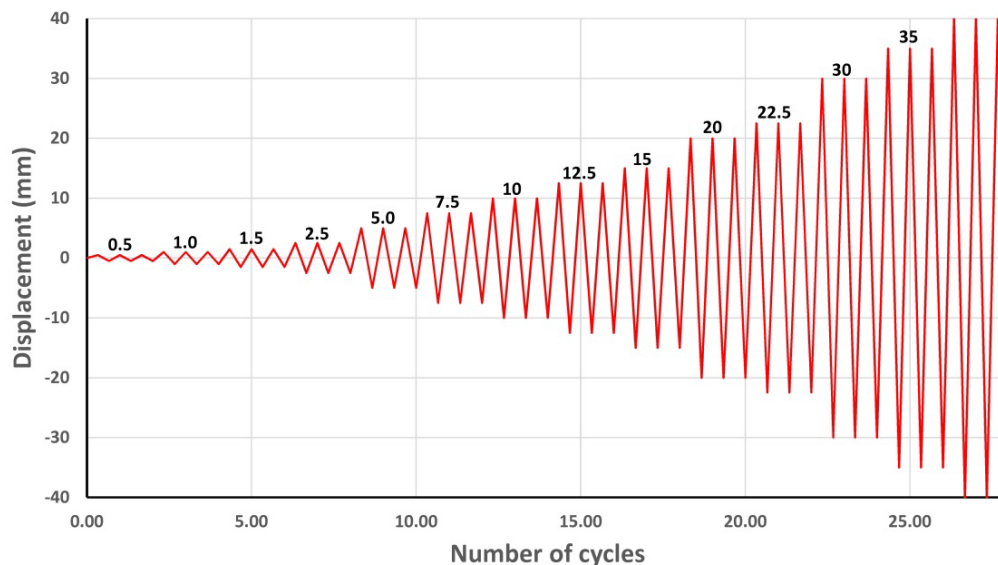


Figure 10. The incremental cyclic loading history [25].

## 3. Results and Discussion

In this section, after presenting the outputs of the experimental study, the results are reviewed, compared, and analyzed. The said outputs include cyclic behavior, effective stiffness, dissipated energy, and equivalent viscous damping. Furthermore, a damage index was also calculated and presented for the specimens.

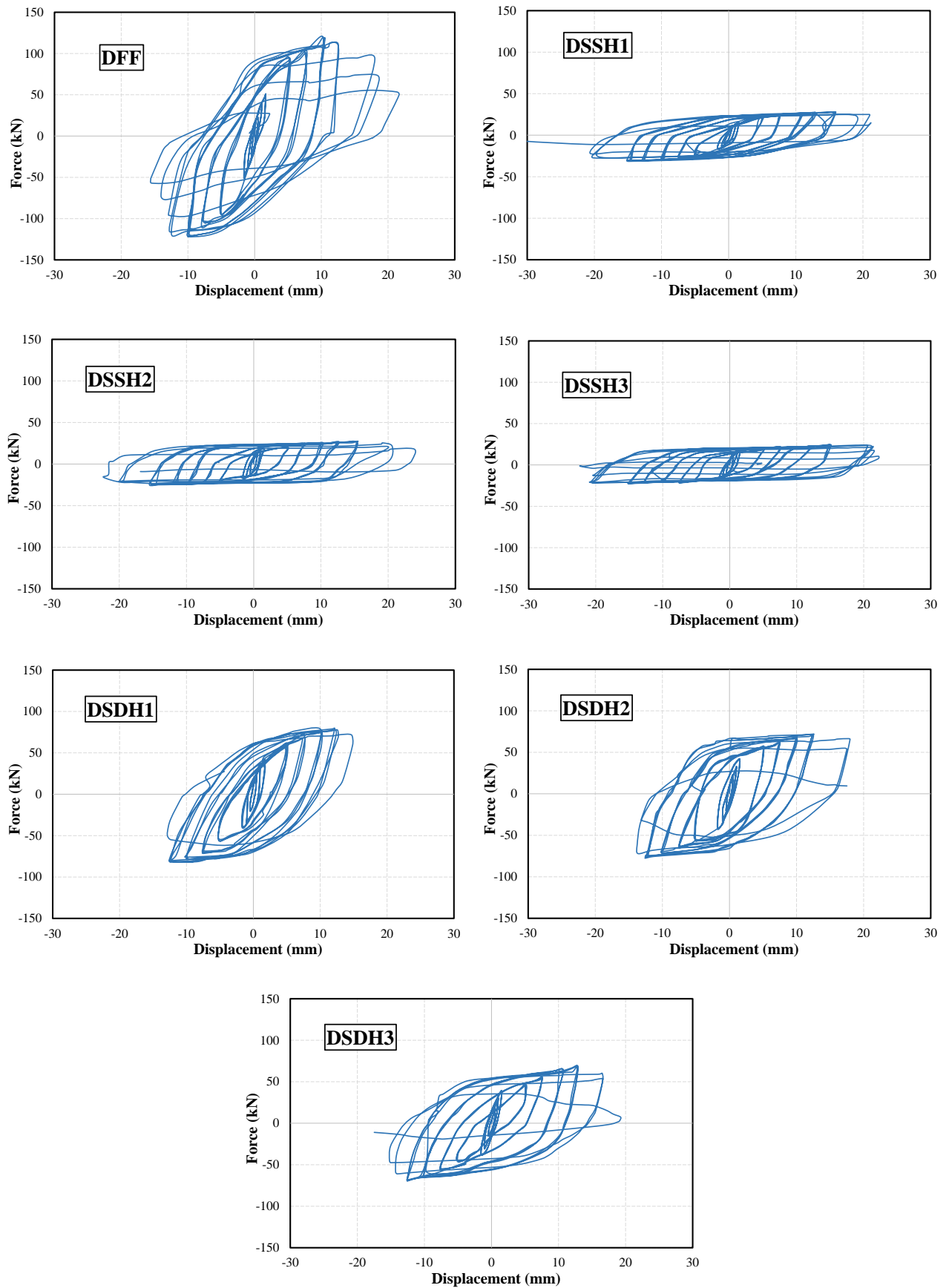
### 3.1. The Cyclic Behavior of the Specimens

The specimens were tested by static cyclic loading according to the scheme presented in Figure 10, recording the force variations, displacements, and other parameters. The resulting cyclic diagrams under the said loading are presented in Figure 11. Moreover, Figure 12 presents the envelope curve of the specimens. The envelope curve is plotted by specifying the maximum force endured in every three cycles (equal displacements) and connecting the maximum points obtained for the cycles.

Table 4 presents the maximum force and maximum displacement results, representing the force and displacement capacities of each specimen. The maximum displacement corresponds to a force that does not exhibit a drop of over 20 % relative to the maximum force.

It is safe to conclude from Table 4 that the load-bearing capacity of the specimens increases by reducing the  $h/b$  ratio (the blade height) and increasing blade rows from one to two. A comparison of the maximum displacement of the specimens shows it to decrease by adding to the number of blade rows. It must be noted that reducing the  $h/b$  ratio translates into the dominance of the shear behavior over the flexural behavior in the blades. In specimens with identical number of blade rows, DSSH2 and DSDH2, exhibiting 40 and 1.9 % improvements relative to the reference specimen, correspond to the highest displacement capacities, whereas DSSH1 and DSDH1, with 17.58 % increase and 16 % reduction in comparison to the reference specimen, showed the smallest displacement capacities in each group. Generally speaking, an increase in the  $h/b$  ratio increases the maximum displacement, however, the increase is the largest in a certain range. Figure 13 illustrates the deformed DSSH1 and DSDH1 at their respective maximum force capacities.





**Figure 11. The cyclic force-displacement behavior of the specimens.**

Given the fact that the two specimens (DSSH1 and DSDH1) correspond to the smallest  $h/b$  ratios in their respective groups, they offered the largest load-bearing capacities. The deformation of the specimens shows that yield takes place inside the blade and the outside region is not affected much, which verifies the assumptions made to simplify the analytical relations.

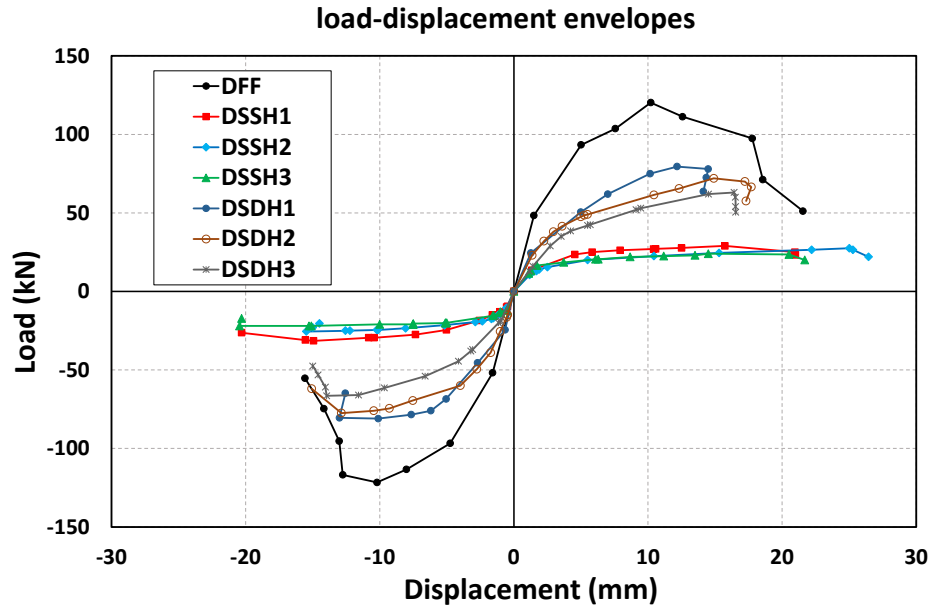


Figure 12. The envelope curves of the tested specimens.

Table 4. Maximum force and displacement in the specimens.

Specimen	<i>b</i>	<i>t</i>	<i>h</i>	<i>c</i>	Maximum Force (kN)	Maximum Displacement (mm)
DFF	100	8	100	---	118	17.86
DSSH1	16.5	8	80	---	31.5	21
DSSH2	16.5	8	90	---	27.5	25
DSSH3	16.5	8	100	---	25	21.3
DSDH1	16.5	8	26	28	82	15
DSDH2	16.5	8	31	28	77.5	18.2
DSDH3	16.5	8	36	28	66.5	16.7



Figure 13. The deformation of DSSH1 and DSDH1 at maximum force.

### 3.2. Effective Stiffness

The elastic potential energy of the damper can be calculated in each cycle using the effective stiffness. This energy tends to restore the damper to its initial conditions. It is evident that, with the damper entering the plastic phase, the energy is not sufficient to restore the damper and is mostly supplied by the exerted external force. The elastic potential energy and the energy dissipated in one cycle are presented in Figure 14. The effective stiffness ( $K_{i,eff}$ ) can be calculated using Eq. (15).

$$K_{i,eff} = \frac{\left( |P_{i,max}^+| + |P_{i,max}^-| \right)}{\left( |\delta_{i,max}^+| + |\delta_{i,max}^-| \right)}. \quad (15)$$

All parameters in this relation are defined and illustrated in Figure 14.

Figure 15 plots the changes in the effective stiffness of the specimens against displacement. According to Eq. (15), the higher the force endured at a small displacement, the higher the effective stiffness of the specimen. The changes in the effective stiffness curve indicate it to be large at small displacements but to decrease drastically to a fixed level by increasing the displacement.

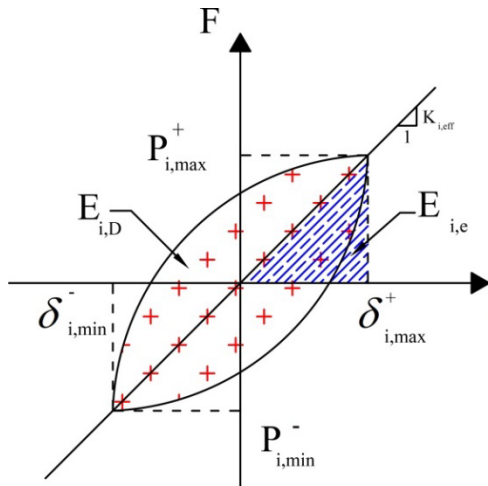


Figure 14. The effective stiffness and the cyclic energy in cyclic loading [9].

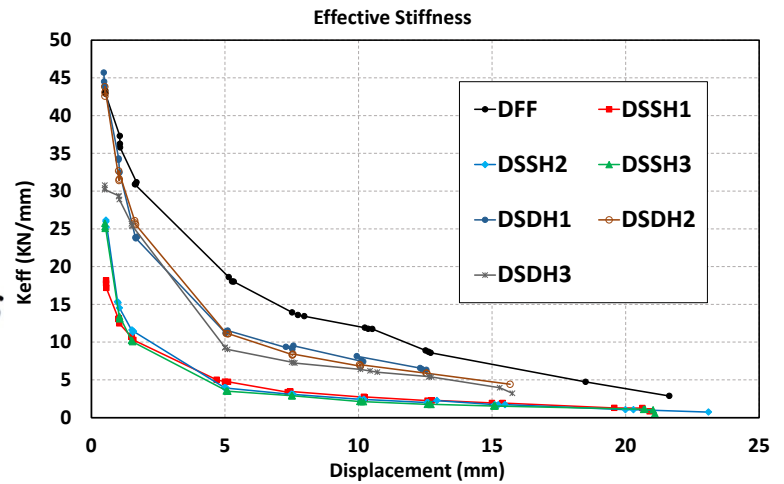


Figure 15. Effective Stiffness of the Specimens.

Figure 15 indicates the reference specimen to correspond to the highest effective stiffness, as well as initial stiffness, followed by the specimens with two rows of blades and those with one row of blades. Equation 15 shows that the double-row specimens exhibited a higher stiffness than the single-row ones for the same displacement. Specimens with a similar number of blades were found to be similar in terms of stiffness, however, it is safe to say that, in general, the effective stiffness is reduced by increasing the  $h/b$  ratio. The behavior of the specimens is also suggestive of that the effective stiffness difference between the specimens is rapidly reduced by further increasing the displacement. A comparison of the diagrams shows the rate of decrease of the effective stiffness is much higher in specimens with two rows of blades (DSDH with dominant shear behavior) than in those with a single row of blades (DSSH with dominant flexural behavior). It is evident that the high softening rate (drastic drop in stiffness) is not favorable in structures and promotes the formation of a soft story.

### 3.3. Dissipated Energy and Equivalent Viscous Damping

Dissipated energy is the hysteresis area in cyclic loading. The dissipated energy was calculated for all specimens for different displacements as illustrated in Figure 16 together with the cumulative dissipated energy. The curves suggest that specimens with two rows of blades (DSDH) are much stronger energy dissipators than those with a single row. In other words, it can be said that the dissipated energy increases under the dominance of shear behavior. In specimens with two rows of blades, energy absorption increases at larger  $h/b$  ratios, however, DSDH2 exhibited the highest energy absorption among single-row specimens, whereas the other two specimens were similar in their performance.

The observation of these curves, on the other hand, indicates that the tendency of the samples to the shear behavior can reduce the displacement capacity and increase the energy absorption of them.

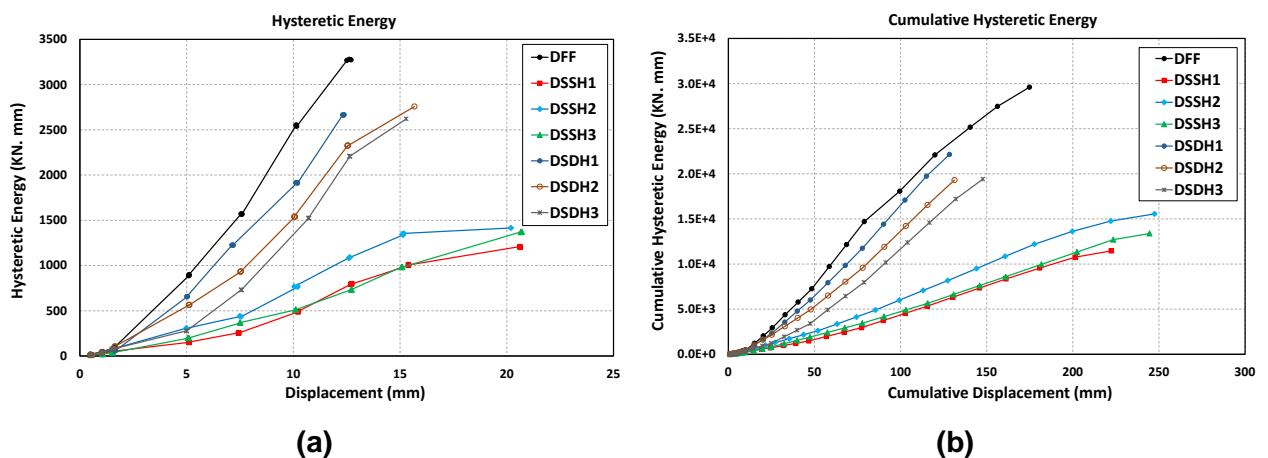


Figure 16. a) The energy dissipated in each cycle; b) cumulative energy dissipation.

Figure 17 plots the equivalent viscous damping against displacement for each damper. The equivalent viscous damping or effective damping – that equates the behavior of a nonlinear system to a linear one with viscous damping – represents, in fact, the ratio of dissipated energy to elastic potential energy resulting from



secant stiffness at maximum displacement (effective stiffness) in each cycle. The effective damping can be calculated from Eq. (16) according to Figure 14 [26].

$$\beta_{i,eff} = \frac{E_{i,D}}{4\pi E_{i,e}} = \frac{2E_{i,D}}{\pi K_{i,eff} \left( \left| \delta_{i,max}^+ \right| + \left| \delta_{i,max}^- \right| \right)^2} \quad (16)$$

where  $\beta_{i,eff}$  represents effective damping in the  $i$  the cycle. The other parameters in this relation were defined and illustrated earlier in Figure 14.

According to Figure 17, illustrating the cumulative damping in different displacements for all specimens, it can be said that, overall, single-row specimens are better dampers than their double-row counterparts. Furthermore, in specimens with a similar number of blade rows, those with a larger  $h/b$  ratio have a higher equivalent viscous damping, suggesting that the dominance of the flexural behavior increases effective damping.

It must be noted that, given the fact that effective stiffness, or equivalent viscous damping, is obtained by equating a nonlinear system to a linear one, a large effective stiffness is not an advantage to the system on its own. In other words, the required effective stiffness must be evaluated based on the seismic demand of the structure (according to Eq. (16), effective stiffness contributes to this parameter) and its effective stiffness.

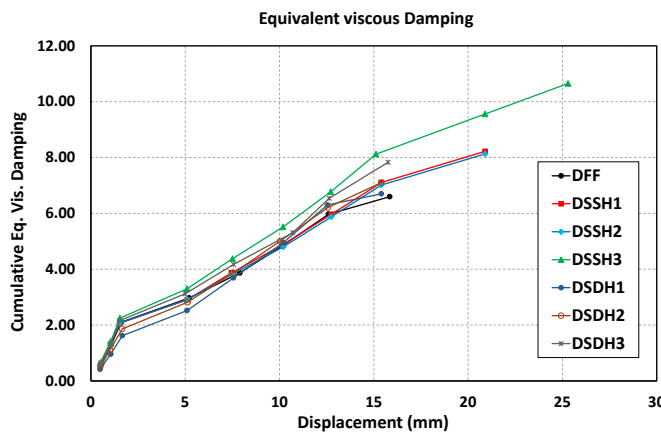


Figure 17. The cumulative effective damping (equivalent viscous damping).

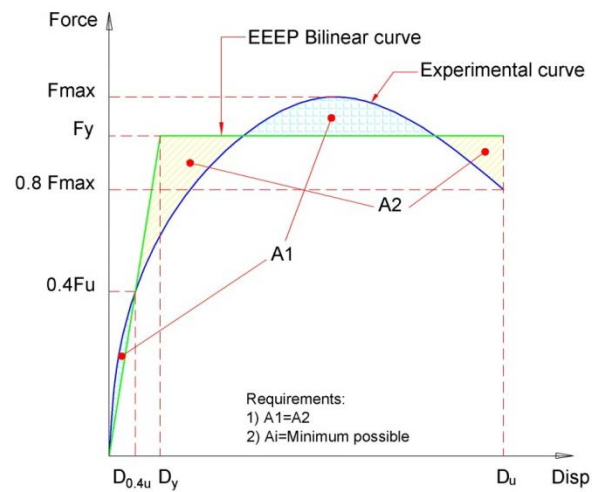


Figure 18. Using the Equivalent Energy Elastic-Plastic (EEEP) bilinear model [27].

### 3.4. Ductility

Various models have been proposed for modeling ductility, including the Equivalent Energy Elastic-Plastic (EEEP) bilinear model – that is based on the ASTM E2126-09 standard [27] – which was used in this study. Figure 18 presents a detailed illustration of the method. The model assumes a damper system with ideal elastic-plastic behavior, which is capable of dissipating as much energy as in the real damper by equating the areas A1 and A2. The elastic displacement, ultimate displacement, and ductility of all specimens are presented in Table 5. The ductility ratio in specimens (ultimate to yield displacement ratio) is calculated using Eq. (17).

$$\mu = \frac{\text{Ultimate displacement}}{\text{Yield displacement}} = \frac{\Delta u}{\Delta y} \quad (17)$$

Table 5. Ductility calculations.

Specimen	Elastic Displacement (mm)	Maximum Displacement (mm)	Ductility $\mu$	$\frac{\mu}{\mu_{DFF}}$
DFF	4.983	17.86	3.58	1
DSSH1	2.489	21	8.44	2.36
DSSH2	2.709	25	9.23	2.58
DSSH3	2.482	21.3	8.58	2.4
DSDH1	3.555	15	4.22	1.178
DSDH2	4.304	18.2	4.23	1.181
DSDH3	4.531	16.7	3.68	1.03

Based on the results, it can be inferred that the specimens with a single row of blades feature a higher ductility than the others. Among specimens with one and two rows of blades, DSSH2 and DSDH2 have the highest ductilities, which are 2.58 and 1.181 times the reference. It can be said that the more flexural the behavior of the specimen, the higher the ductility.

### 3.5. Damage Index

Several damage indices have been proposed by researchers. The indices are quantitative illustrations of the extent of damage to specimens at different displacements. The index measures damage on a scale of 0 to 1, with 0 indicating no damage and 1 suggesting destruction. It is safe to say that the combined damage index, for taking into account the displacement, force, and energy, is the best one, which was used in this study. The index was first proposed in 1985 by Park and Ang [28] and has been used in several experimental works ever since [29, 30].

$$D = \frac{\delta_m}{\delta_u} + \beta \frac{\int dE}{f_y \delta_u}, \quad (18)$$

where  $\delta_m$  and  $\delta_u$  are the maximum displacement endured by the specimen under cyclic displacement and the displacement capacity of the specimen,  $f_y$  is the yield force,  $dE$  is the cyclic energy increment, and  $\beta$  is a constant.

The damage curves of the tested specimens were obtained and presented in Figure 19.

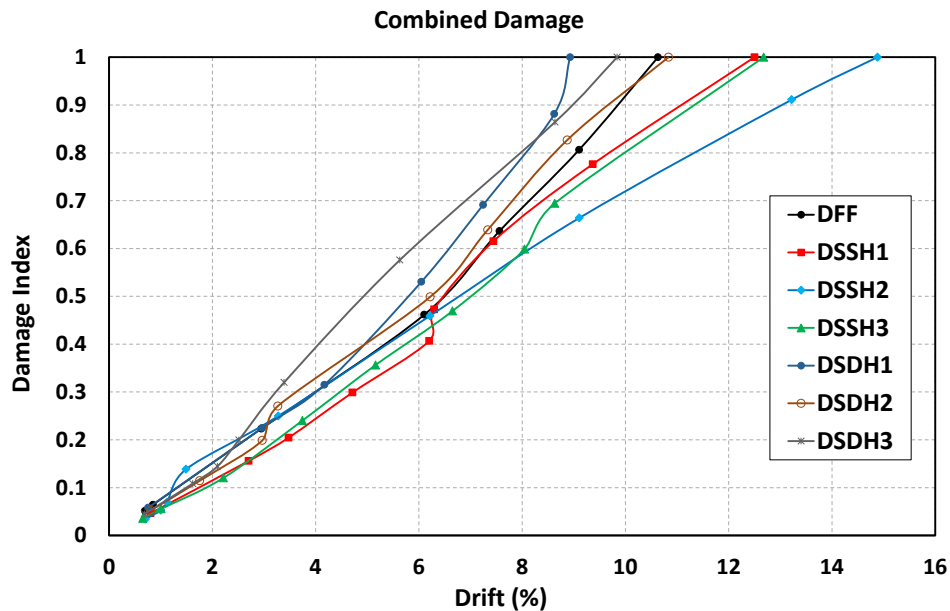
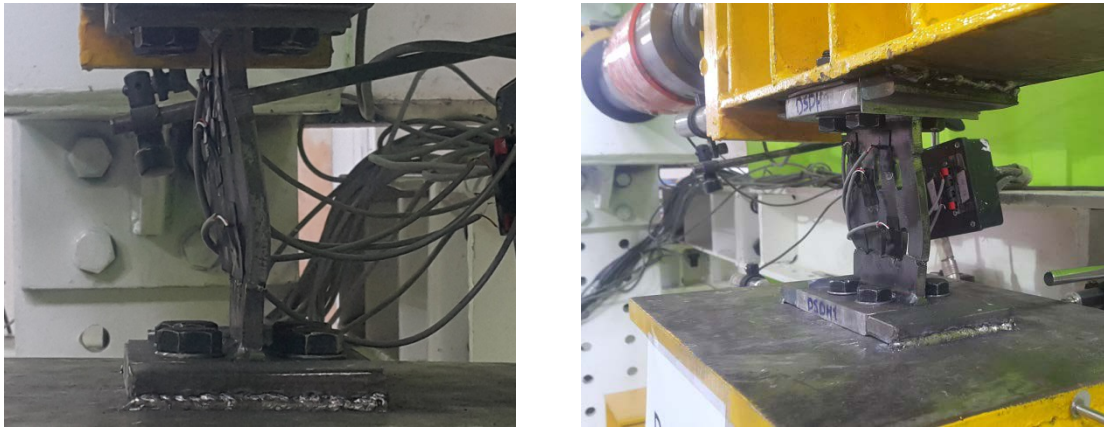


Figure 19. The Calculated Combined Damage Index.

The slope of the line representing the damage index indicates the rate of damage to the corresponding specimen. The figure shows that specimens with two rows of blades have a steeper slope than those with a single row, suggesting faster damage and destruction. Among specimens with a similar number of blade rows, DSSH2 and DSDH2 with  $h/b$  ratios of 5.45 and 1.58 have a more gradual slope and, therefore, a lower rate of damage. Furthermore, DSSH1 and DSDH1 – that correspond to the lowest  $h/b$  ratios of their respective groups – feature the highest rate of damage.

### 3.6. Buckling and the Optimal $h/b$ ratio

As it was mentioned in previous sections, a reduction in the  $h/b$  ratio promotes shear behavior in the damper, paving way for a favorable performance. Given that a reduction in the  $h/b$  ratio increases the damper stiffness, an overall buckling before the damper reaches its maximum capacity becomes more likely. It is, therefore, safe to say that reducing the  $h/b$  is allowable and optimal to the extent it does not result in the overall or lateral buckling of the damper. The DFF ( $h/b = 1.09$ ) and DSDH1 ( $h/b = 1.28$ ) had the lowest  $h/b$  among the studied specimens. Given the fact that the occurrence of overall buckling depends on the slenderness, the  $h_0/t$  ratio can be considered as the slenderness ratio. Figure 20 illustrates the overall buckling of DSDH1.



**Figure 20. Overall buckling in DSDH1.**

The slenderness ratio ( $h_0/t$ ) was calculated at 12.5 and 10 for the two specimens. Given that overall buckling took place in the said specimens under the applied cyclic loading, the minimum  $h/b$  was proposed to be 1.58 (for DSDH2 with a slenderness ratio of  $h_0/t = 11.25$ ). Assuming a linear buckling between  $h_0/t$  and  $h/b$ , proportions can be used at other  $h_0/t$  ratios; meaning that, if  $h_0/t$  doubles, the minimum recommended  $h/b$  also increases twofold. However, new theoretical analyses, numerical models, or experimental studies are recommended for other  $h/t$  ratios.

#### 4. Conclusion

Steel slit dampers with one and two rows of blades of different length-to-width ( $h/b$ ) ratios were experimentally studied. The specimens were subjected to static cyclic loading and the following results were obtained after processing the test results.

1. The initial cyclic loading results suggested that by reducing the length-to-width ratio of the blades and with the rise of shear behavior to dominance, the force capacity of the dampers is increased but their displacement capacity remains relatively unchanged. A similar result was obtained with dampers with two rows of blades in comparison with the single-row ones.

2. A comparison of the specimens showed effective stiffness to drop drastically by increasing the displacement and extending the yield of the steel in dampers with dominant shear behavior. However, the inclination of the damper to flexural behavior reduces the rate of reduction of effective stiffness. This is of great importance as regards preventing the formation of a soft story, the concentration of damage over certain floors, and improving the overall performance of the structure.

3. From the standpoint of energy absorption, dampers with two rows of blades (shear behavior) can be said to have an advantage over the single-row ones (flexural behavior). Moreover, energy absorption is promoted by reducing the  $h/b$  ratio.

4. A parametric study with varying effective damping shows that effective damping is reduced in the damper with the rise of shear behavior to dominance. In both groups (one and two rows of blades), dampers with the highest length-to-width ( $h/b$ ) ratios exhibited the highest damping.

5. Observations of the ductility indicated that dampers with a single row of blades have a higher ductility than those with two rows of blades due to their larger displacement capacity.

6. Analyzing the damage index, it was found that specimens with a single row of blades have a smaller rate of damage. In each group, the first specimens (smallest  $h/b$ ) have the highest rate of damage, but the second ones (medium  $h/b$ ) feature the lowest rate.

7. The damper stiffness is increased by reducing the length-to-width ratio of the blade, which can result in the overall buckling of the damper and failing to attain the maximum capacity. The optimal recommended length-to-width ratio for the blade depends on the height-to-thickness ratio of the damper, which is a measure of the damper slenderness. For a  $h_0/t = 11.25$  slenderness ratio, a length-to-width ratio  $h/b = 1.58$  was recommended for the blade.

Considering the compared parameters in all specimens and considering that the specimens with shear behavior showed a better and more significant performance in parameters such as force strength, effective stiffness and absorbed energy, as well as considering the absence of buckling of the specimens in loading, it can be concluded that the use of dual-row dampers with a medium  $h/b$  ratio is the best and most optimal choice for using this type of dampers.



## References

- Benavent-Climent, A. A brace-type seismic damper based on yielding the walls of hollow structural sections. 2010. Engineering Structures. 32(4). Pp. 1113–1122. DOI: 10.1016/j.engstruct.2009.12.037
- Whittaker, A.S., Bertero, V.V., Thompson, C.L., Alonso, L.J. Seismic Testing of Steel Plate Energy Dissipation Devices. Earthquake Spectra. 1991. 7(4). Pp. 563–604. DOI: 10.1193/1.1585644
- Mohammadi, R.K., Nasri, A., Ghaffary, A. TADAS dampers in very large deformations. International Journal of Steel Structures. 2017. 17(2). Pp. 515–524. DOI: 10.1007/s13296-017-6011-y
- Li, H.-N., Li, G. Experimental study of structure with «dual function» metallic dampers. Engineering Structures. 2007. 29(8). Pp. 1917–1928. DOI: 10.1016/j.engstruct.2006.10.007
- Chan, R.W.K., Albermani, F. Experimental study of steel slit damper for passive energy dissipation. Engineering Structures. 2008. 30(4). Pp. 1058–1066. DOI: 10.1016/j.engstruct.2007.07.005
- Teruna, D.R., Majid, T.A., Budiono, B. Experimental Study of Hysteretic Steel Damper for Energy Dissipation Capacity. Advances in Civil Engineering. 2015. Pp. 1–12. DOI: 10.1155/2015/631726
- Zheng, J., Li, A., Guo, T. Analytical and experimental study on mild steel dampers with non-uniform vertical slits. Earthquake Engineering and Engineering Vibration. 2015. 14(1). Pp. 111–123. DOI: 10.1007/s11803-015-0010-9
- Lee, C.-H., Ju, Y.-K., Min, J.-K., Lho, S.-H., Kim, S.-D. Non-uniform steel strip dampers subjected to cyclic loadings. Engineering Structures. 2015. Vol. 99. Pp. 192–204. DOI: 10.1016/j.engstruct.2015.04.052
- Ahmadie Amiri, H., Najafabadi, E.P., Estekanchi, H.E. Experimental and analytical study of Block Slit Damper. 2018. Journal of Constructional Steel Research. Vol. 141. Pp. 167–178. DOI: 10.1016/j.jcsr.2017.11.006
- Lin, X., Wu, K., Skalomenos, K.A., Lu, L., Zhao, S. Development of a buckling-restrained shear panel damper with demountable steel-concrete composite restrainers. Soil Dynamics and Earthquake Engineering. 2019. Vol. 118. Pp. 221–230. DOI: 10.1016/j.soildyn.2018.12.015
- Xu, L.-Y., Nie, X., Fan, J.-S. Cyclic behaviour of low-yield-point steel shear panel dampers. Engineering Structures. 2016. Vol. 126. Pp. 391–404. DOI: 10.1016/j.engstruct.2016.08.002
- Chaofeng, Z., Youchun, W., Longfei, W., Meiping, W. Hysteretic mechanical property of low-yield strength shear panel dampers in ultra-large plastic strain. Engineering Structures. 2017. 148. Pp. 11–22. DOI: 10.1016/j.engstruct.2017.06.028
- Zhang, C., Zhu, T., Wang, L., Wu, M. Ultra-low cycle fatigue performance evaluation of the miniaturized low yield strength steel shear panel damper. Journal of Constructional Steel Research. 2017. 135. Pp. 277–284. DOI: 10.1016/j.jcsr.2017.05.001
- Zhang, C., Wang, L., Sun, C., Wu, M. Feasibility of the evaluation of the deformation capacity of the shear panel damper by FEM. 2018. Journal of Constructional Steel Research. 147 pp. 433–443. DOI: 10.1016/j.jcsr.2018.04.033
- Chen, Z., Dai, Z., Huang, Y., Bian, G. Numerical simulation of large deformation in shear panel dampers using smoothed particle hydrodynamics. Engineering Structures. 2013. 48. Pp. 245–254. DOI: 10.1016/j.engstruct.2012.09.008
- Shen, J., Seker, O., Akbas, B., Seker, P., Momenzadeh, S., Faytarouni, M. Seismic performance of concentrically braced frames with and without brace buckling. Engineering Structures. 2017. 141. Pp. 461–481. DOI: 10.1016/j.engstruct.2017.03.043
- Deng, K., Pan, P., Li, W., Xue, Y. Development of a buckling restrained shear panel damper. Journal of Constructional Steel Research. 2015. 106. Pp. 311–321. DOI: 10.1016/j.jcsr.2015.01.004
- Bazzaz, M., Kafi, M.A., Kheyroddin, A., Andalib, Z., Esmaeili, H. Evaluating the seismic performance of off-center bracing system with circular element in the optimum place. International Journal of Steel Structures. 2014. 14(2). Pp. 293–304. DOI: 10.1007/s13296-014-2009-x
- Andalib, Z., Kafi, M.A., Kheyroddin, A., Bazzaz, M. Experimental investigation of the ductility and performance of steel rings constructed from plates. Journal of Constructional Steel Research. 2014. 103. Pp. 77–88. DOI: 10.1016/j.jcsr.2014.07.016
- Latour, M., D'Aniello, M., Zimbru, M., Rizzano, G., Piluso, V., Landolfo, R. Removable friction dampers for low-damage steel beam-to-column joints. Soil Dynamics and Earthquake Engineering. 2018. 115. Pp. 66–81. DOI: 10.1016/j.soildyn.2018.08.002
- Zeynali, K., Saeed Monir, H., Mirzai, N.M., Hu, J.W. Experimental and numerical investigation of lead-rubber dampers in chevron concentrically braced frames. Archives of Civil and Mechanical Engineering. 2018. 18(1). Pp. 162–178. DOI: 10.1016/j.acme.2017.06.004
- Qu, B., Dai, C., Qiu, J., Hou, H., Qiu, C. Testing of seismic dampers with replaceable U-shaped steel plates. Engineering Structures. 2019. 179. Pp. 625–639. DOI: 10.1016/j.engstruct.2018.11.016
- Sahoo, D.R., Singhal, T., Tarathia, S.S., Saini, A. Cyclic behavior of shear-and-flexural yielding metallic dampers. Journal of Constructional Steel Research. 2015. 114. Pp. 247–257. DOI: 10.1016/j.jcsr.2015.08.006
- ASTME8M-04. Standard Test Methods for Tension Testing of Metallic Materials [Metric] (2008) 2008.
- ATC-24. Guidelines of Cyclic Seismic Testing on Components For Steel Structures, Applied Technology Council, Redwood City, Calif, USA, 1992. [Online]. URL: <https://books.google.com/books?id=hQpZs4k38sEC>.
- Chopra, A.K., Chopra, A.K. Dynamics of structures: theory and applications to earthquake engineering. Prentice Hall Englewood Cliffs, NJ, 1995.
- ASTM Standard test methods for cyclic (reversed) load test for shear resistance of vertical elements of the lateral force resisting systems for buildings. 2009. E2126-09.
- Park, Y., Ang, A. Mechanistic Seismic Damage Model for Reinforced Concrete. Journal of Structural Engineering. 1985. 111(4). Pp. 722–739. DOI: 10.1061/(ASCE)0733-9445(1985)111:4(722)
- Haji, M., Naderpour, H., Kheyroddin, A. Experimental study on influence of proposed FRP-strengthening techniques on RC circular short columns considering different types of damage index. 2019. Composite Structures. 209. Pp. 112–128. DOI: 10.1016/j.compstruct.2018.10.088
- Promis, G., Ferrier, E., Hamelin, P. Effect of external FRP retrofitting on reinforced concrete short columns for seismic strengthening. Composite Structures. 2009. 88(3). Pp. 367–379. DOI: 10.1016/j.compstruct.2008.04.019

## Contacts:

Mohammad Ali Kafi, +982331535206; [mkafi@semnan.ac.ir](mailto:mkafi@semnan.ac.ir)

Kianoosh Nik Hoosh, +982333331100; [K.NikHoosh.PHD@semnan.ac.ir](mailto:K.NikHoosh.PHD@semnan.ac.ir)



DOI: 10.18720/MCE.87.2

## The effect of perforations on the deformability of welded beam with corrugated webs

**A.A. Bryantsev<sup>a</sup>, V.E. Absimetov<sup>b</sup>, V.V. Lalin<sup>c</sup>,**

<sup>a</sup> *Kazakh Leading Academy of Engineering and Construction Inc., Almaty, Republic of Kazakhstan*

<sup>b</sup> *"AstanaSroyKonsalting" LLP, Astana, Kazakhstan*

<sup>c</sup> *Peter the Great St. Petersburg Polytechnic University, St. Petersburg, Russia*

\* *E-mail: Bryancev8989@mail.ru*

**Keywords:** beam with corrugated web, web perforation; triangular shape of corrugations, beam deflection, finite element analysis, ring stiffener.

**Abstract.** Perforating steel beams is inevitable in some cases such as setting the technical equipment, though it decreases the carrying capacity of the element. The lack of information about the nature of the work, the values of critical stresses, the stability of the corrugated webs of the beams weakened by the perforations necessitated relevant studies for which the perforations of different diameters and with various ways of reinforcement were formed in the webs of the beams. Hence, this research focuses on the behavioral condition of welded beams with corrugated triangular webs weakened by different sized perforations at different locations. The impacts of these perforations on the transverse load-carrying capacity of the element and the suitable ways for stiffening them were investigated. An analysis is made of the influence of the edging thickness, paired vertical stiffeners at different widths of the ring stiffener on behavior of models of beams with a corrugated web with perforations. The influence of the bending of the lip around the exterior circumferential edge of the stiffener ring on the bearing capacity of beams with a corrugated web weakened by perforations was analyzed. The most effective location of the perforations along the web height has been determined.

### 1. Introduction

The main aim of this research directed on identification behavioral condition and deformability of welded beams with corrugated triangular webs weakened by perforations.

During this research the main tasks need to defined: 1) necessity of stiffening the web and the perforation; 2) the most optimal sized of perforations, distance between perforations and types of strengthening; 3) influence of a lip around the exterior circumferential edge of the stiffener ring on bearing capacity of the beam weakened by the perforations; 4) the most effective location of the perforation along the web height.

A Corrugated beam is a beam with flanges made of different section metal and corrugated (curved) web in transverse direction [1]. Corrugated webs of beams can be with a triangular corrugation profile [2], wavy, trapezoidal [3, 4], rectangular, etc. flanges of such beams are made of rolled steel, molded sections, electric-welded pipes, reinforced concrete elements. Beams with corrugated webs are used in many countries (Table 1).

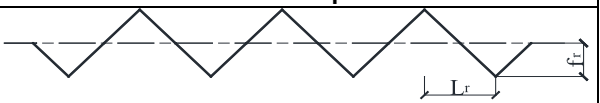
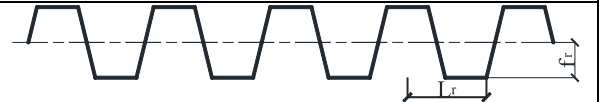

Literary sources with open access [5, 6] have a few solutions of the problems of designing perforations in the corrugated webs. There are also limited data on experimental and theoretical studies of influence of local concentrated loads and local weakening on the bearing capacity and deformation of beams. This question was mainly considered in thin-walled beams [7–13] and in beams with flat webs and with perforated webs [14, 15]. The need for perforations application in the corrugated webs is due to the fact that laying of the piping system for various purposes: water supply, heating, ventilation, air conditioning.

Bryantsev, A.A., Absimetov, V.E., Lalin, V.V. The effect of perforations on the deformability of welded beam with corrugated webs. Magazine of Civil Engineering. 2019. 87(3). Pp. 18–34. DOI: 10.18720/MCE.87.2.

Брянцев А.А., Абсиметов В.Э., Лалин В.В. Влияние отверстий на деформативность стенки сварной гофрированной балки // Инженерно-строительный журнал. 2019. № 3(87). С. 18–34. DOI: 10.18720/MCE.87.2



**Table 1. Area of application and corrugated web shape, where  $L_r$  is the length of the corrugation half-wave;  $f_r$  is the height of the corrugation half-wave.**

Beam Name	Place of Application	Web shape
Beams with cross-corrugated web and triangular-shaped corrugations	Kazakhstan, Russia, Tajikistan	
Beams with corrugations of a trapezoidal and rectangular shape	Sweden, the USA, Japan, Finland	
Beams with cross-corrugated web and wavy-shaped corrugations	Austria, Ukraine, Poland, Russia	

The issues of the perforations affect the work of the beam web which are performed according to the Vierendeel principle or the four-angular bend [16], are studied in various works [17–19]. Also, the problems of placing and stiffening of perforations in the corrugated webs of trapezoidal and wavy shape of corrugations were solved in different countries by many scientists [20, 21]. However, except the study [16], for beams with a corrugated web and corrugations of a triangular shape no more study was revealed.

In view of the absence in the regulatory documents on the territory of the Republic of Kazakhstan and Russia a proper explanation of the pitch, diameter and methods of reinforcing perforations, there is a need to conduct a study of the influence of the diameter and pitch of perforations on the deformability of the corrugated beam, in order to develop a methodology for designing welded corrugated beams, weakened by perforations.

The stressed state of the corrugated web in the perforation zone is a separate issue requiring additional studies that take into account the ratio of the diameter of the perforations and the beam web height, the perforations pitch, the stiffness of the element supporting the shape of the perforation.

## 2. Methods

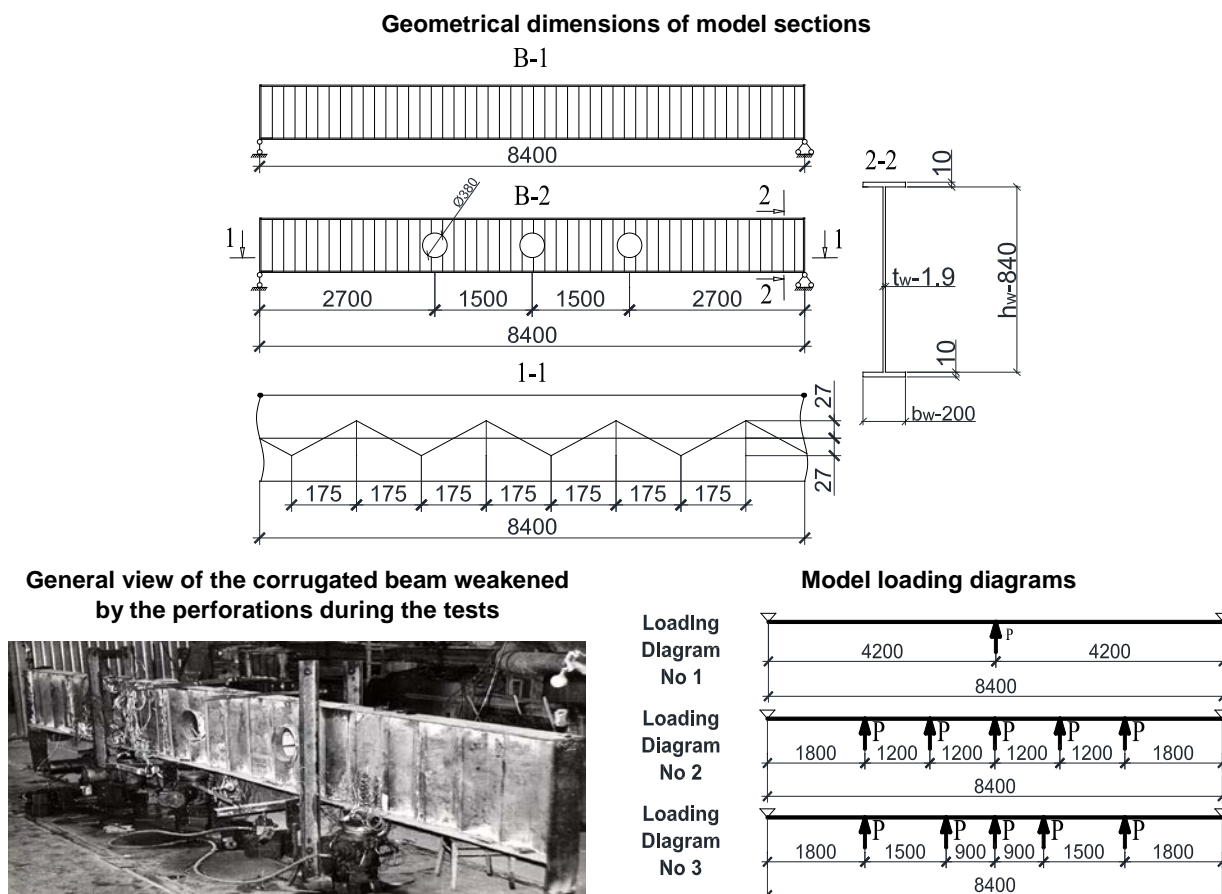
Experimental studies of corrugated beams are a very important part of the substantiation of various hypotheses about the principles of work and the effectiveness of the design decisions [22–26]. There are no specific requirements on the number, pitch and diameter of the perforations in both Kazakhstan and foreign building regulations.

The experimental study was performed on two support beams with a corrugated web with a triangular shape of the corrugations, without perforations and weakened by three perforations. Three circular perforations with a diameter of  $0.5h_w$ , where  $h_w$  is the web height (Figure 1), were provided to ensure the various types of communication passage in the beams webs. Since there is no exact method for calculating the corrugated beams with weakening, then the beams with thin corrugated webs weakened by perforations require appropriate field tests for the practical application in construction. The geometric parameters, materials, loads and boundary conditions adopted during the experiment are presented below.

As a result of theoretical and experimental studies carried out at the beginning of the 90s by the Institute “Proektstalkonstruksiya” [27] based in its own laboratories, the use of corrugated webs in girder structures has expanded significantly. The test was performed on large-scale models (scale 1:3) of corrugated beams of constant section (flange is 220×10 mm, web is 840×1.9 mm) with a span of 8400 mm. The first beam B-1 was accepted without perforations. Three circular perforations with a diameter of  $0.5h_w$ , which edges were reinforced with stiffeners made of strip steel with a cross section of 85×3 mm, are formed in the web of the second beam B-2. The maximum allowable deflection of the beam is assumed to be  $1/220L$ , and is equal to 38.2 mm.

In the perforation zone in four sections of the web, rectangular sockets of three electrical strain gauges with a base of 10 mm were glued along the length. The indications of electrical strain gauges were taken visually by a CTM-5 device, and were also output to Iskra-108D printer and to a punched tape for further processing by a computer. The load at the time of testing in the elastic stage of the beam behavior was measured using a DOSM-5 model dynamometer with an accuracy class of 1.5 and duplicated using M100 manometers. Displacements of beams in the plane of the load action were measured using PAO-6 deflectometer with a division value of 0.01 mm. The deflectometers measured the vertical displacement and were located in sections where the load was applied, as well as on supports. The general view of the beams and their geometric dimensions is given in Figure 1.





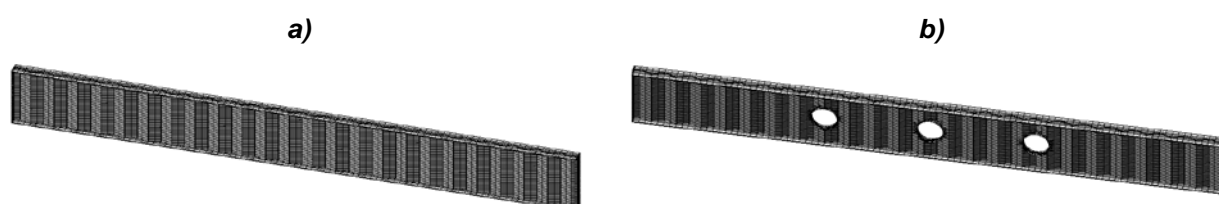
**Figure 1. Data on the geometric dimensions of the model section, the general view of the beam during the tests and the tested models loading diagrams.**

The web corrugations of triangular shape with roundings in the peaks had a wave length  $L_r = 50$  mm and a wave height  $f_r = 54$  mm. Material of the web and flanges was taken steel S245 in accordance with Russian State Standard GOST 27772 [28] with the following characteristics: yield strength  $\sigma_y = 245$  N/mm<sup>2</sup> and ultimate strength  $\sigma_u = 370$  N/mm<sup>2</sup>. The Beams were made in the laboratory for metal structures testing. The general view of the corrugated beam weakened by the perforations, is given in Figure 2.

The beams were loaded with DGO 100/2/G50H A0CM5 hydraulic jacks through steel plates of 100×20 mm long equal to the width of the beam flange ( $L = 200$  mm). To ensure equal loads jacks installed symmetrically relative to the middle of the beam, were connected by hoses and loaded manually with a single pump. Loading diagrams are shown in Figure 1.

The beams deformation property was also studied along with the study of the beam elements stressed state, since there is little information about the beams deformation property with thin corrugated webs, and especially weakened by perforations; and their interest in construction practice is special. The effect of local wall stability loss on the structure behavior was not taken into account in this work.

The performed tests make it possible to conduct a comparative analysis of the beams deformation property (Figure 2) of the same cross-section with perforations in the web and without such perforations under the same operating conditions, as well as to check the computer simulation data of the tests in the LIRA-SAPR 2017 software package with the aim of further usage of this program as the main one for further numerical investigations of the corrugated beam weakened by circular perforations of different pitch and diameter.



**Figure 2. The model of beams: a) B-1; b) B-2.**

Table 2 presents the values of the bending moments in the middle of the span  $M_e$ , the transverse force at the supports  $Q_e$ , the stresses in the flanges  $\sigma_{\max}$ , the stresses in the web  $\tau_{\max}$ , as well as the experimental  $Y_e$ , theoretical  $Y_t$  and computer  $Y_c$  deflections of the B-1 beam without the perforations ones. The values of deflections in the middle of the B-2 beam with perforations for 1, 2 and 3 loading diagrams of experimental  $Y_e^*$  and computer  $Y_c^*$  data in the linear region of behavior are also presented. For the numerical experiment, the following grid was adopted: 0.04×0.09 m, in the area of the perforations, the grid is reduced to 2 times. Computer simulation of the beams was performed using the program LIRA-SAPR, program for the finite element analysis. The boundary conditions were applied to both ends of the beam model at the nodes of the end plate surface by limiting the required degrees of freedom. The beam at both ends has a fastening along the axes  $Y$  and  $Z$ . The material of the web and flanges is S245 steel in accordance with Russian State Standard GOST 27772 [28]. The yield strength is  $\sigma_y = 245 \text{ N/mm}^2$  the elastic modulus is  $E = 206000 \text{ MPa}$  and the Poisson ratio is 0.3. The values of the experimental stresses  $\sigma_{\max}$  and  $\tau_{\max}$  resented in Table 2 were obtained in the study of beams with a corrugated web weakened by perforation.

**Table 2. The results of the experimental data.**

Loading diagram No.	Total load on the beam $\Sigma Q$ , kN	The bending moment in the middle of the span $M_e$ , kNm	The transverse force at the supports $Q_e$ , kN	The stress in the flanges $\sigma_{\max}$ , MPa	The stress in the web $\tau_{\max}$ , MPa	Deflection (mm)					
						$Y_t$ B-1	$Y_e$ B-1	$Y_c$ B-1	$Y_e^*$ B-2	$Y_c^*$ B-2	$Y_e^* / Y_c^*$
1	40	84	20	49.4	12.5	3.41	4	4.28	3.44	5.15	—
2	150	207	75	121.8	47.0	12.8	9.5	12	12.7	13.6	0,93
2	200	276	100	162.4	62.7	17.1	13.2	16	17.1	18.1	0,94
3	250	360	125	211.8	78.3	21.4	18.6	20.5	25.1	23.8	1,05

Analysis of the data in Table 2 shows that the deformation property of the tested B-2 beam in the linear region of behavior  $Q_e \approx 0.65\text{--}0.7 Q_{e,\max}$  is 20–30 % larger than that of the similar B-1 beam without weakening, where  $Q_{e,\max}$  is maximum experimental load. The value of the relative deflection is  $1/430L$ . With further loading, the B-2 beams deformation property was 3–50 % higher than the deformation property of the B-1 beam without the perforation. The first group of limit state came when the deflections were equal to  $1/225L$ .

Comparative analysis of experimental  $Y_e^*$  and computer  $Y_c^*$  data on deflections for the tested B-2 beam with perforations in loading diagram No. 2 and No. 3 gives a difference in deflections on average no more than 6 %. The data obtained allow using this program as the main one for further numerical studies of corrugated beam with different diameter, type and pitch of perforations in the corrugated web.

According to the above analysis, it can be concluded that stiffening of the web in the areas between the flanges and stiffening element of the perforation by the pair stiffeners is necessary in order to avoid local buckling under the concentrated load in the perforation zone.

### 2.1. Parametric study of the corrugated beam with different diameter, type and pitch of perforations in the corrugated web

The study of the stress-strain state, the bending moment, the linear analysis of beams with a corrugated metal webs was carried out by various scientists [2–32].

Numerical parametric study of the beam web with corrugation of triangular shape includes analysis of basically 28 models. Of these 28 models, 1 beam the model without web perforations and 27 models with perforations of different sizes and they are located at different distances from each other.

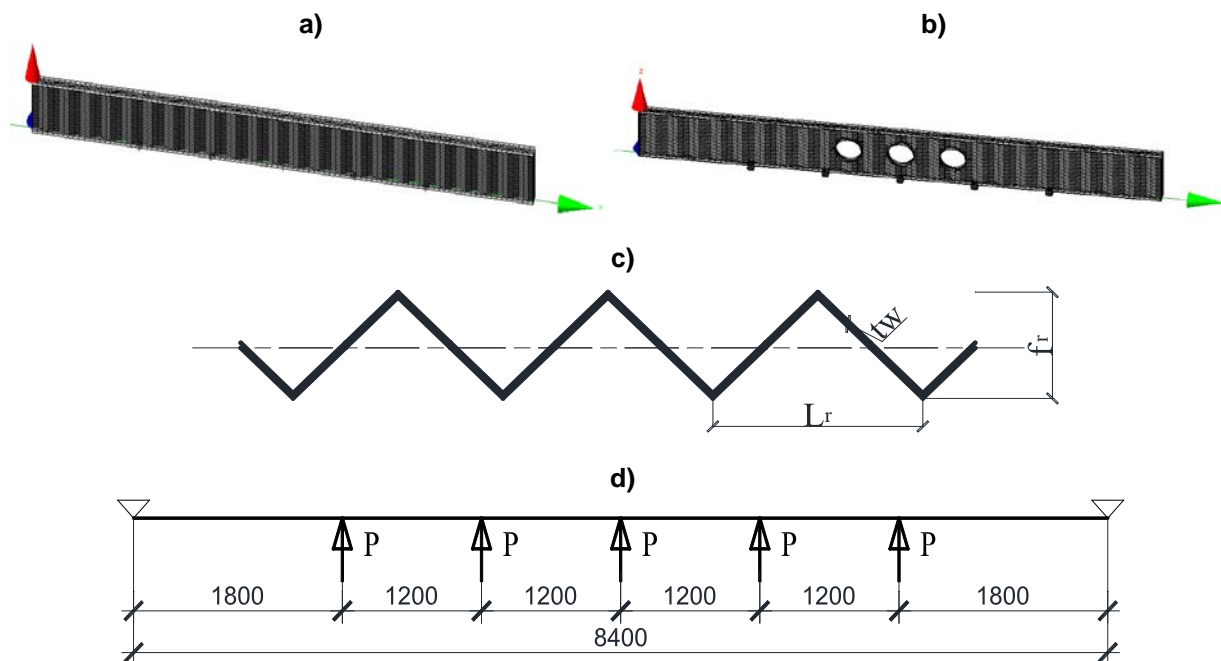
According to above analysis, it is necessary to check the effect of the diameter of  $0.25h_w$ ,  $0.5h_w$  and  $0.75h_w$  from the web height and the pitch of the perforations with two diameters ( $2d$ ), three diameters ( $3d$ ) and four diameters ( $4d$ ) taken as the distance between the centers of the perforations on the corrugated web with the corrugations of triangular shape operation. The center of the perforations is located in the middle of the web height.

Numerical simulation of the beams was performed using the program LIRA-SAPR, program for the finite element analysis, which includes the requirements for constructions in accordance with EN-1993-1-5:2006 [33]. This program can be used to solve various tasks, from simple linear analysis and on out to complex nonlinear analysis requiring consideration of various manufacturing deviations and material errors. The parametric study was performed for the beam taking into account the various sizes of the perforations in the beam web, distances between the perforations, existence and absents of the perforation stiffening, as well as for the corrugated beam without web perforation. The ability of the beam web with and without the perforation

to withstand the load was considered and an assessment of the effect of web flexibility in accordance with [33] was performed.

For numerical simulation was accepted the beam with a web height  $h_w = 840$  mm and a web thickness  $t_w = 1.9$  mm. The web corrugations of triangular shape with roundings in the peaks had a wave length  $L_r = 350$  mm and a wave height  $f_r = 54$  mm (Figure 3). The material of the web and flanges is S245 steel in accordance with Russian State Standard GOST 27772 [28]. The yield strength is  $\sigma_y = 245$  N/mm<sup>2</sup> and the ultimate strength is  $\sigma_u = 370$  N/mm<sup>2</sup>.

Finite element models adopted for beams with the corrugations of triangular shape with and without perforations are given in Figure 3.



**Figure 3. Models adopted for the beams analysis, where a) M-1 corrugated beam with a triangular profile without perforations; b) from M-2 to M-28 corrugated beams with a triangular profile weakened by perforations; c) values of length, height and thickness of web with corrugations of triangular shape adopted in computer simulation; d) model loading diagram for parametric study.**

The corrugated beam of constant section (flanges are 200×10 mm, webs are 840×1.9 mm) are made with span of 8400 mm. Two end plates with a thickness  $t = 20$  mm is accepted at the ends of each model. Stiffening ring thickness is 3 mm. Paired vertical stiffeners width and thickness is 85×3 mm. Other characteristics of the investigated beams are shown in Table 3.

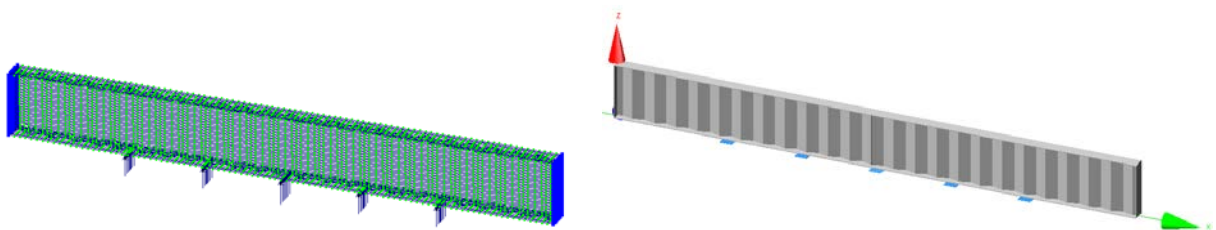
The load is applied through steel plates of 100×20 mm long equal to the width of the beam flange ( $L = 200$  mm), which is in direct contact with the surface of the flange. The load is transmitted at five points from the bottom to the top. The load is applied in the beam center, as well as at a distance from the center in both directions of 1200 mm in accordance with the model loading diagram (Figure 3, 4). The boundary conditions were applied to both ends of the beam model at the nodes of the end plate surface by limiting the required degrees of freedom. The beam at both ends has a fastening along the axes  $Y$  and  $Z$ .

The tested beam has three circular perforations; the perforations' centers are located in the middle of the web height. The distance between the centers of the perforations is assumed to be  $2d$ ,  $3d$  and  $4d$  of the perforations. One of the perforations has a constant location in the center of the beam at a distance of 4200 mm from the left and right support to the perforation center. The material of the web and flanges is S245 steel in accordance with GOST 27772 [28]. The yield strength is  $\sigma_y = 245$  N/mm<sup>2</sup>, the elastic modulus is  $E = 206000$  MPa and the Poisson ratio is 0.3. For the beam models with the length of 8400 mm, the maximum allowable deflection is  $1/220L$  or 38.2 mm. Loading ( $Q$ ) of models is from 50 kN to 350 kN. Loading step is 50 kN. The maximum load value was accepted on the basis of the maximum load that the beam withstood during the experiment. The ultimate strength of the models presented above was studied using finite element analysis.



**Table 3. Characteristics of the investigated beams.**

Grade of the model	Diameter of the perforation	Stiffening	Perforation pitch	Stiffening ring width (mm)
M-1	without web perforations	—	—	—
M-2	$0.25h_w$	without the perforations stiffening	$2d$	50
M-3	$0.5h_w$	without the perforations stiffening	$2d$	50
M-4	$0.75h_w$	without the perforations stiffening	$2d$	50
M-5	$0.25h_w$	perforation with edging	$2d$	50
M-6	$0.5h_w$	perforation with edging	$2d$	50
M-7	$0.75h_w$	perforation with edging	$2d$	50
M-8	$0.25h_w$	perforation with edging and paired vertical stiffeners	$2d$	50
M-9	$0.5h_w$	perforation with edging and paired vertical stiffeners	$2d$	50
M-10	$0.75h_w$	perforation with edging and paired vertical stiffeners	$2d$	50
M-11	$0.25h_w$	without the perforations stiffening	$3d$	110
M-12	$0.5h_w$	without the perforations stiffening	$3d$	110
M-13	$0.75h_w$	without the perforations stiffening	$3d$	110
M-14	$0.25h_w$	perforation with edging	$3d$	110
M-15	$0.5h_w$	perforation with edging	$3d$	110
M-16	$0.75h_w$	perforation with edging	$3d$	110
M-17	$0.25h_w$	perforation with edging and paired vertical stiffeners	$3d$	110
M-18	$0.5h_w$	perforation with edging and paired vertical stiffeners	$3d$	110
M-19	$0.75h_w$	perforation with edging and paired vertical stiffeners	$3d$	110
M-20	$0.25h_w$	without the perforations stiffening	$4d$	180
M-21	$0.5h_w$	without the perforations stiffening	$4d$	180
M-22	$0.75h_w$	without the perforations stiffening	$4d$	180
M-23	$0.25h_w$	perforation with edging	$4d$	180
M-24	$0.5h_w$	perforation with edging	$4d$	180
M-25	$0.75h_w$	perforation with edging	$4d$	180
M-26	$0.25h_w$	perforation with edging and paired vertical stiffeners	$4d$	180
M-27	$0.5h_w$	perforation with edging and paired vertical stiffeners	$4d$	180
M-28	$0.75h_w$	perforation with edging and paired vertical stiffeners	$4d$	180

**Figure 4. Diagram of model loading.**

### 3. Results and Discussion

Maximum allowable deflection is not reached when analyzing the obtained data for the M-1 beam model. The deflection for the M-1 beam model under the maximum load effect is 28 mm.

Figures 5–7 show the load-deflection dependence of the middle from M-2 to M-28 beam models with  $2d$ ,  $3d$  and  $4d$  perforation pitch when operating in the elastic stage. Table 4 shows the shape of deflection of some models.

The Figure 5 shows the load-deflection dependence of the middle from M-2 to M-10 beam models with  $2d$  perforation pitch.

The Figure 6 shows the load-deflection dependence of the middle from M-11 to M-19 beam models with  $3d$  perforation pitch.

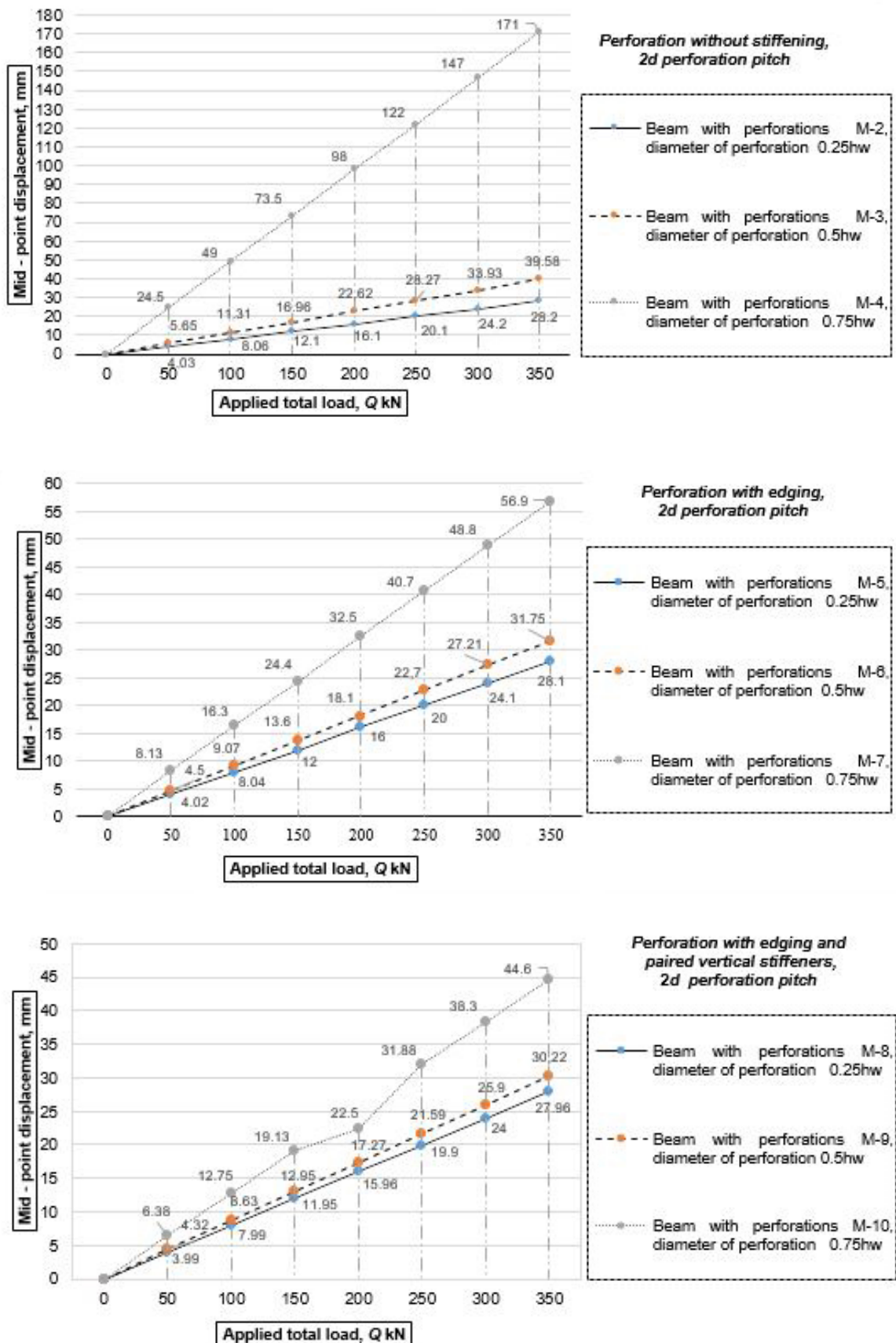


Figure 5. Displacement and applied total load value dependence from M-2 to M-10 beam models with the  $2d$  perforation pitch without the perforations stiffening, perforation with edging and perforation with edging and paired vertical stiffeners.

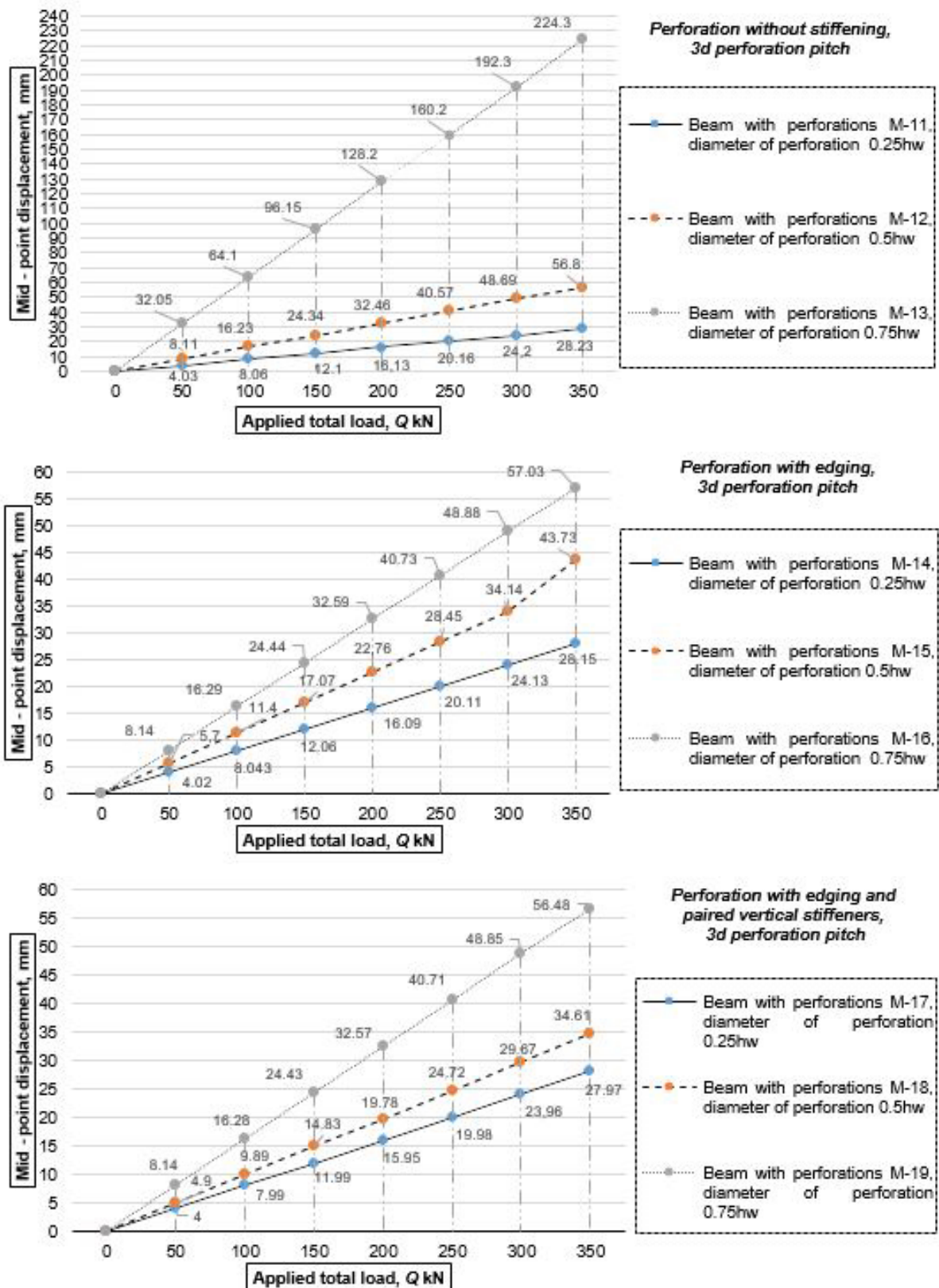


Figure 6. Displacement and applied total load value dependence from M-11 to M-19 beam models with the 3d perforation pitch without the perforations stiffening, perforation with edging and perforation with edging and paired vertical stiffeners.

The Figure 7 shows the load-deflection dependence of the middle from M-20 to M-28 beam models with 4d perforation pitch.

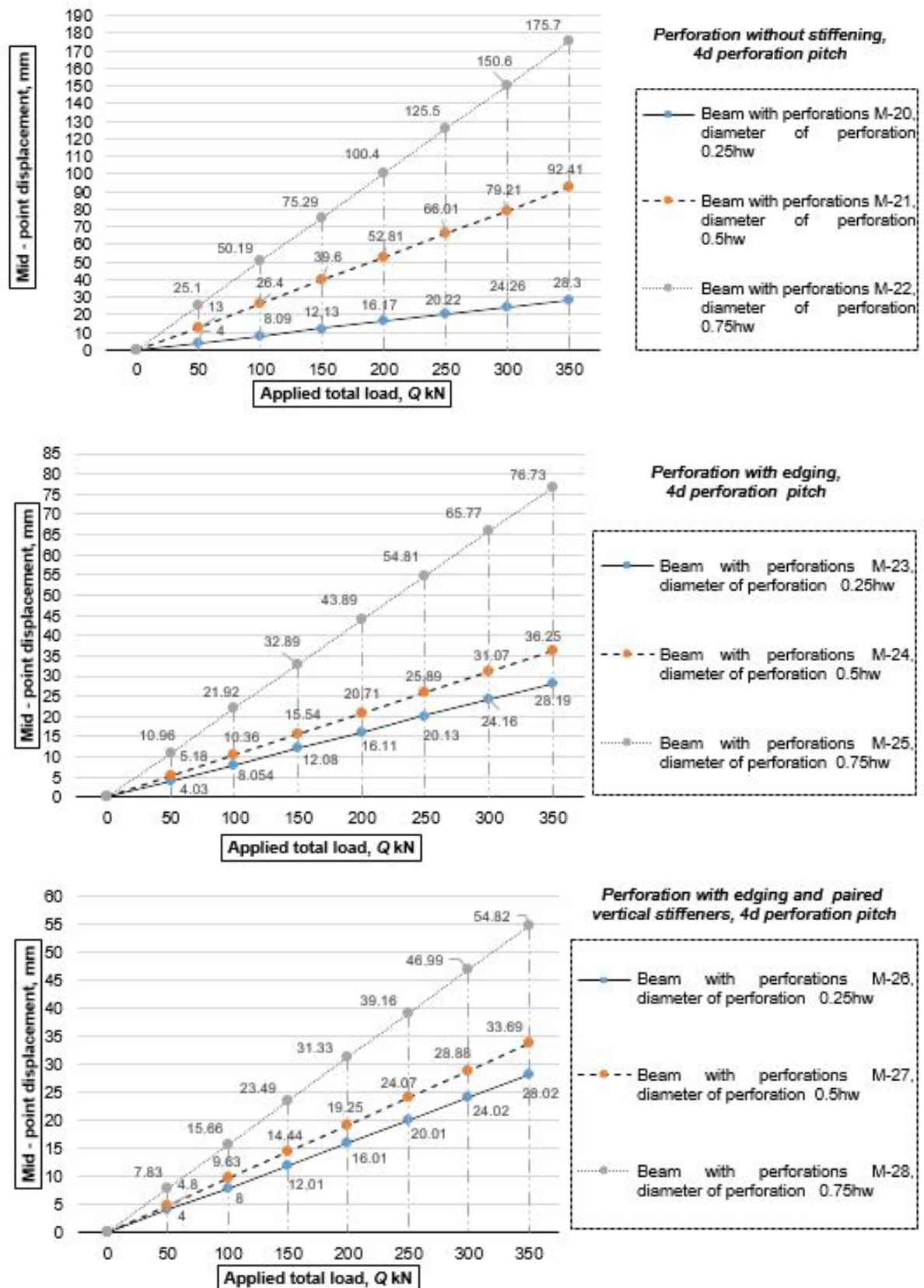



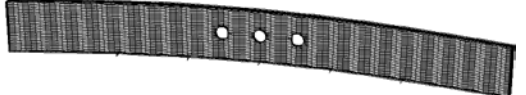
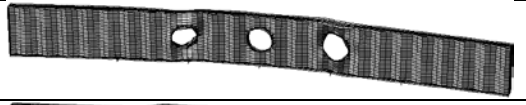


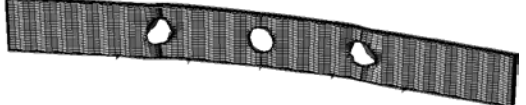
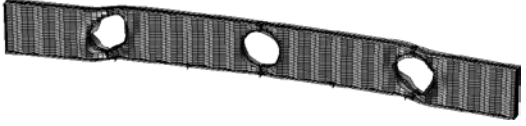


Figure 7. Displacement and applied total load value dependence from M-20 to M-28 beam models with the 4d perforation pitch without the perforations stiffening, perforation with edging and perforation with edging and paired vertical stiffeners



**Table 4. Deflection shape of beam models with different diameters and methods of stiffening.**

Grade of the Model	Diameter of the perforation	Perforation pitch	Stiffening	Deformation shape
M-2	$0.25h_w$	$2d$	without the perforations stiffening	
M-3	$0.5h_w$	$2d$	without the perforations stiffening	
M-4	$0.75h_w$	$2d$	without the perforations stiffening	
M-14	$0.25h_w$	$3d$	perforation with edging	
M-15	$0.5h_w$	$3d$	perforation with edging	
M-16	$0.75h_w$	$3d$	perforation with edging	
M-26	$0.25h_w$	$4d$	perforation with edging and paired vertical stiffeners	
M-27	$0.5h_w$	$4d$	perforation with edging and paired vertical stiffeners	
M-28	$0.75h_w$	$4d$	perforation with edging and paired vertical stiffeners	

It was decided to begin the analysis of beam models with corrugated web with  $2d$  perforations pitch without perforations stiffening to determine the most effective version of the model of corrugated beam with perforations. The obtained data allow to make conclusions that the best result was shown by the M-2 model with a diameter of the perforations of  $0.25h_w$  with maximum displacement does not exceeding the maximum permissible one. The deflection of the M-3 beam model with the perforation pitch of  $2d$  is greater by 28.8 % than that of the M-2 beam model, and the deflection of the M-4 beam model with the perforation pitch of  $0.75h_w$  is greater than that of the M-2 beam model by 510.7 %.

In the same way, the work of other models of beams ranging from M-4 to M-28 was investigated. The results were carefully analyzed; the conclusions are given below.

According to the analysis of beam models with perforations of various diameters and pitches, the following main conclusions can be drawn:

– the most effective model of a beam with the diameter of the perforation of  $0.25h_w$  with  $2d$  pitch was the M-8 beam model with the actual shearing stress in the section of the corrugated web with the perforation  $\tau_{act} \leq 0.1R_s$  under the maximum load effect  $Q = 350$  kN, and the maximum possible load  $Q_{max}$  on this beam model for achieving the limit deflection is equal to  $Q_{max} = 478.2$  kN; with  $3d$  pitch was the M-17 beam model with  $\tau_{act} \leq 0.14R_s$ , and the maximum possible load  $Q_{max} = 478$  kN; with  $4d$  pitch was the M-26 beam model with  $\tau_{act} \leq 0.19R_s$ , and the maximum possible load  $Q_{max}$  on this beam model for achieving the limit deflection is equal  $Q_{max} = 477.2$  kN. All beam models with the perforations stiffened by edging with sheet steel and paired stiffeners located on both sides of the perforation, showed the best results. In the design among these three models of beams, M-8 beam model can be recommend having the best performance with the diameter of the perforation of  $0.25h_w$ , is minimal, it is recommended to perform them with edging;

– the most effective model of a beam with the diameter of the perforation of  $0.5h_w$ , with  $2d$  pitch was the M-9 beam model with  $\tau_{act} \leq 0.29R_s$ , and the maximum possible load  $Q_{max}$  on this beam model for achieving the limit deflection is equal to  $Q_{max} = 442.4$  kN; with  $3d$  pitch was the M-18 beam model with  $\tau_{act} \leq 0.43R_s$ , and the maximum possible load  $Q_{max}$  on this beam model for achieving the limit deflection is equal to  $Q_{max} = 386.3$  kN; with  $4d$  pitch was the M-27 beam model with  $\tau_{act} \leq 0.58R_s$ , and the maximum possible load  $Q_{max}$  on this beam model for achieving the limit deflection is equal to  $Q_{max} = 396.8$  kN. All specified models with the perforations stiffened by edging with sheet steel and paired stiffeners located on both sides of the perforation, showed the best results. In the design among these three models of beams, M-9 beam model can be recommend, having the best performance with the diameter of the perforation of  $0.5h_w$ , and  $2d$  pitch;

– the most effective model of a beam with the diameter of the perforation of  $0.75h_w$ , with  $2d$  pitch was the M-10 beam model with  $\tau_{act} \leq 0.58R_s$ , but the maximum possible load  $Q_{max}$  on this beam model for achieving the limit deflection is equal to  $Q_{max} = 299.6$  kN; with  $3d$  pitch was the M-19 beam model with  $\tau_{act} \leq R_s$ , under the load of  $Q_{max} = 270$  kN; with  $4d$  pitch was the M-28 model  $\tau_{act} \leq R_s$ , under the load of  $Q_{max} = 202$  kN. The M-19 and M-29 models with the perforations stiffened by edging with sheet steel and paired stiffeners located on both sides of the perforation showed that the yield point of steel along the shearing stress was reached. When designing, for the listed beam models stiffened by this method, it is not recommended to apply them without additional measures to increase the bearing capacity.

In general, all models showed reduction in resistance of the elements to buckling with increase of the perforation size. Therefore, to decrease the deflections and increase the stability and strength of the beam weakened by the perforations it is necessary to stiffen the perforation. Analysis of behavior of the beam models with perforations under a concentrated load showed reduction of the beam bearing capacity with an increase of the perforations pitch from  $2d$  to  $4d$  and the diameter of the perforations from  $0.25h_w$  to  $0.75h_w$ . The most optimal diameter of the perforation when designing can be the diameter of the perforation of  $0.25h_w$  and  $0.5h_w$  with  $2d$  or  $3d$  perforations pitch. Stiffening the perforation by edging with sheet steel, as well as the perforation stiffening with paired vertical stiffeners is necessary to increase the load-bearing capacity of the corrugated beam weakened by perforations. In the case of an acute need of the perforation with a diameter of  $0.75h_w$  it is recommended to use steel with higher strength characteristics in order to increase the bearing capacity and reduce the laboriousness of its manufacture.

In scientific works [17–22], there are no requirements for theoretical and experimental studies on the effect of stiffened perforations on the bearing capacity of the beam with cross-corrugated web with the corrugations of a triangular shape. Therefore, the issue of stiffening of the perforations requires special attention and further studies.

Table 5 shows the result of the obtained deflection data of beam models with corrugated web for perforations with the diameter of  $0.25h_w$ ,  $0.5h_w$  and  $0.75h_w$  for  $2d$  perforations pitch when the perforation is stiffened with ring stiffener and parallel stiffeners with a lip around the exterior circumferential edge of the stiffener ring and without a lip around the exterior circumferential edge of the stiffener ring with different width of the stiffening ring.

The most effective thickness of the edging and stiffeners for the perforation with the diameter of  $0.25h_w$ , for  $2d$  perforations pitch is the thickness of 2 to 4 mm; for the perforation with the diameter of  $0.5h_w$ , for  $2d$  perforations pitch is from 4 to 6 mm; for the perforation with the diameter of  $0.75h_w$ , for  $2d$  perforations pitch is the thickness from 6 to 8 mm.

Figure 8 shows the form for stiffening of beams with corrugated web weakened by circular perforations. Figure 8 (a) shows edging by stiffening ring without a lip around the exterior circumferential edge of the ring and Figure 8 (b) shows edging by stiffening ring with a lip around the exterior circumferential edge of the ring. The ring stiffener provides resistance to web buckling inward.

Figure 9 shows the results of behavior analysis of the M-1 beam models with corrugated web without perforation, the M-3 beam model with the diameter of the perforation of  $0.5h_w$  without perforation stiffening, M-6, M-9 beam models with various perforation stiffening options, as well as beam model with elements of the lip around the exterior circumferential edge of the ring stiffener. There is reduction in deflection in all models of beams with perforations stiffened with ring stiffeners of different thickness and width, stiffeners in comparison with models without stiffening. In addition, the deflection reduction was obtained by using a ring stiffener with elements from the lip around the exterior circumferential edge of the ring.

**Table 5. Deflections of beams with and without lips.**

Grade of the model	Perforation diameter and pitch	Total load, (kN)	Stiffening ring width (mm)	Thickness of stiffening ring and stiffeners without a lip around the exterior circumferential edge of the ring (mm)	Deflection without lip (mm)	Thickness of a lip around the exterior circumferential edge of the ring (mm)	Deflection with lip (mm)
M-8	$0.25h_w, 2d$	350	50	2	28.07	2	28.03
				4	28.01	4	27.96
				6	27.97	6	27.91
				8	27.94	8	27.88
				10	27.91	10	27.86
			75	2	28.06	2	28.04
				4	28	4	27.96
				6	27.96	6	27.91
				8	27.92	8	27.88
				10	27.89	10	27.86
			100	2	28.06	2	28.04
				4	27.99	4	27.99
				6	27.94	6	27.93
				8	27.92	8	27.89
				10	27.92	10	27.86
M-9	$0.5h_w, 2d$	350	110	2	31.32	2	29.17
				4	29.93	4	28.67
				6	29.28	6	28.43
				8	28.89	8	28.27
				10	28.64	10	28.15
			165	2	31.28	2	28.8
				4	29.62	4	28.42
				6	29.05	6	28.24
				8	28.73	8	28.11
				10	28.51	10	28.02
			220	2	31.16	2	28.72
				4	29.39	4	28.38
				6	28.89	6	28.21
				8	28.62	8	28.09
				10	28.43	10	28
M-10	$0.75h_w, 2d$	350	180	2	67.55	2	35.94
				4	44.32	4	32.2
				6	35.85	6	30.89
				8	32.85	8	30.16
				10	31.32	10	29.68
			270	2	69.68	2	33.47
				4	43.62	4	31
				6	34.7	6	30.04
				8	32.03	8	29.49
				10	30.72	10	29.12
			360	2	70.83	2	33.29
				4	42.94	4	30.94
				6	33.84	6	30.01
				8	31.44	8	29.47
				10	30.27	10	29.10

To determine the perforation location effect on the stiffness of the corrugated web with corrugations of triangular shape, it was decided to displacement the center of the perforation by 100 mm towards the tension flange and by 100 mm towards the compressed flange. The diameter of  $0.5h_w$  has been adopted as the diameter of the models perforation since the perforation with a diameter of  $0.25h_w$  does not have a significant effect on the corrugated web behavior. The  $2d$ ,  $3d$  and  $4d$  is adopted as considered perforation pitch. The perforation is edged with stiffening ring of 165 mm width, 3 mm thick with the lip around the exterior circumferential edge of the ring, as well as with stiffeners of 10 mm thick. The web thickness was accepted 1.9 mm. The data obtained for the deflection of the models are summarized in Table 6.

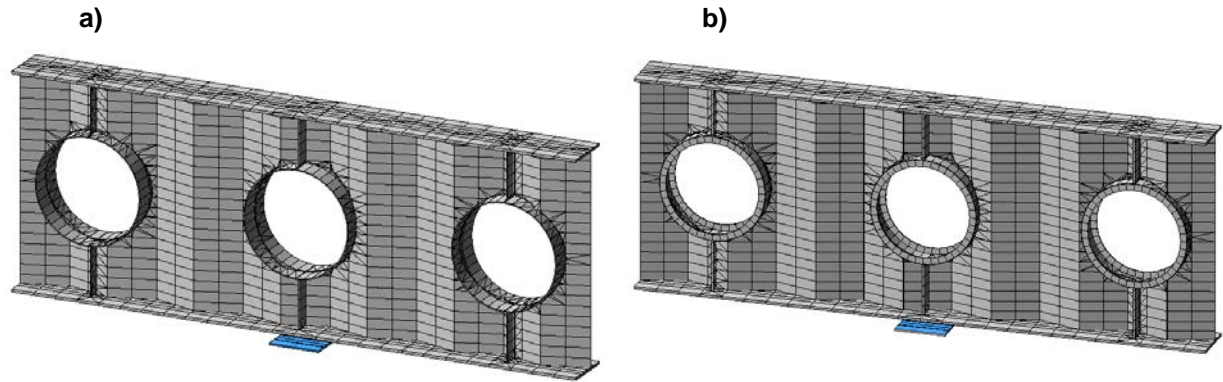


Figure 8. The form for stiffening of circular perforation with the diameter of  $0.5h_w$  a) edging by stiffening ring and stiffening without a lip around the exterior circumferential edge of the ring b) edging by stiffening ring and stiffening with a lip around the exterior circumferential edge of the ring

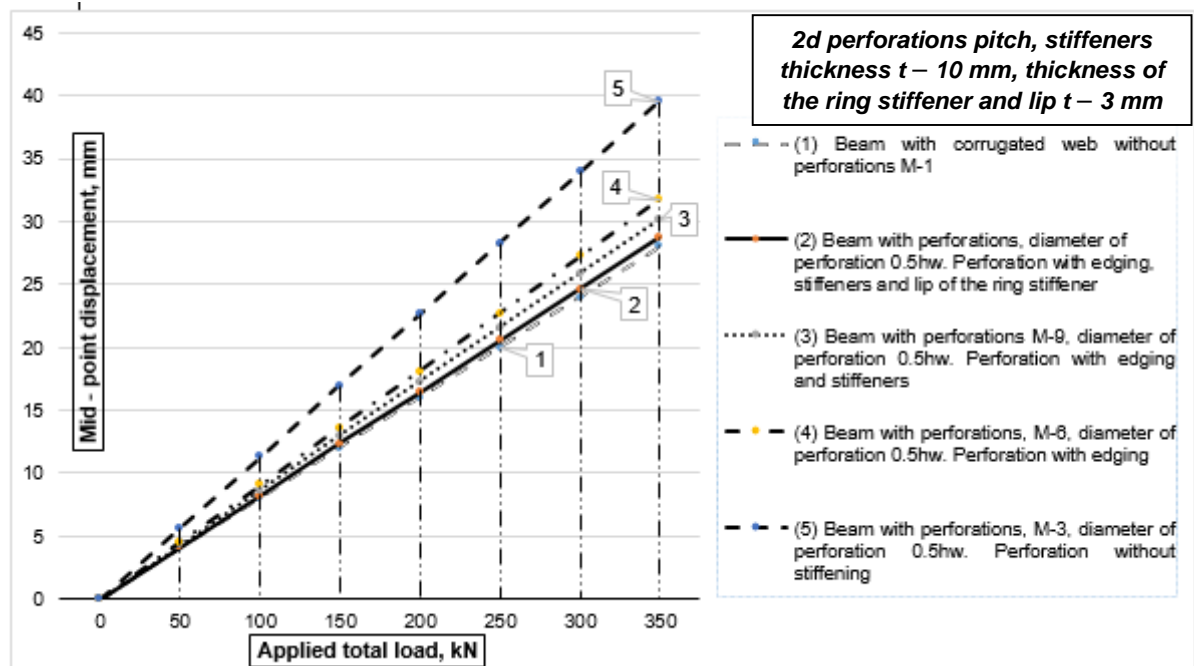


Figure 9. Effectiveness of the perforation stiffening effect on behavior of the beam with corrugated web.

Table 6. The perforation location effect along the height of the corrugated web on the deflection of the beam with stiffened perforations.

Beam model grade	Perforation pitch	Buckling from center to Z axis (mm)	Deflection in (mm) with load in (kN)						
			50	100	150	200	250	300	350
M-9	$2d$	+100	4.04	8.08	12.12	16.17	20.21	24.24	28.29
M-9	$2d$	0	4.08	8.16	12.24	16.32	20.40	24.48	28.56
M-9	$2d$	-100	4.11	8.23	12.35	16.47	20.59	24.71	28.82
M-18	$3d$	+100	4.12	8.24	12.36	16.48	20.60	24.72	28.85
M-18	$3d$	0	4.16	8.33	12.49	16.66	20.82	25.00	29.15
M-18	$3d$	-100	4.22	8.44	12.65	16.87	20.99	25.30	29.52
M-27	$4d$	+100	4.12	8.24	12.36	16.47	20.59	24.71	28.83
M-27	$4d$	0	4.15	8.30	12.45	16.60	20.75	24.90	29.05
M-27	$4d$	-100	4.19	8.34	12.56	16.75	20.94	25.13	29.32

Analyzing the data of Table 6, it can be concluded that the least deflection of beam models with diameter of the perforation of  $0.5h_w$  was obtained with the  $2d$  perforations pitch. In all three cases of a different perforations pitch, the buckling of the perforation in direction of the tension or compressed flange did not significantly affect the deflection. However, it can be noted that a slight reduction in the deflection of the models is achieved by buckling the perforation in the direction of the tension beam flange. This gives grounds to state that the central part of the web is the most optimal option for the perforation location along the height of the



beam web, but in cases where it is necessary to displacement the perforation, it will be more effective to displacement towards the tension flange of the beam with corrugated web.

#### 4. Conclusions

The undertaken study and the obtained results lead to the following conclusions:

1. Stiffening of the web and perforation by the pair stiffeners is necessary in order to avoid local buckling under the concentrated load in the perforation zone.
2. A numerical parametric study of a beam with corrugation of triangular shape showed the efficiency of perforations location in the corrugated web with the  $2d$  perforation pitch and with the diameter of the perforation of  $0.25h_w$ ,  $0.5h_w$  and  $0.75h_w$  stiffened with ring plates and parallel stiffeners.
3. The reduction in deflection in all models of beams with perforations stiffened with ring stiffeners of different thickness and width, stiffeners in comparison with models without stiffening has been found.
4. The deflection reduction has been reached by using a ring stiffener with elements from the lip around the exterior circumferential edge of the ring.
5. The most effective location of the perforation along the web height has been determined, which can also be used as a guide during decision making process of beam perforations in general.

The findings showed that the optimized perforation needs to be less than half of the beam height, while the central part of the web is the most optimal option for the perforation location along the height of the beam web and most efficiency distance between the perforations is  $2d$  perforation pitch.

#### References

1. Bryantsev, A.A., Absimetov, V.E., Lalin, V.V. Effective application of I-beams with corrugated webs in the industrial building. Construction of Unique Buildings and Structures. 2017. No. 3 (54). Pp. 93–104.
2. Zhiyenbayeva, A.T., Khvan, K.R., Bryantsev, A.A. Historical development of corrugated beams. Actual scientific research in the modern world. 2016. No. 10-3 (18). Pp. 6–8. [Online]. URL: [https://elibrary.ru/download/elibrary\\_27238281\\_29111764.pdf](https://elibrary.ru/download/elibrary_27238281_29111764.pdf) (date of reference: 24.11.2018).
3. Revathi, N., Satheshkumar, G.K., Arunkumar, G. Numerical investigation on flexural behaviour of cold formed steel I section with triangular corrugated web. International Journal of Research and Innovation in Engineering. 2016. Vol. 02. Pp. 48–53.
4. Priyanga, R.S., Mathivathani, J., Venkatesan, A. Flexural behaviour of trapezoidal corrugation beam by varying aspect ratio. International Journal of Scientific Research Engineering & Technology (IJSRET). 2016. Vol. 4. Pp. 170–174.
5. Jager, B., Dunai, L., Kövesdi, B. Girders with trapezoidally corrugated webs subjected by combination of bending, shear and path loading. Thin-Walled Structures. 2015. Vol. 96. Pp. 227–239.
6. Sarah, A.P., Jacob, P.A. A review of optimization of plate girders with corrugated webs. International journal of Innovative Research in Science and Engineering. 2016. No. 2. Pp. 63–71.
7. Cheng, J. Summary of corrugated web H-shaped steel beam joints. International Journal of Science. 2016. Vol.3. No. 4. Pp. 136–140.
8. Hajsadeghi, M., Zirakian, T., Keyhani, A., Naderi, R., Shahmohammadi, A. Energy dissipation characteristics of steel coupling beams with corrugated webs. Journal of Constructional Steel Research. 2014. No. 101. Pp. 124–132.
9. Pavlenko, A.D., Rybakov, V.A., Pikht, A.V., Mikhailov, E.S. Non-uniform torsion of thin-walled open-section multi-span beams. Magazine of Civil Engineering. 2016. 67(7). Pp. 55–69. doi: 10.5862/MCE.67.6
10. Nazmeeva, T.V., Vatin, N.I. Numerical investigations of notched C-profile compressed members with initial imperfections. Magazine of Civil Engineering. 2016. 62(2). Pp. 92–101. doi: 10.5862/MCE.62.9
11. Hadjipantelis, N., Gardner, L., Wade, M.A. Prestressed cold-formed steel beams: Concept and mechanical behaviour. Engineering Structures. 2018. Vol. 172. Pp. 1057–1072.
12. Soegihardjo, O., Suhardjono, S., Pramujati, B., Pramono, A.S. Parametric beam modeling to predict the first natural bending frequency of thin wall box shaped structures verified using experimental modal analysis. International Review of Mechanical Engineering. 2017. Vol. 11. No. 1. Pp. 77–86.
13. Atavin, I.V., Melnikov, B.E., Semenov, A.S., Chernysheva, N.V., Yakovleva, E.L. Influence of stiffness of node on stability and strength of thin-walled structure. Magazine of Civil Engineering. 2018. 80(4). Pp. 42–59. doi: 10.18720/MCE.80.5
14. Kikot, A.A. Design of cold-formed tension members using the CFSteel software. Magazine of Civil Engineering. 2016. 61(1). Pp. 42–59. doi: 10.5862/MCE.61.5
15. Feng, R., Zhan, H., Meng, S., Zhu, J. Experiments on H-shaped high-strength steel beams with perforated web. Engineering Structures. 2018. Vol. 172. Pp. 1057–1072.
16. De'nan, F., Hasan, H., Nassir, D. Kh., Osman, M.H., Saad, S. Finite element analysis for torsion behavior of flat web profile beam steel section with opening. Procedia Engineering. 2015. Vol.125. Pp. 1129–1134.
17. Kudryavtsev, S.V., Rogalevich, V.V. Kontsentratsiya napryazheniy vblizi krugovykh otverstiy v gofirovannykh stenkakh balok [The stress concentration near circular holes in the corrugated webs of the beams]. Izvestiya VUZov. Stroitelstvo. 2008. No. 11. Pp. 8–13. (rus).
18. Chung, K.F. Steel beams with large web openings of various shapes and sizes: an empirical design method using a generalized moment–shear interaction curve. Journal of constructional steel research. 2003. No. 59. Pp. 1177–1200.
19. Hagen, N.C. Shear capacity of steel plate girders with large web openings, Part 1: Modeling and simulations. Journal of constructional steel research. 2009. No. 65. Pp. 142–150.

20. Shanmugan, N.E., Lian, V.T., Thevendran, V. Finite element modeling of plate girders with web openings. Thin-walled structures. 2002. No. 40. Pp. 443–464.
21. Romeijn, A., Sarkhosh, R., Hoop, H. Basic parametric study on corrugated web girders with cut outs. Journal of Constructional Steel Research. 2009. No. 65. Pp. 395–407.
22. Kiyamaz, G., Coskun, E., Cosgun, C., Seckin, E. Transverse load carrying capacity of sinusoidal corrugated steel web beams with web openings. Steel and Composite Structures. 2010. No. 10 (1). Pp. 69–85.
23. Krishnan, L., Dineshraj, C.S., Prema, S. Experimental Investigation of cold-formed steel section-flexural member with triangular web. Journal of Mechanical and Civil Engineering (IOSR-JMCE). 2015. Vol. 12. Pp. 36–39.
24. Syerko, E., Diskovsky, A.A., Andrianov, I.V., Comas-Cardona, S., Binetruy, C. Corrugated beams mechanical behavior modeling by the homogenization method. International Journal of Solids and Structures. 2013. No. 50 (6). Pp. 928–936.
25. De'nan, F., Hasan, H., Choong, K. Experimental study on lateral torsional buckling of triangular web profile steel section. Applied Mechanics and Materials. 2015. Vol. 802. Pp. 178–183.
26. Pasnur, P., Kumbhare, M. Study of beam with plain web, trapezoidal corrugated web, and triangular corrugated web. Journal of Advances and Scholarly Researches in Allied Education. 2018. Vol. XV. No. 2. Pp. 630–634.
27. Maksimov, Yu.S., Ostrikov, G.M., Ibraimov, N.E. Stroitelnyie gofirovannyye konstruksii [Building corrugated constructions]. Almaty. 2016. 128 p. (rus)
28. International standart of Commonwealth of Independent States GOST 27772-2015 Prokat dlya stalnyih stroitelnyih konstruksiy. Obschie tehicheskie usloviya. [Rolled products for structural steel constructions. General specifications]. (rus)
29. Baby, A., Jacob, K. A parametric study on the effect of multi-corrugated web profile on the performance of steel beam section. International Research Journal of Advanced Engineering and Science. 2017. Vol. 2. Pp. 210–214.
30. Wang, Zh., Wang, Q., Liu, Y., Sun, M. Fatigue behaviour of welded joints assembled by longitudinal corrugated plates. Journal of Central South University. 2015. Vol. 22. Pp. 2752–2760.
31. Divahar, R., Joanna, P.S. Lateral buckling of cold formed steel beam with trapezoidal corrugated web. International Journal of Civil Engineering and Technology (IJCET). 2014. Vol. 5. Pp. 217–225.
32. De'nan, F., Shoong, K.K., Hashim, N.S., Ken, Ch.W. Nonlinear Analysis of Triangular Web Profile Steel Section Under Bending Behaviour. Global Civil Engineering Conference. 2017. Vol. 9. Pp. 463–472.
33. Manju, T., Arundhavapriya, E., Bharath, K.B. Study on behavior of corrugated webs in cold formed steel sections with varying thickness. Asian journal of civil engineering (BHRC). 2016. Vol. 17. No. 7. pp. 1025–1033
34. Gowri, P.M., Manu, S.S. Experimental Study on Flexural Behaviour of Cold formed Hollow Flanged Z – Sections. International Research Journal of Engineering and Technology (IRJET) 2018. Vol. 05. Pp. 364–369.
35. EN 1993-1-5: Eurocode 3: Design of steel structures – Part 1–5: Plated structural elements.

### **Contacts:**

*Alexandr Bryantsev, +77779618571; Bryancev8989@mail.ru*  
*Vladimir Absimetov, +77015112106; Absimetov47@mail.ru*  
*Vladimir Lalin, +79213199878; vllalin@yandex.ru*

© Bryantsev, A.A., Absimetov, V.E., Lalin, V.V., 2019



DOI: 10.18720/MCE.87.2

## Влияние отверстий на деформативность стенки сварной гофрированной балки

**А.А. Брянецев<sup>а\*</sup>, В.Э. Абсиметов<sup>б</sup>, В.В. Лалин<sup>с</sup>,**

<sup>а</sup> Казахская Головная Архитектурно-Строительная Академия, г. Алматы, Республика Казахстан

<sup>б</sup> ТОО «АстанаСтройКонсалтинг», г. Астана, Казахстан

<sup>с</sup> Санкт-Петербургский политехнический университет Петра Великого, Санкт-Петербург

\* E-mail: [Bryantsev8989@mail.ru](mailto:Bryantsev8989@mail.ru)

**Ключевые слова:** балка с гофрированной стенкой, отверстие в стенке, треугольное очертание гофр, прогиб балки, анализ методом конечных элементов, кольцевой усилитель

**Аннотация.** При проектировании некоторых объектов возникает необходимость устройства в гофрированных стенках балок отверстий различного диаметра для пропуска технологического оборудования в пределах строительной высоты балки, хотя это снижает несущую способность стенки. Отсутствие информации о характере работы, величинах критических напряжений, устойчивости гофрированных стенок балок, ослабленных отверстиями, вызвало необходимость проведения соответствующих исследований, для которых в стенках балок были образованы отверстия различного диаметра и с различными способами их подкрепления. Данное исследование, решает несколько задач: анализ работы сварных двутавровых балок с гофрированными стенками треугольного очертания, ослабленных технологическими отверстиями различного диаметра и различного расстояния между отверстиями на несущую способность; определяется влияние отверстий на способность воспринимать поперечную нагрузку, рассматриваются способы усиления отверстий. Приводится анализ влияния толщины окаймления, парных вертикальных ребер жёсткости при различной ширине кольцевого усилителя на работу моделей балок с гофрированной стенкой с отверстиями. Определено влияние загиба внешней грани кольцевого усилителя на несущую способность балок с гофрированной стенкой ослабленных отверстиями, а также наиболее эффективное месторасположение отверстия по высоте стенки, при проектировании.

### Литература

1. Bryantsev A.A., Absimetov V.E., Lalin V.V. Effective application of I-beams with corrugated webs in the industrial building // Construction of Unique Buildings and Structures. 2017. No. 3 (54). Pp. 93–104.
2. Жиенбаева А.Т., Хван К.Р., Брянецев А.А. История развития гофрированных балок // Актуальные научные исследования в современном мире. 2016. № 10-3 (18). С. 6–8.
3. Revathi N., Satheshkumar G.K., Arunkumar G. Numerical investigation on flexural behaviour of cold formed steel I section with triangular corrugated web // International Journal of Research and Innovation in Engineering. 2016. Vol. 02. Pp. 48–53.
4. Priyanga R.S., Mathivathani J., Venkatesan A. Flexural behaviour of trapezoidal corrugation beam by varying aspect ratio // International Journal of Scientific Research Engineering & Technology (IJSRET). 2016. Vol. 4. Pp. 170–174.
5. Jager B., Dunai L., Kövesdi B. Girders with trapezoidally corrugated webs subjected by combination of bending, shear and path loading // Thin-Walled Structures. 2015. Vol. 96. Pp. 227–239.
6. Sarah A.P., Jacob P.A. A review of optimization of plate girders with corrugated webs // International journal of Innovative Research in Science and Engineering. 2016. No. 2. Pp. 63–71.
7. Cheng J. Summary of corrugated web H-shaped steel beam joints // International Journal of Science. 2016. Vol.3. No. 4. Pp. 136–140.
8. Hajsadeghi M., Zirakian T., Keyhani A., Naderi R., Shahmohammadi A. Energy dissipation characteristics of steel coupling beams with corrugated webs // Journal of Constructional Steel Research. 2014. No. 101. Pp. 124–132.
9. Павленко А.Д., Рыбаков В.А., Пихт А.В., Михайлов Е.С. Стесненное кручение многопролетных тонкостенных балок открытого профиля // Инженерно-строительный журнал. 2016. № 7(67). С. 55–69. doi: 10.5862/MCE.67.6
10. Назмеева Т.В., Ватин Н.И. Численные исследования сжатых элементов из холодногнутого просечного С-профиля с учетом начальных несовершенств // Инженерно-строительный журнал. 2016. №2(62). С. 92–101. doi: 10.5862/MCE.62.9

11. Hadjipantelis N., Gardner L., Wade M.A. Prestressed cold-formed steel beams: Concept and mechanical behaviour // *Engineering Structures*. 2018. Vol. 172. Pp. 1057–1072.
12. Soegihardjo O., Suhardjono S., Pramujati B., Pramono A.S. Parametric beam modeling to predict the first natural bending frequency of thin wall box shaped structures verified using experimental modal analysis // *International Review of Mechanical Engineering*. 2017. Vol. 11. No. 1. Pp. 77–86.
13. Атавин И.В., Мельников Б.Е., Семенов А.С., Чернышева Н.В., Яковлева Е.Л. Влияние жесткости узловых соединений на устойчивость и прочность тонкостенных конструкций // *Инженерно-строительный журнал*. 2018. № 4(80). С. 48–61. doi: 10.18720/MCE.80.5
14. Кикоть А.А. Расчет растянутых элементов из стальных тонкостенных холодногнутых профилей в программе CFSteel // *Инженерно-строительный журнал*. 2016. №1(61). С. 42–59. doi: 10.5862/MCE.61.5
15. Feng R., Zhan H., Meng S., Zhu J. Experiments on H-shaped high-strength steel beams with perforated web // *Engineering Structures*. 2018. Vol. 172. Pp. 1057–1072.
16. De'nan F., Hasan H., Nassir D. Kh., Osman M.H., Saad S. Finite element analysis for torsion behavior of flat web profile beam steel section with opening // *Procedia Engineering*. 2015. Vol.125. Pp. 1129–1134.
17. Кудрявцев С.В., Роголевич В.В. Концентрация напряжений вблизи круговых отверстий в гофрированных стенках балок // *Известия ВУЗов. Строительство*. 2008. № 11. С. 8–13.
18. Chung K.F. Steel beams with large web openings of various shapes and sizes: an empirical design method using a generalized moment–shear interaction curve // *Journal of constructional steel research*. 2003. No. 59. Pp. 1177–1200.
19. Hagen N.C. Shear capacity of steel plate girders with large web openings, Part 1: Modeling and simulations // *Journal of constructional steel research*. 2009. No. 65. Pp. 142–150.
20. Shanmugan N.E., Lian V.T., Thevendran V. Finite element modeling of plate girders with web openings // *Thin-walled structures*. 2002. No. 40. Pp. 443–464.
21. Romeijn A., Sarkhosh R., Hoop H. Basic parametric study on corrugated web girders with cut outs // *Journal of Constructional Steel Research*. 2009. No. 65. Pp. 395–407.
22. Kiyamaz G., Coskun, E., Cosgun C., Seckin E. Transverse load carrying capacity of sinusoidal corrugated steel web beams with web openings // *Steel and Composite Structures*. 2010. No. 10 (1). Pp. 69–85.
23. Krishnan L., Dineshraj C.S., Prema S. Experimental Investigation of cold-formed steel section-flexural member with triangular web // *Journal of Mechanical and Civil Engineering (IOSR-JMCE)*. 2015. Vol. 12. Pp. 36–39.
24. Syerko E., Diskovsky A.A., Andrianov I.V., Comas-Cardona S., Binetruy C. Corrugated beams mechanical behavior modeling by the homogenization method // *International Journal of Solids and Structures*. 2013. No. 50 (6). Pp. 928–936.
25. De'nan F., Hasan H., Choong K. Experimental study on lateral torsional buckling of triangular web profile steel section // *Applied Mechanics and Materials*. 2015. Vol. 802. Pp. 178–183.
26. Pasnur P., Kumbhare M. Study of beam with plain web, trapezoidal corrugated web, and triangular corrugated web // *Journal of Advances and Scholarly Researches in Allied Education*. 2018. Vol. XV. No. 2. Pp. 630–634.
27. Максимов Ю.С., Остриков Г.М., Ибраимов Н.Э. Строительные гофрированные конструкции. Алматы. 2016. 128 с.
28. ГОСТ 27772 – 2015 Прокат для стальных строительных конструкций. Общие технические условия.
29. Baby A., Jacob K. A parametric study on the effect of multi-corrugated web profile on the performance of steel beam section // *International Research Journal of Advanced Engineering and Science*. 2017. Vol. 2. Pp. 210–214.
30. Wang Zh., Wang Q., Liu Y., Sun M. Fatigue behaviour of welded joints assembled by longitudinal corrugated plates // *Journal of Central South University*. 2015. Vol. 22. Pp. 2752–2760.
31. Divahar R., Joanna P.S. Lateral buckling of cold formed steel beam with trapezoidal corrugated web // *International Journal of Civil Engineering and Technology (IJCIET)*. 2014. Vol. 5. Pp. 217–225.
32. De'nan F., Shoong K.K., Hashim N.S., Ken Ch.W. Nonlinear Analysis of Triangular Web Profile Steel Section Under Bending Behaviour // *Global Civil Engineering Conference*. 2017. Vol. 9. Pp. 463–472.
33. Manju T., Arundhavapriya E., Bharath K.B. Study on behavior of corrugated webs in cold formed steel sections with varying thickness // *Asian journal of civil engineering (BHRC)*. 2016. Vol. 17. No. 7. pp. 1025–1033
34. Gowri P.M., Manu S.S. Experimental Study on Flexural Behaviour of Cold formed Hollow Flanged Z – Sections // *International Research Journal of Engineering and Technology (IRJET)* 2018. Vol. 05. Pp.364–369.
35. EN 1993-1-5: Eurocode 3: Design of steel structures – Part 1–5: Plated structural elements.

#### **Контактные данные:**

*Александр Александрович Брянцев, +77779618571; эл. почта: Bryancev8989@mail.ru*  
*Владимир Эскендерович Абсиметов, +77015112106; эл. почта: Absimetov47@mail.ru*  
*Владимир Владимирович Лалин, +79213199878; эл. почта: vllalin@yandex.ru*

© Брянцев А.А., Абсиметов В.Э., Лалин В.В., 2019





DOI: 10.18720/MCE.87.3

## Bearing capacity of fastener steel tube full hall scaffolds

**Z. Lu\*, G. Chao,**

*Shenyang Jianzhu University, Shenyang City, Liaoning, P.R.China*

*\* E-mail: luzhengranglovel@126.com*

**Keywords:** fastener steel tube full hall scaffold, eccentric axial load, bearing capacity, failure mode, nonlinear finite element analysis.

**Abstract.** In fastener steel tube full hall scaffolds (FSTFHSs), the upper load is transferred to the posts through the top horizontal tubes. Further, the posts and horizontal tubes are not always in the same plane owing to the eccentricity of the coupler connections. Moreover, building materials and construction machinery are usually eccentrically stacked atop the FSTFHSs. Therefore, the members in FSTFHSs are subject to eccentric axial loading. This paper reports a systematic experimental and analytical study on the bearing capacity of FSTFHSs with eccentric axial loads on the tubes. Five full-scale FSTFHS specimens were built and tested for failure to obtain the strength and failure modes of FSTFHSs whose members are subject to eccentric axial loads. Advanced nonlinear finite element analysis (FEA) was conducted on the specimen models to obtain the strength and failure modes of the FSTFHS under eccentric axial load of the member and to compare with the experimental results. Parametric studies were conducted based on the FEA results to investigate the influence of eccentric axial loads on the bearing capacity of FSTFHSs with different geometric properties. The experimental and analytical results show that eccentric axial loading negatively affects the FSTFHS bearing capacity and that the main failure mode of FSTFHS is the local instability of the posts in the heaped load areas, accompanied by the twisting of the entire structure and bending of the top horizontal tubes.

### 1. Introduction

Fastener steel tube full hall scaffold (FSTFHS) systems are widely used as temporary structures in concrete casting construction, which involves the management of large loads (e.g. construction of girders and continuous box girder bridges), owing to their ease in fabrication, installation, and dissemination. However, FSTFHS systems have collapsed in many places (Figure 1), resulting in many casualties [1–4].



**Figure 1. Collapse of FSTFHS system during construction in Yunnan Province on January 3, 2010.**

Lu, Z., Chao, G. Bearing capacity of fastener steel tube full hall scaffolds. Magazine of Civil Engineering. 2019. 87(3). Pp. 35–45. DOI: 10.18720/MCE.87.3.

Лу Ч., Чао Г. Несущая способность крепёжной стальной трубы строительных лесов // Инженерно-строительный журнал. 2019. № 3(87). С. 35–45. DOI: 10.18720/MCE.87.3



This open access article is licensed under CC BY 4.0 (<https://creativecommons.org/licenses/by/4.0/>)

An FSTFHS system comprises three or more rows of vertical posts connected by couplers, horizontal tubes, and X-bracing. Depending on the load-transfer modes, such system can be classified as either fastener steel tube full hall formwork support (FSTFHFS, Figure 2) or FSTFHS (Figure 3). In FSTFHFS, the load is directly transferred to the posts through adjustable U-heads. However, in FSTFHS, the load is first transferred to the top horizontal tubes through wood braces or scaffold boards, which then transfer the load to the posts. The distance between the resultant action point of upper load and the neighbouring post is expressed as eccentricity  $e$ , as shown in Figure 3. This load-transfer mode has eccentricity [5–7]. The difference between the FSTFHFS and FSTFHS is really worthy of study to determine the influence of the eccentric load-transfer mode on the critical load of the system. Furthermore, all tubes are connected using couplers whose centre lines are not always in the same plane (Figure 4). Moreover, building materials and construction machinery are usually eccentrically stacked atop FSTFHSs (Figure 5). These loading conditions mean that the members of an FSTFHS are subject to eccentric axial loads, which might cause part of the posts to buckle due to overloading, consequently resulting in the collapse of the FSTFHS.

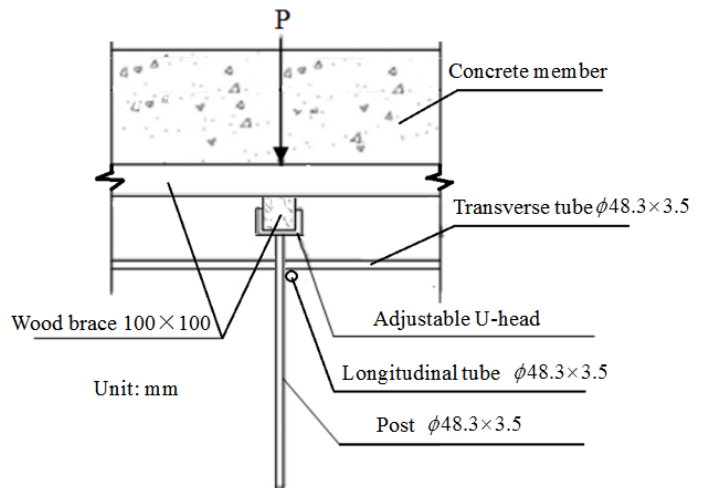
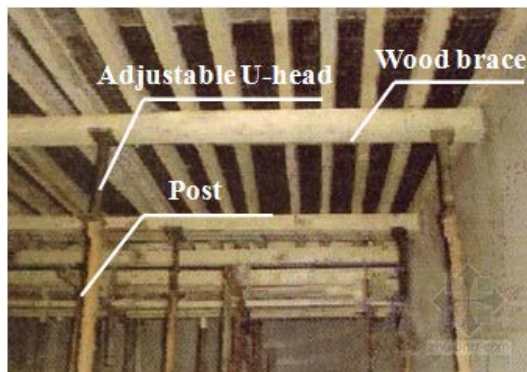


Figure 2. Load transfer through adjustable U-head in FSTFHFS.

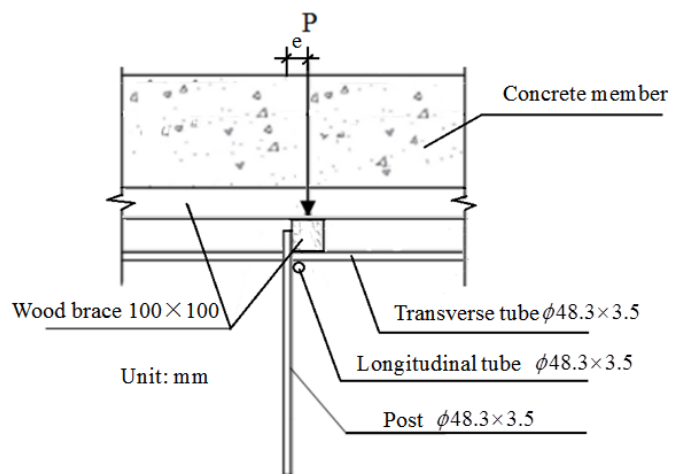
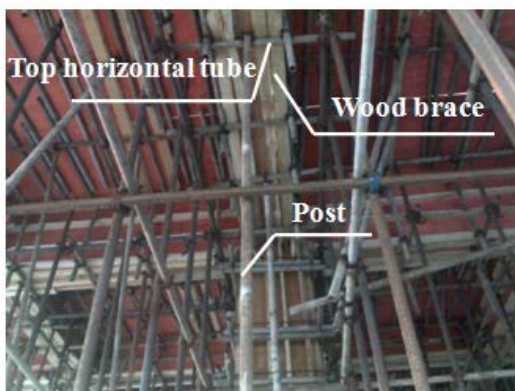


Figure 3. Load transfer through top horizontal tube in FSTFHS.

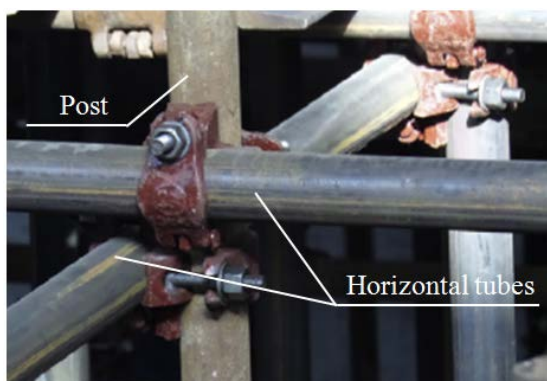


Figure 4. Eccentricity induced by connection of right-angle coupler.



Figure 5. Eccentric local heaped load.

Many studies on FSTFHFS have been conducted since the 2000s. Yuan [8], Hu [9], and Xie [10] have performed reliability analyses of FSTFHFS. Beale [11–13], Ao [14], Yue [15], and Liu [16, 17] have published numerous experimental and theoretical studies on the stability capacity and the design method of FSTFHFS. Similarly, systematic studies [18–20] have also been conducted on the bearing capacity and design method of FSTFHFS, including 12 FSTFHFS prototype tests and several finite element analyses (FEAs). In contrast, FSTFHSSs, which are used in the construction of large-span spatial structures such as gymnasiums, train stations, garages, and bridges, have been scarcely investigated. In addition, using the above-mentioned research results in which the member eccentric axial loads are neglected is inaccurate and inappropriate in designing FSTFHSSs. Disastrous collapse of FSTFHSS has occurred in several countries, which casts doubt on the safety of such systems. Understanding the structural behaviour of FSTFHSS through experimental and theoretical studies is essential to prevent such collapse.

This work aims to conduct experimental and theoretical studies to investigate the following: (1) the bearing capacity and failure modes of several different FSTFHSSs with eccentric axial loads on tubes, (2) the effect of setting parameters and loading conditions on the FSTFHSSs, and (3) the effect of eccentric axial load on the bearing capacity of the FSTFHSSs with various geometric properties.

## 2. Methods

### 2.1. Experimental Investigation

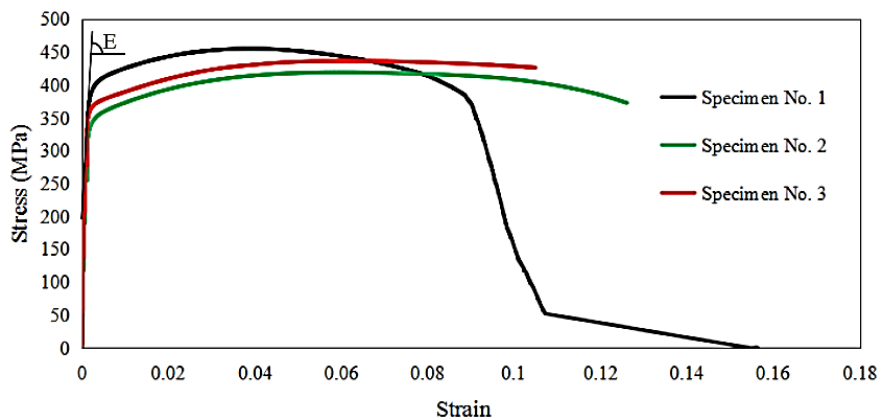
All steel members and couplers used in the tests were obtained from actual construction sites. The steel tubes used in the test specimens had a diameter of 48.3 mm and a thickness of 3.02 mm. Three randomly selected steel tubes were processed into arc-shaped work pieces in accordance with code GB/T228-2002[21] as shown in Figure 6(a) for material testing. The test specimen was fixed on the tensile testing machine (Figure 6(b)). Figure 6(c) shows the corresponding tensile curves. The average yield strength, ultimate strength, and Young's modulus  $E$  of the steel tubes were 374.92 MPa, 436.92 MPa, and 184 GPa, respectively.



(a) Three arc-shaped test specimens



(b) Test specimen fixed on the tensile testing machine

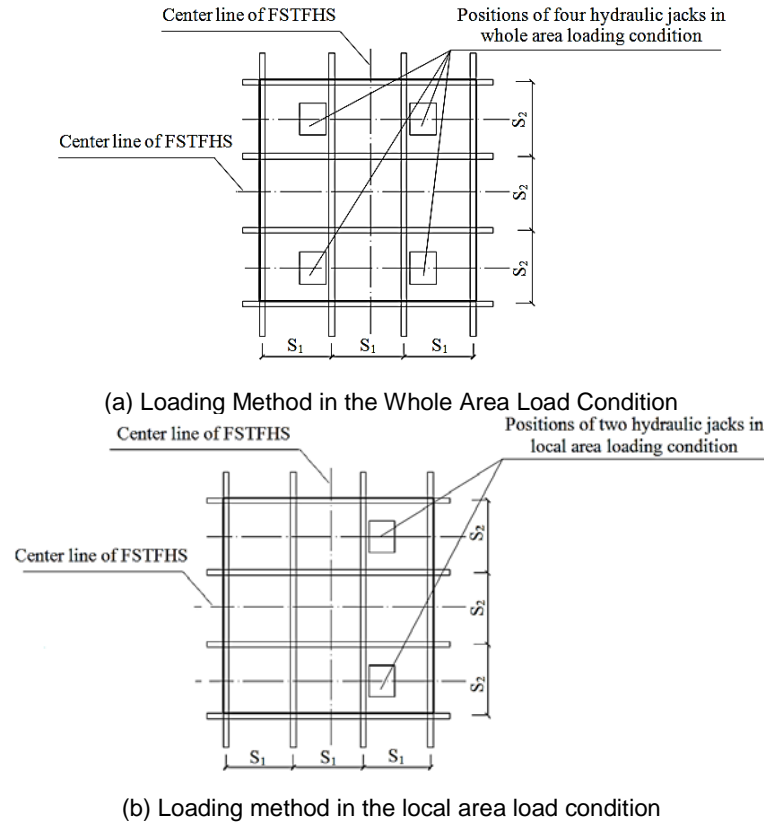


(c) Tensile curves

**Figure 6. Tensile curves of the materials.**

Building materials are usually eccentrically stacked atop FSTFHSSs, meaning that they are subject to large eccentric local heaped loads. Thus, two loading methods were adopted in the tests: uniform load over the entire FSTFHSS [hereinafter referred to as whole area load, Figure 7(a)] and uniform load over local regions on the FSTFHSS [hereinafter referred to as local area load, Figure 7(b)].





Note: (a) and (b) show the plans of the test specimens without X-bracing under the whole and local area load conditions, respectively, and the thick solid lines indicate the planes with vertical X-bracing.

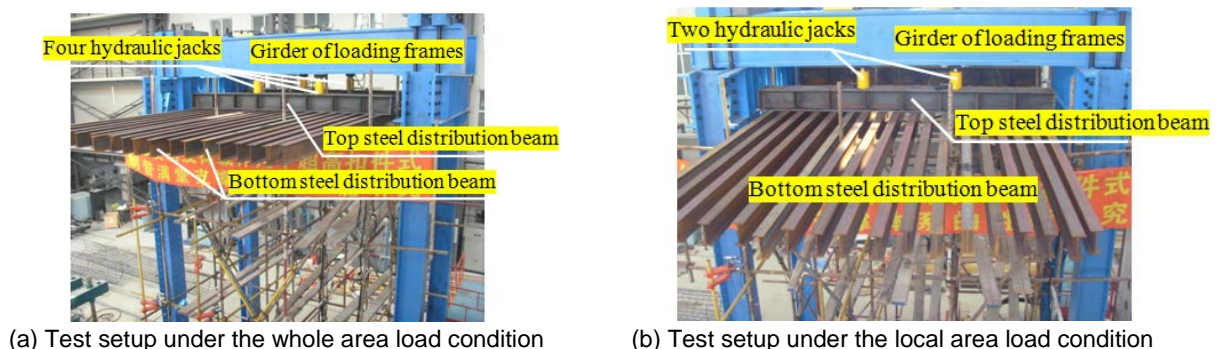
**Figure 7. Placement of the hydraulic jacks in the two loading methods.**

Loading frames, four 50-ton hydraulic jacks (two in the local area load condition), and two layers of steel distribution beams were used in the tests. Vertical uniform loads were applied at the top horizontal tubes of the FSTFHS in the specified loading area as follows: the hydraulic jacks were fastened to the bottom of girders in the loading frames, and vertical loads were applied to the top-layer distribution beams. The loads were then transferred to a group of bottom distribution beams in the perpendicular direction and finally to the FSTFHS. Figures 8 and 9 show the test setup and general layout of the test specimens, respectively.

The multistage loading method where loads were applied in increments of 20 kN for 3 min each was adopted in the tests. When the applied total load approached the anticipated bearing capacity computed using the JGJ 130–2011 code [22], the load step increment was reduced to 2 kN with each step load applied until the strain and displacement stabilized. For safety purposes, the specimens were not loaded until the collapse. The pressure in the hydraulic jacks decreased when the FSTFHS specimens reached their peak load and started to unload owing to instability. At this point, the specimens were considered to have failed, and thus, the test was stopped.

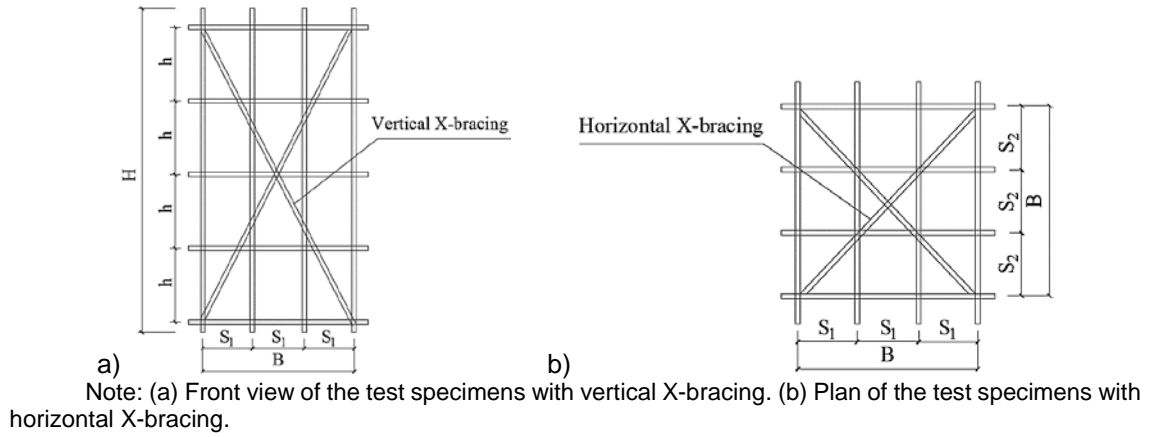
## 2.2. Numerical Investigation

A nonlinear analysis was performed using the FEA software ANSYS to study the behaviour and predict the strength of the FSTFHS test specimens. To simulate the semi-rigid behaviour of the right-angle couplers, spring-damper element (COMBIN14) with a spring constant of 19.0 kN·m/rad—the mean initial rotational stiffness obtained from earlier right-angle coupler tests [23]—was used in the analysis.



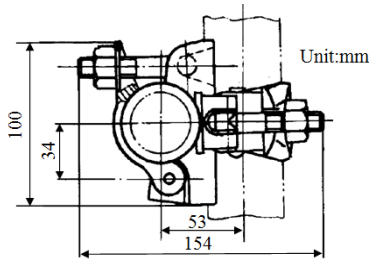
**Figure 8. Test setup.**



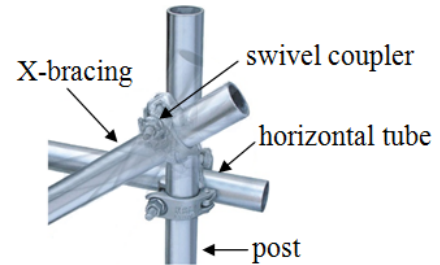


**Figure 9. General layout of the FSTFHS.**

In the FSTFHS, longitudinal and transverse horizontal tubes are connected to the posts using right-angle couplers (Figure 10), and the X-bracing members are connected to the posts or horizontal tubes using swivel couplers (Figure 11). The centre lines of all connected tubes may not be in the same plane but are at a certain eccentric distance. This eccentric distance was set to 53 mm in the FEA as shown in Figure 10. The main node (Figure 12) was the intersection between a post and two tubes in the perpendicular directions, and the vertical distance between the nodes connecting the two tubes in different directions was set to 150 mm.

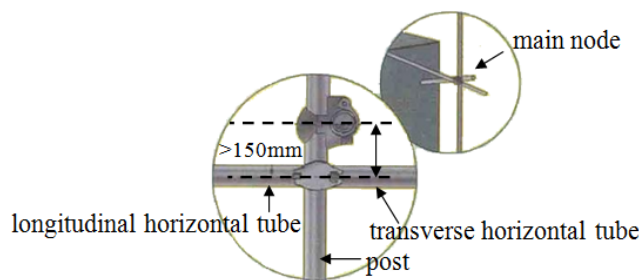


**Figure 10. Eccentricity between tubes connected by right-angle coupler**

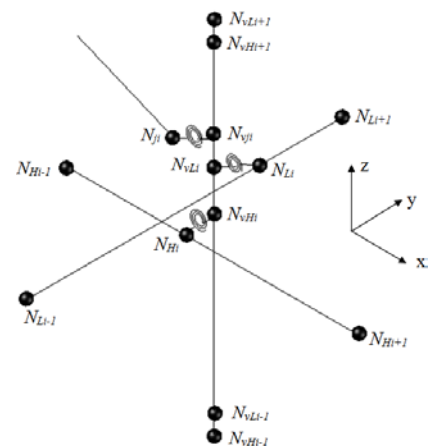


**Figure 11. Connection mode of the X-bracing**

Because the transverse and longitudinal tubes and the posts are continuous and no discontinuity in the members exists at the right-angle coupler location in practice, a three-dimensional beam element (BEAM188) was used to model the transverse and longitudinal tubes and the vertical posts. Figure 13 shows the modelling process. At the main node, two nodes  $N_{vHi}$  and  $N_{vLi}$  were defined along the  $z$  axis (i.e. the extension direction of the post) at a vertical separation of 150 mm. These two nodes belong to the post element. Node  $N_{Hi}$ , which belongs to the transverse horizontal tube element, was defined by shifting  $N_{vHi}$  53 mm along the  $y$  axis (i.e. the extension direction of the longitudinal horizontal tube), and node  $N_{Li}$ , which belongs to the longitudinal horizontal tube element, was defined by shifting  $N_{vLi}$  53 mm along the  $x$  axis (i.e. the extension direction of the transverse horizontal tube). To simulate the semi-rigid behaviour of the right-angle couplers, a spring-damper element (COMBIN14), which simulates the rotational restraint around the  $y$  axis ( $x$  axis), was added between node  $N_{vHi}$  ( $N_{vLi}$ ) on the post and node  $N_{Hi}$  ( $N_{Li}$ ) on the transverse horizontal tube (longitudinal horizontal tube). The coupling of these nodes was defined such that the nodes would have the same displacement in all directions and the same rotation around the vertical axis.



**Figure 12. Connection mode of the main node.**

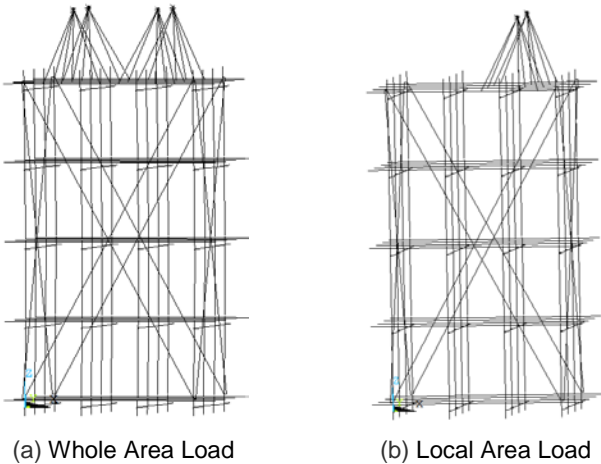


**Figure 13. Establishment of nodes in FEA by considering the coupler eccentricity.**

X-bracing members were considered to solely enhance the overall stiffness of the FSTFHS; hence, a three-dimensional link element (Link180) was used to model the X-bracing. To simulate the connection between the post and the X-bracing, two nodes  $N_{vji}$  and  $N_{ji}$  were defined at the location of the swivel coupler (Figure 11), where node  $N_{vji}$ , which belongs to the post element, was defined by shifting node  $N_{vLi}$  150 mm along the  $z$  axis (i.e. the extension direction of the post), and node  $N_{ji}$ , which belongs to the X-bracing element, was defined by shifting node  $N_{vji}$  53 mm along the  $x$  axis (when the X-bracing was set in the  $y-z$  plane) or the  $y$  axis (when the X-bracing was set in the  $x-z$  plane). The COMBIN14 element, which simulates the sliding constraint along the  $z$  axis, was added between nodes  $N_{ji}$  and  $N_{vji}$  with a spring constant of 1410 N/mm [24]. Coupling was defined for these two nodes in the remaining directions.

Four key points (two key points under the local area load condition), considered as the master nodes, were defined in the centroid of the designated loading areas atop the FSTFHS model. These points were located at positions corresponding to those of the hydraulic jacks in the tests. Beam-type constraints were

a  
d  
d  
e  
d  
  
b  
e  
t  
w  
e  
e  
n  
  
t  
h  
e



**Figure 14. Finite Element Models of the FSTFHS by Considering the Upload Transference Eccentricity.**

First, eigenvalue buckling analysis was conducted to obtain the elastic critical buckling loads as well as the failure modes for application in subsequent nonlinear analyses. Neither material nonlinearity nor geometric imperfections were considered in the eigenvalue buckling analysis because of the purely linearly elastic nature of the analysis. Subsequently, nonlinear analysis was conducted by considering the geometrical imperfections, geometric nonlinearity, and material nonlinearity. A concentrated load was incrementally applied to each key point on the designated loading area. This load was transformed into a uniform load through beam-type constraints and was transferred to the top horizontal steel tube until the FSTFHS became unstable or failure of the solution to converge occurred. The maximum load applied to the model was considered to be its strength. Material nonlinearity was accounted for using a perfect elastic-plastic material model, and the parameter values were determined through coupon tests. According to previous literature, the maximum imperfection allowed in practice is 0.05 m for a FSTFHS with height less than 10m [22]. Therefore, the first buckling mode identified from the eigenvalue buckling analysis with a maximum amplitude of 0.05 m was applied to the model as the initial geometric imperfection.

e  
a  
c  
h

### 3. Results and Discussion

Table 1 lists the geometric properties, test specimen loading methods, and corresponding test results. For comparison, the table also lists the results of two FSTFHS prototype tests (PTS6 and PTS7) that we conducted before [19].

n

**Table 1. Geometric parameters and test results for the full-scale specimens**

NO.	Storey Height $h$ (m)	Post Spacing $S_1 \times S_2$ (m $\times$ m)	Aspect Ratio $H/B$	Total Height (m)	Spans	Sweeping Staff Height (m)	X-bracing	Loading Method	$P_{test}$ (kN)
TS1	1.8	1.3 $\times$ 1.3	2	8.00	3 $\times$ 3	0.3	None	Whole area load	8.58
TS2							Vertical	Whole area load	18.30
TS3								Local area load	16.08
TS4							Vertical + Horizontal	Whole area load	25.83
TS5								Local area load	18.33
PTS6	1.8	1.5 $\times$ 1.5	1.8	8.00	3 $\times$ 3	0.3	None	Whole area load	6.40
PTS7	1.5	1.2 $\times$ 1.2	1.6	8.00	4 $\times$ 4	0.3	None	Whole area load	12.22

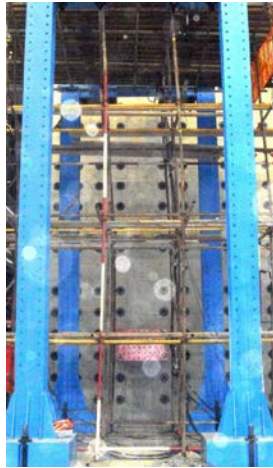
Note:  $P_{test}$  stands for the strength of a single post obtained from the test. Symbols in Table 1 are shown in Figure 9.

t  
o  
p

The data listed in Table 1 [specifically, the comparison of TS1 ( $P_{\text{test}} = 8.58 \text{ kN}$ ) and PTS6 ( $P_{\text{test}} = 6.40 \text{ kN}$ )] clarify that although increasing the post spacing could reduce the specimen aspect ratio, the strength of the FSTFHS without X-bracing would be reduced to some extent under the whole area load condition. In addition, when the storey height was large (e.g.  $\approx 1.8 \text{ m}$ ), the aforementioned decrease was approximately 25 %. Therefore, to increase the strength of the FSTFHS, not only methods to reduce the aspect ratio but also other parameters such as the storey height, post spacing, and aspect ratio should be comprehensively considered in the design.

Furthermore, the data listed in Table 1 [specifically, the comparison of test TS1 ( $P_{\text{test}} = 8.58 \text{ kN}$ ) and PTS7 ( $P_{\text{test}} = 12.22 \text{ kN}$ ) as well as PTS6 ( $P_{\text{test}} = 6.40 \text{ kN}$ ) and PTS7 ( $P_{\text{test}} = 12.22 \text{ kN}$ )] clarify that the FSTFHS strength would increase to some extent if both the storey height and post spacing are decreased.

For an FSTFHS without X-bracing, such as TS1, the typical failure mode was the global lateral buckling around the longitudinal weak axis [Figure 15(a)], similar to that for PTS6 [Figure 15(b)].



(a) TS1



(b) PTS6

**Figure 15. Typical Failure Modes of an FSTFHS without X-bracing.**

Table 2 lists the influence of the loading condition on the bearing capacity of the five FSTFHS test specimens. Compared with that of the whole area loading condition, the FSTFHS strength under the local area loading condition decreased to some extent. For the FSTFHS with all-around vertical X-bracing, the strength was reduced by 12.13 %, and for the FSTFHS with vertical and horizontal X-bracing (similar to the actual configuration in most construction projects), the strength was reduced by 29.04 %. For safety reasons, the FSTFHS test specimen without X-bracing was subjected to the whole area loading only.

**Table 2. Effect of Loading Condition on the Bearing Behaviour of the FSTFHS.**

Loading Condition	X-bracing		
	Vertical	Vertical + Horizontal	None
Whole area load $P_{\text{test}_q}$	18.30	25.83	8.58
Local area load $P_{\text{test}_p}$	16.08	18.33	–
$\text{Diff1} (\%)$	–12.13	–29.04	–

Note: 1. Unit: kN

2.  $P_{\text{test}_q}$  stands for the strength of a single post obtained from the test under whole area loading condition

3.  $P_{\text{test}_p}$  stands for the strength of a single post obtained from the test under local area loading condition

$$4. \text{Diff1} = \frac{P_{\text{test}_p} - P_{\text{test}_q}}{P_{\text{test}_q}} \times 100 \%$$

The failure modes of the tested FSTFHSs differed according to the applied loading condition. Figure 16(a) shows the typical deformed shape of TS2 under the whole area loading condition. All posts exhibited the same deformed shape, but only the posts in the two uppermost stories buckled evidently due to the vertical X-bracing and the action of the whole area uniform loading ( $e_1 > e_2$  in the figure). Figure 16(b) shows the side view of the failure mode of TS3 under the local area loading condition. Part of the posts in the area close to the two working hydraulic jacks underwent large deformation ( $e_3 > e_4$  in the figure). Figure 16(c) shows the plan view of the failure mode of TS3 under the local area loading condition. During buckling, the entire structure twisted anticlockwise ( $e_5 < e_6$  in the figure). Moreover, the top horizontal tube bent [Figure 16(d)]. Thus, the typical failure mode of the FSTFHS under local area loading condition (e.g. local heaped load, which is common in construction sites) is



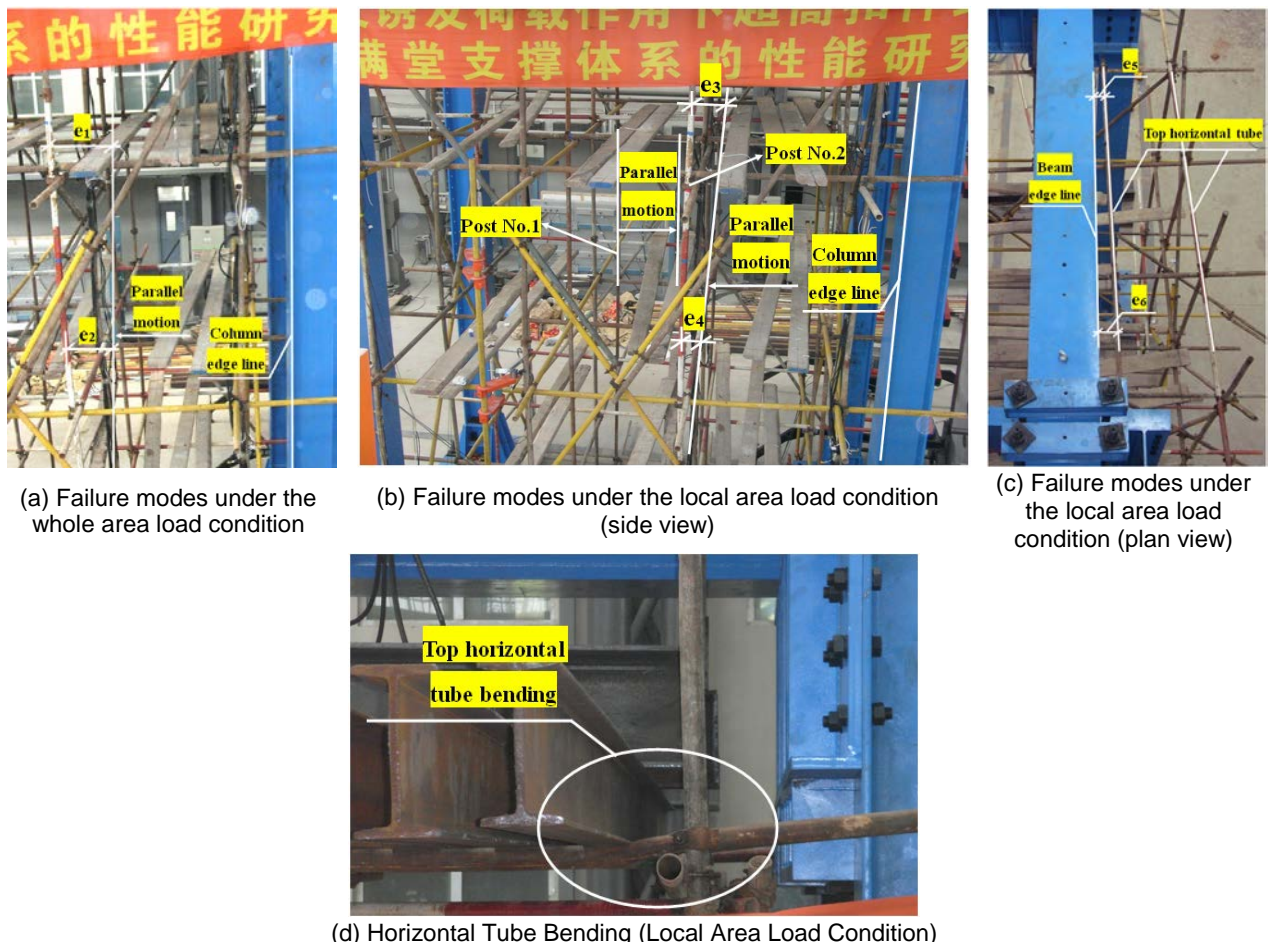
the lateral buckling of part of the posts in the local loading area around the weak axis, accompanied by torsion of the entire structure and bending of the top horizontal tubes.

Table 3 lists the influence of X-bracing on the bearing capacity of the five FSTFHS test specimens. The X-bracing clearly increased the bearing capacity of the FSTFHS irrespective of the loading condition. Under the whole area loading condition, for the FSTFHS with all-around vertical X-bracing, the bearing capacity was approximately twice that of the FSTFHS without X-bracing. Under the same loading condition, by adding three X-bracing structures (one each at the top, middle, and bottom layers), the bearing capacities increased by 41.15 % and 13.99 % under the whole and local area loading conditions, respectively.

The comparison with our previous experimental and analytical results of the bearing capacity of FSTFHS in [18, 19] indicates that the strength of the FSTFHS is lower than that of the FSTFHS because of the difference in the load-transfer mechanisms in these two structures. In addition, the effect of the X-bracing on the bearing capacity of the FSTFHS was more evident than on that of the FSTFHS (the effect varies with the geometric parameters and X-bracing configuration). These observations highlight the importance of X-bracing in enhancing the bearing capacity of the FSTFHS.

$P_{FEA}$  is generally consistent in the full-scale test results with a maximum difference of -4.80 %, and the models can therefore be used in future parametric studies. The reasons attributed to the slight discrepancies could include variance in the rotational stiffness of couplers, variance in the mechanical properties of steel tubes, initial imperfections of the steel tubes, etc. Figure 17 shows the typical failure modes for TS1 and TS3 obtained through FEA, which were quite consistent with those observed in the full-scale tests. For the FSTFHS without X-bracing under whole area loading condition, global lateral buckling occurred around the longitudinal weak axis [Figure 17(a)]. In contrast, under local area loading condition, only the posts near the loading area underwent local large deformation [Figure 17(b)], accompanied by the twisting of the entire structure [Figure 17(c)] and bending of the top horizontal tubes [Figure 17(b)].

To investigate the influence of the eccentric axial load on the bearing capacity of the FSTFHS with various geometric properties, parametric studies were conducted on the developed FSTFHS models. The investigated parameters included storey height, post spacing, rotational stiffness of the couplers, and sweeping staff height. The primary layout of the finite element model included five spans along the longitudinal axis and five spans along the transverse axis using standard tubes of P48 mm × 3.5 mm in both directions. Table 5 lists the summary of the geometric dimensions used in the parametric studies.



**Figure 16. Typical failure modes of the FSTFHS under different loading conditions**

**Table 3. Effect of X-bracing on the bearing behaviour of FSTFHS.**

X-bracing	Loading condition	
	Whole Area Load	Local Area Load
None ( $P_{test\_w}$ )	8.58	–
Vertical ( $P_{test\_v}$ )	18.30	16.08
<i>Diff1</i>	2.13 times	–
Vertical + Horizontal ( $P_{test\_y}$ )	25.83	18.33
<i>Diff2</i>	3.01 times	–
<i>Diff3</i> (%)	41.15	13.99

Note: 1. Unit: kN

2.  $P_{test\_w}$ ,  $P_{test\_v}$  and  $P_{test\_y}$  all stand for the strength of the single post obtained from the test

$$3. Diff1 = \frac{P_{test\_v}}{P_{test\_w}}, Diff2 = \frac{P_{test\_y}}{P_{test\_w}}, \text{ and } Diff3 = \frac{P_{test\_y} - P_{test\_v}}{P_{test\_v}} \times 100 \%$$

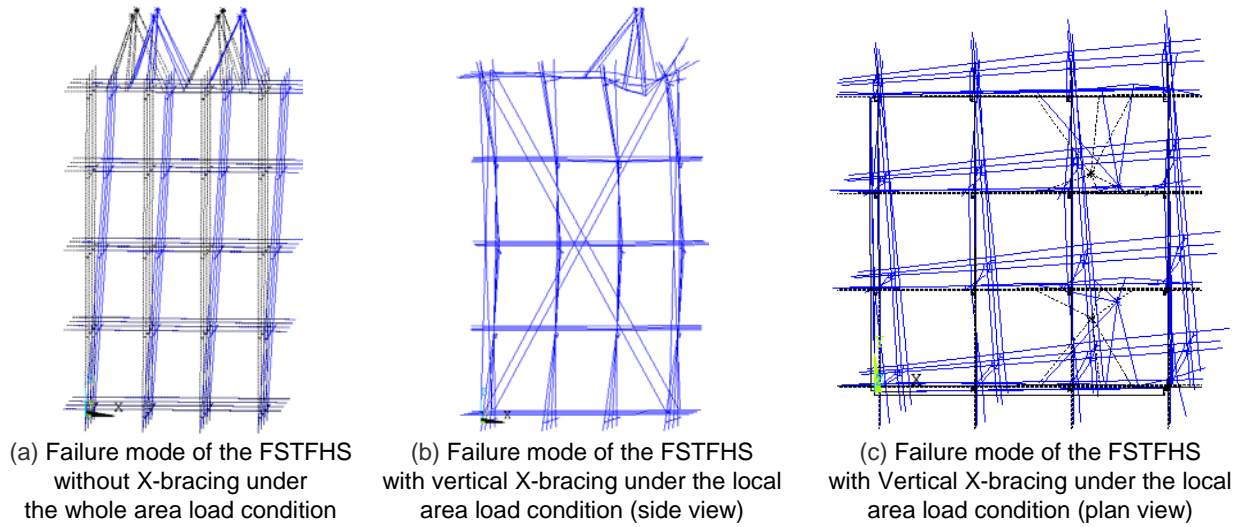
**Figure 17. Failure modes of the FSTFHS in FEA.**

Table 4 lists the summary of the strength of single post  $P_{FEA}$  obtained through the nonlinear analyses and the experiments.

**Table 4. Comparison of the results between FEA and the test.**

NO.	Storey Height (m)	Post Spacing $S_1 \times S_2$ (m × m)	Aspect Ratio	X-bracing	Loading Condition	$P_{test}$ (kN)	$P_{FEA}$ (kN)	Diff (%)
TS1	1.8	1.3 × 1.3	2	None	Whole area load	8.58	8.24	–3.96
TS2				Vertical	Whole area load	18.30	17.80	–2.73
TS3					Local area load	16.08	15.97	–0.68
TS4				Vertical + Horizontal	Whole area load	25.83	24.59	–4.80
TS5					Local area load	18.33	18.06	–1.47

Note: 1.  $P_{test}$  and  $P_{FEA}$  stand for the strength of a single post obtained from the test and FEA, respectively.

$$2. Diff = \frac{P_{FEA} - P_{test}}{P_{test}} \times 100 \%$$

**Table 5. Study parameters on the effect of eccentric load.**

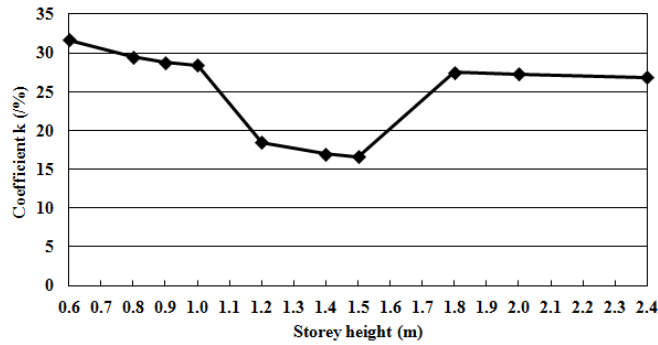
NO.	Storey height (m)	Post Spacing $S_1 \times S_2$ (m × m)	Sweeping Staff Height (m)	Rotational Stiffness (kN·m/rad)	Total Height (m)
1	0.6–2.4	1.0 × 1.0	0.2	19	7.5–8.5
2	1.5	0.4 × 0.4–1.8 × 1.8	0.2	19	8.0
3	1.5	1.0 × 1.0	0.2	11–35	8.0

To further elucidate the influence of member eccentric axial loading, coefficient  $k$ , expressed in Eq. (1), was used to represent the adverse effect of the eccentric axial loading on the strength of the FSTFHS. The results clarified that the FSTFHS strength was reduced to some extent because of the eccentric axial loading on the members (Figure 18).

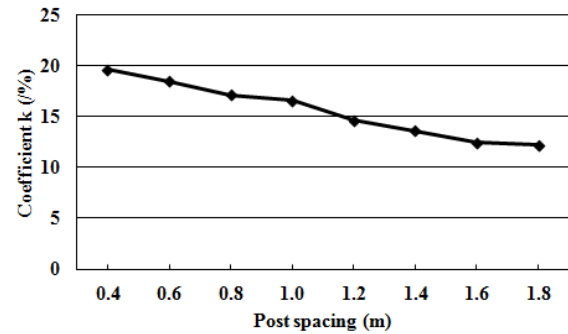


$$k = \left( 1 - \frac{\text{Strength of single post with consideration of eccentric load}}{\text{Strength of single post without consideration of eccentric load}} \right) \times 100 \% . \quad (1)$$

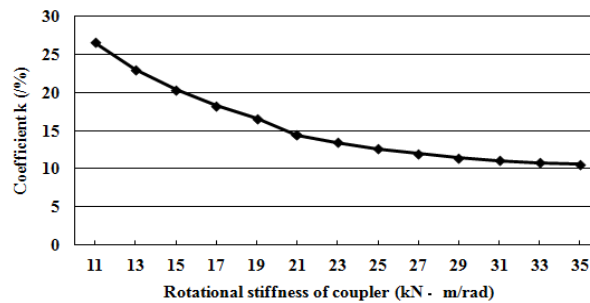
As the storey height increased, coefficient  $k$  decreased [Figure 18(a)], indicating a reduction in the adverse effects on the strength. When the storey height was 1.0–1.5 m, coefficient  $k$  evidently decreased. This could be because when the storey height is less than 1 m, numerous layers are necessary to fabricate the FSTFHS to a total erection height of 8 m, leading to the accumulation and expansion of the adverse effects of the layer-by-layer eccentric load transmission through the couplers. When the storey height increased, the required number of layers decreased, consequently ameliorating this effect. When the storey height was greater than 1.8 m, the effective length of the post was so large that its bearing capacity became very low, rendering the FSTFHS easily susceptible to failure due to eccentric axial loading and thus increasing  $k$ .



(a) Curve of influence coefficient  $k$  that varies with the storey height



(b) Curve of influence coefficient  $k$  that varies with the post spacing



(c) Curve of influence coefficient  $k$  that varies with the coupler rotational stiffness

**Figure 18. Parameter studies on the effect of member eccentric axial load.**

Coefficient  $k$  decreased with post spacing [Figure 18(b)], probably because the reduced post spacing increased the height-to-width ratio, which in turn significantly reduced the bearing capacity of the FSTFHS. Moreover, such a configuration rendered the FSTFHS easily susceptible to failure due to eccentric axial loading.

Furthermore,  $k$  decreased with the coupler rotational stiffness [Figure 18(c)], indicating that the adverse effect of the eccentric axial loading on the members can be reduced to some extent by increasing the bolt-tightening torque to increase the rotational stiffness of the coupler, thus improving the FSTFHS bearing capacity.

## 4. Conclusions

A comprehensive research on the stability and strength of the FSTFHS with eccentric axial loading on the members was conducted through five full-scale tests as well as detailed FEAs. Therefore, combines with our previous results in [18–19, 25–28], the bearing capacity of FSTFHS that most commonly used in practical in China was studied, and the following conclusions are drawn:

1) The FSTFHS strength under local area loading condition is significantly lower than that under whole area loading condition.

2) The typical failure mode of the FSTFHS under local area loading condition is the lateral buckling of part of the posts around the weak axis near the local large loading area, accompanied by torsion of the entire structure and bending of the top horizontal tubes.

3) X-bracing evidently increases the bearing capacity of the FSTFHS regardless of the loading condition. The effect of X-bracing is stronger on the bearing capacity of the FSTFHS than on that of the FSTFHS.

4) The FEA results are generally consistent with the test results, validating the FEA models for future applications.

5) The adverse effect of the eccentric axial loading on the strength of the FSTFHS decreases with the increase in the storey height, post spacing, and rotational stiffness of the couplers.

## References

1. Chan, S.L., Zhou, Z.H., Chen, W.F., Peng, J.L., Pan, A.D. Stability Analysis of Semirigid Steel Scaffolding. *Engineering Structures*. 1995. Vol. 17. No. 8. Pp. 568–574.
2. Peng, J.L., Pan, A.D.E., Chan, S.L. Simplified Models for Analysis and Design of Modular Falsework. *Journal of Constructional Steel Research*. 1998. Vol. 48. No. 2–3. Pp. 189–209.
3. Peng, J.L., Pan, A.D.E., Chen, W.F. Approximate Analysis Method for Modular Tubular Falsework. *Journal of Structural Engineering, ASCE*. 2001. Vol. 127. No. 3. Pp. 256–263.
4. Peng, J.L., Pan, A.D., Rosowsky, D.V., Chen, W.F., Yen, T., Chan, S.L. High Clearance Scaffold Systems During Construction—1: Structural Modeling and Modes of Failure. *Engineering Structure*. 1996. Vol. 18. No. 3. Pp. 247–257.
5. Peng, J.L., Chen, K.H., Chan, S.L., Chen, W.T. Experimental and Analytical Studies on Steel Scaffolds under Eccentric Loads. *Journal of Constructional Steel Research*. 2009. Vol. 65. No. 2. Pp. 422–435.
6. Xiong, Y.Y., Xie, Y.X., Zhou, J.G. Discussion on Induced Load of Formwork with Fastener- Style Steel- Pipe Support System. *Building Construction*. 2004. Vol. 26. No. 1. Pp. 56–57.
7. Zeng, F.K., Liu, X.B., Hu, C.M., Yu, J., Zhang, T. Analysis of Two Kinds of Special Loads that High- formwork Supports System. *Journal of Qingdao Agricultural University (Natural Science)*. 2007. Vol. 24. No. 4. Pp. 308–309.
8. Yuan, X.X., Jin, W.L., Liu, X., Lu, Z., Chen, T.M. Model for Fuzzy Risk Analysis of Fastener-style Tubular Steel Supported Scheme. *Journal of Zhejiang University (Engineering Science)*. 2006. Vol. 40. No. 8. Pp. 1371–1376.
9. Hu, C.M., Jian, C.J., Duan, D.D., Fu, L.Y., Ren, W.J. Study of Time-varying Behavior of Multi-template Support System During Construction. *Industrial Construction*. 2016. Vol. 46. No. 3. Pp. 102–107.
10. Xie, N., Liang, R.Z., Wang, J.J. Occurrence of Human Errors in High Falsework and Influence on Structural Safety. *Engineering Mechanics*. 2012. Vol. 29. No. S1. Pp. 63–67.
11. Milojkovic, B., Beale, R.G., Godley, M.H.R. Determination of the Factors of Safety of Standard Scaffold Structures. *Proceedings of the Third International Conference on Advances in Steel Structures*. 2002. Vol. 1. Pp. 303–310.
12. Beale, R.G., Godley, M.H.R. Numerical Modeling of Tube and Fitting Access Scaffold Systems. *Advanced Steel Construction*. 2006. Vol. 2. No. 3. Pp. 199–223.
13. Beale, R.G. Scaffold Research – A Review. *Journal of Constructional Steel Research*. 2014. Vol. 98. Pp. 188–200.
14. Ao, H.F., Li, G.Q. Investigation of Overall Load-bearing Stability Capacity of Tube-and-coupler Scaffolds. *Chinese Quarterly Mechanics*. 2004. Vol. 25. No. 2. Pp. 213–218.
15. Yue, F., Yuan, Y., Li, G.Q., Ye, K.M., Chen, Z.M., Wang, Z.P. Wind Load on Integral-lift Scaffolds for Tall Building. *Journal of Structural Engineering, ASCE*. 2005. Vol. 131. No. 5. Pp. 816–824.
16. Liu, H.B., Zhao, Q.H., Wang, X.D., Zhou, T., Wang, D., Liu, J., Chen, Z.H. Experimental and Analytical Studies on the Stability of Structural Steel Tube and Coupler Scaffolds without X-bracing. *Engineering Structures*. 2010. Vol. 32. No. 4. Pp. 1003–1015.
17. Liu, H.B., Chen, Z.H., Wang, X.D., Zhou, T. Theoretical Analysis and Experimental Research on Stability Behavior of Structural Steel Tube and Coupler Falsework with X-bracing. *Advanced Steel Construction*. 2010. Vol. 6. No. 4. Pp. 949–962.
18. Lu, Z.R., Chen, Z.H., Wang, X.D., Guo, C., Liu, Q. Study of the Bearing Capacity of Fastener Steel Tube Full Hall Formwork Support using the Theory of Stability of Pressed Pole with Three-point Rotation Restraint. *China Civil Engineering Journal*. 2012. Vol. 45. No. 5. Pp. 104–113.
19. Lu, Z.R., Chen, Z.H., Wang, X.D., Liu, Q., Liu, H.B. Experimental and Theoretical Study of the Bearing Capacity of Fastener Steel Tube Hull-hall Formwork Support System. *China Civil Engineering Journal*. 2012. Vol. 45. No. 1. Pp. 49–60.
20. Chen, Z.H., Lu, Z.R., Wang, X.D., Liu, H.B., Liu, Q. Experimental and Theoretical Research on Capacity of Unbraced Steel Tubular Formwork Support Based on Sway Frame with Semi-rigid Connection Theory. *Journal of Building Structures*. 2010. Vol. 31. No. 12. Pp. 56–63.
21. Chinese Standards Institution, GB/T 228—2002: Metallic materials-Tensile testing at ambient temperature 2002.
22. Chinese Standards Institution, JGJ 130—2011: Technical Code for Safety of Steel Tubular Scaffold with Couplers in construction: 2011.
23. Chen, Z.H., Lu, Z.R., Wang, X.D. Numerical Analysis and Experimental Study of the Stiffness of Right Angle Couplers in Tubular Steel Scaffolds. *China Civil Engineering Journal*. 2010. Vol. 43. No. 9. Pp. 100–108.
24. Zheng, L.Q., Cai, X.F., Zhuang, J.P., Wu, J.L. Experimental Research on Anti-slipping Performance of Steel Pipe Joints with Swivel Coupler. *Journal of Henan University (Natural Science)*. 2013. Vol. 43. No. 6. Pp. 711–715.
25. Lu, Z.R., Guo, C., Li, G.C., Chen, Z.H., Zhao, L., Yu, L. Testing Research on the Bearing Capacity of Fastener Steel Tubular Full Hall Formwork Scaffold. *Construction Technology*. 2016. Vol. 45. No. 15. Pp. 82–86.
26. Lu, Z.R., Guo, C., Li, G.C., Cao, S., Li, C.Y. Bearing Capacity of Bridge Full Hall Formwork Scaffold under Eccentric Load. *Journal of Tianjin University (Science and Technology)*. 2016. Vol. 49, Supp1. Pp. 64–72.
27. Lu, Z.R., Guo, C., Yang, Y.M., Chen, Z.H. Study on the Effect of Coupler Eccentricity on Bearing Behavior of Steel Tubular Formwork Support. *Industrial Construction*. 2016. Vol. 46. No. 1. Pp. 140–146.
28. Lu, Z.R., Guo, C., Wen, Y.Q., Chen, Z.H., Liu, T., Cao, S. Study of Bearing Capacity of Fastener Steel Tubular Full Hall Formwork Support System under Eccentric Load. *Journal of Dalian University of Technology*. 2016. Vol. 56. No. 1. Pp. 20–27.

## Contacts:

Zhengran Lu, 18842586845; luzhengranglovel@126.com

Guo Chao, 862424692693; guochaoglovel@126.com



DOI: 10.18720/MCE.87.4

## Aggregate concrete factor ( $\lambda$ ) for burnt clay brick aggregate concrete

**S. Islam,**

*Tennessee Technological University, Cookeville, Tennessee, USA*

*E-mail: mislam46@students.tntech.edu*

**Keywords:** aggregate, rebar geometries, pull-out test, bond strength, aggregate concrete factor.

**Abstract.** This research aims to evaluate the lightweight burnt clay brick aggregate concrete factor ( $\lambda$ ) which is commonly used as coarse aggregate in Bangladesh as well as Asia regions. The pull-out tests were carried out on four different types of concrete cylinder specimens (100 mm by 200 mm) made with natural crushed stone and first class burnt clay brick aggregates to determine the aggregate concrete factor ( $\lambda$ ) and bond strength. Three different rebar diameter of 8 mm, 10 mm, and 12 mm with two different embedded lengths of 100 mm and 200 mm were investigated. In addition, compressive and splitting tensile strength tests were also performed to calculate bond strength and then  $\lambda$ . The experimental results showed that bond strength of 10 mm diameter rebar is higher compared to other bar diameter for both aggregates and both embedded length of 100 and 200 mm. While the bond strength of 200 mm embedded length rebar is higher than the embedded length of 100 mm. From this research study, it has been found that the average  $\lambda$  equal to 0.88 for Bangladeshi burnt clay brick aggregate. However, based on the test results a new equation is proposed for the lightweight brick aggregate concrete factor ( $\lambda$ ).

### 1. Introduction

According to ACI code, it is necessary to unite the reinforcement properly into the concrete for a finite length in order to confirm a good bonding. This sufficient length to anchor bars near the end of connections is referred to as the development length ( $l_d$ ) [1]. According to ACI committee 408 (2003), the development length concept is based on the attainable average bond stress over the length of embedment of the reinforcement [2]. In reinforced cement concrete (RCC) bonding between concrete and steel is very important because inadequate development length is one of the major reasons for bond failure. If the tensile force on the bar is increased, friction between sufficiently bonded by a mass of surrounding concrete and bar can overcome the situation of bond failure of structural element [3–5]. The surrounding concrete remains intact except the crushing that takes place ahead of the ribs immediately adjacent to the bar interface [6–7]. According to ACI-318, section 12.2.3 (2001), the basic equation (Eq. 1) for development of tension bars (deformed) is as follows:

$$l_d = \left( \frac{3}{40} \frac{f_y}{\sqrt{f'_c}} \frac{\alpha \beta \gamma \lambda}{\left( \frac{C + K_{tr}}{d_b} \right)} \right) d_b, \quad (1)$$

where  $l_d$  is development length,

$\alpha$  is reinforcement location factor,

$\beta$  is coating factor,

Islam, S. Aggregate concrete factor ( $\lambda$ ) for burnt clay brick aggregate concrete. Magazine of Civil Engineering. 2019. 87(3). Pp. 46–58. DOI: 10.18720/MCE.87.4.

Ислам С. Легкие бетоны с крупным керамическим заполнителем // Инженерно-строительный журнал. 2019. № 3(87). С. 46–58. DOI: 10.18720/MCE.87.4



This open access article is licensed under CC BY 4.0 (<https://creativecommons.org/licenses/by/4.0/>)

$\gamma$  is reinforcement size factor,

$\lambda$  is light weight aggregate concrete factor,

$C$  is concrete covering,

$K_{tr}$  is transverse reinforcement index,

$d_b$  is diameter of bar,

$f_y$  is ultimate strength of steel,

$f'_c$  is compressive strength of concrete.

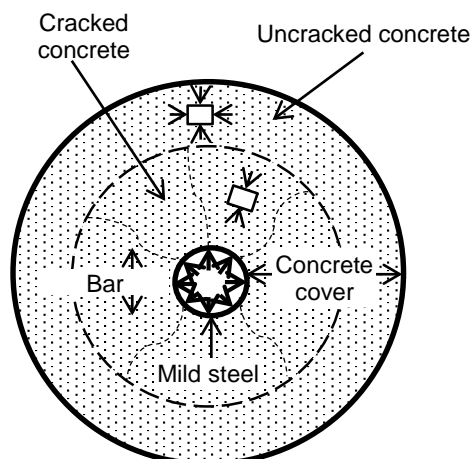
However, for lightweight concretes, the tensile strength is usually less than from normal density concrete having the same compressive strength. Hence, the development length must be increased [1]. According to ACI-318-02, section 12.2.4 (2001)  $\lambda$  (lambda) is a lightweight aggregate concrete factor. For normal weight concrete,  $\lambda = 1.0$ , sand-lightweight concrete,  $\lambda = 0.85$ , and all lightweight concrete,  $\lambda = 0.75$ .

When  $f_{ct}$  is specified,

$$\lambda = 6.7 \frac{\sqrt{f'_c}}{f_{ct}} \leq 1.0, \quad (2)$$

where  $f'_c$  is compressive strength of concrete,  $f_{ct}$  is splitting tensile strength of concrete.

According to Nadir and Sujatha (2018) "Bond strength is responsible for the transfer of forces between the two materials ensuring strain compatibility and composite action" [9]. Ganesan et al. 2014, Steele (2014) and A.V. Benin et al. (2013) concluded that the bond strength depends on its development length, types and size of aggregates, mild steel surface geometry, diameter and spacing of reinforcement bar and so on [10–12]. The bond strength between reinforcing bar as well as concrete can be estimated by different test methods such as pull-out test, beam-end test, splice beam test, anchorage test and so on [11]. Among all test methods, pull-out test is the most popular and effective method to calculate the bond strength due to its ease of fabrication. In the pullout test, major load is transmitted by surface friction and mechanical interlocking of ribs in the deformed bars against the concrete. When the external load is applied to the pull-out specimen, tangential stresses i.e., tensile stresses act along the bar and at that time some new stresses develop in the concrete which is radial stress and it is perpendicular to the bar axis [13]. This radial stress surrounding the concrete performs as a thick walled concrete ring subjected to internal pressure. Therefore, tangential ring stress i.e., hoop stress as well as radial compressive stress grow in the concrete cover. But slip of the bar occurs when tensile stress exceeds the tensile strength due to radially developed cracks in the concrete cover which is also shown in Figure 1 [14].



**Figure 1. Transverse stresses around a pulled bar in the plan view of concrete cylinder [14].**

Although numerous experimental and numerical studies have been conducted in order to gain a better understanding of the bond strength of concrete made with different types of aggregate, but almost no research is found on Bangladeshi burnt clay brick aggregate concrete factor ( $\lambda$ ). Since Bangladesh has very limited availability of natural stones, therefore, the construction industries are mostly dependent on burnt clay brick aggregates due to cheap and availability. Indeed, in the past and even today, most of the buildings in Bangladesh are made of concrete with burnt clay brick aggregate [15]. Therefore, aggregate concrete factor ( $\lambda$ ) has been an important issue for Bangladeshi clay brick aggregate.

In summary, the main objectives of the present study are to evaluate the aggregate concrete factor ( $\lambda$ ) for burnt clay brick aggregate commonly used as coarse aggregate in Bangladesh by experimentally and then develop a relationship between experimental results and equation from ACI-318 (2001). To this aim, bond strength of concrete made with both burnt clay brick and natural crushed stone aggregate is observed for different bar diameter and bonding depth. Moreover, the measured bond strength has also been verified with the results found in the literature.

## 2. Experimental Methods

### 2.1. Materials

An extensive laboratory testing has been carried out to obtain the value of aggregate concrete factor ( $\lambda$ ) for burnt clay brick aggregate found in Bangladesh. In the present study, burnt clay brick chips from local market and stone chips were used as coarse aggregate, locally available Sylhet sand as fine aggregate and Portland composite cement as a binding material and also mild steel have been used for pull-out test which are discussed in next subsection 2.1.1.

#### 2.1.1 Coarse aggregate (CA), Fine aggregate (FA), and Cement (C):

Crushed first class brick and stone chips are commonly used in Bangladesh as coarse aggregate (CA) and in the present study, both of the aggregates have been used to determine the value of  $\lambda$ . Collected samples were broken into pieces manually having a sieve size of 19 mm downgraded and retained on 4.75 mm (sieve #4). The aggregates were then sieved to control a standard grading. In addition, unit weight, void content, specific gravity and absorption capacity of the coarse aggregate were determined according to the ASTM standard. However, fineness modulus of the brick aggregate (BA) and stone aggregate (SA) was obtained 6.58 and 6.64 respectively. On the other hand, sand as Fine Aggregate (FA) was collected from the river in Sylhet district of Bangladesh called «Sylhet sand» ensuring no big particle or no clay were present into the present samples. Table 1 presents the properties of all types of aggregates that have been tested in the laboratory. Portland composite cement containing 70–79 % clinker, 21–25 % fly ash, slag, limestone, and 0–5 % gypsum (CEM II/B-M) and fresh drinking water have been used in this study. Deform mild steel bar of 8 mm, 10 mm, and 12 mm in diameter have been used in order to determine the shear strength from pull out test of concrete.

**Table 1. Physical properties of fine and coarse aggregates.**

Sample	Fineness Modulus, (FM)	Unit Weight (Kg/m <sup>3</sup> )	% Voids	Bulk Specific Gravity (SSD)	Bulk Specific Gravity (OD)	Apparent Specific Gravity (OD)	Absorption Capacity (%)	Abrasion test (%)
CA (Brick Chips)	6.58	1102	40	2.02	1.75	2.40	15.37	34
CA (Stone Chips)	6.64	1645	36.90	2.63	2.31	2.67	0.85	22
FA (Sand)	2.912	1664	32.78	2.54	2.48	2.66	2.65	-

### 2.2. Mix proportion:

The concrete mixes were divided into two groups: Brick aggregate concrete (BAC) and Stone aggregate concrete (SAC) as control case. In order to get the similar compressive strength of both BAC and SAC, a trial mix has been carried out with different water to cement ( $w/c$ ) ratio as presented in Table 2. Sand to total aggregate volume ratio ( $s/a$ ) was 0.42 and air volume in the mixes was considered 2 %. No chemical admixtures were used to the concrete during mixing. It has been found that the compressive strength of brick aggregate concrete (BAC1) having the  $w/c$  ratio of 0.38 is 16.70 MPa at 7 days. On the other hand, almost similar compressive strength has been found for stone aggregate concrete (SAC3) having the  $w/c$  of 0.5 is 17.19 MPa which is around 3 % more than that of BAC1. In the other case, compressive strength of BAC4 having the  $w/c$  ratio of 0.44 at 7 days is 20.96 MPa which is much closer to SAC4 with have been  $w/c$  ratio of 0.52. It is also about 3 % more than that of SAC4 (20.39 MPa). Therefore, both case selected for the final casting to determine the value of  $\lambda$  for BAC as shown in Table 3.

**Table 2. Details of concrete mixing for Trial Casting.**

Trial No.	Cases	Cement (Kg/m <sup>3</sup> )	BA (Kg/m <sup>3</sup> )	SA (Kg/m <sup>3</sup> )	FA (Sylhet sand) (Kg/m <sup>3</sup> )	Water (Kg/m <sup>3</sup> )	Water to Cement ratio (w/c)	Compressive strength (MPa)
1.	BAC1	390	793.87	–	784.33	148.20	0.38	16.70
2.	BAC2	390	785.05	–	775.61	156.00	0.40	21.25
3.	BAC3	390	776.22	–	766.89	163.80	0.42	24.00
4.	BAC4	390	767.40	–	758.17	171.60	0.44	20.96
5.	BAC5	390	758.58	–	749.46	179.40	0.46	18.02
6.	SAC1	390	–	958.00	775.00	280.00	0.46	15.40
7.	SAC2	390	–	976.17	740.74	187.20	0.48	16.06
8.	SAC3	390	–	964.68	732.02	195.00	0.50	17.19
9.	SAC4	390	–	953.19	723.31	202.80	0.52	20.39
10.	SAC5	390	–	935.96	710.23	214.50	0.55	9.760

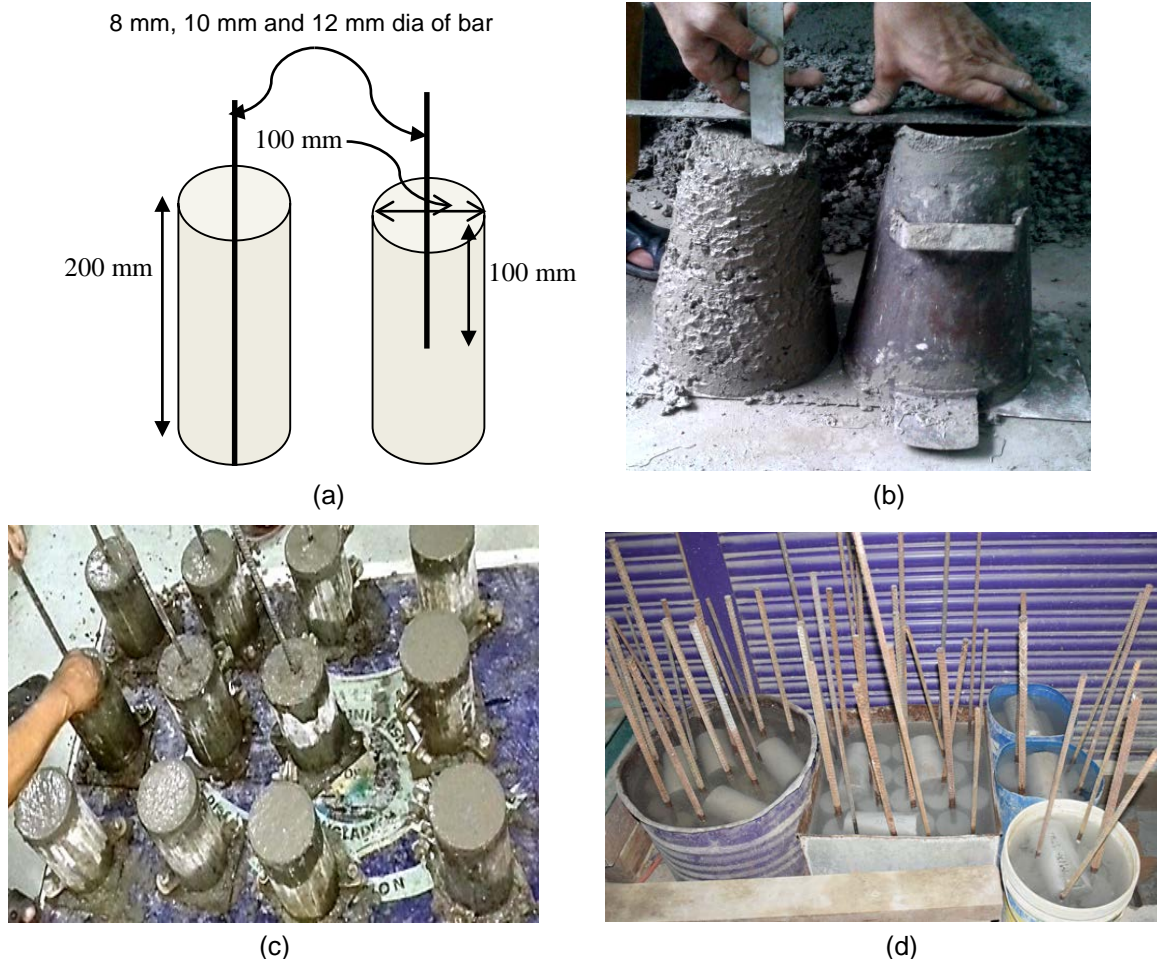


**Table 3. Details of concrete mixing for final casting of concrete.**

Final casting No.	Cases	Cement (Kg/m <sup>3</sup> )	BA (Kg/m <sup>3</sup> )	SA (Kg/m <sup>3</sup> )	FA (Kg/m <sup>3</sup> )	Weight of water (Kg/m <sup>3</sup> )	Water to Cement (w/c)	Crushing strength (MPa)
1.	BAC1	390	793.87	—	784.33	148.20	0.38	16.70
2.	SAC3	390	—	964.68	732.02	195.00	0.50	17.19
3.	BAC4	390	767.40	—	758.17	171.60	0.44	20.96
4.	SAC4	390	—	953.19	723.31	202.80	0.52	20.39

### 2.2.1 Sample Preparation, mixing, casting, and curing of concrete:

In the present study, concrete cylinder with a diameter of 100 mm and height of 200 mm is made as specimen to determine the compressive and splitting tensile strength of concrete. The same dimension is also used for the specimens to determine the shear strength from pull-out test with the full (i.e., 200 mm) and half (i.e., 100 mm) height of the specimen as development length. Automatic mixture machine having the speed 30–35 revolutions per minute is used for mixing the concrete homogeneously. Before pouring the concrete into the cylinder, deformed steel bar was placed at the center of the cylinder as shown in Figure 2a. In this study, slump test was conducted to measure the workability concrete as shown in Figure 2b. Slump cone having a dimension of 300 mm in height, 100 mm diameter in top, and 20 mm diameter in bottom is filled by 3 layers with 25 tamping on each layer following ASTM C143 [16]. Concrete specimens have been properly compacted using vibrating hammer following the specification of ASTM C 1435-99 [17]. In order to avoid the void in concrete, all concrete specimens are compacted carefully in the laboratory and after compaction of these specimens; scaling and hammering have been made (see Figure 2c). Wet water curing method is applied to ensure adequate moisture and temperature as required specification of ASTM C192/C192M-02 [18] as shown in Figure 2d.



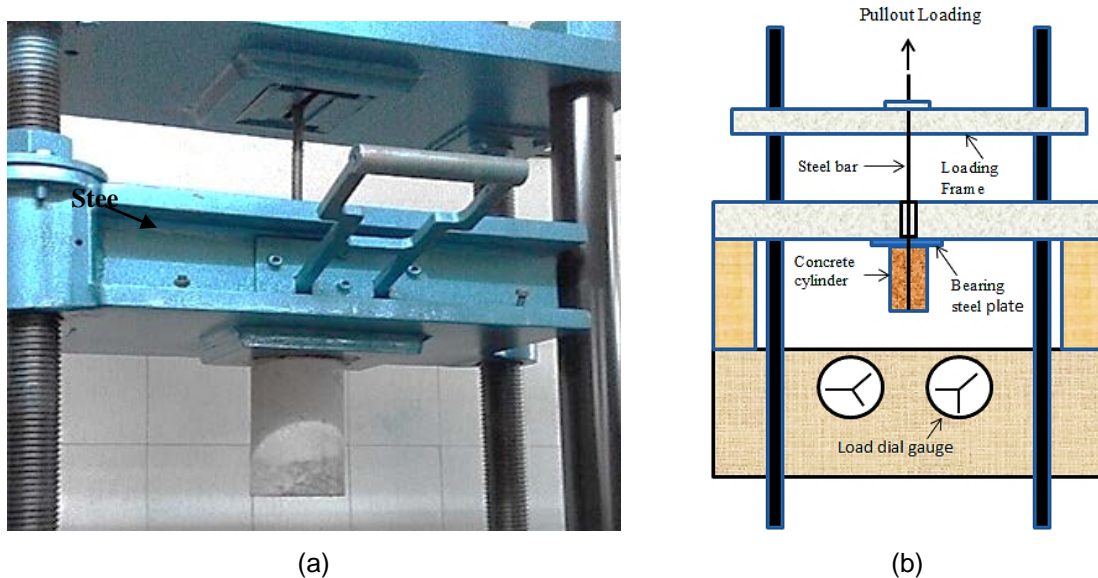
**Figure 2. Preparation of concrete specimen: (a) dimension of the sample; (b) workability test by slump cone; (c) concrete casting; (d) concrete under water for curing.**

## 2.3. Experimental plan

### 2.3.1 Test setup

An experimental study has been conducted to evaluate compressive strength, splitting tensile strength, and bond strength for determining aggregate concrete factor ( $\lambda$ ) of brick and stone aggregate concrete. All tests were conducted at the age of 28 days. The compressive strength of concrete, splitting tensile strength, and bond strength as shear strength by pull-out test is determined by using Universal

Testing Machine (UTM) which has maximum capacity of 800 kN. In the present study, compressive strength is performed as per ASTM C39M-03 [19], indirect tensile strength test is carried out to determine the splitting tensile strength of plain concrete cylinder as per ASTM C496M-04 [20]. After crushing the concrete cylinders, the failure surfaces of concrete have been observed carefully. Shear strength by pull-out test covers the determination of the strength of hardened concrete by measuring the force required to pull embedded mild steel inserted and the attached concrete fragment from a concrete test specimen (ASTM C 900-15 [21]). An embedded deformed steel bar is attached into a concrete cylinder is used for determining shear strength from pull out test is as shown in Figure 3a. and Figure 3b. A special arrangement is arranged with the UTM. Here, a cramp is being used to embay the upper portion of the steel bar in order to avoid slipping. A hollow steel ram is also used at the lower portion of the steel bar which is embedded into the concrete cylinder.



**Figure 3. Laboratory test setup: (a) compressive strength test, (b) indirect (splitting) tensile strength test, (c) original image of shear strength by pull-out test, (d) schematic diagram of pull-out test.**

### 3. Results and Discussion

In the present study, shear strength (i.e., bond strength) with different diameter and length of deformed mild steel has been investigated. In order to establish the aggregate concrete factor for development length equation of stone and burnt clay brick aggregate, mechanical properties of concrete have been carried out. Indeed, it is quite important to have same mechanical properties such as compressive and tensile strength as well as bond strength in order to establish aggregate concrete factor ( $\lambda$ ) for both brick and stone aggregate concrete.

#### 3.1. Hardened concrete properties

##### 3.1.1 Compressive strength

Table 4 presents the compressive strength of concrete measured at 28 days. It can be seen that the compressive strength of concrete made with burnt clay brick and stone aggregates are very close to each other. For example, the compressive strength of concrete made with brick aggregate (BAC1) and stone aggregates (SAC3) are, respectively, 33 MPa and 30.49 MPa which is around 7 % higher for BAC1 than SAC3. While a little difference (5 % higher for brick aggregate) in value is found for compressive strength of BAC4 and SAC4. Though both two different mixes for two different concretes are not comparable due to same amount of cement is used, this behavior could be due to higher water to cement ratio of stone aggregate concrete (0.5 and 0.52) than the brick aggregate concretes (0.38 and 0.44). Indeed, higher amount of water causes higher amount of void in the concrete, resulting in weaker Interfacial Transition Zone (ITZ) around the stone aggregates than brick aggregates. ITZ is the weakest path for failure of concrete during mechanical loading.

**Table 4. Compressive and splitting tensile strength of concrete at 28 days.**

Sl No.	Name of sample	Compressive strength (MPa)	Splitting tensile strength (MPa)
1.	BAC1	33.00	3.10
2.	SAC3	30.49	2.91
3.	BAC4	36.02	3.05
4.	SAC4	34.13	3.15

### 3.1.2 Tensile strength

It can be seen from the experimental results that tensile strength of BAC1 and SAC3 are 3.10 MPa and 2.91 MPa accordingly which is about 6 % lower than that of BAC1 as presented in table 4. In another case, the tensile strength of BAC4 and SAC4 are 3.05 MPa and 3.15 MPa respectively. Around only 3 % discrimination in tensile strength is observed for both BAC4 and SAC4. Since the differences of tensile strength of concrete made with brick and stone aggregate are quite low (3 to 6 % in all cases), hence it is believed that the value of  $\lambda$  will not be affected significantly. A relationship between tensile and compressive strength of concrete is being proposed and shown in Figure 4. Depending on the experimental data, the following equation (Eq. 3) is submitted which could be valid for stone and burnt clay brick aggregate concrete made in Bangladesh.

$$f_t = 0.56\sqrt{f'_c}, \quad (3)$$

where  $f'_c$  is compressive strength of concrete in MPa and  $f_t$  is tensile strength of concrete in MPa.

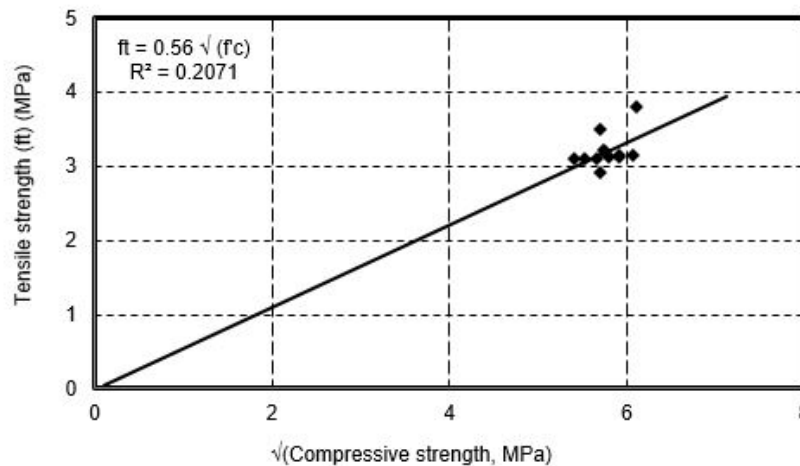


Figure 4. Relationship between tensile and compressive strength at 28 days.

### 3.1.3. Bond strength

In order to deeper understanding the effect of aggregate types on bond strength of concrete, the pull-out tests have been conducted at 28 days of curing. Totally, four types of concrete made with first class burnt clay brick and stone aggregate with different water to cement ratios and three different diameters of steel bars (8 mm, 10 mm, and 12 mm) have been investigated in this research project. Additionally, two different embedded lengths of 100 mm and 200 mm have been considered to investigate the bond strength behavior by pull-out test of all concretes. As concern the effect of rebar diameter, the experimental results have shown that bond strength of 10 mm diameter rebar exhibited higher strength as compared to the diameter of 8 mm and 12 mm for both aggregates and both embedded length of 100 and 200 mm as shown in Figures 5–8. For example, the average bond strength of concrete (BAC4) with rebar diameter of 8 mm, 10 mm, and 12 mm are, respectively, 7.97 MPa, 13.68 MPa (about 42 % higher than 8 mm), and 10.87 MPa for brick aggregate, while 8.76 MPa, 16.87 MPa (about 48 % higher than 8 mm), and 12.11 MPa for stone aggregate with embedded length of 100 mm. Almost similar behavior has been observed for the other concretes with embedded length of 100 mm and 200 mm. Based on the experimental results, higher surface area provides higher mechanical and physical adhesion between the concrete and rebar surface resulting in higher bond strength. Probably, because of the higher surface area, the propagation of cracks and microcracks are prevented in the plane parallel to the longitudinal axis of the rebar, thus increasing the bond force for 10 mm than 8 mm at which the bond failure occurs. On the other hand, relatively lower bond strength of 12 mm diameter deformed rebar is possibly due to size and shapes of grooves are different from 8 mm as well as 10 mm diameter deformed bar that is available in Bangladesh.

As regards the effect of embedment length, as the embedment length increased, the average bond strength increased. Except for concrete BAC4 with a diameter of 10 mm and embedded length of 100 mm rebar, the average bond strength of 200 mm embedded length rebar is higher as compared to 100 mm embedded length for all concretes and all diameters, see Figures 5–8. This behavior could be explained by the mechanical interlocking of rebar ribs and concrete keys. Embedded length of 200 mm is double than the length of 100 mm, theoretically, it can believe that the number of ribs will be doubled for the embedded length for 200 mm than 100 mm, which provide higher strength for 200 mm than 100 mm. Moreover, this behavior also could be due to the increased bonding area between the rebar and concrete parallel to the longitudinal axis of the rebar.

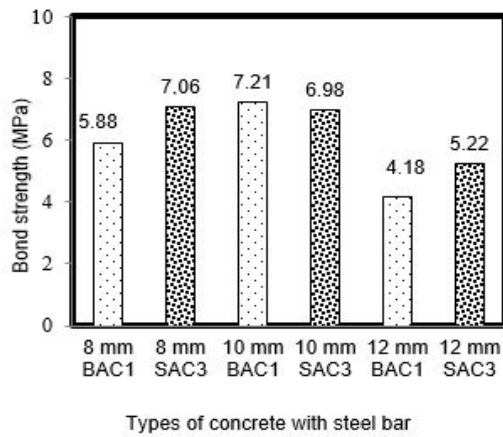


Figure 5. Bond strength of concrete with different diameters with 100 mm embedded length.

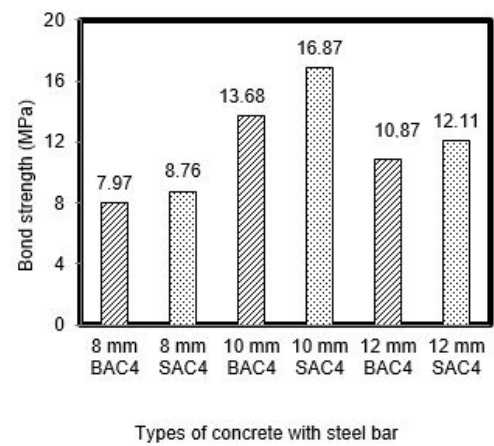


Figure 6. Bond strength of concrete with different diameters with 100 mm embedded length.

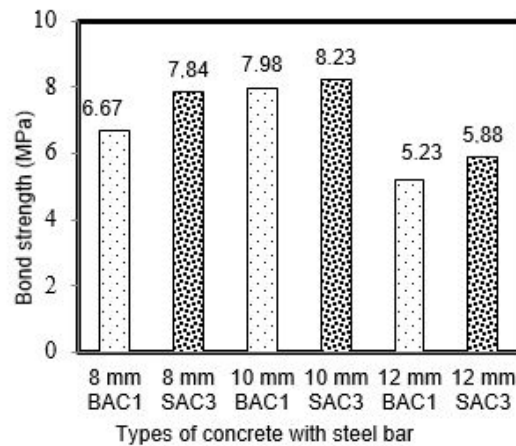


Figure 7. Bond strength of concrete with different diameters with 200 mm embedded length.

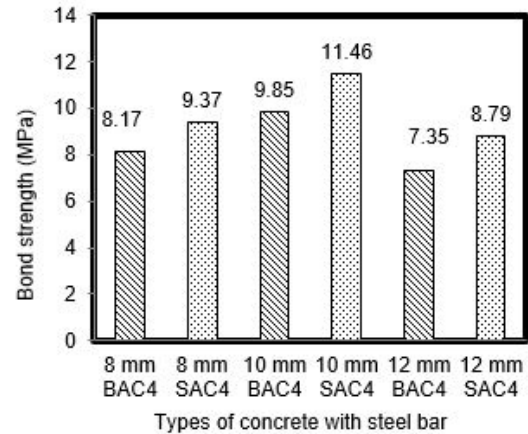


Figure 8. Bond strength of concrete with different diameters with 200 mm embedded length.

However, in most of the cases, it has been found that the bond strength of concretes made with stone aggregates are higher than the concretes made with first class burnt clay brick aggregates as shown in Figures 5–8. This behavior could be due to better interlock/stronger Interfacial Transition Zone (ITZ) around the rebar and stone aggregates than brick aggregates. This behavior also could be explained by the higher abrasion resistance of stone aggregate (abrasion = 22 %) than the brick aggregate (abrasion = 34 %) (Table 1). Indeed, the higher the abrasion resistance, the higher the strength of concrete, resulting in higher bond strength. Also, the percentage of void in stone aggregate (36.9 %) was lower than the brick aggregate (40 %) (Table 1). This higher percentage of void in brick aggregate caused higher porosity and higher permeability, meaning that weaker ITZ and then lower bond strength.

In order to deeper understanding the effect of aggregate type on bond strength of concrete, the relation between bond strength of burnt clay brick aggregate and stone aggregate is plotted and shown in Figure 9. Though almost a linear relation has been observed, it seems that the values of stone aggregate concrete are slightly above the line of equality than that of brick aggregate concrete.

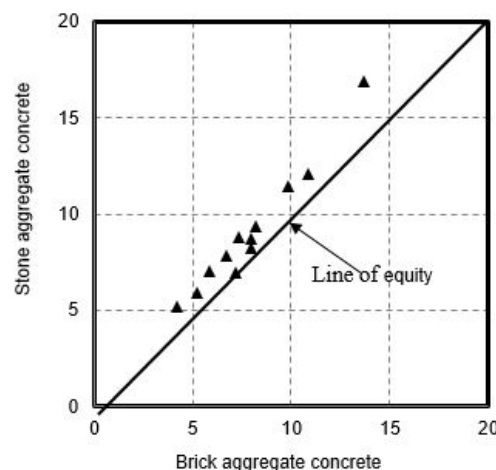


Figure 9. Bond strength of concrete made with brick and stone aggregates.

### 3.1.4. Comparison of experimental bond strength with different mathematical model

However, Bond strength of concrete by pull-out tests were conducted by several researchers which can be found in literature and attempted to formulate the equation. Orangun et al., (1977) [22] carried out the tests and proposed the following Eq. 4.

$$U = 0.083045\sqrt{f'_c} \left[ 1.2 + 3\frac{c}{d_b} + 50\frac{d_b}{L_d} \right], \quad (4)$$

where  $c$  is minimum concrete cover,

$f'_c$  is compressive strength in MPa,

$d_b$  is diameter of rebar,

$L_d$  is development length.

In order to investigate the bond strength of concrete, Australian standard, (1994) [23] recommends the following Eq. 5.

$$U = 0.265\sqrt{f'_c} \left( \frac{c}{d_b} + 0.5 \right), \quad (5)$$

where  $d_b$  is diameter of rebar,

$c$  is minimum concrete cover,

$f'_c$  is compressive strength in MPa

M.N.S. Hadi (2008) [24] conducted research on bond strength of concrete with high strength reinforcing steel and proposed the following Eq. 6.

$$U = 0.083045\sqrt{f'_c} \left[ 22.8 - 0.208\frac{c}{d_b} - 38.212\frac{d_b}{L_d} \right], \quad (6)$$

where  $c$  is minimum concrete cover,

$f'_c$  is compressive strength in MPa,

$d_b$  is diameter of rebar,

$L_d$  is development length.

However, according to Arthur et al., (2003) [1], the measured uniform bond strength can be expressed as follows

$$U = P_{\max} / \pi d_b L_d. \quad (7)$$

where  $P_{\max}$  is maximum applied load,

$d_b$  is diameter of rebar,

$L_d$  is development length.

In order to deeper analysis of the experimental results and to compare with proposed analytical equations found in literature, the bond strength of concretes were calculated based on the equation discussed above and compared with experimental results of concrete made with brick aggregate as shown in Figures 10–13. In Figures 10–13, different rebar diameter and embedded length were considered. In most of the cases, the bond strength of the experimental results are in good agreement, especially for the rebar diameter of 10 mm than 8 mm and 12 mm. This behavior could be due to different compressive and tensile strength of the concrete, aggregate and cement types, grade of rebar and so on considered in the proposed equations found in the literature than the experimental one.

### 3.1.5. Lightweight aggregate concrete factor ( $\lambda$ ) by the equation of ACI-318 (2001)

The determination of the development length of the mild steel in tension comprises evaluating an expression that includes a modification factor that either increases or decreases the development length. That factor  $\lambda$  is shown in the Eq. 2 according to the specification of ACI-318 (2001), section 12.2.4 and the results obtained from that equation which is shown in Figure 14. According to the ACI-318 (2001), the  $\lambda$  should not less than 1.0. Except for concrete BAC4, other three concretes  $\lambda$  is 1.0 which is in good agreement with the  $\lambda$  of normal weight concrete as proposed in ACI-318 (2001).



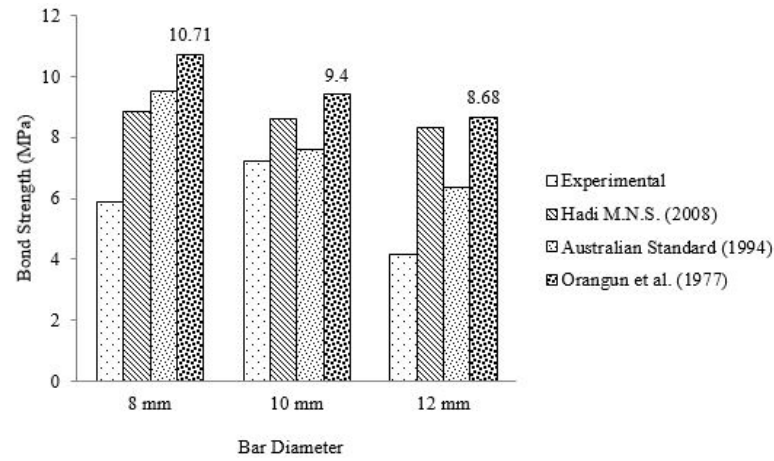


Figure 10. Rebar diameter with 100 mm embedded length of BAC1.

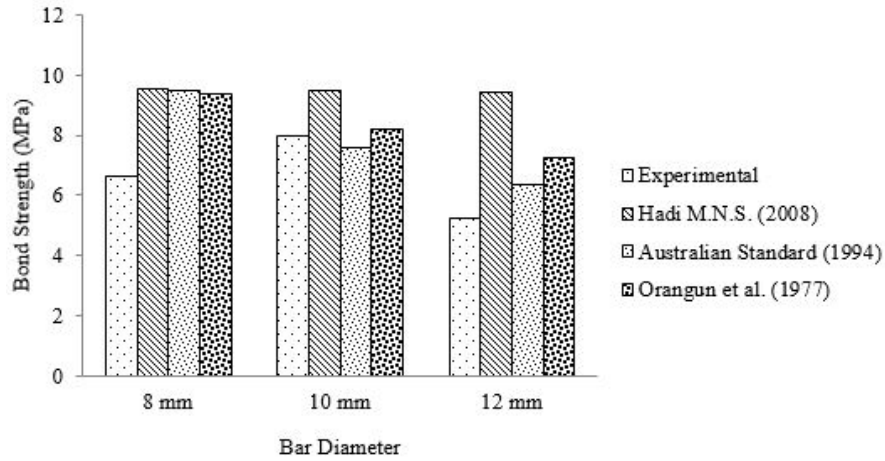


Figure 11. Rebar diameter with 200 mm embedded length of BAC1.

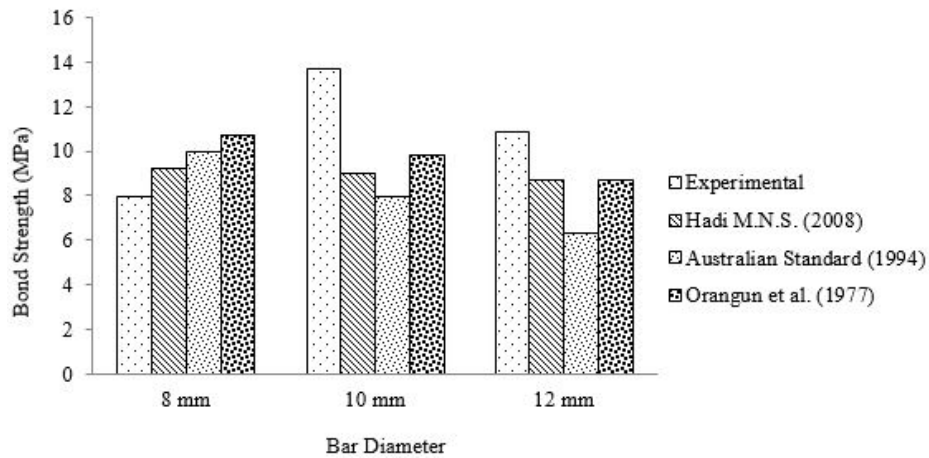


Figure 12. Rebar diameter with 100 mm embedded length of BAC4.

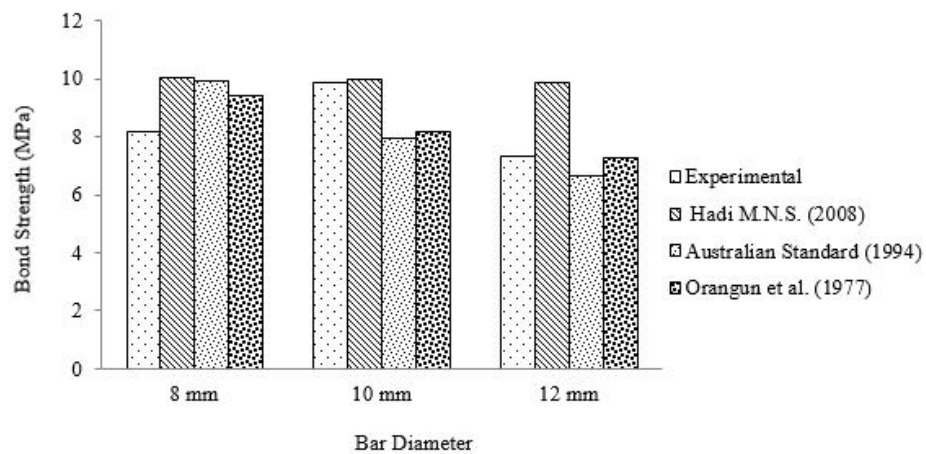
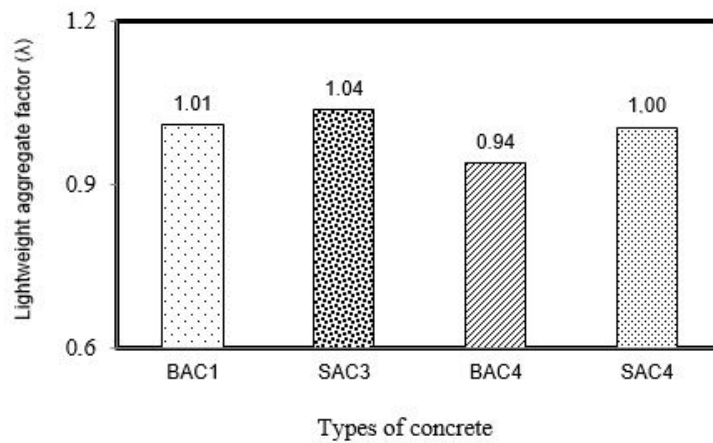


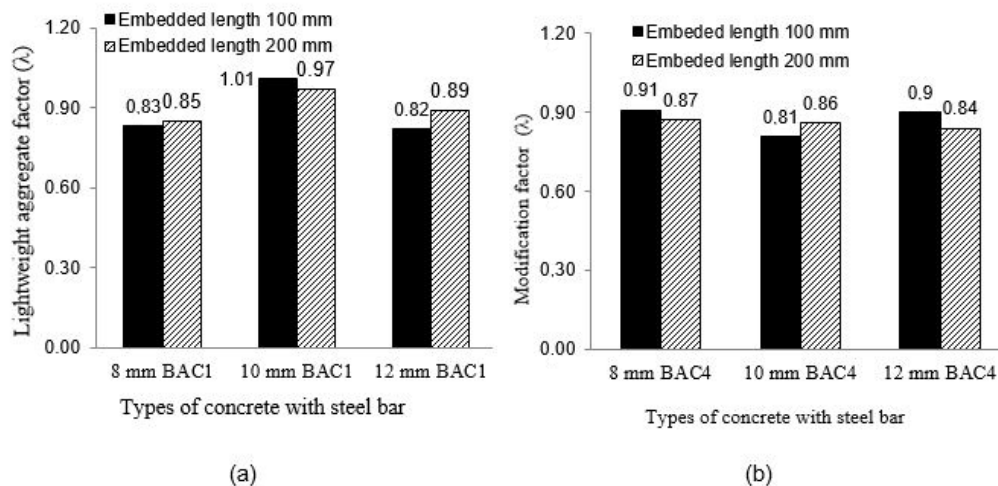
Figure 13. Rebar diameter with 200 mm embedded length of BAC4.



**Figure 14. Lightweight aggregate concrete factor ( $\lambda_{eq}$ ) for different w/c ratios determined from the equation of ACI-318 (2001).**

### 3.1.6. Proposed analytical equation for lightweight brick aggregate concrete factor ( $\lambda$ )

According to ACI-318 (2001), section 12.2.4, the value of  $\lambda$  for normal-weight aggregate (i.e., stone aggregate) concrete is 1 when it is to be used for calculating development length of deformed rebars. In the present study, the value of  $\lambda$  for lightweight aggregate (i.e., brick aggregate which is commonly used in Bangladesh) concrete has been determined considering stone aggregate as the base line. Here, the value of bond strength of stone aggregate concrete has been considered as 100 %. Hence, the value of  $\lambda$  can be determined from the ratio of brick aggregate and stone aggregate concrete obtained from the experimental results. The lightweight aggregate factor ( $\lambda$ ) of concrete made with brick aggregate (BAC1 and BAC4) with different rebar diameter and embedded length are presented in Figure 15. For the concrete type BAC1 with embedded length 100 mm and 200 mm, the value of  $\lambda$  is ranges 3 % to 5 % for all diameters of rebar as shown in Figure 15 (a). Similar results are also found for the concrete type BAC4 as shown in Figure 15 (b). Here, the value of  $\lambda$  ranges from 0.8 to 1.02 which quite satisfactory according to the ACI-318 (2001). From this research study, the average  $\lambda$  equal to 0.88 has been found for Bangladeshi first class burnt clay brick aggregate.



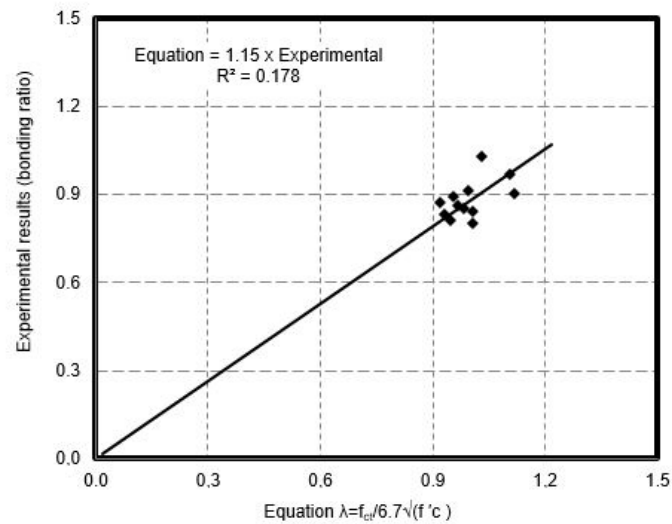
**Figure 15. Aggregate concrete factor ( $\lambda$ ) from experimental bond strength test: (a) BAC1 and (b) BAC4 with embedded length of 100 mm and 200 mm.**

However, the relationship of lightweight aggregate concrete factor ( $\lambda$ ) obtained from the equation of ACI-318 (2001), section 12.2.4 and experimental result has been developed and shown in Figure 16. The relationship between experimental results and equation from ACI-318 (2001) which is Eq. 8 is being also proposed.

$$\lambda_{eq} = 1.15 \lambda_{ex} \quad (8)$$

where  $\lambda_{eq}$  is aggregate concrete factor obtained from equation of ACI-318 (2001), section 12.2.4;

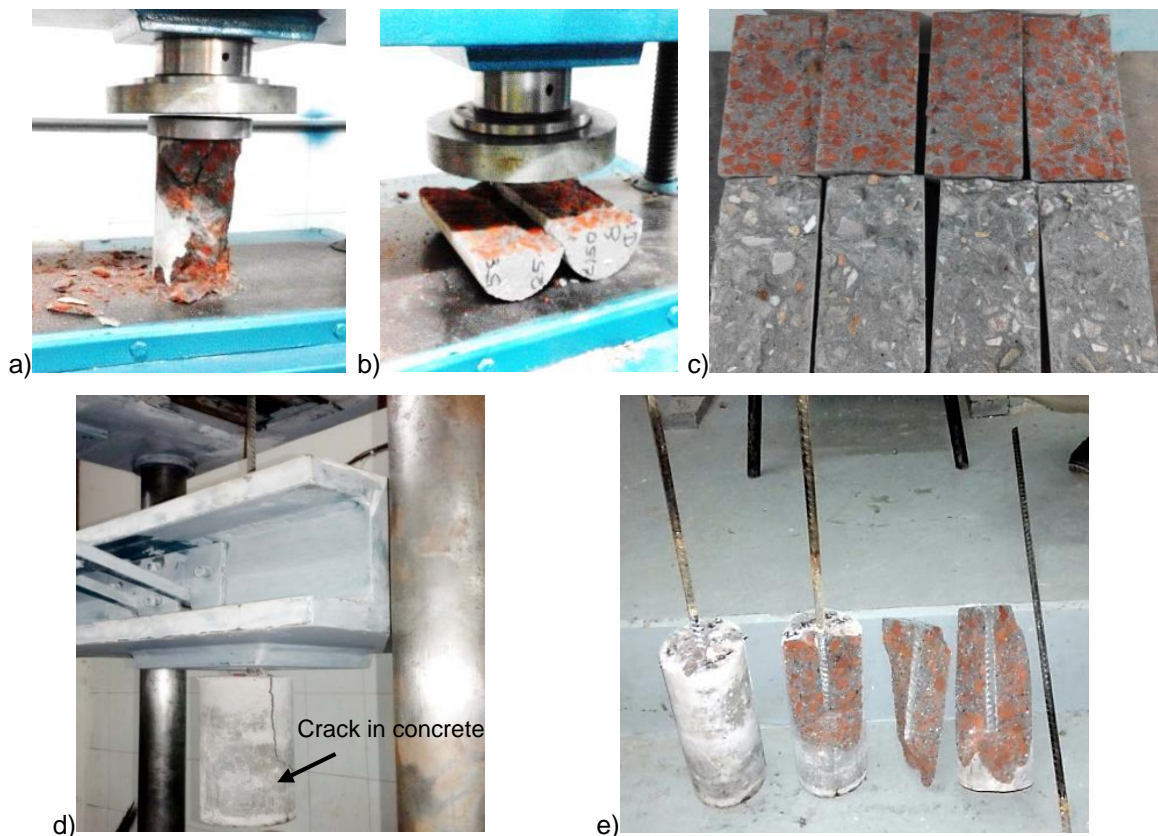
$\lambda_{ex}$  is brick aggregate concrete factor obtained from experimental results.



**Figure 16. Relationship of lightweight aggregate concrete factor ( $\lambda$ ) obtained from equation according to ACI-318 (2001) and experimental results.**

### 3.1.7. Fracture surface:

Figure 17, shows the failure modes of the specimens by compressive strength, splitting tensile strength, and bond strength tests. As expected, combined failure (both mortar and aggregate failed) was observed instead of bond failure for both compressive and tensile strength test of concrete made with both stone and burnt clay brick aggregates. This behavior could be due to better interlock/bond between mortar and aggregate. The pull-out test specimens were failed in pull-out failure and splitting failure for concrete specimens made with stone and brick aggregates. The pullout failure mode occurred when the concrete provided adequate confinement, thus preventing a splitting failure of the test specimen. This was occurred by inducing cracks on the top loaded face of the specimens. While splitting mode of failure was occurred by splitting the specimens. This behavior could be explained by the initiation of a crack along the loading axis (parallel to the longitudinal axis of the rebar, see Figure 17 d.) and then reach failure by splitting the specimens. This behavior also could be due to brittleness of the concrete specimens since fibers did not use in any of the concrete mixes.



**Figure 17. Fractured surface of specimen: (a) compressive strength; (b) & (c) splitting tensile strength; (d) & (e) pull-out and splitting failure of bond strength test.**

## 4. Conclusions

This paper presents an experimental program to investigate the lightweight aggregate (i.e., brick aggregate) concrete factor ( $\lambda$ ). The pull-out tests were carried out on four different types of concrete, three different types of rebar diameter, and two different types of embedded lengths. Additionally, different proposed equations for calculating the bond strength found in literature has been investigated and compared with the experimental results. While  $\lambda$  has been calculated according to the ACI-318 (2001), section 12.2.4 and proposed an equation for brick aggregate. The main findings regarding the bond strength and  $\lambda$  can be summarized as follows:

1. The bond strength of 10 mm diameter rebar is higher as compared to the diameter of 8 mm and 12 mm for both aggregates and both embedded length of 100 and 200 mm for all concretes, this is probably due to higher surface area of rebar of 10 mm than 8 mm. But relatively lower bond strength of 12 mm diameter deformed rebar is possibly due to size and shapes of grooves are different from 8 mm as well as 10 mm diameter deformed bar.
2. The embedded length of 200 mm showed higher bond strength than the embedded length of 100 mm. This is probably due to better mechanical interlocking of rebar ribs and concrete keys as well as higher ribs per unit length which can play an important role on the bond strength of concrete.
3. Based on the experimental results, the optimum diameter for both embedded length of concretes bond strength is 10 mm that gives maximum bond strength for all cases.
4. From this research study, it has been found that the average  $\lambda$  equal to 0.88 for Bangladeshi burnt clay brick aggregate which can be used for modeling and the development of appropriate design guidelines.
5. Based on the test results a new equation is proposed for the lightweight aggregate (i.e., brick aggregate) concrete factor ( $\lambda$ ) which is commonly used as coarse aggregate in Bangladesh.

The proposed aggregate (i.e., brick aggregate) concrete factor ( $\lambda$ ) value (0.88) and the equation for brick aggregate are promising that can be used to determine  $\lambda$  or use the proposed value in the design which deals with concrete made with brick aggregate. Nevertheless, further tests need to be carried out by taking into account different concrete grades/strength, rebar geometries (e.g., diameter and embedded length), and specimen type and dimensions to validation and calibration of the  $\lambda$  value and the proposed equation.

## 5. Acknowledgments

The authors have no conflict of interests as well as they express their thanks to all lab technician/assistants of Civil Engineering Department (CE), World University of Bangladesh (WUB), for all kinds of assistance during the experimental study performed. The authors are also grateful to Mr. Hamidur Rahman, Mr. Arif Ahmed Siddiqui, and Mr. Morshed Alam, undergraduate civil engineering students at WUB, for their altruistic and relentless involvements throughout the study.

## References

1. Arthur, H.N., David, D., Charles, W.D. Design of Concrete Structures. USA. Mc Graw Hill Education. 2003. 13th edition.
2. ACI committee 408. Bond and development of straight reinforcement in tension, ACI 408R-03, American Concrete institute, Farmington Hills, MI. 2003.
3. Mathey, R.G., Watstein, D. Investigation of bond in Beam and Pullout specimens with High strength Reinforcing bars. Journal of ACI. 1961. 32(9). Pp. 1071–1090.
4. Darwin, D., McCabe, S.L., Idun, E.K., Schoenekase, S.P. Development Length Criteria: Bars Not Confined by Transverse Reinforcement. ACI Structural Journal. 1992. 89(6). Pp. 709–720.
5. Rahman, M.H., Siddiqui, M.A.A., Murshed, M.A. Determination of « $\lambda$ » factor of concrete made with lightweight brick aggregate for bond and development lengths equation. B.Sc. thesis. Dept. of Civil Engineering. World University of Bangladesh. 2017.
6. Esfahani, M.R., Rangan, B.V. Bond Between Normal Strength and High-Strength Concrete (HSC) and Reinforcing Bars in Splices in Beam. ACI Structural Journal. 1998. 95(3). Pp. 272–280.
7. Abrishami, H.H., Mitchell, D. Simulation of Uniform Bond Stress. ACI Materials Journal. 1992. 89(2). Pp. 161–168.
8. ACI-318-02, section 12.2.3. Building Code Requirements for Structural Concrete and Commentary, American Concrete institute. 2001.
9. Nadir, Y., Sujatha, A. Bond strength determination between coconut shell aggregate concrete and steel reinforcement by pull-out test. Asian Journal of Civil Engineering. 2018. DOI. org/10.1007/s42107-018-0060-1.
10. Ganesan, N., Santhakumar, A., Indira, P.V. Bond behaviour of reinforcing bars embedded in steel fibre reinforced geopolymer concrete. Magazine of Concrete Research. 2014. 67(1). Pp. 9–16.
11. Steele, A.R. Bond Performance of Recycled Aggregate Concrete. Masters Theses, Paper 7278, Missouri University of Science and Technology. USA. 2014.
12. Benin, A.V., Semenov, A.S., Semenov, S.G., Melnikov, B.E., Simulation of degradation of bond between reinforcing bar and concrete. Part 1. Models with account of the discontinuity. Magazine of Civil Engineering. 2013. 40(5). Pp. 86–99. doi: 10.5862/MCE.40.10
13. Kabir, Md.R., Islam, Md.M. Bond stress behavior between concrete and steel rebar: critical investigation of pull-out test via finite element modeling. International Journal of Civil and Structural Engineering. 2014. 5(1). Pp. 80–90.



14. Tastani, S.P., Pantazopoulou, S.J. Direct tension pullout bond test: experimental results. *Journal of Structural Engineering*. 2010. doi.org/10.1061/(ASCE)ST.1943-541X.0000159.
15. Islam, M.S., Siddique, M.A.A. Behavior of low grade steel fiber reinforced concrete made with fresh and recycled brick aggregates. *Advances in Civil Engineering*, Vol. 2017, Article ID 1812363. DOI: 10.1155/2017/1812363.
16. ASTM C143. Slump of hydraulic cement concrete. ASTM, West Conshohocken, Pa, USA: ASTM. 2007.
17. ASTM C 1435-99. Standard practice for molding roller-compacted concrete in cylinder molds using a vibrating hammer. West Conshohocken, Pa, USA: ASTM. 2005.
18. ASTM C192/C192M-02. Standard practice for making and curing concrete test specimens in the laboratory. West Conshohocken, Pa, USA: ASTM. 2013.
19. ASTM C39 M-03. Standard test method for compressive strength of cylindrical concrete specimens. West Conshohocken, Pa, USA: ASTM. 2003.
20. ASTM C496M-04. Standard test method for splitting tensile strength of cylindrical concrete specimens. West Conshohocken, Pa, USA: ASTM. 2004.
21. ASTM C900-15. Standard Test Method for Pullout Strength of Hardened Concrete. West Conshohocken, Pa, USA: ASTM. 2015.
22. Orangun, C.O., Jirsa, I.O., Breen, J.E. A Reevaluation of Test Data on Development Length and Splice. *Journal of ACI Journal*. No. 1977. 74(3), Pp. 114–122.
23. AS3600. Australian Standard for Concrete Structures. North Sydney, Australia. 1994.
24. Hadi, M.N.S. Bond of high strength concrete with high strength reinforcing steel. *The Open Civil Engineering Journal*. 2008. Vol 2. Pp. 143–147.

**Contacts:**

*Shariful Islam, +19312528959; mislam46@students.tntech.edu*

© Islam, S., 2019



DOI: 10.18720/MCE.87.5

## Mechanical properties of magnesium potassium phosphate cement

H. Wang<sup>a</sup>, Y. He<sup>a</sup>, Y. Pan<sup>b</sup>, G. Yu<sup>a\*</sup>,

<sup>a</sup> Northeast Forestry University, Harbin, P.R.China

<sup>b</sup> Zhejiang Sci-Tech University, Hangzhou, P.R.China

\* E-mail: 327248688@qq.com

**Keywords:** magnesium potassium phosphate cement (MKPC), epoxy resin, glass fibre sheet, interface bonding performance of concrete.

**Abstract.** Magnesium potassium phosphate cement (MKPC) is a kind of phosphate hydrate formed by super-burning magnesia, soluble phosphate, a retarder and water in a suitable ratio and neutralised by acid-base neutralisation. A new type of environmentally friendly cementitious material, MKPC has received increasing attention in the field of civil engineering, especially in the field of building structural repair and reinforcement engineering. In this paper, the preparation process and compressive strength of MKPC were studied, and the mechanism of the compressive strength of MKPC was revealed. The shear strength characteristics of MKPC and epoxy resin in the interface between glass fibre sheets and concrete were compared. The results showed that when the water-cement ratio was 0.12 and the composite retarder ratio was 8 %, the compressive strength of MKPC increased to a maximum of 81.4 MPa. The formed BO33- covered the surface of KMgPO<sub>4</sub>·6H<sub>2</sub>O and hindered the continuation of the reaction, which resulted in a slow increase in the early compressive strength. MKPC can well replace the epoxy resin in the field of reinforced concrete structure and can significantly improve the interface bonding performance between glass fibre sheets and concrete.

### 1. Introduction

As the nation of China grows in economy, the number of offshore structures, such as sea-crossing bridges and large seaports, has been increasing. For example, the Hong Kong-Zhuhai-Macao Bridge has been designed and used for over 120 years, and the durability problem during structural service is apparent. If scientific methods can be used to accurately assess the damage degree of the structure, predict the evolution law of structural failure and adopt timely effective reinforcement techniques, the damage process of the reinforced concrete structure can be delayed, and the service life of the structure can be prolonged. At present, the techniques for reinforcing concrete structures commonly used in engineering mainly include the increased section reinforcement method, outer steel plate reinforcement method, prestressed reinforcement method, shotcrete reinforcement method, additional member reinforcement method, and additional fulcrum reinforcement method [1]. These methods have certain defects and deficiencies, which inevitably increase the self-weight of reinforced concrete structures. In addition, the node processing of new and old structures is a difficult point. If the treatment is not good, it will have a more adverse effect on the reinforcement process and reinforcement effects. With the advancement of research, the application of fibre reinforced plastic (FRP) composite materials in civil engineering has gradually become a popular research topic at home and abroad.

Because building fires can cause enormous losses and impacts and occur frequently in people's lives, the high temperature at the time of occurrence severely restricts the carbon fibre fabric reinforcement technology in the event of a fire. Ordinary epoxy resin is not resistant to high temperature, and high-temperature-resistant epoxy resin is not only expensive but also needs to be adhered to the carbon fibre fabric in an ultra-high-temperature environment. Additionally, the ordinary epoxy resin is difficult to scale up in engineering processes. To improve the high-temperature resistance of the adhesive, the use of inorganic rubber instead of the organic epoxy adhesive is a promising method. Therefore, there is an urgent need to

---

Wang, H., He, Y., Pan, Y., Yu, G. Mechanical properties of magnesium potassium phosphate cement. Magazine of Civil Engineering. 2019. 87(3). Pp. 59–65. DOI: 10.18720/MCE.87.5.

Ванг Х., Хе Я., Пан Ю., Ю Г. Механические свойства магниев-калий-фосфатного цемента // Инженерно-строительный журнал. 2019. № 3(87). С. 59–65. DOI: 10.18720/MCE.87.5



This open access article is licensed under CC BY 4.0 (<https://creativecommons.org/licenses/by/4.0/>)

study a high-temperature-resistant inorganic cementitious material that is used simultaneously as an adhesive for concrete structures and to seal the anaerobic layer, but such research is relatively rare.

Magnesium phosphate cement is a kind of phosphate hydrate formed by super-burning magnesia, soluble phosphate, a retarder and water in a suitable ratio and neutralised by acid-base neutralisation. A new type of environmentally friendly cementitious material, magnesium phosphate cement has received increasing attention in the field of civil engineering, especially in the field of building structural repair and reinforcement engineering [1–2]. Compared with ordinary cement, magnesium phosphate cement has many advantages, such as fast coagulation speed, high early strength, strong adhesion to different materials, dry shrinkage, and good wear resistance [3–6].

According to the difference in soluble phosphate content, magnesium phosphate cement can be divided into three main types: phosphosilicate cement (SPC) [7], magnesium ammonium phosphate cement (MAPC) [8] and magnesium potassium phosphate cement (MKPC) [9–10]. Since ammonium dihydrogen phosphate ( $\text{NH}_4\text{H}_2\text{PO}_4$ ) is used as the main reactant in the neutralisation reaction, MAPC will release irritating ammonia to the environment. Pollution has restricted the application of MAPC in the field of building structural reinforcement. Therefore, in this paper, potassium dihydrogen phosphate ( $\text{KH}_2\text{PO}_4$ ) was used instead of ammonium dihydrogen phosphate ( $\text{NH}_4\text{H}_2\text{PO}_4$ ) as the acidic component of MKPC. Additionally, potassium magnesium phosphate reinforced with glass fibre sheets was proposed, and the change regularity of the compressive strength of MKPC after strengthening was researched. The strengthening mechanism of glass-fibre-reinforced MKPC is discussed. This work will provide basic research for high-performance MKPC as an adhesive material instead of an epoxy resin-reinforced concrete structure and will expand the application of MKPC in civil engineering.

## 2. Methods

### 2.1. Materials and reagents

#### 2.1.1. Cementitious material

High-purity magnesium oxide (ZH-V3L) was used in this study as the alkaline component in MKPC and was purchased from Zehui Chemical Group (Wuxi, China). The content of MgO in the high-purity magnesium oxide exceeds 98 %, and the relative molecular mass is 40.30. Potassium dihydrogen phosphate was used as the acidic component and was purchased from Haiteng Chemical Co., Ltd. (Suzhou, China). The density of potassium dihydrogen phosphate is  $2.34 \text{ g/cm}^3$ , and the relative molecular mass of  $\text{KH}_2\text{PO}_4$  is 136.09.

Since the reaction rate of magnesium oxide and potassium dihydrogen phosphate is too fast to control, an appropriate amount of composite retarder was applied to slow the rate of the neutralisation reaction in this study. The composite retarder is composed of sodium tetraborate decahydrate, acetic acid and sodium polyphosphate, which were all purchased from Tianjin Yongda Chemical Reagent Co., Ltd. (Tianjin, China).

Through a number of pre-tested trials, the basic ratio of magnesium oxide, potassium dihydrogen phosphate and composite retarder is 64: 32: 4 by weight. The final setting time of MKPC generally does not exceed 20 minutes, which can result in good work performance.

#### 2.1.2. Sand, stone and concrete mix ratio

In this study, a glass fibre sheet-concrete interface bonding test was carried out. The fine aggregate of the plain concrete is Songhua river sand (fineness modulus is 2.47), the coarse aggregate is granite gravel, and the cement is P.O. 42.50 Portland cement produced by Jilin Yatai Group. The mix ratio of the plain concrete (cement: water: sand: gravel) is equal to 360: 160: 625: 1275 by weight. The size of the plain concrete specimen was  $100 \text{ mm} \times 100 \text{ mm} \times 400 \text{ mm}$  and was maintained for 28 days under standard curing conditions. The measured value of the cubic compressive strength is  $32.82 \text{ MPa}$ .

#### 2.1.3. Glass fibre sheet and epoxy resin

The glass fibre sheet is a CWR90-90 type alkali-free glass fibre roving fabric produced by Sanxing Glass fibre Co., Ltd. (Zigong, China) and has an areal density of  $800 \text{ g/m}^2$  and a thickness of 2.4 mm. To compare the interfacial adhesion properties of MKPC, the epoxy resin-bonded glass fibre sheet was used in this study. A diglycidyl ether of bisphenol-F (DGEF) epoxy resin with the brand name NPEF-170 was purchased from Nan-Ya Plastic Corporation (New Taipei, China). The epoxide equivalent is  $163.80 \text{ g/eg}$ , and the density is  $1.19 \text{ g/cm}^3$ . The hardener is methyl hexahydrophthalic anhydride (MeHHPA), provided by Qing Yang Chemistry Co., Ltd. (Jiaxing, China). The preparation of DGEF and MeHHPA is 100:80 by weight.

### 2.2. Mix design and preparation of magnesium potassium phosphate cement

The magnesium oxide and potassium dihydrogen phosphate were taken and placed in a dry cement mortar mixer vessel. Then, the composite retarder was gradually added under stirring at 1000 rpm until completely incorporated, and the stirring was continued for approximately 2 minutes. Finally, distilled water was added twice, 90 % distilled water was stirred at 500 rpm, and the last 10 % distilled water was stirred at 1000 rpm. The mixture was stirred in a fast gear position, stirred for another 3 minutes, and the slurry was

completely uniform, thereby obtaining the MKPC cementitious material. The composition ratio of MKPC is shown in Table 1. Sample No. MKPC-1, MKPC-2, MKPC-3, MKPC-4 and MKPC-5 were designed to research the effect of water cement ratio on the performance of MKPC, and sample No. MKPC-6, MKPC-7, MKPC-8, MKPC-9 and MKPC-10 were designed to research the effect of composite retarder mixture on the performance of MKPC.

**Table 1. Composition ratio of MKPC (kg/m<sup>3</sup>).**

Sample No.	MgO	KH <sub>2</sub> PO <sub>4</sub>	Compound retarder	Distilled water	Water cement ratio
MKPC-1	1500	750	75	186	0.08
MKPC-2	1500	750	75	232.5	0.10
MKPC-3	1500	750	75	279	0.12
MKPC-4	1500	750	75	325.5	0.14
MKPC-5	1500	750	75	372	0.16
MKPC-6	1514.3	852.2	2 % MgO = 30.2	283.9	0.12
MKPC-7	1496.7	842.3	4 % MgO = 59.8	280.6	0.12
MKPC-8	1478.5	832.1	6 % MgO = 88.7	277.2	0.12
MKPC-9	1459.0	821.1	8 % MgO = 116.7	273.6	0.12
MKPC-10	1433.4	806.7	10 % MgO = 143.3	268.8	0.12

### 2.3. Characterisation

#### 2.3.1. Compressive strength test

After a standard maintenance period of 28 days, the cured MKPC sample was subjected to a standard compressive strength test. The size of the MKPC sample was 100 mm × 100 mm × 100 mm. The compressive strength test was performed at room temperature in a computer-controlled universal mechanical testing machine (JQ03A, Zhongchen Data Technical and Equipment Co., China), according to GB 50010-2010 (code for the design of concrete structures). The loading speed was 1 mm/min, and five specimens were tested for each MKPC sample.

#### 2.3.2. Effect of different cementitious materials on the bonding properties of glass fibre sheets and concrete

The surfaces of all the specimens were roughened by a needle scaler to expose coarse aggregates. A manual lay-up procedure was conducted to bond the glass fibre onto the surface of the concrete substrates. A bonding graph of the glass fibre sheets and concrete is shown in Figure 1. One layer of glass fibre sheet with a width of 50 mm was bonded on one side of a plain concrete prism along the axial direction with MKPC or epoxy resin. All specimens had a bonded length of 100 mm, which was longer than the effective bond length estimated from the previous model. The specimens were cured for 3 days, 7 days, 14 days and 28 days to compare the effect of different cementitious materials on the bonding properties of glass fibre sheets and concrete. The bonding properties of the glass fibre sheet and concrete were evaluated at room temperature in a computer-controlled universal mechanical testing machine (JQ03A, Zhongchen Data Technical and Equipment Co., China), and the loading model graph is shown in Figure 1.

## 3. Results and Discussion

### 3.1. Influence of different water-cement ratios and retarder dosage on the strength of MKPC

The compressive strength of MKPC under different water-cement ratios (0.08, 0.10, 0.12, 0.14, and 0.16) was analysed, as shown in Figure 2. The data are expressed as the mean ± SEM and were analysed with SPSS 13.0 software. Statistical comparisons between two groups were performed using Student's t-test. Statistical comparisons among multiple groups were examined using analysis of variance (ANOVA). A two-tailed  $P < 0.05$  was considered statistically significant.

With the increase in the water cement ratio, the compressive strength of MKPC increases first and then decreases, showing a parabolic change law. When the water cement ratio reaches 0.12, the compressive strength of MKPC reaches a maximum value of 73.8 MPa. When the water cement ratio of MKPC exceeds 0.12, the compressive strength of MKPC is greatly reduced, and the fluidity is too large. Thus, MKPC is not easily applied in subsequent engineering processes, such as bonding of glass fibre sheets. To some extent, the application of MKPC is limited.

Several studies have shown that the optimal molar ratio of over-burnt magnesium oxide to potassium dihydrogen phosphate is between 5:1 and 7:1, and the strength and fluidity of MKPC will reach optimum [11–12]. Therefore, the relationship between the content of composite retarder (2 % M, 4 % M, 6 % M, 8 % M, or 10 % M) and the compressive strength of MKPC was analysed when the molar ratio of over-burnt magnesium oxide to potassium dihydrogen phosphate was 6:1 and the water cement ratio was 0.12, as shown in Figure 3.

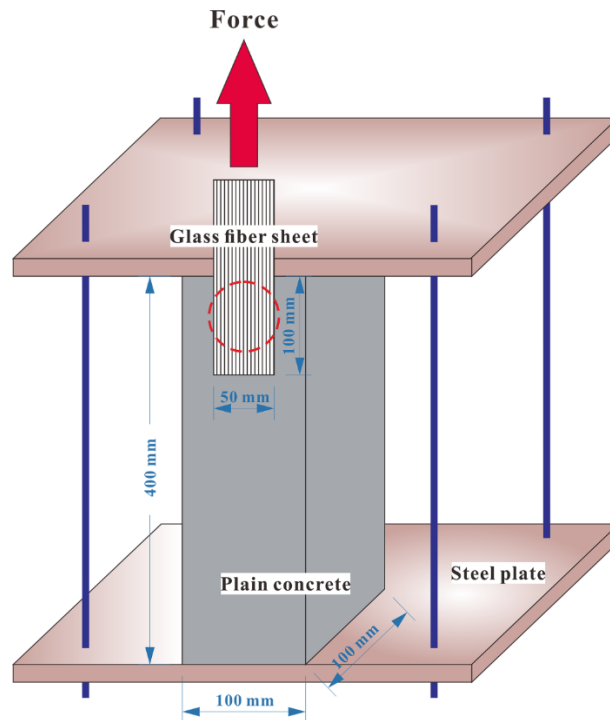


Figure 1. Bonding graph of glass fiber sheet and concrete.

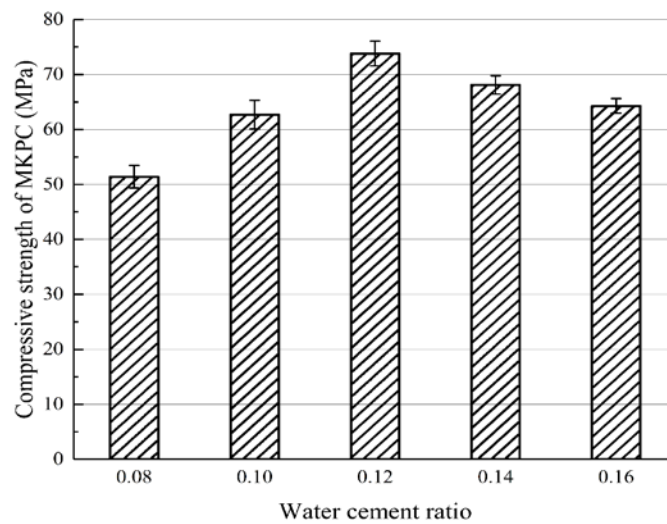


Figure 2. Relationship between water cement ratio and compressive strength of MKPC.

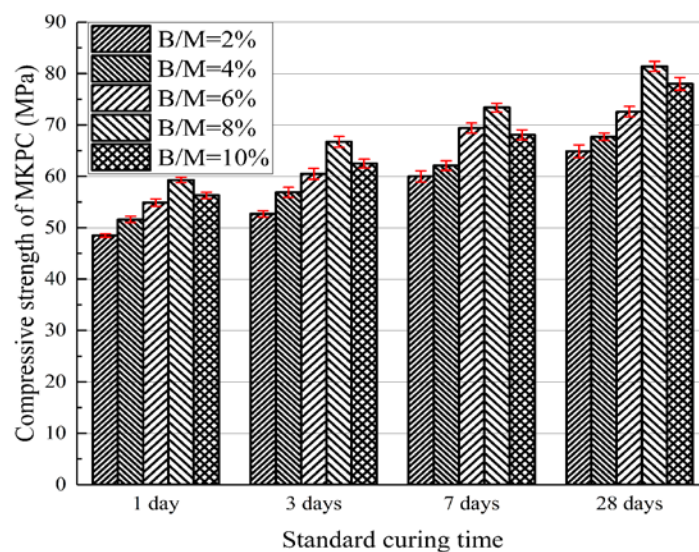


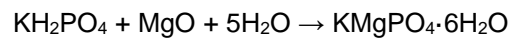
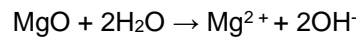
Figure 3. Relationship between compound retarder content and compressive strength of MKPC.



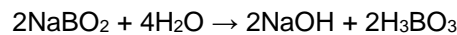
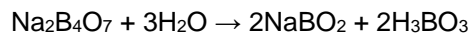
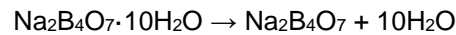
In Figure 3, the data are expressed as the mean  $\pm$  SEM and were analysed with SPSS 13.0 software. Statistical comparisons between two groups were performed using Student's t-test. Statistical comparisons among multiple groups were examined using analysis of variance (ANOVA). A two-tailed  $P < 0.05$  was considered statistically significant.

As the proportion of composite retarder increased from 2 % to 10 %, the compressive strength of MKPC first increased and then decreased. When the mass of composite retarder added was approximately 8 % that of the over-burnt magnesium oxide, the compressive strength reached the maximum value (81.4 MPa).

The main reason for this change is that the fluidity of MKPC increases with increasing water cement ratio. When the water cement ratio is 0.08, the fluidity is low and the workability is poor, and the initial setting time is too short to be suitable for engineering applications. According to the main chemical reaction in MKPC processing (related formula as shown below), when the water cement ratio exceeds the optimal water cement ratio of 0.12, excess water will rapidly prompt the hydration products towards the direction of the potassium magnesium phosphate complex ( $\text{KMgPO}_4 \cdot 6\text{H}_2\text{O}$ ), which will lead to a decrease in the compressive strength of MKPC [13–15]. At the same time, excess water will lead to excessive fluidity, which is not conducive to engineering applications [16, 17].



The composite retarder was applied as an additive in MKPC. The main component of borax ( $\text{Na}_2\text{B}_4\text{O}_7 \cdot 10\text{H}_2\text{O}$ ) is formed in the hydration process [18–20]. The hydrolysis reaction is shown in the following formula.



The surface of the potassium magnesium phosphate complex ( $\text{KMgPO}_4 \cdot 6\text{H}_2\text{O}$ ) was covered by the generated  $\text{BO}_3^{3-}$ , which hindered the continuation of the reaction. Therefore, the early compressive strength of MKPC increases slowly, and the addition of excess composite retarder will reduce the reaction rate. The hydration of borax was completed by increasing the curing time of MKPC, and the hydration of potassium dihydrogen phosphate is a dynamic equilibrium process, which leads to the rapid increase in the compressive strength of MKPC in the later period. However, excess composite retarder will still offset the growth trend of the compressive strength of MKPC.

### 3.2. Influence of different cementitious materials on the bonding properties of the glass fibre sheet-concrete interface

In recent years, FRP composite-reinforced concrete has been widely applied in concrete structure repair and has achieved remarkable reinforcement effects. This method of reinforcing concrete involves pasting or wrapping the FRP composite material on the outside of the concrete beam to improve the bearing capacity. The main advantages are high strength, low quality, convenient construction and good corrosion resistance.

In this paper, a glass fibre sheet was attached to the surface of ordinary concrete using MKPC ( $W/M + K = 0.12$ ,  $B = 8\%$  M) and epoxy resin materials, as shown in Figure 1. After the paste was completed, all the test specimens were placed in a laboratory environment and were maintained for 3 days, 7 days, 14 days and 28 days. Then, a standard single-shear test was performed, and the shear strength of the interface between the glass fibre sheet and concrete is shown in Table 2.

**Table 2. Shear strength of the interface between the glass fibre sheet and concrete (MPa).**

Standard curing time	MKPC	Epoxy resin
3 days	2.08	1.67
7 days	2.34	1.92
14 days	2.51	1.94
28 days	2.72	1.94

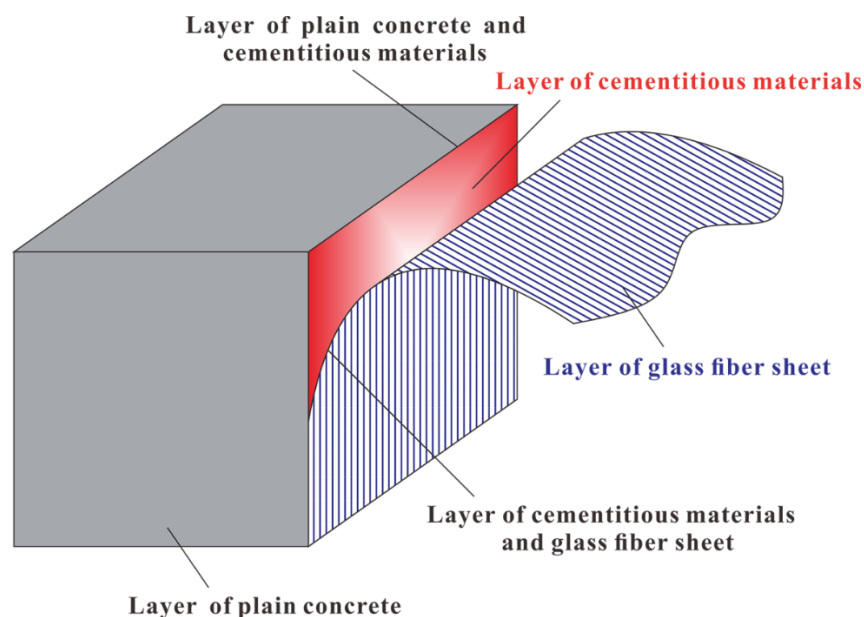
According to the variation in the shear strength of the glass fibre sheet-concrete interface bonded with different cementing materials with curing time, with the gradual increase in the curing age, the interfacial shear strength of the glass fibre sheet bonded with MKPC and ordinary concrete is greater than that of the epoxy tree at the same curing age.

When the curing age reaches 28 days, the shear strength of the bonding interface reaches 2.72 MPa, which is the maximum value of all the test groups. The maximum failure mode is the delamination tearing of

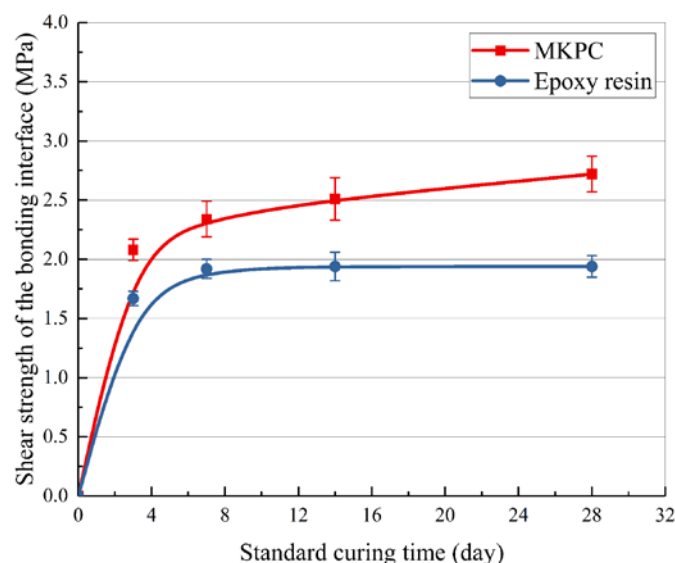
the glass fibre sheet (as shown in Figure 4), and the MKPC layer is not damaged (as shown in Figure 4). This mode indicates that MKPC plays a very good role as cementing material in the interface area between glass fibre sheets and concrete.

The shear strength of the bonding interface between MKPC and epoxy resin at different curing ages was compared and analysed, as shown in Figure 5. With increasing curing time, the shear strength of the glass fibre-concrete interface bonded with MKPC increased gradually and slowed down gradually after 14 days, and the growth rate slowed down significantly after 28 days. The shear strength is expected to continue to increase with curing time, but the growth rate is relatively slow. When the epoxy resin was applied, the shear strength increased rapidly at 3 days and then stabilised gradually. After 14 days, the shear strength increased slightly, which can be considered as no longer increasing.

The main reason for these different observations is that the strength evolution laws of the two cementitious materials are different. MKPC is a kind of fast-hardening and high-strength material. Its strength develops rapidly in the early stage and has great growth potential. Epoxy resin is a typical thermosetting polymer composite. Its strength hardly changes significantly with the external environment after curing, and its stability is good. From the above analysis, the MKPC prepared in this paper can better replace the epoxy resin to reinforce concrete structures, and the interfacial shear performance of MKPC has been significantly improved. Additionally, ammonia is no longer released during construction, thus expanding the application of MKPC in civil engineering.



**Figure 4. Structural relationship of glass fiber sheet and concrete bonded with cementitious material.**



**Figure 5. Shear strength of interface between glass fiber sheet and concrete.**

## 4. Conclusions

This paper presented the influence of the water cement ratio and retarder content on the compressive strength of MKPC and its variation law. The  $\text{BO}_3^{3-}$  formed by hydration caused the compressive strength of MKPC to increase first and then decrease, and excess composite retarder hindered the solidification of MKPC. MKPC can better replace epoxy resin to reinforce concrete structures and significantly improve their interfacial shear strength. Additionally, ammonia was no longer released during construction, thus expanding the application of MKPC in civil engineering.

## 5. Acknowledgements

The research in this paper has been supported by the Fundamental Research Funds for the Central Universities of China (Grant No. 2572019BJ01), National Natural Science Foundation of China (Grant No. 51708092) and China Postdoctoral Science Fund Project (Grant No. 2018M631894).

## References

1. Pliya, P., Beaucour, A.L., Noumowé, A. Contribution of cocktail of polypropylene and steel fibres in improving the behaviour of high strength concrete subjected to high temperature. *Construction and Building Materials*, 2011. 25(4). Pp. 1926–1934.
2. Bourbigot, S., Flambard X. Heat resistance and flammability of high performance fibers: a review. *Fire and Materials*, 2002. No. 26. Pp. 155–168.
3. Guoxin, Li, Junjie Zhang, Ge, Zhang. Mechanical property and water stability of the novel CSA-MKPC blended system. *Construction and Building Materials*, 2017. No. 136. Pp. 99–107.
4. Kyung-Ho, Lee, Hyun-Sub, Yoon, Keun-Hyeok, Yang. Tests on magnesium potassium phosphate composite mortars with different water-to-binder ratios and molar ratios of magnesium-to-phosphate. *Construction and Building Materials*, 2017. No. 146. Pp. 303–311.
5. Hugo, Lahalle, Céline, Cau Dit, Coumes, Cyrille, Mercier, David, Lambertin, Céline, Cannes, Sylvie, Delpech, Sandrine, Gauffinet. Influence of the w/c ratio on the hydration process of a magnesium phosphate cement and on its retardation by boric acid. *Cement and Concrete Research*, 2018. No. 109. Pp. 159–174.
6. Gardner, L.J., Bernal, S.A., Walling, S.A., Corkhill, C.L., Provis, J.L., Hyatt, N.C. Characterisation of magnesium potassium phosphate cements blended with fly ash and ground granulated blast furnace slag. *Cement and Concrete Research*, 2015. No. 74. Pp. 78–87.
7. Dongshuai, Hou, Handong, Yan, Jinrui, Zhang, Penggang, Wang, Zongjin, Li. Experimental and computational investigation of magnesium phosphate cement mortar. *Construction and Building Materials*, 2016. No. 112. Pp. 331–342.
8. Chau, C.K., Qiao, Fei, Li, Zongjin. Microstructure of magnesium potassium phosphate cement. *Construction and Building Materials*, 2011. No. 25 (6). Pp. 2911–2917.
9. Mácová, P., Viani, A. Investigation of setting reaction in magnesium potassium phosphate ceramics with time resolved infrared spectroscopy. *Materials Letters*, 2017. No. 205. Pp. 62–66.
10. Jihui, Qin, Jueshi, Qian, Chao, You, Yingru, Fan, Zhen, Li, Hongtao, Wang. Bond behavior and interfacial micro-characteristics of magnesium phosphate cement onto old concrete substrate. *Construction and Building Materials*, 2018. No. 167. Pp. 166–176.
11. Ahmad, M.R., Chen, Bing, Yu, Jiang. A comprehensive study of basalt fiber reinforced magnesium phosphate cement incorporating ultrafine fly ash. *Composites Part B: Engineering*, 2019. No. 168. Pp. 204–217.
12. Singh, D., Mandalika, V.R., Parulekar, S.J., Wagh, A.S. Magnesium potassium phosphate ceramic for  $^{99}\text{Tc}$  immobilization. *Journal of Nuclear Materials*. 2006. 348(3). Pp. 272–282.
13. Ahmad, M.R., Chen, Bing. Effect of silica fume and basalt fiber on the mechanical properties and microstructure of magnesium phosphate cement (MPC) mortar. *Construction and Building Materials*, 2018. No. 190. Pp. 466–478.
14. Mathieu Le, Rouzic, Thierry, Chaussadent, Gérard, Platret, Lavinia, Stefan. Mechanisms of k-struvite formation in magnesium phosphate cements. *Cement and Concrete Research*, 2017. No. 91. Pp. 117–122.
15. Yunsong, J. A new type of light magnesium cement foamed material. *Materials Letters*. 2002. No. 56(3). Pp. 353–356.
16. Wu, F., Su, J., Wei, J., Guo, H., Liu, C. Injectable bioactive calcium-magnesium phosphate cement for bone regeneration. *Biomedical Materials*. 2008. No. 3(4). Pp. 044105.
17. Maldonado-Alameda, A., Lacasta, A.M., Giro-Paloma, J., Chimenos, J.M., Haurie, L., Formosa, J. Magnesium phosphate cements formulated with low grade magnesium oxide incorporating phase change materials for thermal energy storage. *Construction and Building Materials*, 2017. No. 155. Pp. 209–216.
18. Hongyan, Ma, Biwan, Xu. Potential to design magnesium potassium phosphate cement paste based on an optimal magnesia-to-phosphate ratio. *Materials & Design*, 2017. No. 118. Pp. 81–88.
19. Mathieu Le, Rouzic, Thierry, Chaussadent, Lavinia, Stefan, Mickaël, Saillio. On the influence of Mg/P ratio on the properties and durability of magnesium potassium phosphate cement pastes. *Cement and Concrete Research*, 2017. No. 96. Pp. 27–41.
20. Niubó, M., Formosa, J., Maldonado-Alameda, A., del Valle-Zermeño, R., Chimenos, J.M. Magnesium phosphate cement formulated with low grade magnesium oxide with controlled porosity and low thermal conductivity as a function of admixture. *Ceramics International*, 2016. 42(13). Pp. 15049–15056.

## Contacts:

Hongguang Wang, +86-133-8460-8986; wanghongguang@zoho.com

Yao He, +86-136-5953-0625; 1436287817@qq.com

Yunfeng Pan, +86-150-8868-5990; yfpan@zstu.edu.cn

Guanglong Yu, +86-159-4515-2466; 327248688@qq.com



DOI: 10.18720/MCE.87.6

## The semi-shear theory of V.I. Slivker for the stability problems of thin-walled bars

**V.V. Lalin, V.A. Rybakov, S.F. Diakov, V.V. Kudinov, E.S. Orlova\***,  
*Peter the Great St. Petersburg Polytechnic University, St. Petersburg, Russia*  
\* E-mail: [ye-cat-erina@yandex.ru](mailto:ye-cat-erina@yandex.ru)

**Keywords:** stability, geometric stiffness matrix, thin-walled bar, finite element method, semi-shear theory.

**Abstract.** The theory of thin-walled bars is important because light steel thin-walled structures are widely used. Traditionally, in calculations two theories are used: theory for open-profile and closed profile bars. The calculations are difficult, because different finite elements are used for different bar types. In 2005 V.I. Slivker worked out a semi-shear theory, which is suitable for thin-walled bars of open sections and closed sections. Similarly, this article presents the research on finite element modeling for the stability problems of thin-walled bars using the same theory to the geometric stiffness matrix. It was shown that the FEM solution converges to the exact one as the number of the finite elements increases. The numeral solutions were compared to critical forces obtained by the classical Euler formula. It was found that using the cross-sections as the thin-walled ones can reduce the critical force, especially for the open cross-sections.

### 1. Introduction

The importance of the theory of thin-walled [1, 2] for structural analysis [3] bars has significantly increased both in Russia [4] and abroad during the last years. This theory has such advantages as prefabrication and lightness of elements, which are analyzed in articles of Russian and foreign researchers. In these articles the calculations of stress strain state [5, 6], strength [7] and stability of thin-walled bars [8, 9] are quoted.

The problems of stress strain state and stability of bars can be accurately solved by using of plate or volume finite elements, due to technical complexity this method cannot find wide practical application.

The buckling of thin-walled bars was investigated by G.I. Bely [10, 11]. In his articles some characteristics of steel galvanized bars were considered. As a result an algorithm for determination of the most suitable cross-section parameters was presented. The parameters depend on the flexibility of the structures.

The problem of stability is so difficult that sometimes it is necessary to use experimental methods [12, 13].

The theory of thin-walled bars, which was developed by V.Z. Vlasov, is one of the first fundamental method to solve a problem of stability. This theory is suitable for open profile bars. At the same years A.A. Umanskiy developed the thin-walled theory for closed profile bars, which has some differences from Vlasov theory in mathematical apparatus. Both theories have joint properties, such as bimoment and warping effect, which are additional force factor and deformation. At the same time other Russian scientists [14, 15] published works repeating and complementing these two problems.

With the development of the finite element method (FEM), some scientists tried to establish a thin-walled theory, which are more suitable in practice than Umanskiy theory [16, 17]. The problem of thin-walled stability is researched by foreign scientists. They analyze the problem of plane [18, 19] and spatial buckling [20, 21] for bearing elements and angle stiffeners of buildings [22, 23], for permanent and dynamic loads. Also there are some articles about stability of rods on cushion course [24].

---

Lalin, V.V., Rybakov, V.A., Diakov, S.F., Kudinov, V.V., Orlova, E.S. The semi-shear theory of V.I. Slivker for the stability problems of thin-walled bars. Magazine of Civil Engineering. 2019. 87(3). Pp. 66–79. DOI: 10.18720/MCE.87.6

Лалин В.В., Рыбаков В.А., Дьяков С.Ф., Кудинов В.В., Орлова Е.С. Полусдвиговая теория В.И. Сливкера в задачах устойчивости тонкостенных стержней // Инженерно-строительный журнал. 2019. № 3(87). С. 66–79. DOI: 10.18720/MCE.87.6



This open access article is licensed under CC BY 4.0 (<https://creativecommons.org/licenses/by/4.0/>)

In [25] it is shown how to get stiffness matrix for binodal finite element, which has seven degrees of freedom in each node. Author applied this matrix for solving dynamic problems. The matrix was obtained without taking into account that the assumption that the angles of rotation are small.

The buckling of bars can be treated as general buckling and wrinkling. The modes of buckling were analyzed in the works of Askinazi V.U. After detailed evaluation of modes of buckling (torsional, bending and bending-torsional modes) it is concluded that modes of buckling depend on bars characteristics such as stiffness, pitch and others.

However V.I. Slivker used only Lagrangian and stability functionals. It means, this topic can be developed in future. Authors of this article applied special finite elements for solving static [26] and dynamic [27] problems.

The semi-shear theory of V.I. Slivker [28] has some advantages in comparison with Vlasov and Umanskiy theory. The Slivker theory allows using one analytical model for bars of opened and closed profile, so it is more suitable in practice.

In the semi-shear theory the shear deformations are taken into account, which leads to more accurate solution. The main tangential stresses in the semi-shear theory are torsional stresses, while bending stresses are considered secondary. The shape of cross-section of bars is considered by shape coefficient.

In this article authors use FEM according to Slivker theory to solve stability problems of thin-walled elements. The process incorporates the following stages:

- 1) the stiffness matrix and the geometrical stiffness matrix are constructed;
- 2) critical force for different cross-section types (open-profile and closed profile bars) is estimated;
- 3) critical force for thin-walled rods and Euler's critical force are compared;
- 4) the recommendations are given in which cases the cross-section should be used as a thin-walled.

## 2. Methods

Let us consider a coordinate system  $(X, Y, Z)$  – a right-handed Cartesian system where an axis  $X$  matches an axial axis of the bar passing the center of gravity. Axes  $Y$  and  $Z$  are the main central axes of inertia of the bar.

Equilibrium stability functional for the beam column bar within the semi-shear theory can be written as follows:

$$S = \frac{1}{2} \int_0^L [GI_x \theta'^2 + GI_\beta (\theta' - \beta)^2 + EI_z \eta''^2 + EI_y \zeta''^2 + EI_\omega \beta'^2 + K \theta'^2 + N(\eta'^2 + \zeta'^2) + 2(M_\eta \eta'' - M_\zeta \zeta'')\theta] dx, \quad (1)$$

where  $L$  is length of the thin-walled bar,

$\theta$  is angle of torsion,

$\beta$  is warping measure function,

$\eta$  is shear center displacement with respect to the  $Y$  axis,

$\zeta$  is shear center displacement with respect to the  $Z$  axis,

$\eta'$  is angle of rotation with respect to the  $Z$  axis,

$\zeta'$  is angle of rotation with respect to the  $Y$  axis,

$E$  is Young's modulus,

$G$  is shear modulus:

$$G = \frac{E}{2(1+\nu)}, \quad (2)$$

$\nu$  is Poisson's ratio,

$I_x$  is torsional moment of inertia,



$I_\beta$  is warping moment of inertia:

$$I_\beta = \frac{I_r}{\mu_{\omega\omega}} \quad (3)$$

$I_r$  is polar moment of inertia:

$$I_r = I_z + I_y \quad (4)$$

$I_z, I_y$  are moments of inertia about the axes  $Z$  and  $Y$ ,

$\mu_{\omega\omega}$  is a cross-section form coefficient:

$$\mu_{\omega\omega} = \frac{I_r}{I_\omega^2} \int_\Omega \frac{S_{\omega\omega}^2}{t} ds \quad (5)$$

$I_\omega$  is sectorial moment of inertia,

$\Omega$  is a cross-section profile length,

$t$  is wall thickness of the bar,

$S_{\omega\omega}^2$  is sectorial static moment of the cut-off part of the cross-section,

$N$  is normal force in the bar, which is considered to be positive in case of bar extension.

$K, M_\eta, M_\zeta$  are characteristics which depend on the internal force factors.

$$K = Nr_p^2 + M_y b_z + M_z b_y + Bb_\omega, \quad M_\eta = M_y - Nz_p, \quad M_\zeta = M_z - Ny_p \quad (6)$$

$M_y$  is bending moment about the  $Y$ -axis is assumed to be positive if it causes tension in fibers with positive coordinate  $z$ .

$M_z$  is bending moment about the  $Z$ -axis is assumed to be positive if it causes tension in fibers with positive coordinate  $y$ .

$B$  is bimoment is assumed to be positive if it causes tension in points of the bar which have a positive sectorial coordinate  $\omega$ .

$y_p, z_p$  is coordinates of the bending center in the Cartesian system (axes  $Y, Z$ )

$r_p$  is polar radius of inertia of the bar's cross-section about the bending center:

$$r_p^2 = \frac{I_r}{A} + y_p^2 + z_p^2. \quad (7)$$

$A$  is cross-section area,

$b_z, b_y, b_\omega$  are geometrical parameters of the cross section:

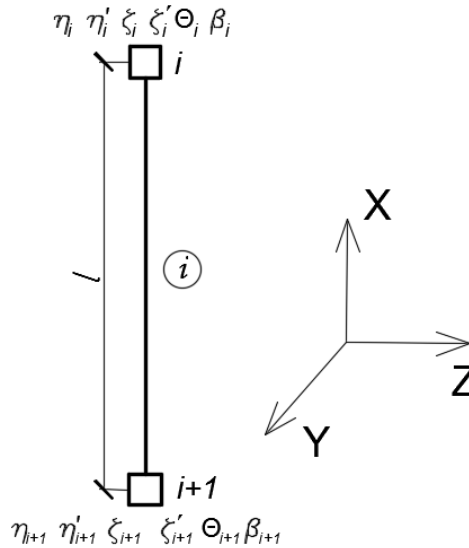
$$b_z = \frac{J_{zzz} + J_{yyz}}{I_y} - 2z_p, \quad b_y = \frac{J_{yyy} + J_{yzz}}{I_z} - 2y_p, \quad b_\omega = \frac{J_{yy\omega} + J_{zz\omega}}{I_\omega} \quad (8)$$

$J_{zzz}, J_{yyz}, J_{yyy}, J_{yzz}, J_{yy\omega}, J_{zz\omega}$  are moments of inertia of the third order:

$$J_{zzz} = \int_\Omega z^3 h ds, \quad J_{yyz} = \int_\Omega y^2 z h ds, \quad J_{yyy} = \int_\Omega y^3 h ds, \quad J_{yzz} = \int_\Omega y z^2 h ds, \quad (9)$$

$$J_{yy\omega} = \int_\Omega y^2 \omega h ds, \quad J_{zz\omega} = \int_\Omega z^2 \omega h ds.$$

Let us divide  $L$ -length thin-walled bar into  $n$  two-node finite elements. Then,  $i$ -th finite element, having length  $l$ , nodes  $i$  and  $i+1$  and 6 degrees of freedom will look like:



**Figure 1. The two-node finite element with twelve degrees of freedom.**

$$[U]^T = (\eta_i, \eta'_i, \zeta_i, \zeta'_i, \theta_i, \beta_i, \eta_{i+1}, \eta'_{i+1}, \zeta_{i+1}, \zeta'_{i+1}, \theta_{i+1}, \beta_{i+1}). \quad (10)$$

Column of node displacements of the finite element is:

To use FEM within the theory of thin-walled bars functions of the transverse displacements  $\eta(x)$  и  $\zeta(x)$  should be represented with the Hermite polynomials  $H_j$ :

$$\begin{aligned} \eta(x) &= H_1 \eta_i + H_2 \eta'_i + H_3 \eta_{i+1} + H_4 \eta'_{i+1}, \\ \zeta(x) &= H_1 \zeta_i + H_2 \zeta'_i + H_3 \zeta_{i+1} + H_4 \zeta'_{i+1}. \end{aligned} \quad (11)$$

As the functions  $\eta$  и  $\zeta$  in functional (1) have derivatives of order at most second, they should be approximated by the cubic functions.

Hermite polynomials look like this:

$$\begin{aligned} H_1(x) &= \frac{2}{l^3} x^3 - \frac{3}{l^2} x^2 + 1, \quad H_2(x) = \frac{1}{l^2} x^3 - \frac{2}{l} x^2 + x, \\ H_3(x) &= \frac{-2}{l^3} x^3 + \frac{3}{l^2} x^2, \quad H_4(x) = \frac{1}{l^2} x^3 - \frac{1}{l} x^2. \end{aligned} \quad (12)$$

Let us write equation (11) in the matrix form in order to represent functional (1) in the matrix view.

$$\eta(x) = [H]_{\eta\zeta} [U_\eta], \quad \zeta(x) = [H]_{\eta\zeta} [U_\zeta], \quad (13)$$

where  $[H]_{\eta\zeta}$  is row-matrix made of four Hermite polynomials:

$$[H]_{\eta\zeta} = [H_1(x), H_2(x), H_3(x), H_4(x)], \quad (14)$$

$[U_\eta]$ ,  $[U_\zeta]$  are node displacement columns.

$$\begin{aligned} [U_\eta]^T &= (\eta_i, \eta'_i, \eta_{i+1}, \eta'_{i+1}), \\ [U_\zeta]^T &= (\zeta_i, \zeta'_i, \zeta_{i+1}, \zeta'_{i+1}). \end{aligned} \quad (15)$$

Then:

$$(\eta')^2 = ([H']_{\eta\zeta} [U_\eta])^2 = ([H']_{\eta\zeta} [U_\eta])^T ([H']_{\eta\zeta} [U_\eta]) = [U_\eta]^T [H']_{\eta\zeta}^T [H']_{\eta\zeta} [U_\eta] \quad (16)$$

Similarly:

$$\begin{aligned}(\eta'')^2 &= [U_\eta]^T [H'']_{\eta\zeta}^T [H'']_{\eta\zeta} [U_\eta], \\ (\zeta')^2 &= [U_\zeta]^T [H']_{\eta\zeta}^T [H']_{\eta\zeta} [U_\zeta], \\ (\zeta'')^2 &= [U_\zeta]^T [H'']_{\eta\zeta}^T [H'']_{\eta\zeta} [U_\zeta].\end{aligned}\quad (17)$$

where

$$\begin{aligned}[H']_{\eta\zeta} &= \left[ \frac{dH_1(x)}{dx}, \frac{dH_2(x)}{dx}, \frac{dH_3(x)}{dx}, \frac{dH_4(x)}{dx} \right], \\ [H'']_{\eta\zeta} &= \left[ \frac{d^2H_1(x)}{dx^2}, \frac{d^2H_2(x)}{dx^2}, \frac{d^2H_3(x)}{dx^2}, \frac{d^2H_4(x)}{dx^2} \right].\end{aligned}\quad (18)$$

Let us represent functions  $\theta(x)$  и  $\beta(x)$  as a sum of products of linear polynomials and node displacements, as in functional (1) they have derivatives of order at most first.

$$\begin{aligned}\theta(x) &= H_5\theta_i + H_6\theta_{i+1}, \\ \beta(x) &= H_5\beta_i + H_6\beta_{i+1}.\end{aligned}\quad (19)$$

The polynomials are:

$$H_5(x) = -\frac{1}{l}x + 1, \quad H_6(x) = \frac{1}{l}x. \quad (20)$$

In matrix form for formulas (19) is:

$$\begin{aligned}\theta(x) &= [H]_{\theta\beta} [U_\theta], \\ \beta(x) &= [H]_{\theta\beta} [U_\beta],\end{aligned}\quad (21)$$

where

$$[H]_{\theta\beta} = [H_5(x), H_6(x)], \quad (22)$$

$$\begin{aligned}[U_\theta]^T &= (\theta_i, \theta_{i+1}), \\ [U_\beta]^T &= (\beta_i, \beta_{i+1}).\end{aligned}\quad (23)$$

Then:

$$\begin{aligned}(\theta')^2 &= [U_\theta]^T [H']_{\theta\beta}^T [H']_{\theta\beta} [U_\theta], \\ (\beta')^2 &= [U_\beta]^T [H']_{\theta\beta}^T [H']_{\theta\beta} [U_\beta],\end{aligned}\quad (24)$$

where

$$[H']_{\theta\beta} = \left[ \frac{dH_5(x)}{dx}, \frac{dH_6(x)}{dx} \right]. \quad (25)$$

Difference  $(\theta' - \beta)$  will be:

$$\theta'(x) - \beta(x) = [\Phi][U_{\theta\beta}], \quad (26)$$

where

$$[\Phi] = \left( \frac{dH_5(x)}{dx}, -H_5(x), \frac{dH_6(x)}{dx}, -H_6(x) \right), \quad (27)$$

$$[U_{\theta\beta}]^T = (\theta_i, \beta_i, \theta_{i+1}, \beta_{i+1}), \quad (28)$$

$$(\theta'(x) - \beta(x))^2 = [U_{\theta\beta}]^T [\Phi]^T [\Phi] [U_{\theta\beta}]. \quad (29)$$

To make the geometric stiffness matrix symmetric an item  $2(M_\eta \eta'' - M_\zeta \zeta'')\theta$  can be expanded as follows:

$$\begin{aligned} 2(M_\eta \eta'' - M_\zeta \zeta'')\theta &= 2M_\eta \eta''\theta - 2M_\zeta \zeta''\theta = 2M_\eta \left( \frac{1}{2}\eta''\theta + \frac{1}{2}\theta\eta'' \right) - \\ &- 2M_\zeta \left( \frac{1}{2}\zeta''\theta + \frac{1}{2}\theta\zeta'' \right) = M_\eta (\eta''\theta + \theta\eta'') - M_\zeta (\zeta''\theta + \theta\zeta'') = \\ &= M_\eta ([U_\eta]^T [H'']_{\eta\zeta}^T [H]_{\theta\beta} [U_\theta] + [U_\theta]^T [H]_{\theta\beta}^T [H'']_{\eta\zeta} [U_\eta] - \\ &- M_\zeta ([U_\zeta]^T [H'']_{\eta\zeta}^T [H]_{\theta\beta} [U_\theta] + [U_\theta]^T [H]_{\theta\beta}^T [H'']_{\eta\zeta} [U_\zeta])). \end{aligned} \quad (30)$$

Using (16), (17), (24), (29) и (30) the functional (1) will be:

$$\begin{aligned} S &= \frac{1}{2} \int_0^L [GI_x [U_\theta]^T [H']_{\theta\beta}^T [H']_{\theta\beta} [U_\theta] + GI_\beta [U_{\theta\beta}]^T [\Phi]^T [\Phi] [U_{\theta\beta}] + \\ &+ EI_z [U_\eta]^T [H'']_{\eta\zeta}^T [H'']_{\eta\zeta} [U_\eta] + EI_y [U_\zeta]^T [H'']_{\eta\zeta}^T [H'']_{\eta\zeta} [U_\zeta] + \\ &+ EI_\omega [U_\beta]^T [H']_{\theta\beta}^T [H']_{\theta\beta} [U_\beta] + K [U_\theta]^T [H']_{\theta\beta}^T [H']_{\theta\beta} [U_\theta] + \\ &+ N ([U_\eta]^T [H']_{\eta\zeta}^T [H']_{\eta\zeta} [U_\eta] + [U_\zeta]^T [H']_{\eta\zeta}^T [H']_{\eta\zeta} [U_\zeta]) + \\ &+ M_\eta ([U_\eta]^T [H'']_{\eta\zeta}^T [H]_{\theta\beta} [U_\theta] + [U_\theta]^T [H]_{\theta\beta}^T [H'']_{\eta\zeta} [U_\eta]) - \\ &- M_\zeta ([U_\zeta]^T [H'']_{\eta\zeta}^T [H]_{\theta\beta} [U_\theta] + [U_\theta]^T [H]_{\theta\beta}^T [H'']_{\eta\zeta} [U_\zeta])] dx. \end{aligned} \quad (31)$$

Let us consider  $P$  as the concentrated load applied along the axis  $X$  on the end of the bar at any point of the cross-section  $A$ , which has coordinates  $(e_y, e_z)$  about the axes  $Y, Z$ . As the result, regarding the accepted rules of signs, we will get:

$$N = -P, \quad M_y = -Pe_z, \quad M_z = -Pe_y, \quad B = -P\omega_A, \quad (32)$$

where  $\omega_A$  sectorial coordinate of the point  $A$  where load  $P$  is applied.

Using (32) we can write (6) as follows:

$$\begin{aligned} K &= Nr_p^2 + M_y b_z + M_z b_y + Bb_\omega = -Pr_p^2 - Pe_z b_z - Pe_y b_y - P\omega_A b_\omega = \\ &= -P(r_p^2 + e_z b_z + e_y b_y + \omega_A b_\omega), \\ M_\eta &= M_y - Nz_p = -Pe_z + Pz_p = -P(e_z - z_p), \\ M_\zeta &= M_z - Ny_p = -Pe_y + Py_p = -P(e_y - y_p) \end{aligned} \quad (33)$$

Using (33) functional (31) can be written:

$$\begin{aligned} S &= \frac{1}{2} \int_0^L \{ GI_x [U_\theta]^T [H']_{\theta\beta}^T [H']_{\theta\beta} [U_\theta] + GI_\beta [U_{\theta\beta}]^T [\Phi]^T [\Phi] [U_{\theta\beta}] + \\ &+ EI_z [U_\eta]^T [H'']_{\eta\zeta}^T [H'']_{\eta\zeta} [U_\eta] + EI_y [U_\zeta]^T [H'']_{\eta\zeta}^T [H'']_{\eta\zeta} [U_\zeta] + \\ &+ EI_\omega [U_\beta]^T [H']_{\theta\beta}^T [H']_{\theta\beta} [U_\beta] - P[(r_p^2 + e_z b_z + e_y b_y + \omega_A b_\omega) [U_\theta]^T [H']_{\theta\beta}^T \\ &[H']_{\theta\beta} [U_\theta] + [U_\eta]^T [H']_{\eta\zeta}^T [H']_{\eta\zeta} [U_\eta] + [U_\zeta]^T [H']_{\eta\zeta}^T [H']_{\eta\zeta} [U_\zeta] + \\ &+ (e_z - z_p) ([U_\eta]^T [H'']_{\eta\zeta}^T [H]_{\theta\beta} [U_\theta] + [U_\theta]^T [H]_{\theta\beta}^T [H'']_{\eta\zeta} [U_\eta]) - \\ &- (e_y - y_p) ([U_\zeta]^T [H'']_{\eta\zeta}^T [H]_{\theta\beta} [U_\theta] + [U_\theta]^T [H]_{\theta\beta}^T [H'']_{\eta\zeta} [U_\zeta]) \} dx \end{aligned} \quad (34)$$

Estimating integrals and putting the results together according to the nodal displacements' indexing in (10) equation (34) will be:

$$S = \frac{1}{2}[U]^T ([K] - P[G])[U], \quad (35)$$

where  $[U]$  is a column of nodal displacements from equation (10),

$[K]$  is stiffness matrix,

$[G]$  is geometric stiffness matrix.

Matrixes  $[K]$  and  $[G]$  are:

$$[K] = \begin{pmatrix} K_{11} & K_{12} \\ K_{21} & K_{22} \end{pmatrix}, \quad [G] = \begin{pmatrix} G_{11} & G_{12} \\ G_{21} & G_{22} \end{pmatrix}. \quad (36)$$

where

$$K_{11} = \begin{pmatrix} \frac{12}{l^3}EI_z & \frac{6}{l^2}EI_z & 0 & 0 & 0 & 0 \\ \frac{6}{l^2}EI_z & \frac{4}{l}EI_z & 0 & 0 & 0 & 0 \\ 0 & 0 & \frac{12}{l^3}EI_y & \frac{6}{l^2}EI_y & 0 & 0 \\ 0 & 0 & \frac{6}{l^2}EI_y & \frac{4}{l}EI_y & 0 & 0 \\ 0 & 0 & 0 & 0 & \frac{1}{l}GI_x + \frac{1}{l}GI_\beta & \frac{1}{2}GI_\beta \\ 0 & 0 & 0 & 0 & \frac{1}{2}GI_\beta & \frac{l}{3}GI_\beta + \frac{1}{l}EI_\omega \end{pmatrix},$$

$$K_{12} = \begin{pmatrix} -\frac{12}{l^3}EI_z & \frac{6}{l^2}EI_z & 0 & 0 & 0 & 0 \\ -\frac{6}{l^2}EI_z & \frac{2}{l}EI_z & 0 & 0 & 0 & 0 \\ 0 & 0 & -\frac{12}{l^3}EI_y & \frac{6}{l^2}EI_y & 0 & 0 \\ 0 & 0 & -\frac{6}{l^2}EI_y & \frac{2}{l}EI_y & 0 & 0 \\ 0 & 0 & 0 & 0 & -\frac{1}{l}GI_x - \frac{1}{l}GI_\beta & \frac{1}{2}GI_\beta \\ 0 & 0 & 0 & 0 & -\frac{1}{2}GI_\beta & \frac{l}{6}GI_\beta - \frac{1}{l}EI_\omega \end{pmatrix},$$

$$K_{21} = \begin{pmatrix} -\frac{12}{l^3}EI_z & -\frac{6}{l^2}EI_z & 0 & 0 & 0 & 0 \\ \frac{6}{l^2}EI_z & \frac{2}{l}EI_z & 0 & 0 & 0 & 0 \\ 0 & 0 & -\frac{12}{l^3}EI_y & -\frac{6}{l^2}EI_y & 0 & 0 \\ 0 & 0 & \frac{6}{l^2}EI_y & \frac{2}{l}EI_y & 0 & 0 \\ 0 & 0 & 0 & 0 & -\frac{1}{l}GI_x - \frac{1}{l}GI_\beta & -\frac{1}{2}GI_\beta \\ 0 & 0 & 0 & 0 & \frac{1}{2}GI_\beta & \frac{l}{6}GI_\beta - \frac{1}{l}EI_\omega \end{pmatrix},$$



$$\begin{aligned}
K_{22} &= \begin{pmatrix} \frac{12}{l^3}EI_z & -\frac{6}{l^2}EI_z & 0 & 0 & 0 & 0 \\ -\frac{6}{l^2}EI_z & \frac{4}{l}EI_z & 0 & 0 & 0 & 0 \\ 0 & 0 & \frac{12}{l^3}EI_y & -\frac{6}{l^2}EI_y & 0 & 0 \\ 0 & 0 & -\frac{6}{l^2}EI_y & \frac{4}{l}EI_y & 0 & 0 \\ 0 & 0 & 0 & 0 & \frac{1}{l}GI_x + \frac{1}{l}GI_\beta & -\frac{1}{2}GI_\beta \\ 0 & 0 & 0 & 0 & -\frac{1}{2}GI_\beta & \frac{l}{3}GI_\beta + \frac{1}{l}EI_\omega \end{pmatrix}, \\
G_{11} &= \begin{pmatrix} \frac{6}{5l} & \frac{1}{10} & 0 & 0 & \frac{1}{l}(z_p - e_z) & 0 \\ \frac{1}{10} & \frac{2l}{15} & 0 & 0 & z_p - e_z & 0 \\ 0 & 0 & \frac{6}{5l} & \frac{1}{10} & \frac{1}{l}(e_y - y_p) & 0 \\ 0 & 0 & \frac{1}{10} & \frac{2l}{15} & e_y - y_p & 0 \\ \frac{1}{l}(z_p - e_z) & z_p - e_z & \frac{1}{l}(e_y - y_p) & e_y - y_p & \frac{1}{l}(r_p^2 + e_z b_z + e_y b_y + \omega_A b_\omega) & 0 \\ 0 & 0 & 0 & 0 & 0 & 0 \end{pmatrix}, \\
G_{12} &= \begin{pmatrix} -\frac{6}{5l} & \frac{1}{10} & 0 & 0 & \frac{1}{l}(e_z - z_p) & 0 \\ -\frac{1}{10} & -\frac{l}{30} & 0 & 0 & 0 & 0 \\ 0 & 0 & -\frac{6}{5l} & \frac{1}{10} & \frac{1}{l}(y_p - e_y) & 0 \\ 0 & 0 & -\frac{1}{10} & -\frac{l}{30} & 0 & 0 \\ \frac{1}{l}(e_z - z_p) & 0 & \frac{1}{l}(y_p - e_y) & 0 & -\frac{1}{l}(r_p^2 + e_z b_z + e_y b_y + \omega_A b_\omega) & 0 \\ 0 & 0 & 0 & 0 & 0 & 0 \end{pmatrix}, \\
G_{21} &= \begin{pmatrix} -\frac{6}{5l} & -\frac{1}{10} & 0 & 0 & \frac{1}{l}(e_z - z_p) & 0 \\ \frac{1}{10} & -\frac{l}{30} & 0 & 0 & 0 & 0 \\ 0 & 0 & -\frac{6}{5l} & -\frac{1}{10} & \frac{1}{l}(y_p - e_y) & 0 \\ 0 & 0 & \frac{1}{10} & -\frac{l}{30} & 0 & 0 \\ \frac{1}{l}(e_z - z_p) & 0 & \frac{1}{l}(y_p - e_y) & 0 & -\frac{1}{l}(r_p^2 + e_z b_z + e_y b_y + \omega_A b_\omega) & 0 \\ 0 & 0 & 0 & 0 & 0 & 0 \end{pmatrix},
\end{aligned}$$

$$G_{22} = \begin{pmatrix} \frac{6}{5l} & -\frac{1}{10} & 0 & 0 & \frac{1}{l}(z_p - e_z) & 0 \\ -\frac{1}{10} & \frac{2l}{15} & 0 & 0 & e_z - z_p & 0 \\ 0 & 0 & \frac{6}{5l} & -\frac{1}{10} & \frac{1}{l}(e_y - y_p) & 0 \\ 0 & 0 & -\frac{1}{10} & \frac{2l}{15} & y_p - e_y & 0 \\ \frac{1}{l}(z_p - e_z) & e_z - z_p & \frac{1}{l}(e_y - y_p) & y_p - e_y & \frac{1}{l}(r_p^2 + e_z b_z + e_y b_y + \omega_A b_\omega) & 0 \\ 0 & 0 & 0 & 0 & 0 & 0 \end{pmatrix}.$$

### 3. Results and Discussion

Let us consider a bar with the length  $L = 5$  m with three different types of the cross section: a U-section, cross and rectangular pipe. The bar ends are hingedly supported ( $\eta = \zeta = 0$ ;  $\theta = 0$ ). A concentrated force  $P$  is applied sequentially to two points 1 and 2 of each cross section (Figure 2). To determine the value of the force  $P$  with FEM, the stiffness matrix  $[K]$  and the geometrical stiffness matrix  $[G]$  from the equation (36) are used.

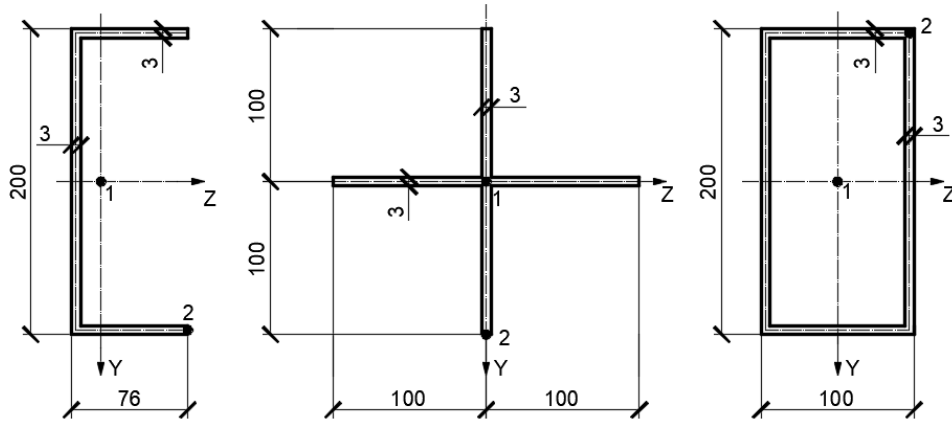


Figure 2. Cross sections of the rod.

The bar is made of steel S245:

$$E = 20600 \text{ kN/cm}^2, \quad G = 7920 \text{ kN/cm}^2.$$

Geometrical data of the cross sections is:

1) For the U-section

$$I_z = 625 \text{ cm}^4, \quad I_y = 99 \text{ cm}^4, \quad I_x = 0.3 \text{ cm}^4, \quad I_\omega = 5139 \text{ cm}^6, \quad I_\beta = 564 \text{ cm}^4, \quad y_p = 0,$$

$$z_p = -4.2 \text{ cm}, \quad r_p^2 = 87 \text{ cm}^2, \quad b_y = b_\omega = 0, \quad b_z = 11.7 \text{ cm}.$$

2) For the cross

$$I_z = I_y = 200 \text{ cm}^4, \quad I_x = 0.36 \text{ cm}^4, \quad I_\omega = 0, \quad I_\beta = 0, \quad y_p = z_p = 0,$$

$$r_p^2 = 34 \text{ cm}^2, \quad b_y = b_\omega = b_z = 0.$$

3) For the rectangular pipe:

$$I_z = 947 \text{ cm}^4, \quad I_y = 324 \text{ cm}^4, \quad I_x = 745 \text{ cm}^4, \quad I_\omega = 1553 \text{ cm}^6, \quad I_\beta = 78 \text{ cm}^4, \quad y_p = z_p = 0,$$

$$r_p^2 = 72 \text{ cm}^2, \quad b_y = b_\omega = b_z = 0.$$

It is necessary to check the slenderness ratio  $\lambda$  which should be bigger than the critical slenderness  $\lambda_{cr}$ .

Slenderness ratio and the critical slenderness can be found out as follows:

$$\lambda = \frac{\mu L}{i}, \quad \lambda_{cr} = \sqrt{\frac{\pi^2 E}{\sigma_{pr}}},$$

where  $\mu$  is effective length factor which is  $\mu = 1$  for the bar with both ends hingedly supported;

$i$  is the smallest radius of gyration;

$\sigma_{pr}$  is limit of proportionality, which is  $\sigma_{pr} = 19.5 \text{ kN/cm}^2$  for steel S245;

The critical slenderness is  $\lambda_{cr} = 102$ .

The slenderness ratio for hingedly supported beam is:

1) U-section:  $\lambda_h = 161$ ,

2) cross:  $\lambda_h = 122$ ,

3) rectangular pipe:  $\lambda_h = 116$ .

In each case slenderness ratio is greater than the critical slenderness.

Solving the basic equation for the bar in compression:

$$\det([K] - P[G]) = 0 \quad (37)$$

we can determine the least root of the equation, which is the critical load  $P$ .

Let us compare the critical load values obtained by the equation (37) with the Euler buckling loads and critical load values determined by Slivker's analytical equation for the bar with both ends pinned [20]:

$$\begin{vmatrix} EI_z k^2 + N & 0 & -M_\eta & 0 \\ 0 & EI_y k^2 + N & M_\zeta & 0 \\ -M_\eta & M_\zeta & GI_x + GI_\beta + K & -\frac{GI_\beta}{k} \\ 0 & 0 & -\frac{GI_\beta}{k} & EI_\omega + \frac{GI_\beta}{k^2} \end{vmatrix} = 0, \quad (38)$$

where

$$k = \frac{\pi}{l}.$$

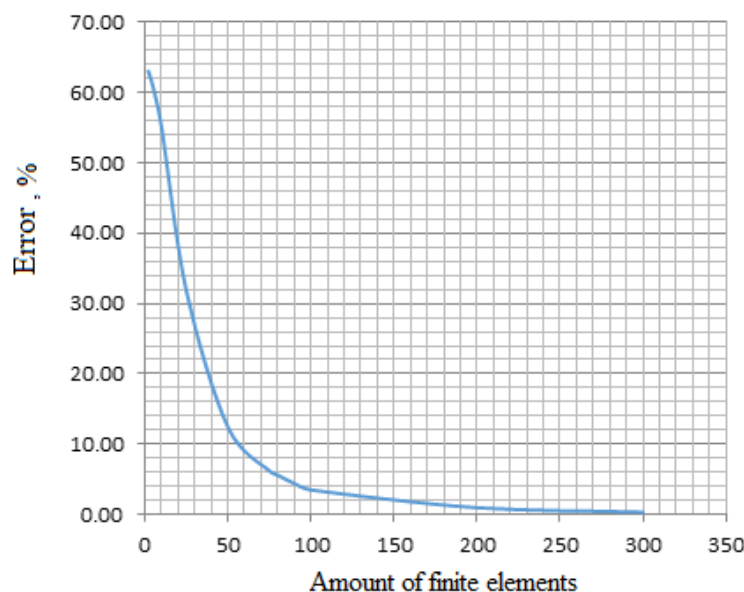
Table 1 shows the critical loads calculated with the equations (37), (38) and Euler buckling loads.

**Table 1. Comparison of the critical loads by equations (37), (38) and Euler buckling loads.**

Type of the cross section	Critical load		
	FEM	Slivker's analytical equation	Euler buckling load
U-section, point 1	73.5 kN	73.5 kN	80.5 kN
U-section, point 2	30.3 kN	30.3 kN	80.5 kN
cross, point 1	84.9 kN	84.9 kN	162.7 kN
cross, point 2	41.8 kN	41.8 kN	162.7 kN
rectangular pipe, point 1	263.4 kN	263.4 kN	263.5 kN
rectangular pipe, point 2	262.3 kN	262.3 kN	263.5 kN

Let us show the convergence of the FEM solution to the analytical solution for one of the cases: U-section, point 2 (Figure 3). For the other cases the graphs are similar.

The results in Table 1 showed that taking warping into account reduces the critical load for the open cross sections (U-section and cross) but doesn't have a significant impact on the closed cross-section (rectangular pipe).



**Figure 3. Graph of the convergence of the FEM solution to analytical solution for the case U-section, point 2.**

#### 4. Conclusions

1. The geometrical stiffness matrix of the thin-walled finite element within the Slivker semi-shear theory was worked out in this paper. Transverse displacements were approximated with cubical functions while torsion and warping with linear functions.

2. With the constructed matrix, using FEM the critical load was determined for the bar with both ends hinged supported and different types of the cross section (U-section, cross and the rectangular pipe).

3. The critical load values were also compared with the Euler buckling loads. The results showed that taking warping into account reduces the critical load for the open cross sections (U-section and cross) but doesn't have a significant impact on the closed cross-section (rectangular pipe).

4. The constructed geometrical stiffness matrix is acceptable to solve buckling problems of the thin-walled bars for both open and closed cross sections.

5. As the number of finite elements increases, the numerical solution converges to the exact one.

Finally, it was showed that thickness of the rods sections can lead to a significant decrease of the critical force for the open profile rod (up to 100 %), especially for non-centered compressive force.

#### References

1. Pavlenko, A.D., Rybakov, V.A., Pikht, A.V., Mikhailov, E.S. Non-uniform torsion of thin-walled open-section multi-span beams. Magazine of Civil Engineering. 2016. 67(7). Pp. 55–69. doi: 10.5862/MCE.67.6
2. Rybakov, V.A., Al, Ali M., Panteleev, A.P., Fedotova, K.A., Smirnov, A.V. Bearing capacity of rafter systems made of steel thin-walled structures in attic roofs. Magazine of Civil Engineering. 2017. No. 8(76). Pp. 28–39. doi: 10.18720/MCE.76.3
3. Vatin, N.I., Nazmeeva, T., Guslinsky, R. Problems of cold-bent notched c-shaped profile members. Advanced Materials Research. 2014. No. 941–944. Pp. 1871–1875.
4. Lalin, V.V., Zdanchuk, E.V., Kushova, D.A., Rosin, L.A. Variational formulations for non-linear problems with independent rotational degrees of freedom. Magazine of Civil Engineering. 2015. 56(4). Pp. 54–65. doi: 10.5862/MCE.56.7
5. Chen, C.H., Zhu, Y.F., Yao, Y., Huang, Y. The finite elements model research of the pre-twisted thin-walled beam. Structural engineering and mechanics. 2016. No. 57. Pp. 389–402.
6. Tusnin, A. Finite element for calculation of structures made of thin-walled open profile rods. Procedia Engineering 2 Cep: 2nd International Conference on Industrial Engineering, ICIE. 2016. Pp. 1673–1679.
7. Kotelko, M., Lis, P., Macdonald, M. Load capacity probabilistic sensitivity analysis of thin-walled beams. Thin-walled Structures. 2017. No. 115. Pp. 142–153.
8. Lanc, D., Turkalj, G., Vo, T.P., Lee, J. Buckling analysis of thin-walled functionality graded sandwich box beams. Thin-walled Structures. 2015. No. 86. Pp. 148–156.
9. Garifullin, M.R., Barabash, A.V., Naumova, E.A., Zhuvak, O.V., Jokinen, T., Heinisuo, M. Surrogate modeling for initial rotational stiffness of welded tubular joints. Magazine of Civil Engineering. 2016. 63(3). Pp. 53–76. doi: 10.5862/MCE.63.4

10. Bely, G.I. Metody rascheta sterzhnevyyh ehlementov konstrukcij iz tonkostennykh holodnogutykh profilej [Methods for calculating the rod from thin-walled cold-formed profiles]. Vestnik grazhdanskih inzhenerov. 2014. No. 4 (45). Pp. 32–37. (rus)
11. Bely, G.I. Osobennosti raboty sterzhnevyyh ehlementov konstrukcij iz ocinkovannykh gnutykh profilej [Features of the work of structures from galvanized bent profiles]. Vestnik grazhdanskih inzhenerov. 2012. No. 3. Pp. 99–103. (rus)
12. Pesece, O., Melcher, J. Lateral-Torsional Buckling of Laminated Structural Glass Beams. Experimental Study. Procedia Engineering. 2017. No. 190. Pp. 70–77.
13. Tusnin, A.R., Prokic, M. Experimental research of I-beams under bending and torsion actions. Magazine of Civil Engineering. 2015. 53(1). Pp. 24–31. doi: 10.5862/MCE.53.3
14. Nazmeeva, T.V., Vatin, N.I. Numerical investigations of notched c-profile compressed members with initial imperfections. Magazine of Civil Engineering. 2016. 62(2). Pp. 92–101. doi: 10.5862/MCE.62.9
15. Atavin, I.V., Melnikov, B.E., Semenov, A.S., Chernysheva, N.V., Yakovleva, E.L. Influence of stiffness of node on stability and strength of thin-walled structure. Magazine of Civil Engineering. 2018. 80(4). Pp. 48–61. doi: 10.18720/MCE.80.5
16. Tusnin, A.R., Tusnina, O.A. numerical analysis of rod systems behavior after buckling. Procedia Engineering. 2016. No. 153. Pp. 791–798.
17. Jian, L., Yun, T., Yumei, L. Stiffness Matrix of Nonlinear FEM Equilibrium Equation. Procedia Engineering. 2012. No. 29. Pp. 3698–3702.
18. Magnucki, K., Milecki, S. Elastic buckling of a thin-walled rectangular frame under in-plane compression. Thin-Walled Structures. 2017. No. 116. Pp. 326–332.
19. Batista, M. On stability of elastic rod planar equilibrium configurations. International Journal of Solids and Structures. 2015. No. 72. Pp. 144–152.
20. Sastry, S.Y.B., Krishna, Y., Koduganti, A. Flexural buckling analysis of thin walled lipped channel cross section beams with variable geometry. International Journal of Innovative Research in Science, Engineering and Technology. 2014. No. 3(6). Pp. 13484–13494.
21. Trouncer, A.N., Rasmussen, K.J.R. Flexural-torsional buckling of ultra light-gauge steel storage rack uprights. Thin-Walled Structures. 2014. No. 81. Pp. 159–174.
22. Kraav, T., Kraav, T., Lellep, J. Elastic stability of uniform and hollow columns. Procedia Engineering. 2017. No. 172. Pp. 570–577.
23. Mario, M., Giles, W. Column buckling with shear deformation – a hyperelastic formulation. International Journal of Solids and Structures. 2008. No. 45. Pp. 4322–4339.
24. Banan, M., Karami, G., Farshad, M. Finite element stability analysis of curved beams on elastic foundation. Mathematical and Computer Modelling. 1990. No. 14. Pp. 863–867.
25. Hsiao, K., Wen, Y., Chen, R. Geometrically nonlinear dynamic analysis of thin-walled beams. Proceeding of the worldcongress on engineering. 2009. No. 2. Pp. 124–139.
26. Lalin, V., Rybakov, V., Sergey, A. The finite elements for design of frame of thin-walled beams. Applied Mechanics and Materials. 2014. No. 578–579. Pp. 858–863.
27. Dyakov, S.F. Sravnitelnyj analiz zadachi krucheniya tonkostennogo sterzhnya po modelyam Vlasova i Slivkera [Comparative analysis of the problem of torsion of a thin-walled rod according to the models of Vlasov and Slivker]. Stroitel'naya mekhanika inzhenernykh konstrukcij i sooruzhenij. 2013. No. 1. Pp. 24–31. (rus)
28. Derevyankin, D.V., Slivker, V.I. O konechnoelementnykh approksimatsiyah v zadachah ustojchivosti sterzhnej Timoshenko [On finite element approximations in problems of stability of rods of Tymoshenko]. Vestnik grazhdanskih inzhenerov. 2008. No. 4(17). Pp. 17–26. (rus)

### Contacts:

Vladimir Lalin, +792 13199878; [vllalin@yandex.ru](mailto:vllalin@yandex.ru)  
 Vladimir Rybakov, +79643312915; [fishermanoff@mail.ru](mailto:fishermanoff@mail.ru)  
 Stanislav Diakov, +79213008917; [stass.f.dyakov@gmail.com](mailto:stass.f.dyakov@gmail.com)  
 Vadim Kudinov, +79618037320; [vadim.russia@hotmail.com](mailto:vadim.russia@hotmail.com)  
 Ekaterina Orlova, +79312997098; [ye-cat-erina@yandex.ru](mailto:ye-cat-erina@yandex.ru)

© Lalin, V.V., Rybakov, V.A., Diakov, S.F., Kudinov, V.V., Orlova, E.S., 2019





DOI: 10.18720/MCE.87.6

## Полусдвига́вая теория В.И. Сливкера в задачах устойчивости тонкостенных стержней

**В.В. Лалин, В.А. Рыбаков, С.Ф. Дьяков, В.В. Кудинов, Е.С. Орлова\***,

*Санкт-Петербургский политехнический университет Петра Великого, Санкт-Петербург, Россия*

\* E-mail: [ye-cat-erina@yandex.ru](mailto:ye-cat-erina@yandex.ru)

**Ключевые слова:** устойчивость, геометрическая матрица жесткости, тонкостенный стержень, метод конечных элементов, полусдвига́вая теория.

**Аннотация.** Теория тонкостенных стержней приобрела большую важность в связи с широким использованием легких стальных тонкостенных конструкций. Традиционно, при расчете тонкостенных стержней используют две разные теории: для стержней открытого профиля и стержней замкнутого профиля. При решении задач методом конечных элементов это неудобно, так как приходится строить разные конечные элементы для разных стержней. В 2005 г. В.И. Сливкером была разработана полусдвига́вая теория расчета тонкостенных стержней, которая позволяет единым образом решать задачи как для стержней открытого, так и замкнутого профилей. В рамках этой теории в данной работе исследовано применение метода конечных элементов для решения задач устойчивости тонкостенных стержней и построена геометрическая матрица жесткости. Показано, что построенное конечно-элементное решение сходится к точному при увеличении количества конечных элементов. Проведено сравнение полученных решений с критическими силами, вычисленными по классической формуле Эйлера. Сделан вывод о том, что учет тонкостенности сечения может привести к значительному уменьшению критических сил, особенно для стержней открытого профиля.

### Литература

1. Павленко А.Д., Рыбаков В.А., Пихт А.В., Михайлов Е.С. Стесненное кручение многопролетных тонкостенных балок открытого профиля // Инженерно-строительный журнал. 2016. № 7(67). С. 55–69. doi: 10.5862/MCE.67.6
2. Рыбаков В.А., Ал Али М., Пантелеев А.П., Федотова К.А., Смирнов А.В. Несущая способность стропильной системы из стальных тонкостенных конструкций в чердачных крышах // Инженерно-строительный журнал. 2017. 76(8). С. 28–39. doi: 10.18720/MCE.76.3
3. Vatin N.I., Nazmeeva T., Guslinsky R. Problems of cold-bent notched c-shaped profile members // Advanced Materials Research. 2014. No. 941-944. Pp. 1871–1875.
4. Лалин В.В., Зданчук Е.В., Кушова Д.А., Розин Л.А. Вариационные постановки нелинейных задач с независимыми вращательными степенями свободы // Инженерно-строительный журнал. 2015. № 4(56). С. 54–65. doi: 10.5862/MCE.56.7
5. Chen C.H., Zhu Y.F., Yao Y., Huang Y. The finite elements model research of the pre-twisted thin-walled beam // Structural engineering and mechanics. 2016. No. 3. Pp. 389–402.
6. Tusnin A. Finite element for calculation of structures made of thin-walled open profile rods // Procedia Engineering 2 Sep: 2nd International Conference on Industrial Engineering, ICIE. 2016. Pp. 1673–1679.
7. Kotenko M., Lis P., Macdonald M. Load capacity probabilistic sensitivity analysis of thin-walled beams // Thin-walled structures. 2017. No. 115. Pp. 142–153.
8. Lanc D., Turkalj G., Vo T.P., Lee J. Buckling analysis of thin-walled functionality graded sandwich box beams // Thin-walled structures. 2015. No. 86. Pp. 148–156.
9. Гарифуллин М.Р., Барабаш А.В., Наумова Е.А., Жувак О.В., Йокинен Т., Хейнисуо М. Суррогатное моделирование для определения начальной жесткости вращения сварных трубчатых соединений // Инженерно-строительный журнал. 2016. № 3(63). С. 53–76. doi: 10.5862/MCE.63.4
10. Белый Г.И. Методы расчета стержневых элементов конструкций из тонкостенных холодногнутых профилей // Вестник гражданских инженеров. 2014. № 4(45). С. 32–37.
11. Белый Г.И. Особенности работы стержневых элементов конструкций из оцинкованных гнутых профилей // Вестник гражданских инженеров. 2012. № 3. С. 99–103.
12. Pesec O., Melcher J. Lateral-Torsional Buckling of Laminated Structural Glass Beams. Experimental Study // Procedia Engineering. 2017. No. 190. Pp. 70–77.
13. Туснин А.Р., Прокич М. Экспериментальные исследования работы балок двутаврового сечения при действии изгиба и кручения // Инженерно-строительный журнал. 2015. № 1(53). С. 24–31. doi: 10.5862/MCE.53.3

14. Назмеева Т.В., Ватин Н.И. Численные исследования сжатых элементов из холодногнутого просечного С-профиля с учетом начальных несовершенств // Инженерно-строительный журнал. 2016. № 2(62). С. 92–101. doi: 10.5862/MCE.62.9
15. Атавин И.В., Мельников Б.Е., Семенов А.С., Чернышева Н.В., Яковлева Е.Л. Влияние жесткости узловых соединений на устойчивость и прочность тонкостенных конструкций // Инженерно-строительный журнал. 2018. № 4(80). С. 48–61. doi: 10.18720/MCE.80.5
16. Tusnin A.R., Tusnina O.A. numerical analysis of rod systems behavior after buckling // Procedia Engineering. 2016. No. 153. Pp. 791–798.
17. Jian L., Yun T., Yumei L. Stiffness Matrix of Nonlinear FEM Equilibrium Equation // Procedia Engineering. 2012. No. 29. Pp. 3698–3702.
18. Magnucki K., Milecki S. Elastic buckling of a thin-walled rectangular frame under in-plane compression // Thin-Walled Structures. 2017. No. 116. Pp. 326–332.
19. Batista M. On stability of elastic rod planar equilibrium configurations // International Journal of Solids and Structures. 2015. No. 72. Pp. 144–152.
20. Sastry S.Y.B., Krishna Y., Koduganti A. Flexural buckling analysis of thin walled lipped channel cross section beams with variable geometry // International Journal of Innovative Research in Science, Engineering and Technology. 2014. No. 3(6). Pp. 13484–13494.
21. Trouncer A.N., Rasmussen K.J.R. Flexural–torsional buckling of ultra light-gauge steel storage rack uprights // Thin-Walled Structures. 2014. No. 81. Pp. 159–174.
22. Kraav T., Kraav T., Lellep J. Elastic stability of uniform and hollow columns // Procedia Engineering. 2017. No. 172. Pp. 570–577.
23. Mario M., Giles W. Column buckling with shear deformation – a hyperelastic formulation // International Journal of Solids and Structures. 2008. No. 45. Pp. 4322–4339.
24. Banan M., Karami G., Farshad M. Finite element stability analysis of curved beams on elastic foundation // Mathematical and Computer Modelling. 1990. No. 14. Pp. 863–867.
25. Hsiao K., Wen Y., Chen R. Geometrically nonlinear dynamic analysis of thin-walled beams // Proceeding of the worldcongress on engineering. 2009. No. 2. Pp. 124–139.
26. Lalin V., Rybakov V., Sergey A. The finite elements for design of frame of thin-walled beams // Applied Mechanics and Materials. 2014. No. 578-579. Pp. 858–863.
27. Дьяков С.Ф. Сравнительный анализ задачи кручения тонкостенного стержня по моделям Власова и Сливкера // Строительная механика инженерных конструкций и сооружений. 2013. № 1. С. 24–31.
29. Деревянкин Д.В., Сливкер В.И. О конечноэлементных аппроксимациях в задачах устойчивости стержней Тимошенко // Вестник гражданских инженеров. 2008. № 4(17). С. 17–26.

#### **Контактные данные:**

*Владимир Владимирович Лалин, +79213199878; эл. почта: vllalin@yandex.ru*  
*Владимир Александрович Рыбаков, +79643312915; эл. почта: fishermanoff@mail.ru*  
*Станислав Федорович Дьяков, +79213008917; эл. почта: stass.f.dyakov@gmail.com*  
*Вадим Викторович Кудинов, +79618037320; эл. почта: vadim.russia@hotmail.com*  
*Екатерина Сергеевна Орлова, +79312997098; эл. почта: ye-cat-erina@yandex.ru*

© Лалин В.В., Рыбаков В.А., Дьяков С.Ф., Кудинов В.В., Орлова Е.С., 2019



DOI: 10.18720/MCE.87.7

## Numerical modeling of nonlinear hydrodynamics of the coastal areas

**I.G. Kantardgi<sup>a\*</sup>, M.I. Zheleznyak<sup>b</sup>, A.S. Anshakov<sup>a</sup>**

<sup>a</sup> National Research Moscow State Civil Engineering University, Moscow, Russia

<sup>b</sup> Institute Environmental Radioactivity, Fukushima University, Fukushima, Japan

\* E-mail: [kantardgi@yandex.ru](mailto:kantardgi@yandex.ru)

**Keywords:** numerical modeling, coastal engineering, chain of models, interactive model

**Abstract.** The nearshore hydrodynamic fields are produced by the nonlinear interactions of the shoaling waves of different time scales and currents. To simulate the wind wave propagated to the coasts, wave generated nearshore currents, nonlinear-dispersive wave transformation and wave diffraction in interaction with coastal and port structure, sediment transport and coastal erosion, the chains of the models should be used. The objective of the paper is to provide an overview of the results of the application of the model chains for the assessment of the wave impacts on new port designed at the Ob lip, Kara Sea to demonstrate needs for further development of the nonlinear models for the coastal engineering applications. The open source models WaveWatch III and SWAN has been used to simulate wave statistics of the dedicated areas of the studied coastal areas in high resolution to calculate the statistical parameters of the extreme wave approaching coastal zone construction in accordance with coastal engineering standards.

### 1. Introduction

The development of interactive model of currents and wind waves in Ob lip, Kara Sea intended for modelling of changes of modes of waves and current at different synoptic situations and configurations of the planned hydraulic structures is presented. Two main tasks are studied.

The first is the verification of selected models of wind waves and currents with the data of natural measurements in the Ob lip in the area of interest. The second task is to demonstrate the possibilities of obtaining with the help of the developed model the characteristics of the waves and currents necessary for the design of hydraulic structures.

The development of interactive mathematical model of waves and currents is used as a model of own development of authors – COASTOX, and models with open source code: spectral model of generation and transformation of fields of wind waves, SWAN, model of calculation of diffracted wave fields in the water area of the sea waterworks, ARTEMIS.

Calculation of the climatic characteristics of wind waves at the specified points on the approach to the investigated area is performed on the basis of spectral models of wind waves, on the fields of wind over the sea for a long (30–50 years) period, when using meteorological fields from the reanalysis of meteorological fields NCEP\NCAR or ERA-40, with their possible downscaling, using numerical models of weather forecast.

Verification of the developed mathematical model with the help of the available data, as well as the data obtained by special measurements, allows to determine the adequacy of the developed model of waves and currents.

The technology of modeling and verification of models of waves and currents is presented. Brief descriptions of SWAN, ARTEMIS and COASTOX models are given. The results of comparison of

---

Kantardgi, I.G., Zheleznyak, M.I., Anshakov, A.S. Numerical modeling of nonlinear hydrodynamics of the coastal areas. Magazine of Civil Engineering. 2019. 87(3). Pp. 80–92. DOI: 10.18720/MCE.87.7.

Кантарджи И.Г., Железняк М.И., Аншаков А.С. Численное моделирование нелинейных гидродинамических процессов береговой зоны // Инженерно-строительный журнал. 2019. № 3(87). С. 80–92. DOI: 10.18720/MCE.87.7.



This open access article is licensed under CC BY 4.0 (<https://creativecommons.org/licenses/by/4.0/>)

characteristics of wave mode and characteristics of current on approach to area of researches in ice-free period, in comparison with data of measuring stations of the region received by Arctic and Antarctic Research Institute in Saint-Petersburg are shown. The results of calculations of statistical characteristics of waves on the approach to the research area, time series of data, calculated recurrence of waves, sea level and currents in key points near the design site are shown.

The modelling of wind-wave processes widely applied in the last decades for determination of calculated parameters of wind waves completely corresponds to actual Russian normative documents. Thus, in construction code [1] It is specified: "A.5. It can define the characteristics of the waves based on hydrodynamic and probabilistic modelling using spectral or spectral-parametric models. Verification of the results of hydrodynamic modelling is recommended to be carried out according to available measurements of the characteristics of waves in natural conditions or on physical models". The point A5 opens the possibility of wide and consistent with the regulations application of mathematical models of waves and currents, while emphasizing the importance of verification of the results of such modelling by natural data.

At the same time, the same construction codes are maintained as a recommendation method for calculating waves in shallow water, based on geometric refraction and applicable for relatively simple conditions of wave development, which, in our opinion, can be used for rapid assessment of wave parameters.

Russian scientists participated in the development of known models, such as SWAN. Besides, models of other Russian authors, both hydrodynamic, and realizing method of calculation of construction code are developed and used. For example, the program PLWAVE intended for calculation of wind-wave processes using wave ray method with empirical additives [2]. Or RAWM (Russian atmosphere-wave model) [3] for the calculation of the wind-wave characteristics based on the wave actions balance equations in spectral form. Or different mathematical models for solving the engineering problems of the wave hydraulics of the coastal zone [4].

Further detailed description of the structure of the interactive model of wind waves and currents, information flows between its three calculation modules based on models SWAN, ARTEMIS and COASTOX, types of input information, specified Interactive mode. The interactive features of the model are illustrated by an example of the user input information for the three-day predictive period of 2018.

## 2. Methods

The developed interactive model includes as the main modules: the freely distributed model of calculation of wind waves of SWAN, refractive-diffraction model with open source code ARTEMIS, based on the equations of gentle slopes, 2-D model COASTOX\_UN of currents calculation based on numerical solution of non-linear equations of shallow water on unstructured triangular grid. Statistical processing of calculation results is carried out in accordance with modern approaches to the statistics of extreme hydrometeorological phenomena.

SWAN model of the Technical University of Delft (Netherlands) [5, 6], distributed in open codes, in the last decade has become generally accepted in the world practice in coastal engineering the tool for calculation of transformation of wind waves from zones deep to the coastal zone.

The model is based on the equation of the balance of the density of wave action (or the balance of wave energy in the absence of currents) with sources and drains [5, 6]. The model describes the following wave processes: wind wave generation; propagation of waves in variable depth; change of amplitude of a wave, as a result of changes of depth and current; refraction, due to changes in depth and current; diffraction; blocking and reflection of waves in opposite directional currents; passing waves through flooded obstacles.

The model also considers the processes of wave generation by the wind and their dissipations: dissipation, caused by the collapse on deep water; dissipation caused by the collapse due to the change in depth; dissipation because of bottom friction; wave interaction on deep and shallow water.

At the initial stage of the work, the calculations were performed by SWAN, version 40.85, then the calculation was made based on a later version of SWAN 41. 10AB. The results of calculations were practically not different for both these versions, for calculation points of the analyzed region.

SWAN model since the beginning of the century is increasingly used as a tool for calculating the wave fields of the coastal zone, in the systems of forecasting the wave mode and calculating the characteristics of waves in the engineering objects of the coastal zone (for example, [6–10]). An important step in the application of SWAN model in the Russia was the work, showed good results in comparison with measurements in calculating the regime characteristics of waves in the coastal zones of the Russian seas. SWAN model is used in the Arctic and Antarctic Research Institute as a calculation module for the coastal zone of the Arctic seas, integrated with the model AARI-PD2, as well as, in recent years, in Russian federal service for hydrometeorology and environmental monitoring it was introduced for the prediction of wind disturbance in the Black Sea with detailing in the offshore zones using SWAN.

The model was successfully applied by the MSUCE in many engineering projects of wave hydrodynamics of the coastal zone and tested according to the corresponding data of measurements. As an example of such projects, it is possible to specify: Port Taman, Port Gelendzhik, Port Belokamenka, etc.

The wide use of the SWAN model for the calculation of wave field formation of the coastal zone of the sea caused the choice of this model in comparison with other spectral regional models of wind waves as a tool of calculation wave mode in the Ob lip in the free-of-ice period.

An open-source ARTEMIS model is included in the structure of the developed interactive mathematical model of wind waves and currents in the proposed construction for the calculation of wave fields at hydraulic facilities. Model ARTEMIS [11], based on an extended version of the gentle slope equations [12], in which, along with the original features of the GSE calculation of the wave transformation in the coastal zone, considering the refractive-diffraction processes. It's also added the ability to calculate the impact of dissipation due to friction on the bottom and the destruction of waves in the coastal zone on the wave characteristics. In ARTEMIS code, the equations of gentle slopes are solved numerically by finite element method using parallel computation algorithm. The model is a part of the program complex of calculating the tasks of wave hydrodynamics TELEMAC [13], the version in open codes of which is called TELEMAC-MASCARET [14].

Models based on different versions of the GSE are widely used in engineering tasks of calculating wave characteristics in ports and near offshore hydraulic structures. From many such models we note here only the most frequently used in engineering projects, along with ARTEMIS, the model EMS: Elliptic Mild Slope Wave Module Popular commercial complex of settlement programs of marine hydraulics MIKE-21 [15, 16].

The choice of ARTEMIS as one of the three components of the computational interactive model developed in this project, along with its status as a freely distributed model, is also due to: the successful ARTEMIS testing for a large number of projects for seaports, for example [17, 18], and also a set of test calculations, which in comparison with measurement data is presented in model documentation; availability of both the version for regular waves and the spectral version of the model; modern numerical implementation of the model on the unstructured calculation grid, which provides the necessary detail of the wave fields in the calculation areas; effective paralleling algorithm, allowing to significantly reduce the time of calculations when using both multiprocessor and multi-core computer systems; user-friendly interface.

The ARTEMIS model was successfully applied by the MSUCE in many engineering projects of the wave hydrodynamics of the coastal zone of the sea and tested according to the corresponding data of measurements [19]. In the interactive model being developed, the wave characteristics are calculated on the approach by the SWAN model and, then, the mode characteristics of the waves at the entrance to the port are transferred to the more detailed in the coastal zone of the ARTEMIS model grid.

COASTOX [20, 21] using the approximation of shallow water describes the fields of coastal currents generated by the joint influence of wind, gradient currents of the deep sea, tides and wind waves. Numerical solution of the model equations is constructed by the method of finite volumes on unstructured triangular grids. The form of the two-dimensional equations of shallow water includes members describing the effects of bottom friction, wave radiation stresses, horizontal turbulent mixing. Due to the universal structure of equations, they can, except coastal currents, under corresponding boundary conditions and the disconnected module of wave radiation stresses, to describe various wave processes: currents in rivers, transformation of tidal waves, storm surges, tsunami waves. Algorithms of parallelization calculations, on multiprocessor and/or multi-core systems are realized.

The model was used in many engineering tasks to calculate the coastal fields of currents. The conducted comparisons showed its good accuracy and stability of the used computational algorithm, for complex bathymetry and coastal outlines, in comparison with widely used in the world practice programs of numerical solution of shallow water equation on unstructured grids such as Mike-11 of the Danish Institute «DHI» [22], ADCIRC USA [23, 24], CMS-Flow Corps of Engineers of the U.S. Army [25].

The choice of the COASTOX model in the version implemented on unstructured grids is due to the ability of the authors of the model to adapt it effectively to the interactive model being developed, while the model of the modules describing the physical processes and the level of numerical realization (the use of algorithms of parallel calculations on unstructured grids) is not inferior to the most known software complexes of two-dimensional modelling of sea currents noted above.

The boundary conditions when performing mathematical modeling were defined according to the simulated tasks.

So, for modeling of tides, on open borders of computational grid, in the sea of Kars the conditions of change of level were asked. Tidal wave parameters were made from the global Tide Model TPXO 7.2, which assimilates the data of the satellite altimeter TOPEX/Poseidon and Jason. The dynamics of the level at the borders was calculated based on 13 tidal harmonics.



River runoff was set on the river borders in the places of confluence of OB, Pur and Taz rivers on the average annual hydrograph of river runoff from the site <http://www.r-arcticnet.sr.unh.edu/v4.0/>. At the borders of the grid adjacent to the land, the normal component of the flow rate was set to zero, and tangential was not fixed.

To calculate the mode of waves in the port area was chosen wave model ARTEMIS, open source, which is part of the software system TELEMAC. The model describes the reflection of the waves from the obstacles, the diffraction of the waves behind the obstacles, the refraction of the waves on the heterogeneity of the bottom, the bottom friction and the collapse of the waves. Thus, it allows to enter various coefficients of reflection of waves on sections of a boundary of the settlement area, corresponding to port constructions of various types: vertical berths, pilework, various slopes, with differing slopes and surface parameters. The model allows to simulate regular monochromatic waves and irregular waves with a given spectral distribution.

Wave pattern for each calculated storm is stationary, so the parameters obtained for the key points of excitement fully represent the time series of waves.

The results of calculations, obtained, with the help of models SWAN and COASTOX, adapted for the calculation of waves and currents in Ob lip, in comparison with the data of measurements in the region are presented. and results of prediction of wave fields of different repeatability on the structures water area with the help of ARTEMIS model.

### 3. Results and Discussion

Interactive Model of Wind Waves and Currents (IMWWC) can be used in two modes:

#### A) Mode of calculating the statistical characteristics of waves and currents

Model allows to calculate the statistical parameters of waves and currents on the wind fields for the selected archival period. Interactivity of the model for the user in this mode is provided by:

A.1) the ability to change the input information on the wind fields (another calculation period, for example, a higher number of past years or the inclusion of recent years in the estimated time series) or use of another source of data on boundary conditions – characteristics of tides on the external boundary of the calculation area;

A.2) the ability to change the configuration of structures and bathymetry, if necessary to use new refined data.

B) The mode of predictive calculations of characteristics of waves and currents interactivity of the model for the user in this mode is provided by:

B.1) The possibility of changing the input information on wind fields for the forecast period and data on the boundary conditions – characteristics of tides on the external boundary of the calculation area during this period;

B.2) The ability to change the configuration of structures and bathymetry, when new refined data appears.

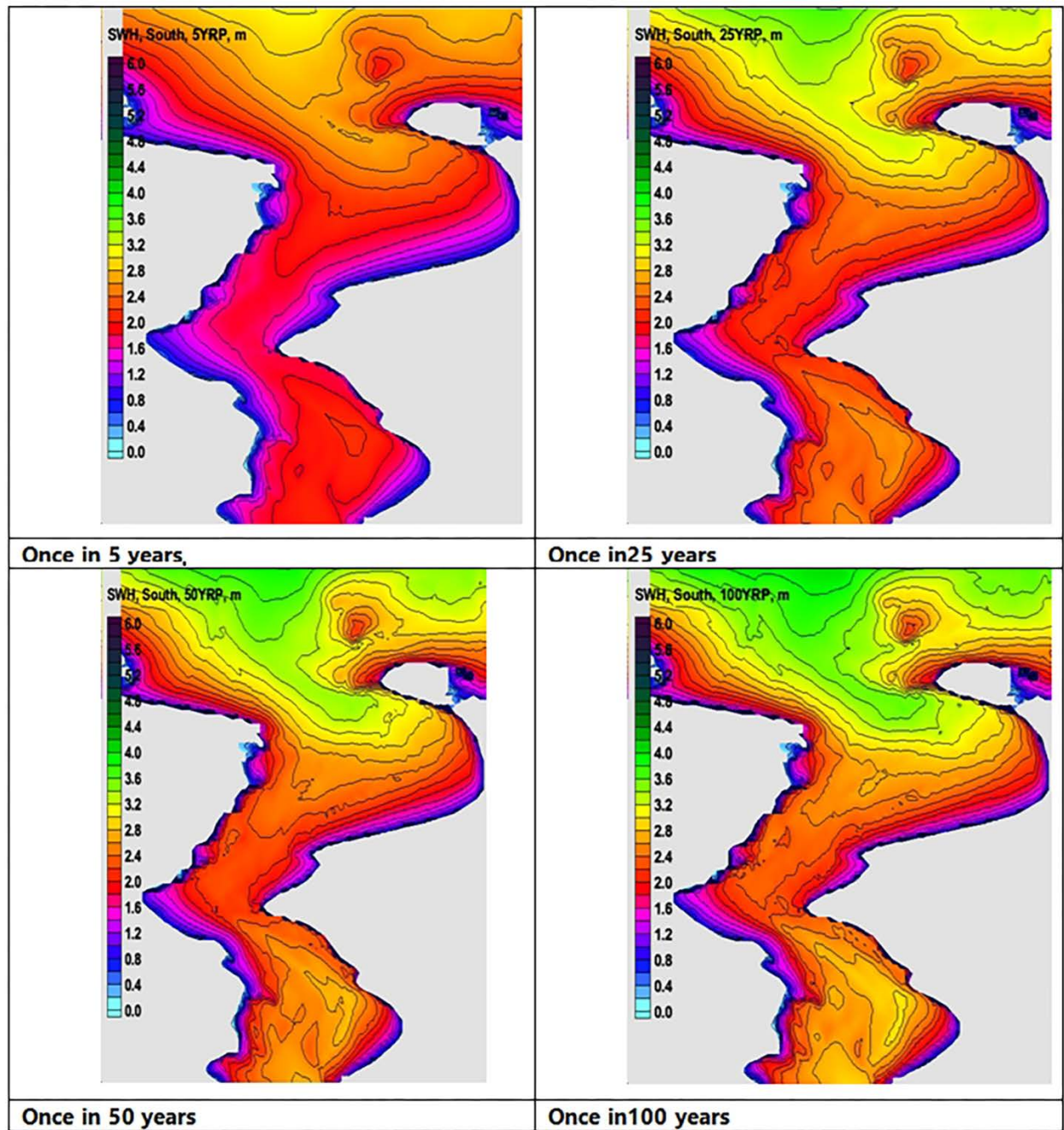
As with the wind field analysis data, the data from the global models of the US Hydrometeorological service, NOAA, were the source of data on predictive wind fields. The values of the wind field component were obtained on a uniform grid with a resolution of 0.25 degrees with 1-h discreteness from the publicly available results of the global model of numerical weather forecast <http://nomads.ncep.noaa.gov>.

The parameters of the waves in the control points near the water area of the object, calculated in this way by SWAN model, were then transferred to the ARTEMIS model for calculations on the water area of the object.

The wave fields designed by SWAN model in interactive predictive mode, on the approach to the construction are used by the ARTEMIS model as boundary conditions for calculating the fields of waves in the water area. This procedure for the transfer of the SWAN output as an input to ARTEMIS is no different from the same data interchange between the interactive model modules to simulate the statistical characteristics of the waves in water area of the Object. Also, as in the case of statistical calculations in interactive predictive mode, the user should choose from a set of prepared calculation grids, which corresponds to the direction of the wave approach to the Object. The parameters of the waves in the control points near the water area of the Object, calculated in this way by SWAN model, were then transferred to the ARTEMIS model for calculations in the water area of the Object.

After setting the parameters of the waves and selecting the appropriate numerical grid, the model calculates the distribution of wave heights on the area of the Object and the height of the waves in control points.

As examples in Figures 1, 2, 3 and 4, the results of prediction of statistical characteristics of heights and periods of waves in the area of researches are shown, in Figure 1 – fields of heights of waves for all Ob lip, on Figure 2 – fields of wave periods for the same area. And in Figures 3 and 4 – the heights of waves in the water area of the port of South direction.

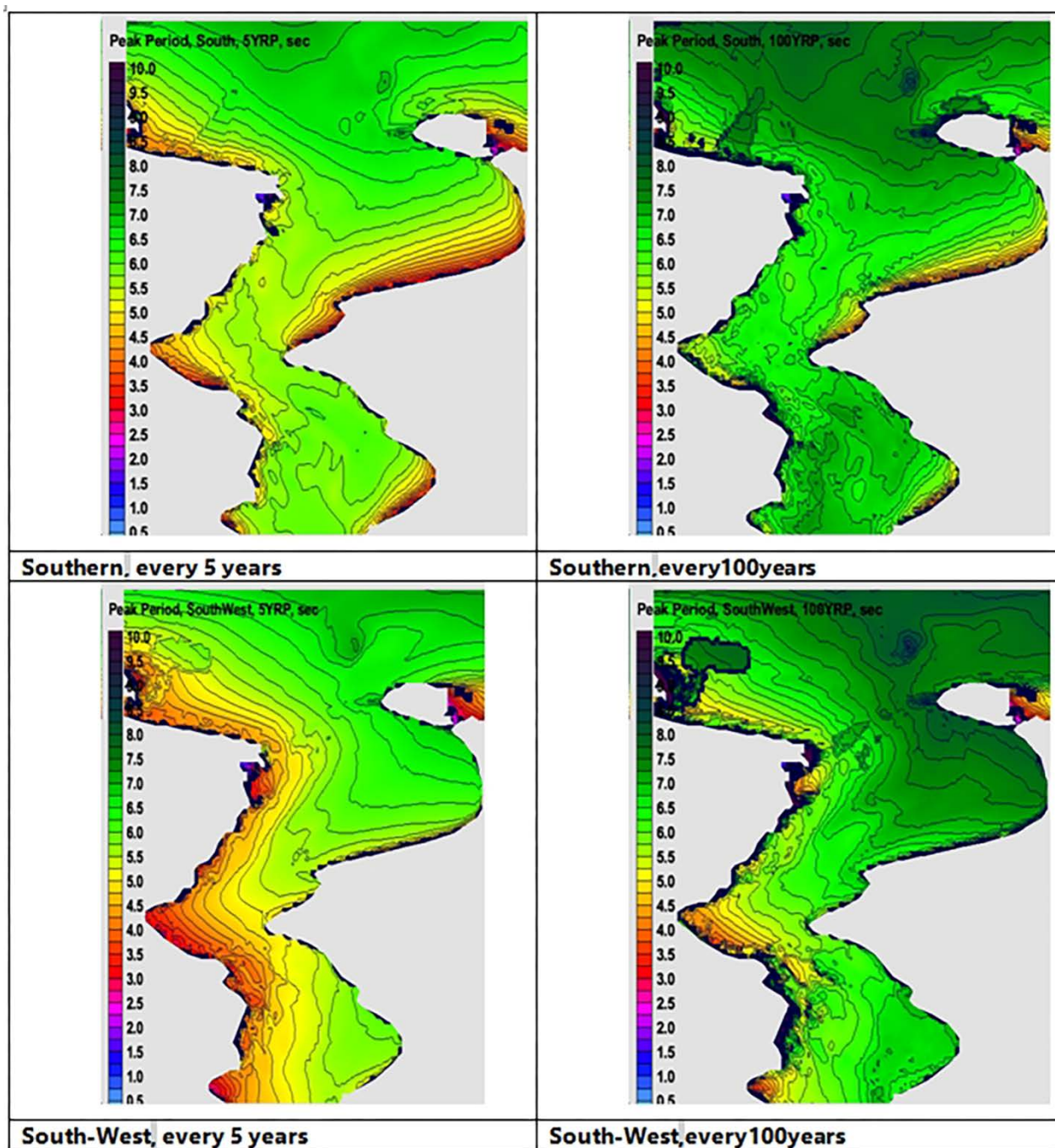


**Figure 1. Fields of heights of significant waves with a direction of approach – Southern, possible once in 5, 25, 50 and 100 years.**

The interactive model can use the input characteristics of tides on the external boundaries of the calculation area, and scenarios of wind fields and pressure for the calculation period.

Wind forecast is obtained on a rectangular grid in geographical coordinates, covering a rectangular area of 66–82.5° latitude, 55–106° longitude, with a step of 0.25° in both directions. Temporary discreteness of the forecast is one hour.

The global tidal model TPXO 7.2 [27] is used to set the tides. The dynamics of the level at the borders is generated based on 13 tidal harmonics.



**Figure 2. Fields of peak wave periods with the direction of the approach – South and South-West, possible once in 5 and 100 years.**

Based on the source data, the current model predicts the distribution of sea level and dimensional the velocity field in the entire area for the selected period. And, the level, seas and velocity of current in the selected control points in the northern part of the Ob lip, near the port of Sabetta and in the area of construction of the facility.

The simulation results are shown in Figures 5 and 6. Figures 5 shows the simulated sea-level distributions in the middle and northern part of the Ob lip and the currents velocity fields, for the full and small water of quadrature and seizing tides in the area of the proposed construction of the Salmanovsky NGKM facility.

Figures 6 show the fields of velocities of currents for full and small water, quadrature and sizing tides, in the area of the intended construction of the object.

Special studies were performed to verify the results of the mathematical simulation. Data of the field measurements of level, currents and waves have been provided by the Arctic and Antarctic Research Institute. The data used included archival materials for 2012, 2013 and 2015–2016. The special measurements were performed in 2017.



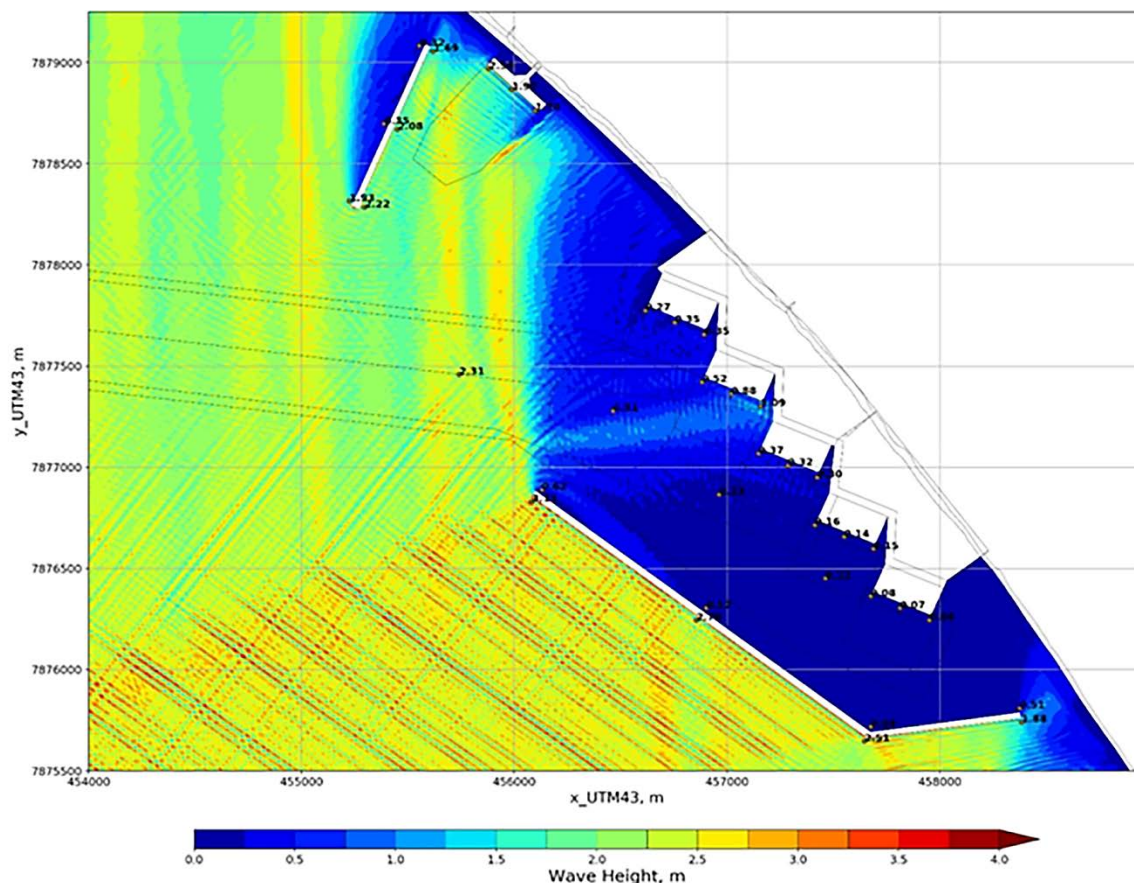


Figure 3. Wave heights in the waters of the remote Terminal “Utrenny” of the seaport of Sabetta, the layout version of no. 3, for a wave of repeatability once in 50 years, 13% of accident, South direction of approach.

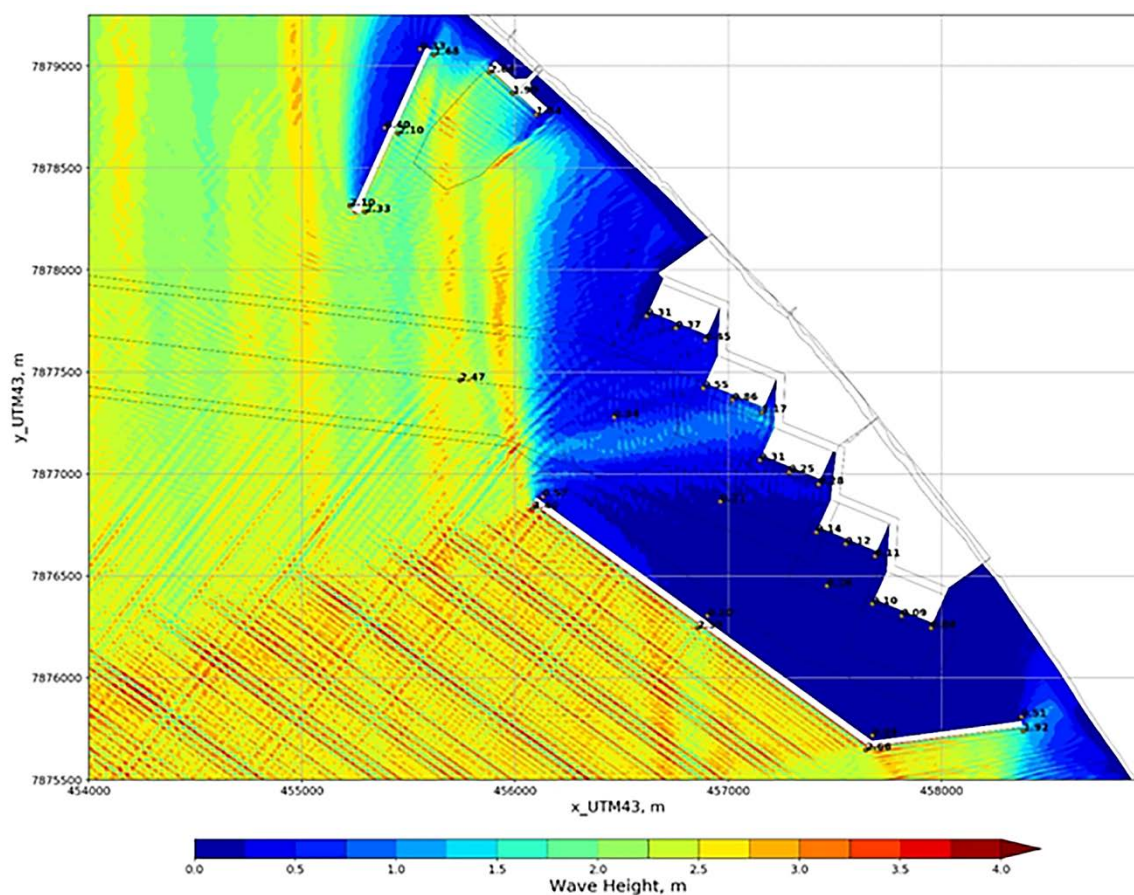
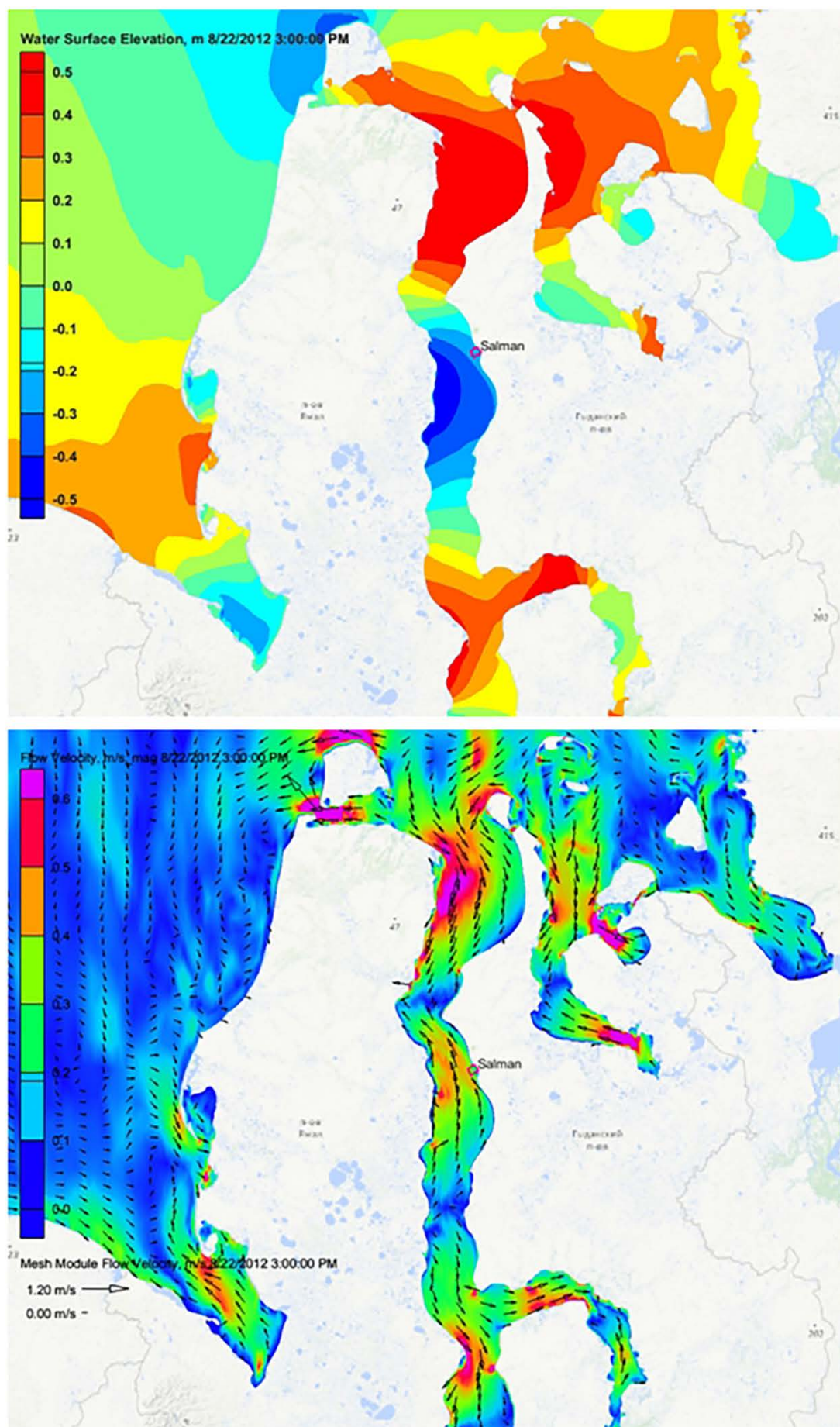
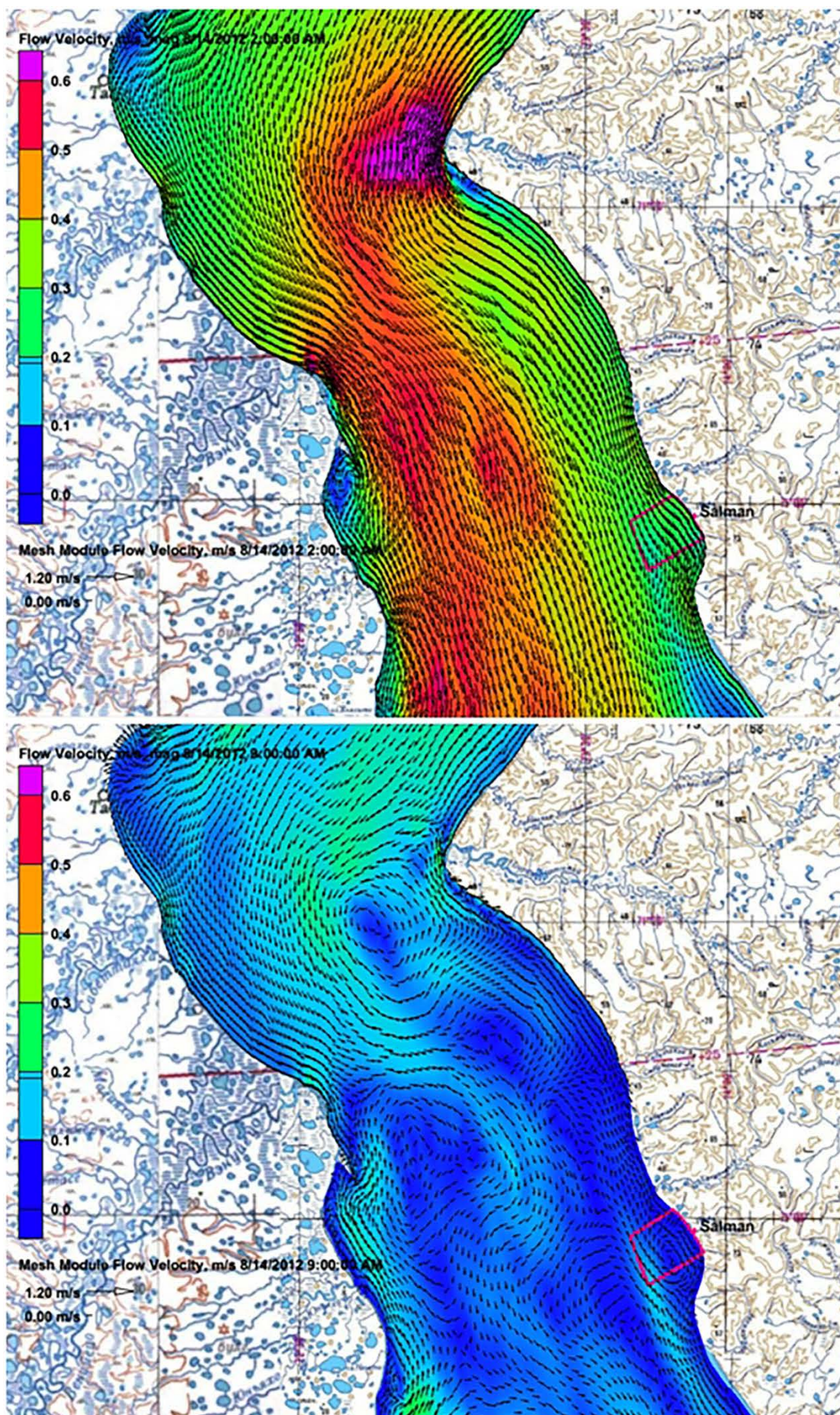


Figure 4. Wave heights in the waters of the remote Terminal «Utrenny» of the seaport of Sabetta, the layout version of no. 3, for a wave of repeatability once in 100 years, 13% of accident, South direction of approach.



**Figure 5.** The distribution of sea level and velocities in the middle and northern part of the Ob lip, calculated by the model COASTOX-UN at the time of the small water of the seizing tide in the area of the proposed construction of the facility near the Salmanovsky NGKM. Web Mercator, EPSG: 3857.





**Figure 6. Velocities in the middle part of the Ob lip, near the area of the expected construction of the object, calculated by the model COASTOX-UN for the quadrature tide in the area at the time of full water (above) and at the time of low water (bottom). Web Mercator, EPSG: 3857.**



For summer-autumn, 2012 (27.07.2012 – 04.10.2012) data on 15 measuring stations were provided: 9 stations in the northern part of Ob lip, closer to the exit from the bay, and 6 stations near the port of Sabetta.

For August-September 2013 (07.08.2013 – 29.09.2013) – data on 3 measuring stations: 1 point in the northern part of the Ob lip, 1 near the port of Sabetta and 1 in the area of the Salmanovsky field.

Data from the beginning of autumn 2015 to the end of summer 2016 are provided for 3 points in the area of the Salmanovsky field.

11 control points of the Ob lip in the area of prospective construction of the facility near the Salmanovsky field were applied for measurements in 2017.

The results of verification are partially published [28], partially shown below.

Results of comparison of calculated and measured heights of waves at two AWAC stations, taking into account the standard deviation of calculated heights of waves from measured about 0.2 m, at altitudes of waves up to 1.5 m and RMS deviation of calculated periods of waves from measured up to 0.47 sec, at periods of high waves in 3–4 sec, it is possible to recognize good consent of the results of the model measured data.

Typical examples of comparisons are shown in Figures 7 and 8.

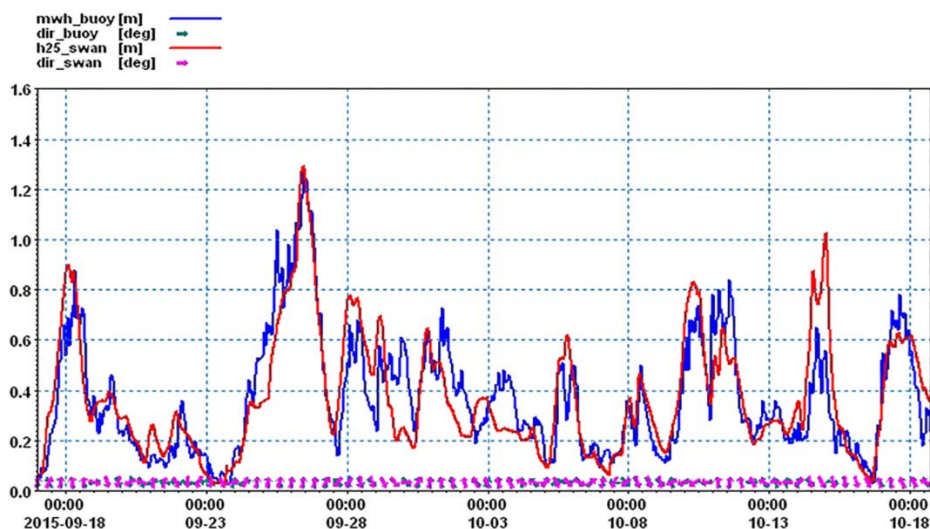


Figure 7. Comparison of calculated and measured heights of waves according to archival data (example).

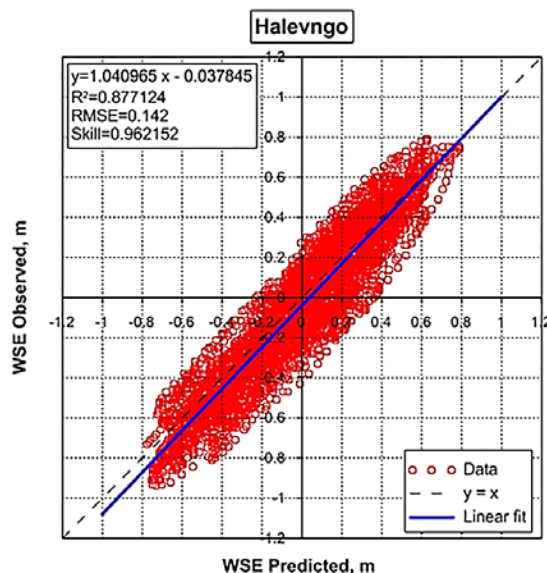


Figure 8. Comparison of measured and simulated sea level values (example).

#### 4. Conclusions

The structure of the developed interactive model of wind disturbance and currents for the area of construction in Ob Guba, information flows between its three calculation modules based on models SWAN, ARTEMIS and COASTOX, types of input information are presented That is specified by the user in interactive mode. The interactive features of the model are illustrated by an example of calculation based on input information for the three-day predictive period 2018.

The developed mathematical model of waves and currents can be used for the solution of such problems as: determination of the calculated parameters of waves in berthing structures for providing safe conditions of mooring of vessels; determination of the calculated parameters of the waves at the structures for the design of structures (elevation of crests, wave loads, etc.); determination of current fields for prediction of sediment transfer, assessment of the port water area, navigation channels, local washouts at the structures.

## References

1. Russian Construction Norms SP 38.13330.2012. Nagruzki i vozdeystvia na gidrotexnicheskie sooruzhenia (volnovie, ledovie i ot sudov) [Loads and impacts on hydraulic structures (wave, ice and from ships)] Minregionrazvitiya RF, 2012. (rus)
2. Zagriadskaya, N.N., Kalinin, S.G. Numerical modeling of sea wave propagation in waterbodies. Hydraulic structures. 2007. No. 5.
3. Kabatchenko, I.M., Matushevskiy, Reznikov, M.V., Zaslavsky, M.M. Modeling of wind and waves under the thermic cyclones in the G.V. Black Sea. Meteorology and Hydrology. 2001. No. 5. Pp. 61–71.
4. Makarov, N.N. Novie matematicheskie modeli i programnie komplekxy v probreynoi morskoi gidrotexnike [New mathematical models and software systems in coastal marine hydraulic engineering]. Sochi State University, 2014. (rus).
5. Holthuijsen, L.H. Waves in oceanic and coastal waters. Cambridge University Press, 2007.
6. SWAN team: Swan cycle III version 41.10AB, Scientific and Technical documentation. Delft University of Technology, Faculty of Civil Engineering and Geosciences, 2017.
7. Rogers, W.E., Kaihatu, J.M., Hsu, L., Jensen, R.E., Dykes, J.D., Holland, K.T. Forecasting and hindcasting waves with the SWAN model in the Southern California Bight. Coastal Engineering. 2007. 54(1). Pp. 1–15.
8. Lemkea, N., Fontourab, J.A.S., Callaria, D.F., Fonseca, D. Comparative study between modeled (SWAN) and measured (waverider buoy) wave data in Potos Lago–RS. Brazil Pan-American Journal of Aquatic Sciences. 2017. 12(1). Pp. 1–13.
9. Dietrich, J.C., Zijlema, M., Westerink, J.J., Holthuijsen, L.H., Dawson, C., Luettich, R.A., Jensen, R.E., Smith, J.M., Stelling, G.S., Stone, G.W. Modeling hurricane waves and storm surge using integrally-coupled, scalable computations. Coastal Engineering. 2011. 58(1). Pp. 45–65.
10. Dietrich, J.C., Tanaka, S., Westerink, J.J., Dawson, C.N., Luettich, R.A., Zijlema, M., Holthuijsen, L.H., Smith, J.M., Westerink, L.G., Westerink, H.J. Performance of the unstructured-mesh, SWAN+ ADCIRC model in computing hurricane waves and surge. Journal of Scientific Computing. 2012. 52(2). Pp. 468–497.
11. Aelbrecht, D. ARTEMIS 3.0: A finite element model for predicting wave agitation in coastal areas and harbours including dissipation. WIT Transactions on The Built Environment 30, 1997.
12. Berkhoff, J.C.W. Computation of combined refraction–diffraction. Proceedings of the 13th International Conference on Coastal Engineering. 1972. Pp. 471–490. Vancouver, Canada, ASCE.
13. Hervouet, J.M. TELEMAT, a hydroinformatic system. La Houille Blanche. 1999. 3-4. Pp. 21–28.
14. Open TELEMAT-MASCARET. Artemis\_documentation\_6.2, Validation case studies 1–10. 2017 [Online]. URL: <http://www.opentemac.org/index.php/manuals/summary/9-artemis/148-artemis-documentation-6-2>
15. Mike-21 EMS: Elliptic Mild Slope Wave Module, Scientific Documentation, DHI Denmark, 2017.
16. Madsen, P.A., Larsen, J. An Efficient Finite-Difference Approach to the Mild-Slope Equation. Coastal Engineering. 1987. 11. Pp. 329–351.
17. Guillou, N., Chapalain, G. Modeling penetration of tide-influenced waves in Le Havre harbor. Journal of Coastal Research. 2012. 28(4). Pp. 945–955.
18. Prodanovic, P. Numerical simulation of coastal climate at a harbour site in the Great Lakes. Proceedings of the 21st TELEMAT-MASCARET User Conference. 2014. 15–17.
19. Kantarzi, I., Zheleznyak, M. Laboratory and numerical study of waves in port water body. Civil Engineering Magazine. 2016. 6. Pp. 49–59.
20. Kantarzi, I., Zheleznyak, M., Demchenko, R., Dykyi, P., Kivva, S., Kolomiets, P., Sorokin, M. Modeling of Nonlinear Hydrodynamics of the Coastal Areas of the Black Sea by the Chain of the Proprietary and Open Source Models. EGU General Assembly Conference Abstracts. 2014. 16.
21. Zheleznyak, M., Kivva, S., Ievdin, I., Boyko, O., Kolomiets, P., Sorokin, M., Mikhalskyi, O., Gheorghiu, D. Hydrological dispersion module of JRODOS: renewed chain of the emergency response models of radionuclide dispersion through watersheds and rivers. Radioprotection. 2016. 51(HS 2). Pp. S129–S131.
22. DHI MIKE 21: 2D modelling of coast and sea. [Online]. URL: <https://www.mikepoweredbydhi.com/products/mike-21>.
23. Westerink, J.J., Luettich, R.A., Feyen, J.C., Atkinson, J.H., Dawson, C., Roberts, H.J., Powell, M.D., Dunion, J.P., Kubatko, E.J., Pourtaheri, H. A basin-to channel-scale unstructured grid hurricane storm surge model applied to southern Louisiana. Monthly weather review. 2008. 136(3). Pp. 833–864.
24. Kumar, V.S., Babu, V.R., Babu, M.T., Dhinakaran, G., Rajamanickam, G.V. Assessment of storm surge disaster potential for the Andaman Islands. Journal of Coastal Research. 2008. 24(sp2). Pp. 171–177.
25. Reed, C.W., Brown, M.E., Sánchez, A., Wu, W., Buttolph, A.M. The coastal modeling system flow model (CMS-Flow): Past and Present. Journal of Coastal Research. 2011. 1–6.
26. Kantarzi, I.G., Anshakov, A.S. Numerical analysis of the wave conditions of a port with a navigation channel (for the Sabetta-Utrenniy port as an example). Power Technology and Engineering. 2019. Vol. 52, No. 6. Pp. 648–651.
27. Egbert, G.D., Erofeeva, S.Y. Efficient Inverse Modeling of Barotropic Ocean Tides. J. Atmos. Oceanic Technol. 2002. 19. Pp. 183–204.
28. Kantarzi, I., Zheleznyak, M., Sorokin, M. Verification of Model Waves in the Port Area with Laboratory Measurements. Proc. of MEDCOAST 17, MEDCOAST Foundation. 2017. Vol. 2. Pp. 979–990.

## Contacts:

*Izmail Kantardgi, +79035337830; kantardgi@yandex.ru*

*Mark Zheleznyak, +818058441091; zheleznyak.m@gmail.com*

*Alexander Anshakov, +79165320804; anshakov.aleks.xx@yandex.ru*



DOI: 10.18720/MCE.87.7

## Численное моделирование нелинейных гидродинамических процессов береговой зоны

**И.Г. Кантаржи<sup>а\*</sup>, М.И. Железняк<sup>б</sup>, А.С. Аншаков<sup>а</sup>**

<sup>а</sup> Национальный исследовательский Московский государственный строительный университет, г. Москва, Россия

<sup>б</sup> Институт радиологии окружающей среды, Университет Фукусима, г. Фукусима, Япония

\* E-mail: [kantardgi@yandex.ru](mailto:kantardgi@yandex.ru)

**Ключевые слова:** численное моделирование, береговая гидротехника, цепочка численных моделей, интерактивная модель

**Аннотация.** Гидродинамические поля в береговой зоне образуются в результате нелинейного взаимодействия трансформирующихся волн различных временных масштабов и течений. Цепочку моделей необходимо использовать для моделирования ветровых волн, распространяющихся к берегу, волновых береговых течений, нелинейно-дисперсионной трансформации волн, дифракции волн при взаимодействии с береговыми и портовыми сооружениями, транспорта наносов и береговой эрозии. Цель статьи продемонстрировать обзор результатов применения цепочки моделей для определения волнового воздействия на сооружения проектируемого порта в Обской губе, Карское море, и обоснования требований к дальнейшему развитию нелинейных моделей для применения в береговой гидротехнике. Модели открытого доступа WaveWatch III и SWAN используются для моделирования статистики волн в выделенных районах береговой зоны с высоким разрешением для определения статистики экстремальных волн, подходящих к береговым конструкциям, в соответствии с нормативами.

### Литература

1. СП 38.13330.2012. Нагрузки и воздействия на гидротехнические сооружения (волновые, ледовые и от судов). Минрегионразвития РФ, 2012.
2. Zagriadskaya N.N., Kalinin, S.G. Numerical modeling of sea wave propagation in waterbodies // Hydraulic structures. 2007. No. 5.
3. Kabatchenko I.M., Matushevskiy, Reznikov M.V., Zaslavsky M.M. Modeling of wind and waves under the thermic cyclones in the G.V. Black Sea // Meteorology and Hydrology. 2001. No. 5. Pp. 61–71.
4. Макаров К.Н. Новые математические модели и программные комплексы в прибрежной морской гидротехнике. Сборник статей / под ред. К.Н. Макарова. Сочинский государственный университет, 2014.
5. Holthuijsen L.H. Waves in oceanic and coastal waters. Cambridge University Press, 2007.
6. SWAN team: Swan cycle III version 41.10AB, Scientific and Technical documentation. Delft University of Technology, Faculty of Civil Engineering and Geosciences, 2017.
7. Rogers W.E., Kaihatu J.M., Hsu L., Jensen R.E., Dykes J.D., Holland K.T. Forecasting and hindcasting waves with the SWAN model in the Southern California Bight // Coastal Engineering. 2007. 54(1). Pp. 1–15.
8. Lemkea N., Fontourab J.A.S., Callaria D.F. Fonseca D. Comparative study between modeled (SWAN) and measured (waverider buoy) wave data in Patos Lago–RS // Brazil Pan-American Journal of Aquatic Sciences. 2017. 12(1). Pp. 1–13.
9. Dietrich J.C., Zijlema M., Westerink J.J., Holthuijsen L.H., Dawson C., Luettich R.A., Jensen R.E., Smith J.M., Stelling G.S., Stone, G.W. Modeling hurricane waves and storm surge using integrally-coupled, scalable computations. Coastal Engineering. Engineering. 2011. 58(1). Pp. 45–65.
10. Dietrich J.C., Tanaka S., Westerink J.J., Dawson C.N., Luettich R.A., Zijlema, M., Holthuijsen, L.H., Smith, J.M., Westerink, L.G., Westerink, H.J. Performance of the unstructured-mesh, SWAN+ ADCIRC model in computing hurricane waves and surge. Journal of Scientific Computing. 2012. 52(2). Pp. 468–497.
11. Aelbrecht D. ARTEMIS 3.0: A finite element model for predicting wave agitation in coastal areas and harbours including dissipation. WIT Transactions on The Built Environment 30, 1997.
12. Berkhoff J.C.W. Computation of combined refraction–diffraction // Proceedings of the 13th International Conference on Coastal Engineering. 1972. Pp. 471–490. Vancouver, Canada, ASCE.
13. Hervouet J.M. TELEMAR, a hydroinformatic system. La Houille Blanche. 1999. 3-4. Pp. 21–28.
14. Open TELEMAR- MASCARET. Artemis\_documentation\_6.2, Validation case studies 1–10. 2017 [Электронный ресурс]. URL: <http://www.opentelemar.org/index.php/manuals/summary/9-artemis/148-artemis-documentation-6-2>
15. Mike-21 EMS: Elliptic Mild Slope Wave Module, Scientific Documentation, DHI Denmark, 2017.

16. Madsen P.A., Larsen J. An Efficient Finite-Difference Approach to the Mild-Slope Equation // Coastal Engineering. 1987. 11. Pp. 329–351.
17. Guillou N. Chapalain G. Modeling penetration of tide-influenced waves in Le Havre harbor // Journal of Coastal Research. 2012. 28(4). Pp. 945–955.
18. Prodanovic P. Numerical simulation of coastal climate at a harbour site in the Great Lakes // Proceedings of the 21st TELEMAC-MASCARET User Conference. 2014. 15–17.
19. Kantarzhi I., Zheleznyak M. Laboratory and numerical study of waves in port water body // Civil Engineering Magazine. 2016. 6. Pp. 49–59.
20. Kantarzhi I., Zheleznyak M., Demchenko R., Dykyi P., Kivva S., Kolomiets P., Sorokin M. Modeling of Nonlinear Hydrodynamics of the Coastal Areas of the Black Sea by the Chain of the Proprietary and Open Source Models // EGU General Assembly Conference Abstracts. 2014. 16.
21. Zheleznyak M., Kivva S., Ievdin I., Boyko O., Kolomiets P., Sorokin M., Mikhalskyi O., Gheorghiu D. Hydrological dispersion module of JRODOS: renewed chain of the emergency response models of radionuclide dispersion through watersheds and rivers // Radioprotection. 2016. 51(HS 2). Pp. S129–S131.
22. DHI MIKE 21: 2D modelling of coast and sea [Электронный ресурс]. URL: <https://www.mikepoweredbydhi.com/products/mike-21>.
23. Westerink J.J., Luettich R.A., Feyen J.C., Atkinson J.H., Dawson C., Roberts H.J., Powell M.D., Dunion J.P., Kubatko E.J., Pourtaheri H. A basin-to channel-scale unstructured grid hurricane storm surge model applied to southern Louisiana // Monthly weather review. 2008. 136(3). Pp. 833–864.
24. Kumar V.S., Babu V.R., Babu M.T., Dhinakaran G., Rajamanickam G.V. Assessment of storm surge disaster potential for the Andaman Islands // Journal of Coastal Research. 2008. 24(sp2). Pp. 171–177.
25. Reed C.W., Brown M.E., Sánchez A., Wu W., Buttolph A.M. The coastal modeling system flow model (CMS-Flow): Past and Present // Journal of Coastal Research. 2011. 1–6.
26. Kantarzhi I.G., Anshakov A.S. Numerical analysis of the wave conditions of a port with a navigation channel (for the Sabetta-Utrenniy port as an example) // Power Technology and Engineering. 2019. Vol. 52, No. 6. Pp. 648–651.
27. Egbert G.D., Erofeeva S.Y. Efficient Inverse Modeling of Barotropic Ocean Tides. J. Atmos // Oceanic Technol. 2002. 19. Pp. 183–204 [Электронный ресурс]. URL: <http://volkov.oce.orst.edu/tides/global.html>.
28. Kantarzhi I., Zheleznyak M., Sorokin M. Verification of Model Waves in the Port Area with Laboratory Measurements // Proc. of MEDCOAST 17, MEDCOAST Foundation. 2019. Vol. 2. Pp. 979–990.

#### **Контактные данные:**

*Измаил Григорьевич Кантаржи, +79035337830; эл. почта: kantardgi@yandex.ru*  
*Марк Иосифович Железняк, +818058441091; эл. почта: zheleznyak.m@gmail.com*  
*Александр Сергеевич Аншаков, +79165320804; эл. почта: anshakov.aleks.xx@yandex.ru*

© Кантаржи И.Г., Железняк М.И., Аншаков А.С., 2019





DOI: 10.18720/MCE.87.8

## The compatibility of deformation of the hollow-core slab with beams

**A.A. Koyankin<sup>a</sup>, V.M. Mitsov<sup>b</sup>, S.V. Deordiev<sup>a</sup>**

<sup>a</sup> Siberian Federal University, Krasnoyarsk, Russia.

<sup>b</sup> Novosibirsk state University of architecture and construction, Novosibirsk-8, Russia

\* E-mail: KoyankinAA@mail.ru

**Keywords:** building construction, reinforced concrete structures, precast-monolithic slab, beam, key joint, bearing capacity, stiffness, crack resistance

**Abstract.** The features of deformation of the key joint of a hollow core slab with precast-monolithic (monolithic) beam of a frame constructive system, including the Saret series. Experimental studies have been performed and numerical research of the stress-strain state of the slab and beam precast monolithic frame joint are carried out. Based on the obtained data, a comparative analysis of the results of numerical studies with experimental research has been performed, which showed a satisfactory convergence of results. As a result of the conducted researches new data concerning design features of the joint of the hollow slab with the beam have been obtained. Conclusions are given about the bearing capacity, stiffness and crack resistance of the structural solution of the joint node. The “weak points” associated with the design and operation of the joint of the slab with the beam are indicated. Technical solutions have been proposed to address the identified shortcomings, such as installation of the upper reinforcement in the hollow plate in longitudinal and transverse directions or exclusion of the key rigid joint to improve the structural reliability of the building.

### 1. Introduction

Precast-monolithic housing is widely used in modern world construction. The technology of precast-monolithic house-building has become the main one with most of the major developers, which confirms the ease of its application for the erection of buildings of various functional purposes operated in difficult climatic conditions [6, 7, 9, 15]. For example, quite popular became the versions of the floor disk with hollow plates, interfaced with precast-monolithic or monolithic beams, as well as the execution of the floor disk with the use of a prefabricated formwork plate and subsequent pouring with monolithic concrete [1, 3, 6, 7, 10, 15]. At the same time, if the floor disk panels, as a rule, are performed without prestressing, the beams are often prestressed. In addition, a variant of the overlap device with hollow blocks of lightweight concrete is known [2], stacked on precast concrete beams with subsequent filling with monolithic concrete.

Significant development of precast-monolithic reinforced concrete has lead to the necessity of research of peculiarities of stress-strain state of precast-monolithic structures. In this regard, researchers worldwide are actively pursuing those and other studies, allowing to assess both the specifics of individual design solutions and components, and systems in general, by the frames constructed in precast-monolithic design. In particular, the results of experimental studies of precast-monolithic slabs on bearing capacity, crack resistance and deformability are presented in [3, 13].

Full-scale tests of a fragment of a composite monolithic frame of the system with flat floors showed the reliability of the proposed system [4]. In the dissertation work [16], the issues of joint deformation of flat plates and hidden beams in prefabricated monolithic cages, which are quite common in the world construction practice, were studied. Partially ribbed precast monolithic overlap with cellular concrete blocks is presented in [19], where, in addition to the description of the design solution, analytical and numerical comparative calculations were performed that showed greater accuracy of the results when performing calculations in a software package based on the finite element method. However, the studies were performed in the linear formulation of the problem, which alienates their accuracy from the actual construction with the physical nonlinearity inherent in reinforced concrete. The author of [21] conducted studies of the fire resistance of prefabricated monolithic structures. Issues of joint deformation under various types of force effects were

Koyankin, A.A., Mitsov, V.M., Deordiev, S.V. The compatibility of deformation of the hollow-core slab with beams. Magazine of Civil Engineering. 2019. 87(3). Pp. 93–102. DOI: 10.18720/MCE.87.8

Коянкин А.А., Митасов В.М., Деордиев С.В. Совместность деформирования пустотной плиты с ригелем // Инженерно-строительный журнал. 2019. № 3(87). С. 93–102. DOI: 10.18720/MCE.87.8



This open access article is licensed under CC BY 4.0 (<https://creativecommons.org/licenses/by/4.0/>)

considered in [29, 32]. The issues of the stability of flat plates in the stage of progressive destruction were considered in [30], and the features of the deformation of the nodal joint of the overlap with the column at different frequencies of repetitive load were studied in [31]. In [22], numerical and experimental studies of beam bending elements with external sheet reinforcement were carried out.

The authors of this article in [33] numerically considered the distinctive features of the stress-strain state of a precast-monolithic flat frame, taking into account the phased installation, and in [1, 24] the authors of this article carried out experimental studies, that allowed to determine a sufficiently high stiffness of the nodal junction of the hollow plate and the beam, as well as the precast-monolithic beam with the column, while identifying certain design disadvantages.

In addition to experimental and numerical studies scholars offer various calculation methods of precast-monolithic structures both with the use of automated software, and performing «manual» calculations. The authors of [5, 8, 26] proposed an algorithm for performing the calculation of prefabricated monolithic structures in software packages based on the finite element method. In [5] the method of calculation of precast-monolithic beams with a keyless contact and load transfer to the precast part is given to take into account the influence of dowel effect of transverse reinforcement on the stress-strain state of the contact between the concrete and the design in general. At the same time, focusing on reducing the stiffness of the node junctions of the hollow plate with a composite monolithic beam by the time the connection carrying capacity is exhausted, the following variants of design schemes [7, 26] are proposed: with rigid joint of the plate with the beam – when calculating the 2nd group of limit states, and with a hinged joint – when calculating the 1st group. The author of publication [12] has proposed a method for calculation of normal cracks formation in precast-monolithic reinforced concrete bendable elements on the basis of the deformation model, where the criterion for the formation of cracks is the achievement of stretched zone of ultimate concrete tensile strength by the fiber. In addition, the set of performed calculations identified the necessity to consider positive effect of thrust strength on bearing capacity of disk panels.

In this case, the calculation of the carrying capacity of a normal section “by hand” is proposed to be performed either using the above section parameters (State Standard “Concrete and reinforced concrete structures”) or through fiber deformations of the fibers. The questions of the equations and calculation methods taking into account the nonlinear creep of three-layer plates and shallow shells are considered in [20].

Apart from that, engineers and scientists actively offer new constructive systems or suggestions for improvement of existing systems. For example, a technical solution of overlapping with the use of hollow slabs based on prefabricated monolithic or monolithic beams through keyway interfacing [11, 14] has become quite popular. In addition, solutions are proposed using prestressed reinforcement mounted directly on the construction site [25, 28]. Along with the design solutions, various aspects of the technology of precast-monolithic construction are considered [10], including the features of construction at negative temperatures [18].

As for the topic and motivation for these studies, a number of previously performed experimental and numerical contributions [1, 24] on the study of the features of deformation of individual nodular joints of precast-monolithic elements, has allowed to reveal a rather unpleasant fact – the formation of cracks in the place of the key interface of the hollow-core slab and precast-monolithic or monolithic beam with subsequent destruction of the hollow plate. In particular, the cracks were fixed in the upper non-reinforced zone of the slab both in its longitudinal direction at the transverse bending from the deformation of the beam [24] and in the transverse direction due to the longitudinal bending of the slab and sufficient rigidity of the key joint for the appearance of the bending moment in it. Along with this, a number of techniques [6] for the calculation of precast-monolithic overlap in software systems is suggested based on the finite element method, where the simulation of this coupling is performed by a hinge, which, of course, will not allow to take into account the occurrence of significant tensile stresses on the surface of the slab in reality.

It is the above mentioned results of experimental studies and observations that prompted the authors of this article to perform additional numerical studies prestressed – deformed state (the subject of research) of the key joint with of the hollow plate with precast monolithic beam (object of research), followed by their comparison with the previously obtained experimental data. The aim of performed numerical research was a detailed study features of joint deformation of the hollow slab and the beam at the key joint in the precast-monolithic frame.

On the basis of these and other related studies of different authors one can state the fact that the prefabricated monolithic frame is a quite reliable construction system, providing the requirements of existing building codes. Of course, some studies, particularly aimed at studying the local aspects, such as junctions of structural elements, identify some shortcomings present in various structural systems.

It is the above mentioned results of experimental studies and observations that have prompted the authors of this paper to perform additional numerical studies of the stress-strain state (the subject of the study) of the key joint of the hollow plate with the precast-monolithic beam (the object of study), with their subsequent comparison with the previously obtained experimental data. The aim of numerical studies was a more detailed research of the features of the joint deformation of the hollow plate and the beam at the key joint in the precast-monolithic frame. To achieve this goal, the following tasks were defined: assessment of the stress-strain state of the joint of

the hollow slab with the beam in terms of bearing capacity and deformability, as well as verification of the results of experimental studies. In this case, the object of research is the key joint of the hollow slab with precast-monolithic or monolithic beam, and the subject of research is its stress-strain state.

Experimental studies were carried out at the laboratory of testing building structures of Siberian Federal University [1]. In addition to "The Lira" software numerical studies of the stress-strain state of the slab – beam joint were carried out and comparison of the results with experimental data was performed.

## 2. Methods

Experimental study was carried out on three full-scale models of the joint of the hollow-core slab with the beam (in the laboratory of building construction tests based on Siberian Federal University of Krasnoyarsk). This type of the joint is quite common in the practice of building construction of precast-monolithic reinforced concrete [6, 7, 10]. Samples were divided into two types depending on the type of the beam. In particular, samples of type 1 (T-1 and T-2) included (Figure 1, a):

- fragments of the hollow-core slab with 1200×220(h) mm cross section and a length of 700 mm, reinforced by prestressed 7Ø12K1500 ropes and interfaced with a monolithic part of the beam through the device in the cavities of the slab, simultaneously with a monolithic part of the beam of concrete 1Ø10A400 reinforced dowels, having a variable length of 200...300 mm;

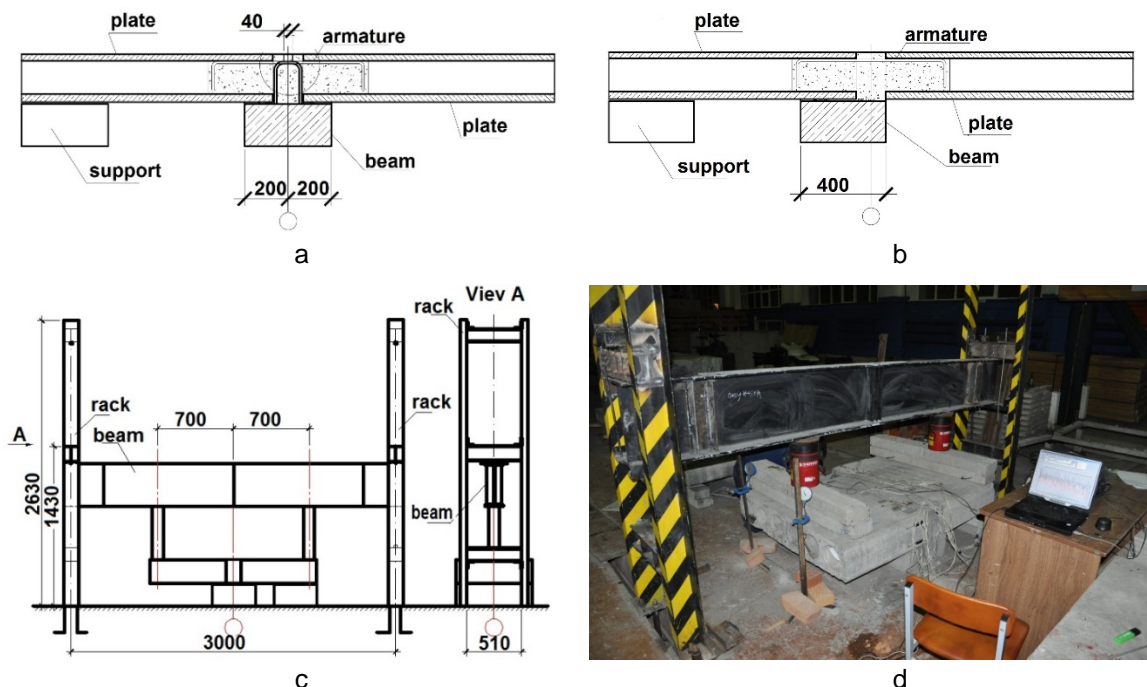
- precast-monolithic beams, including the precast part of 400×200(h) mm cross-section with a length of 1.200 mm, and a stacked on top monolithic part of 140×220(h) mm section performed simultaneously with the dowels in the hollow-core slabs.

Type 2 (T-3) sample was performed similarly to the samples T-1 and T-2, but with the difference that monolithic 140×220(h) mm cross-section beams, 1.200 mm long were used, performed simultaneously with the dowels in hollow slabs (Figure 1,b).

The load on the prototypes was applied top-down on the edges of the consoles with two jacks (Figure 1, c, d).

In conducting numeric research with «Lira» software, based on the method of finite elements, for the simulation of materials operation, physically nonlinear three-dimensional (concrete) and rod (reinforcement) elements were used. The nonlinearity of the work of materials was considered by two – and three-line diagrams of deformation inherent in [State Standard "Concrete and reinforced concrete structures"]. Loading was performed by step load with the step size of 4 kN. Similarly, experimentally calculation of the two type's calculation of the two types of numerical models of key joint of a hollow – core slab with a precast-monolithic beam (model B-1) and monolithic beam (model B-2) was performed. All models had real scale size, as in previously conducted experiments, at the same time, the P-1 numerical model is structurally consistent with the T-1 and T-2 experimental models, and P-2 is similar to T-3.

For the convenience of modeling the holes of hollow core slabs were converted from round to square, based on the equivalence of flexural rigidity.

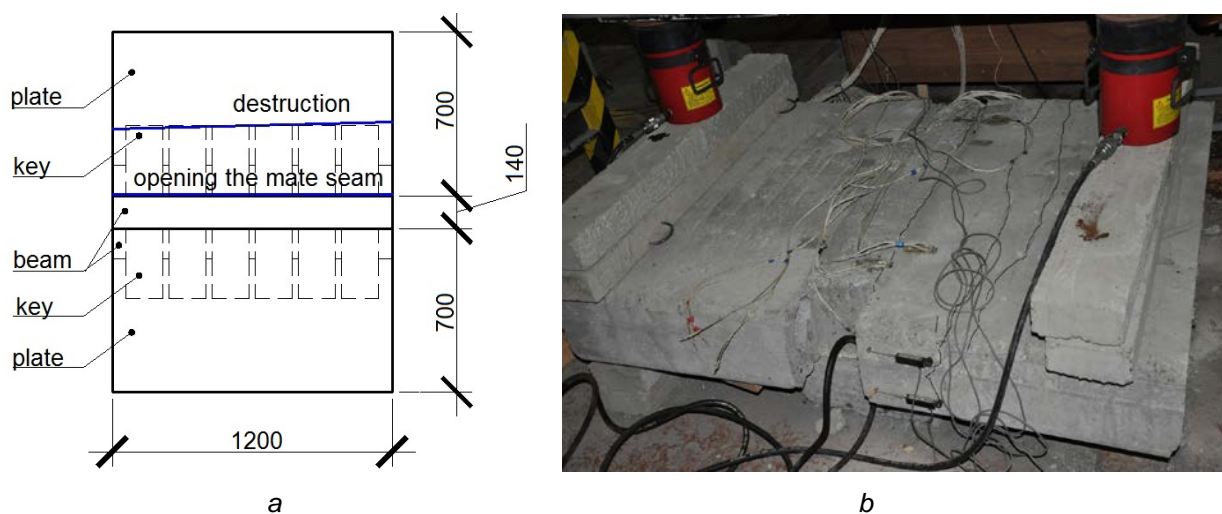


**Figure 1. Model of a key joint of the hollow-core slab: a – with precast-monolithic beam; b – with monolithic beam; c – experimental unit scheme; d – experimental unit photo.**

### 3. Results and Discussion

An important factor which has been determined during experimental studies is that in the real joint of the hollow – core slab with precast-monolithic or monolithic beam, arranged through reinforced concrete dowels, there arises a bending moment, which, in the case of improper design of the hollow core slab, leads to its destruction. This fact must be taken into account in the design of reinforced concrete structures. For example, at present, the joint of the slab with the beam is looked at as a hinged one [7], but, as studies have shown, it should be considered as rigid. The same ability of the key joint of the slab with the beam to perceive the bending moment is recorded in the numerical studies as well.

During all the experiments, the formation of cracks on the upper stretched surface of the hollow-core slab was recorded in the place where the monolithic dowel ends. It is at the moment of formation of this crack that the load-bearing capacity of the tested sample was exhausted (load 20...24 kN), which is due to the absence of any reinforcement of the upper zone of the slab. It should be mentioned that the destructive load of all experimental samples is approximately in the same range, namely, the models T-1 and T-3 collapsed at a load of 20 kN, and the model T-2 – at 24 kN. Any other cracks in the test plates were not recorded, except for the minor seam opening in the joint of precast and monolithic concrete occurring at the penultimate stage loading with loads of 12 to 16 kN. The picture of cracking is presented in Figure 2.



**Figure 2. Scheme of crack formation in experimental models.**

Numerical studies have fully confirmed the results obtained in experimental studies, namely, there is the same picture of structural failure, the formation of a critical crack is also recorded, leading to the rapid subsequent destruction in the hollow slab in the zone of the end of the concrete dowel, i.e., in the place where there is no reinforcement of the upper stretched part. Moreover, such a picture of destruction is observed both in the key joint with a precast monolithic beam (model B-1) and in the joint with a monolithic beam (B-2), which indicates the dependence of the form of destruction of the junction not so much on the type of the beam, but on the length of the dowel and the fact of its reinforcement (Figure 3). The breaking load was 20 kN in both models, which coincides well with the experimental values.

Thus, results of numeric and experimental studies have allowed to draw the conclusion that the junction have been confirmed that the junction of the hollow-core slab with precast-monolithic or monolithic beam, arranged through reinforced concrete dowels, has sufficient rigidity for the occurrence in it of the bending moment. This, in turn, leads to the need of its positioning as hard in the calculation of building structures.

The lack of top reinforcement in hollow-core slabs leads to the fact that the key joint of the hollow slab with the beam being hard, becomes a weak point in the whole structure of the overlap because of the inability of perception of the reference time at the end of monolithic reinforced monolithic dowels.

Thus, the need to implement certain constructive solutions to address this shortcoming is quite obvious. Such measures might possibly include: the device of the corresponding reinforcement of the upper zone of the hollow floor slab, or the refusal to use the reinforced dowel, making the junction of the slab and the beam rigid enough, that is, the implementation of the junction hinged.

The deflections, which were obtained in experimental studies of samples T-1 and T-2, had approximately the same uniform increase with load increasing (Figure 4). At the same time, it is quite expected that the deflections of the slab based on the precast-monolithic beam turned out to be significantly lower than the deflections of the slab joined with the monolithic beam.



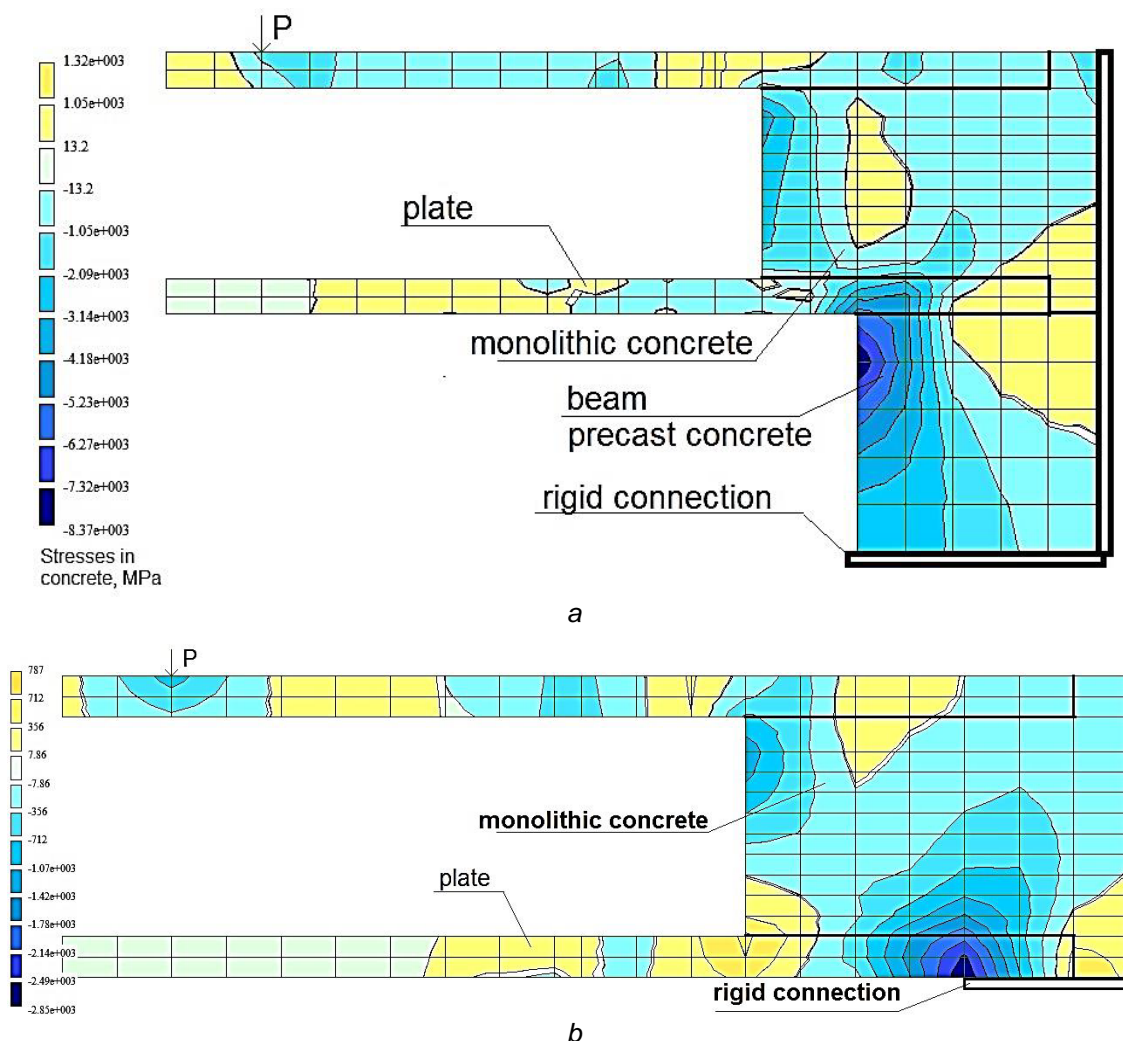


Figure 3. Stress-strain state of the butt joint (MPa): *a* – model B-1; *b* – model – B-2.

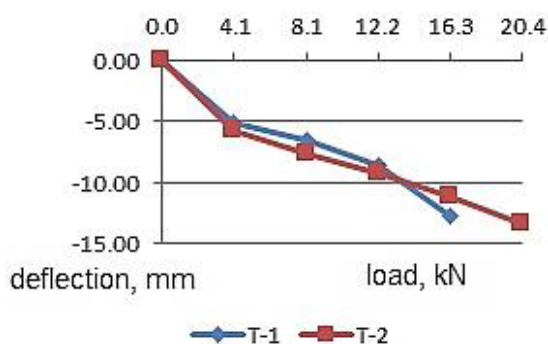


Figure 4. Deflection of experimental models.

The deflections obtained during the numerical research, have turned out to be smaller than previous experimental values; the discrepancy did not exceed 30 %. In particular, with the load of 12 kN the maximum value of the experimental deflection in the joints with precast-monolithic beam amounted to 9.3 mm, while in numerical calculations this value was 12.6 mm.

Numerical and experimental studies have made it possible to clearly and unambiguously note the fact that any destruction of the concrete dowel does not occur. In particular, there is no cut and destruction of the concrete body. In experimental studies no information on deformations and stresses in the concrete dowels was obtained, however, the nature of structural collapse and its subsequent inspection show the integrity of the concrete. Stress values in concrete dowels obtained in numerical studies did not exceed 4 MPa for compression and 0.5 MPa for tension, which confirms the results of the experimental data.

Data from strain gauges, which were obtained in experimental studies have shown that the yield strength in the dowels reinforcement did not exceed 30 MPa, indicating a significant reserve of reinforcement bars safety.



The stresses in the dowel reinforcement in numerical models, as well as in experimental models, have small values (less than 20 MPa), and absolutely cannot be the cause of the exhaustion of the bearing capacity of key joint of the hollow-core slab with the beam because of reaching the reinforcement yield strength.

Similarly to reinforcement, in compressed concrete on the lower surface of the slab, exhaustion of carrying capacity was not recorded both in experimental and numerical studies. In particular, during the experiment this conclusion was made on the basis of the fact that the relative deformations on the compressed (lower) surface of the hollow slab barely reached the value of 0.0003, while their limit values are 0.002.

In particular, during the experiment this conclusion was made on the basis that the limiting relative concrete compression deformations had not been reached. In addition, the data of strain gauges indicate that in the area of the dowels, directly in the place of the joint of the slab with the beam, deformation of the tensile concrete is also less than the ultimate limits of 0.00015 (the maximum value of deformation of concrete stretched in the experiment amounted to about 0.0006) up to the point of structural failure. All the obtained results were confirmed by visual inspection, in which there were no areas of destruction (fragmentation of concrete, cracks and other signs) in the above designated areas.

Thus, there is a significant margin of safety (at least 10x) of the dowel junction on the perception of bending moment in place of the direct dowel device that actually is not used.

In further numeric research compressive stresses of the concrete slab and the beam do not reach the limit values and do not exceed 9 MPa, while the tensile stress in the beam and in the hollow slab at the place of monolithic dowel arrangement also did not exceed the limit tensile stress, which proves the integrity of the structure in these points.

In addition, it should be pointed out that the studies of the joint of the slab key joint with the beam "in its pure form", i.e. when only the junction of the slab with the beam is considered, rather than the construction of the overlap as a whole, were not found. However, the authors of this article have previously conducted studies of a similar overlap disk and its fragments [1, 24], which did not fix the formation of any cracks in the end of the dowel, but this was due not to the reliability of the nodal coupling, but to a significant (much higher than the normative) reserve of the bearing capacity of the entire overlap disk and carrying out tests not before the destruction (which is quite justified), but only to control values of the load.

In addition, earlier studies [1, 24] of the core coupling of the beam with the column revealed another constructive "trouble", which is carried by the key joint, namely, the joint deformation of the hollow slab with the precast monolithic beam during its bending (in the reference zone) leads to the appearance of tensile stresses on the upper surface of the slab in the transverse (non-working) direction. Given the absence of horizontal reinforcement in the upper area of the slab in the longitudinal and transverse directions, the hollow-core slab forms normal cracks in the direction parallel to the voids. And this fact also requires the adoption of constructive measures to avoid the formation of cracks in the hollow slab in the transverse direction, for example, by introducing appropriate reinforcement in the hollow slab or excluding rigid joint work of the hollow slab and the beam.

## 4. Conclusions

Experimental and numerical study of the butt joint of the hollow-core slab with the beam has allowed to draw the following conclusions:

1. butt joint of the hollow- core slab with precast-monolithic and monolithic beam performed through the device of the monolithic dowel is not hinged and has sufficient rigidity for the perception of bending moment, which allowed the experimental model to take the load up to 24 kN during the experiment;
2. "a weak point" of the butt joint is the lack of top reinforcement in hollow-core overlap slabs, leading to brittle fracture of concrete of upper stretched zone of the slab at the end of monolithic reinforced dowels. The discrepancy between the numerical and experimental data for the bearing capacity was not more than 20 %;
3. to avoid the formation of cracks in the hollow slab and the subsequent structure destruction process might be possible, either by the introduction of the reinforcement (top longitudinal reinforcement) of the hollow-core slab, or by eliminating the hard joint work of the hollow plate and the beam (except the key joint);
4. the bearing capacity of the zone of the dowel location has a high bearing capacity both in the perception of the bending moment and in the perception of the transverse force (especially given the rather frequent location of the dowels). At the time of failure of the samples in the elements, determining the bearing capacity of the key joint (compressed concrete and key stretched reinforcement) voltage has not reached 10 % of the limit value;
5. features of deformation of the hollow-core slab with key joint connection in the holding area of the beam require horizontal reinforcement in the slab in the transverse direction.

6. abovementioned constructive decisions can increase significantly the bearing capacity of joint connection towards the perception of the bending moment. However, further investigations (experimental and numerical) focused on detailed study of bearing capacity of key joint for shear are required;

7. according to the analysis of previously performed works, the thrust strengths has a positive effect on strain-stress state of disk panel (increasing the strength of bearing capacity). However, this fact requires additional investigations, primarily, experimental, that will allow to consider thrust strength in calculations definitively.

## References

1. Koyankin, A.A., Mitsov, V.M. Eksperimentalnyye issledovaniya uzlov sopryazheniya pustotnoy plity so sborno-monolitnym i monolitnym rigelem [Experimental research of the joints of a hollow slab with precast-cast-in-place and monolithic girder]. Vestnik MGSU. 2015. No. 10. Pp. 32–39. (rus)
2. Vatin, N.I., Velichkin, V.Z., Kozinets, G.L., Korsun, V.I., Rybakov, V.A., Zhuvak, O.V. Precast-monolithic reinforced concrete beam-slabs technology with claydit blocks. Construction of Unique Buildings and Structures. 2018. 70(7). Pp. 43–59. (rus)
3. Smolyago, G.A., Kryuchkov, A.A., Dronova, A.V., Drokin, S.V. Rezultaty eksperimentalnykh issledovaniy nesushchey sposobnosti, treshchinostoykosti i deformativnosti sborno-monolitnykh i monolitnykh perekrytiy [Results of the experimental studies of bearing capacity, crack resistance and deformability of the precast-monolithic and monolithic overlaps]. Izvestiya Yugo-zapadnogo gosudarstvennogo universiteta. 2011. No. 5-2 (38). Pp. 105–109. (rus)
4. Karyakin, A.A., Sonin, S.A., Popp, P.V., Aliluyev, M.V. Ispytaniya naturnogo fragmenta sborno-monolitnogo karkasa sistemy «ARKOS» s ploskimi perekrytiyami [Test of the full-scale fragment of composite structure of the ARCOS system with flat-slab decks]. Vestnik Yuzhno-Uralskogo gosudarstvennogo universiteta. Seriya «Stroitelstvo i arkhitektura». 2009. No. 9. Pp. 16–20. (rus)
5. Sonin, S.A. Uchet nagelnogo effekta poperechnoy armatury v sborno-monolitnykh balkakh s besshponochnym kontaktom [Consideration of binders dowel effect in composite beams with a keyless contact]. Vestnik Yuzhno-Uralskogo gosudarstvennogo universiteta. Seriya: Stroitelstvo i arkhitektura. 2013. No. 1. Pp. 17–21. (rus)
6. Afanasyev, A.A. Tekhnologii vozvedeniya sborno-monolitnykh karkasnykh zdaniy pri otritsatelnykh temperaturakh [Technology of erection of precast frame buildings at negative temperatures]. Vestnik MGSU. 2012. No. 4. Pp. 175–180. (rus)
7. Selyayev, V.P., Tsyganov, V.V., Utkin, I.Yu. Kombinirovannyye sborno-monolitnyye perekrytiya na osnove predvaritelno napryazhennykh zhelezobetonnykh balok bezopalubochnogo formovaniya [Combined prefabricated monolithic slabs on the basis of non-formwork prestressed reinforced concrete beams]. Regionalnaya arkhitektura i stroitelstvo. 2012. No. 3. Pp. 5–11. (rus)
8. Sursanov, D.N., Sazonova, S.A., Ponomarev, A.B. Analiz rezultatov naturnykh ispytaniy shponochnogo soyedineniya na srez [Analysis of concrete dowel full-scale shearing tests]. Vestnik PNIPU. Stroitelstvo i arkhitektura. 2015. No. 2. Pp. 7–23. [rus]
9. Ogbul, E.K. Perspektivnyye konstruktivnyye resheniya sborno-monolitnogo perekrytiya iz fibrozhelezobetona [Perspective structural solutions in fiber-reinforced concrete cast-in-place and precast floors]. Vestnik grazhdanskikh inzhenerov. 2014. No. 5(46). Pp. 33–38. (rus)
10. Koyankin, A., Mitsov, V. Assessment of structural reliability of precast concrete buildings. MATEC Web of Conferences. IV International Young Researchers Conference «Youth, Science, Solutions: Ideas and Prospects» (YSSIP-2017). 2018. Vol. 143.
11. Varlamov, A.A., Pivovarov, V.S., Pivovarova, O.V. Variant shponochnogo styka sborno-monolitnogo perekrytiya [Variant of keyed joint of precast-monolithic slab]. Arkhitektura. Stroitelstvo. Obrazovaniye. 2014. No. 1. Pp. 249–255. (rus)
12. Smolyago Ye.G. Raschet po obrazovaniyu normalnykh treshchin v sborno-monolitnykh zhelezobetonnykh predvaritelno napryazhennykh izgibayemykh elementakh [Calculation cracked formation in the composite prestressed reinforced concrete bending elements]. Stroitelstvo i rekonstruktsiya. 2010. No. 2(28). Pp. 39–45. (rus)
13. Varlamov, A.A., Nikitina, O.V. Analiz eksperimentalnykh dannykh issledovaniya raboty sborno-monolitnogo perekrytiya s novym variantom shponochnogo styka [Analysis of experimental research data of precast slabs operation with a new variant of splined joint]. Vestnik Yuzhno-Uralskogo gosudarstvennogo universiteta. Seriya: Stroitelstvo i arkhitektura. 2015. No. 3. Pp. 20–25. (rus)
14. Koyankin, A.A., Mitsov, V.M. Karkas sborno-monolitnogo zdaniya i osobennosti yego raboty na raznykh zhiznennykh tsiklakh [Cast-in-place building frame and its features at separate life cycles]. Vestnik MGSU. 2015. No. 9. Pp. 28–35. (rus)
15. Taran, V.V., Takhtay, D.A., Nedorezov, A.V. Osobennosti konstruktivnykh resheniy vozvedeniya mnogoetazhnykh zdaniy po sisteme «ARKOS» [Peculiarities of design solutions for construction of multistory buildings according to the "ARCOS"]. Vestnik Donbasskoy natsionalnoy akademii stroitelstva i arkhitektury. 2009. No. 6. Pp. 89–92. (rus)
16. Nikonorov, R.M. Sovmestnaya soprotivlyayemost, deformativnost zhelezobetonnykh elementov perekrytiya sborno-monolitnykh karkasov s ploskimi plitami i skrytymi rigelyami [Joint resistance, deformability of reinforced concrete elements of overlaps of precast monolithic frames with flat slabs and concealed beams]. Cand. Diss. Moskva, 2008. 219 p. (rus)
17. Shmelev, G.D., Fomenko, N.A., Gavrilova, V.N. Sravnitelnyy analiz sovremennykh sistem vozvedeniya zdaniy grazhdanskogo naznacheniya [Analysis of the efficiency of management of multi-quarter houses by the example]. Zhilishchnoye khozyaystvo i kommunalnaya infrastruktura. 2018. No. 3(6). Pp. 9–19. (rus)
18. Afanas'ev, A.A. Tekhnologii vozvedeniya sborno-monolitnykh karkasnykh zdaniy pri otritsatelnykh temperaturakh [Technology of erection of precast frame buildings at negative temperatures]. Vestnik MGSU. 2012. No. 4. Pp. 175–180. (rus)
19. Parashchenko, N.A., Gorshkov, A.S., Vatin, N.I. Chastichno-rebristyye sborno-monolitnyye perekrytiya s yacheistobetonnyimi blokami [Partially rib precast and cast-in-situ floors with cellular-concrete blocks]. Magazine of Civil Engineering. 2011. 24(6). Pp. 50–55. (rus) DOI: 10.5862/MCE.24.7
20. Chepurnenko, A.S. Stress-strain state of three-layered shallow shells under conditions of nonlinear creep. Magazine of Civil Engineering. 2017. 76(8). Pp. 156–168. doi: 10.18720/MCE.76.14
21. Nedviga, E., Beresneva, N., Gravit, M., Blagodatskaya, A. Fire Resistance of Prefabricated Monolithic Reinforced Concrete Slabs of «Marko» Technology. Advances in Intelligent Systems and Computing. 2018. 692. Pp. 739–749.
22. Medvedev, V.N., Semeniuk, S.D. Durability and deformability of braced bending elements with external sheet reinforcement. Magazine of Civil Engineering. 2016. 63(3). Pp. 3–15. DOI: 10.5862/MCE.63.1
23. Koyankin, A.A., Mitsov, V.M. Eksperimentalnyye issledovaniya raboty stykovogo soyedineniya rigelya s kolonnoy v sborno-monolitnom perekrytii [Experimental study of the operation of the bolt joint of a bearer with a column in precast-monolithic ceiling]. Vestnik MGSU. 2015. No. 5. Pp. 27–35. (rus)
24. Teplova, Zh.S., Vinogradova, N.A. Sbornomonolitnyye perekrytiya sistemy «MARKO» [Combined and monolithic overlappings of "MARKO" system]. Stroitelstvo unikalnykh zdaniy i sooruzheniy. 2015. No. 8. Pp. 48–59. (rus)

25. Abramyan, S.G., Gnatyuk, D.V. Sbornyye i sborno-monolitnyye karkasnyye sistemy vysotnykh zdaniy s ploskimi plitami perekrytiya [Precast and cast-in-situ frame systems of high-rise buildings with flat slabs]. [Online]. System requirements: AdobeAcrobatReader. URL: <http://naukovedenie.ru/PDF/83TVN117.pdf> (date of application: 06.04.2017). (rus)
26. Koval, P.M., Fal, A.Ye., Marchuk, S.M. Osobennosti proyektirovaniya sborno-monolitnykh proletrykh stroyeniy mostov [Features of designing precast-monolithic bridge spans]. Visnik Dnipropetrovskogo natsionalnogo universitetu zaliznichnogo transportu im. Akademika V. Lazaryana. 2010. No. 33. Pp. 127–130. (ua)
27. Garrido, M. et al. Creep behaviour of sandwich panels with rigid polyurethane foam core and glass-fibre reinforced polymer faces: Experimental tests and analytical modeling. Journal of Composite Materials. 2014. Vol. 48. No. 18. Pp. 2237–2249.
28. Breccolotti, M., Gentile, S., Tommasini, M., Materazzi, A.L., Bonfigli, M.F., Pasqualini, B., Colone, V., Giancesini, M. Beam-column joints in continuous RC frames: Comparison between cast-in-situ and precast solutions. Engineering Structures. 2016. No. 127. Pp. 129–144.
29. Olmati, P., Sagaseta, J., Cormie, D., Jones, AEK. Simplified reliability analysis of punching in reinforced concrete flat slab buildings under accidental actions. Engineering Structures. 2017. No. 130. Pp. 83–98.
30. Qian, K., Li, B. Resilience of Flat Slab Structures in Different Phases of Progressive Collapse. ACI Structural Journal. 2016. No. 113. Pp. 537–548.
31. Drakatos, I.S., Muttoni, A., Beyer, K. Internal slab-column connections under monotonic and cyclic imposed rotations. Engineering Structures. 2016. No. 123. Pp. 501–516.
32. Micallef, K., Sagaseta, J., Fernandez Ruiz, M., Muttoni, A. Assessing Punching Shear Failure in Reinforced Concrete Flat Slabs Subjected to Localized Impact Loading. International Journal of Impact Engineering. 2014. No. 71. Pp. 17–33.
33. Koyankin, A.A., Mitsov, V.M. Stress-strain state of precast and cast-in place building. Magazine of Civil Engineering. 2017. No. 6(74). Pp. 175–184. doi: 10.18720/MCE.74.14

### **Contacts:**

*Alexander Koyankin, +73912934711; KoyankinAA@mail.ru*

*Valery Mitsov, +79139122364; mitassovv@mail.ru*

*Sergey Deordiev, +73912062692; SDeordiev@sfu-kras.ru*

© Koyankin, A.A., Mitsov, V.M., Deordiev, S.V., 2019



DOI: 10.18720/MCE.87.8

## Совместность деформирования пустотной плиты с ригелем

**А.А. Коянкин<sup>а</sup>, В.М. Митасов<sup>б</sup>, С.В. Деордиев<sup>а</sup>**

*Сибирский федеральный университет, г. Красноярск, Россия*

*Новосибирский государственный архитектурно-строительный университет, г. Новосибирск-8, Россия*

\* E-mail: [KoyankinAA@mail.ru](mailto:KoyankinAA@mail.ru)

**Ключевые слова:** строительные конструкции, железобетонные конструкции, сборно-монолитное перекрытие, ригель, шпоночное соединение, несущая способность, жёсткость, трещиностойкость

**Аннотация.** Рассмотрены особенности деформирования узлового шпоночного сопряжения пустотной плиты перекрытия со сборно-монолитным (монолитным) ригелем каркасной конструктивной системы, применяемой для возведения многих зданий, в том числе зданий серии Saret. Выполнены экспериментальные исследования, а также проведены численные исследования напряжённо-деформированного состояния узла сопряжения плиты и ригеля сборно-монолитного каркаса. На основании полученных данных выполнен сопоставительный анализ результатов численных исследований с экспериментальными данными, который показал удовлетворительную сходимость результатов. В результате проведённых исследований получены новые данные касающиеся конструктивных особенностей стыкового соединения пустотной плиты с ригелем. Даны заключения о несущей способности, жёсткости и трещиностойкости конструктивного решения узла сопряжения. Обозначены «слабые места» связанные с проектированием и эксплуатацией узлового соединения плиты с ригелем. Предложены технические решения по устранению выявленных недостатков, такие как установка в пустотной плите верхней арматуры в продольном и поперечном направлениях или исключение шпоночного жёсткого соединения, позволяющие повысить конструктивную надёжность здания.

### Литература

1. Коянкин А.А., Митасов В.М. Экспериментальные исследования узлов сопряжения пустотной плиты со сборно-монолитным и монолитным ригелем // Вестник МГСУ. 2015. № 10. С. 32–39.
2. Ватин Н.И., Величкин В.З., Козинец Г.Л., Корсун В.И., Рыбаков В.А., Жувак О.В. Технология сборно-монолитных балочных железобетонных перекрытий с керамзитобетонными блоками // Строительство уникальных зданий и сооружений. 2018. № 7 (70). С. 43–59.
3. Смоляго Г.А., Крючков А.А., Дронова А.В., Дрокин С.В. Результаты экспериментальных исследований несущей способности, трещиностойкости и деформативности сборно-монолитных и монолитных перекрытий // Известия Юго-западного государственного университета. 2011. № 5-2 (38). С. 105–109.
4. Карякин А.А., Сонин С.А., Попп П.В., Алилуев М.В. Испытания натурного фрагмента сборно-монолитного каркаса системы «АРКОС» с плоскими перекрытиями // Вестник Южно-Уральского государственного университета. Серия «Строительство и архитектура». 2009. № 9. С. 16–20.
5. Сонин С.А. Учёт нагельного эффекта поперечной арматуры в сборно-монолитных балках с бесшпоночным контактом // Вестник Южно-Уральского государственного университета. Серия: Строительство и архитектура. 2013. № 1. С. 17–21.
6. Афанасьев А.А. Технологии возведения сборно-монолитных каркасных зданий при отрицательных температурах // Вестник МГСУ. 2012. № 4. С. 175–180.
7. Селяев В.П., Цыганов В.В., Уткин И.Ю. Комбинированные сборно-монолитные перекрытия на основе предварительно напряжённых железобетонных балок безопалубочного формования // Региональная архитектура и строительство. 2012. № 3. С. 5–11.
8. Сурсанов Д.Н., Сазонова С.А., Пономарёв А.Б. Анализ результатов натурных испытаний шпоночного соединения на срез // Вестник ПНИПУ. Строительство и архитектура. 2015. № 2. С. 7–23.
9. Опбул Э.К. Перспективные конструктивные решения сборно-монолитного перекрытия из фиброжелезобетона // Вестник гражданских инженеров. 2014. № 5(46). С. 33–38.
10. Koyankin A., Mitsov V. Assessment of structural reliability of precast concrete buildings. MATEC Web of Conferences. IV International Young Researchers Conference «Youth, Science, Solutions: Ideas and Prospects» (YSSIP-2017). 2018. Vol. 143.
11. Варламов А.А., Пивоваров В.С., Пивоварова О.В. Вариант шпоночного стыка сборно-монолитного перекрытия // Архитектура. Строительство. Образование. 2014. № 1. С. 249–255.
12. Смоляго Е.Г. Расчёт по образованию нормальных трещин в сборно-монолитных железобетонных предварительно напряжённых изгибаемых элементах // Строительство и реконструкция. 2010. № 2(28). С. 39–45.

13. Варламов А.А., Никитина О.В. Анализ экспериментальных данных исследования работы сборно-монолитного перекрытия с новым вариантом шпоночного стыка // Вестник Южно-Уральского государственного университета. Серия: Строительство и архитектура. 2015. № 3. С. 20–25.
14. Коянкин А.А., Митасов В.М. Каркас сборно-монолитного здания и особенности его работы на разных жизненных циклах // Вестник МГСУ. 2015. № 9. С. 28–35.
15. Таран В.В., Тахтай Д.А., Недорезов А.В. Особенности конструктивных решений возведения многоэтажных зданий по системе «АРКОС» // Вестник Донбасской национальной академии строительства и архитектуры. 2009. № 6. С. 89–92.
16. Никоноров Р.М. Совместная сопротивляемость, деформативность железобетонных элементов перекрытия сборно-монолитных каркасов с плоскими плитами и скрытыми ригелями: дис. ... канд. техн. наук. М., 2008. 219 с.
17. Шмелёв Г.Д., Фоменко Н.А., Гаврилова В.Н. Сравнительный анализ современных систем возведения зданий гражданского назначения // Жилищное хозяйство и коммунальная инфраструктура. 2018. № 3(6). С. 9–19.
18. Афанасьев А.А. Технологии возведения сборно-монолитных каркасных зданий при отрицательных температурах // Вестник МГСУ. 2012. № 4. С. 175–180.
19. Парашенко Н.А., Горшков А.С., Ватин Н.И. Частично-ребристые сборно-монолитные перекрытия с ячеистобетонными блоками // Инженерно-строительный журнал. 2011. № 6. С. 50–55. DOI: 10.5862/MCE.24.7
20. Чепурненко А.С. Расчет трехслойных пологих оболочек с учетом нелинейной ползучести // Инженерно-строительный журнал. 2017. № 8(76). С. 156–168. doi: 10.18720/MCE.76.14
21. Nedviga, E., Beresneva, N., Gravit, M., Blagodatskaya, A. Fire Resistance of Prefabricated Monolithic Reinforced Concrete Slabs of «Marko» Technology. Advances in Intelligent Systems and Computing. 2018. 692. Pp. 739–749.
22. Медведев В.Н., Семенюк С.Д. Прочность и деформативность балочных изгибаемых элементов с внешним листовым армированием // Инженерно-строительный журнал. 2016. № 3(63). С. 3–15. DOI: 10.5862/MCE.63.1
23. Коянкин А.А., Митасов В.М. Экспериментальные исследования работы стыкового соединения ригеля с колонной в сборно-монолитном перекрытии // Вестник МГСУ. 2015. № 5. С. 27–35.
24. Теплова Ж.С., Виноградова Н.А. Сборно-монолитные перекрытия системы «МАРКО» // Строительство уникальных зданий и сооружений. 2015. № 8. С. 48–59.
25. Абрамян С.Г., Гнатюк Д.В. Сборные и сборно-монолитные каркасные системы высотных зданий с плоскими плитами перекрытия [Электронный ресурс]. Систем. требования: AdobeAcrobatReader. URL: <http://naukovedenie.ru/PDF/83TVN117.pdf> (дата обращения: 06.04.2017).
26. Коваль П.М., Фаль А.Е., Марчук С.М. Особенности проектирования сборно-монолитных пролётных строений мостов // Вісник Дніпропетровського національного університету залізничного транспорту ім. Академіка В. Лазаряна. 2010. № 33. С. 127–130.
27. Garrido M. et al. Creep behaviour of sandwich panels with rigid polyurethane foam core and glass-fibre reinforced polymer faces: Experimental tests and analytical modeling // Journal of Composite Materials. 2014. Vol. 48. No. 18. Pp. 2237–2249.
28. Breccolotti M., Gentile S., Tommasini M., Materazzi A.L., Bonfigli M.F., Pasqualini B., Colone V., Ganesini M. Beam-column joints in continuous RC frames: Comparison between cast-in-situ and precast solutions // Engineering Structures. 2016. No. 127. Pp. 129–144.
29. Olmati P., Sagaseta J., Cormie D., Jones AEK. Simplified reliability analysis of punching in reinforced concrete flat slab buildings under accidental actions // Engineering Structures. 2017. No. 130. Pp. 83–98.
30. Qian K., Li B. Resilience of Flat Slab Structures in Different Phases of Progressive Collapse // ACI Structural Journal. 2016. No. 113. Pp. 537–548.
31. Drakatos I.S., Muttoni A., Beyer K. Internal slab-column connections under monotonic and cyclic imposed rotations // Engineering Structures. 2016. No. 123. Pp. 501–516.
32. Micallef K., Sagaseta J., Fernandez Ruiz M., Muttoni A. Assessing Punching Shear Failure in Reinforced Concrete Flat Slabs Subjected to Localized Impact Loading // International Journal of Impact Engineering. 2014. No. 71. Pp. 17–33.
33. Коянкин А.А., Митасов В.М. Напряжённо-деформированное состояние сборно-монолитного здания // Инженерно-строительный журнал. 2017. № 6(74). С. 175–184. doi: 10.18720/MCE.74.14

#### **Контактные данные:**

*Александр Александрович Коянкин, +73912934711; эл. почта: KoyankinAA@mail.ru*

*Валерий Михайлович Митасов, +79139122364; эл. почта: mitassovv@mail.ru*

*Сергей Владимирович Деордиев, +73912062692; эл. почта: SDeordiev@sfu-kras.ru*





DOI: 10.18720/MCE.87.9

## Efficacy of digital elevation and Nash models in runoff forecast

**D.V. Kozlov\*, A.A. Ghebrehiwot,**

*National Research Moscow State Civil Engineering University, Moscow, Russia*

*\* E-mail: kozlovdv@mail.ru*

**Keywords:** digital elevation model, QGIS algorithm, GIUH-Nash model, direct surface runoff, hydrograph, catchment, river network, runoff forecast.

**Abstract.** Digital elevation models (DEMs) are extensively used in hydrological modelling and deriving the geomorphological properties of catchments. Recently, hydrologists have shown interest in researching the effects of DEMs from different sources on simulated outputs. As part of these efforts, this study aimed at evaluating the effects of DEM and algorithm selection on geomorphologic instantaneous unit hydrographs (GIUH)-Nash model based direct surface runoff predictions from ungauged Debarwa river catchment in Eritrea. Four open-source DEMs and two quantum geographic information system (QGIS) algorithms (GRASS and SAGA) were applied and corresponding outputs were evaluated using five observed events. The two algorithms resulted in drainage networks of similar stream orders but different geomorphologic characteristics such as stream ratios. The subjective and objective goodness of fit results indicated that the performance of the model based on SAGA was unsatisfactory whereas that of GRASS algorithm-based GIUH-Nash model was acceptable for all the DEM-scenarios irrespective of their sources and resolutions. The study concluded that DEM in the calculation of flow hydrographs for the conditions of the Debarwa catchment selection has little impact on the GIUH-Nash model based direct surface runoff predictions and can be used indiscriminately. But, great care should be taken while selecting stream network generating algorithms, especially for catchments whose outlets are located near the confluence of two major rivers.

### 1. Introduction

The State of Eritrea is located on east coast of Africa between 12°22' and 18°02' N latitude and 36°26' and 43°13' E longitude and includes the Dahlak archipelago and other islands along the Red Sea coast. It is bordered by Sudan in the north and west, Ethiopia in the south, Djibouti in the south-east and the Red Sea in the north and north-east. It covers an area of 124, 320 km<sup>2</sup> comprising high plateaus and plains. Prior to its independence in 1993, Eritrea was a colony of Turkey, Egypt, Italy, British and Ethiopia.

Eritrea lies not only in Sudano-Sahelian region of Africa, which is predominantly characterized by arid and semi-arid climate and limited water resources [1], but also considered as one of the hottest countries on earth experiencing recurrent droughts. Despite the lack of adequate and reliable information on water resources, there are indications of presence of severe water shortages. The flows through the major rivers are highly seasonal with the exception of Setit River. Setit, the only perennial river that forms the border with Ethiopia, could not be fully utilized for major national development projects. Ground water has been the main water source for various uses supplemented by surface waters stored in dams and ponds. Climate ranges from hot and arid near the Red Sea to temperate sub-humid in the eastern highlands. Mean temperature varies between the agro-ecological zones, ranging from 18 °C in the highlands to 35 °C in the lowlands. Rainfall is torrential, of high intensity, short duration and is characterized by extreme spatio-temporal variability; less than 50 mm to over 1,000 mm falling mainly during the months of June to September. As a result of the topographically ragged nature of the highlands, thin soil formations and completely deforested terrains, most of the runoff turns into violent flash floods. Annual average precipitation is 384 mm [1]. Annual evapotranspiration rates range from 1,900 mm in the northern Red Sea coastal basin and plains, to 1,700 to 2,000 mm in the northern highlands and 8,000 mm in the Gash-Barka region [2].

Kozlov, D.V., Ghebrehiwot, A.A. Efficacy of digital elevation and Nash models in runoff forecast. Magazine of Civil Engineering. 2019. 87(3). Pp. 103–122. DOI: 10.18720/MCE.87.9.

Козлов Д.В., Гебрехивот А.А. Эффективность цифровых моделей рельефа и моделей Нэша в прогнозировании стока // Инженерно-строительный журнал. 2019. № 3(87). С. 103–122. DOI: 10.18720/MCE.87.9



This open access article is licensed under CC BY 4.0 (<https://creativecommons.org/licenses/by/4.0/>)

Studies on the current situation of water resources in Eritrea [3] indicate that the government has made significant progress in the development of water resources through the construction of reservoirs, diversion structures and groundwater exploration for various water uses. Along with the artificial reservoirs with varying sizes that were constructed since independence, recently completed or still under construction such as Gheret, Kerkebet, Fanco, Ghergera, Gahtelay and Adi-Halo are some among others. Despite these promising endeavors, problems linked to the development and management of water resources have yet remained to be at the center stage of the government agenda due to manifold reasons. Critical analyses on the current status and use of water resources [3] reveal the absence of detailed studies on groundwater and surface water potentials. Moreover, modern knowledge about the water resources and hydrological information, which is crucial for the development of water management practices, are fragmented and in their initial stages of development.

Hydrometeorological observations on a regular basis began during the Italian colonial period. Nonetheless, when Eritrea gained independence, the water sector of the country was completely destroyed as a result of successive 30 years military action. Thus, the reasons for the poor quality of hydrometeorological information available today are not only successive breaks in the time series of observations, but also unreliability of the measurements. In recent years, an increasing trend in the establishment of hydrometeorological stations has been observed. However, their distribution and quality often do not meet the current national hydrometeorological observation network requirements. In addition, due to insufficient budget funding and poor coordination among the various executive authorities, the vast majority of existing stations lack proper operational scrutiny. This problem along with the complete absence of historical hydrological and meteorological data, in many cases, to date has been a major obstacle to the planning and development of projects for utilizing Eritrea's water resources [4, 5]. Under these circumstances along with structural and technical failures in the systems operation, it is difficult to achieve intended goals of water resources management projects. In one way or the other, these failures seem to be allied, among other things, to the use of improper assessment of river flow prediction approaches that do not consider the unique characteristics of the area under consideration. For example, the partial or complete failures of recently constructed diversion structures in the western lowlands of Eritrea justify this fact. At present, with the exception of limited and localized research developments [4, 5], there are no methods specifically developed for river basins characterized by the lack of hydrological observations. Hence, accurate and reliable approaches of river flow prediction for catchments under consideration can be either established or identified only on the basis of extensive applied research.

River flow modelling has become an important tool for planning and management of water management systems and facilities as well as the development of river forecasts and dissemination of warnings, for example, floods. The term "hydrological system modelling" includes time series analysis and stochastic modelling, which focuses on reproducing the statistical characteristics of the hydrological variable of a time series. To date, many models of river flow have been developed on such bases [6, 7]. Prediction of floods in hydrologically unexplored and poorly studied catchments, taking into account the unreliability of hydrometeorological information, has recently become one of the main directions of modern hydrological research. The transformation of the flood, during its passage through reservoirs and river beds can be determined by various methods, for example, hydrodynamic and hydrological.

According to the latter, in order to determine the arrival time and spreading of the flood wave formed as a result of heavy precipitation on the surface of the catchment, it is necessary to estimate the flow of water through the river system. For this purpose, a unit hydrograph (UH) theory [8] is usually constructed, which characterizes the time distribution of water flowing from the catchment [9]. In most practical problems, the generally accepted hydrological method of flood forecasting using UH theory cannot be implemented because it requires information about rainfall and runoff. Under such circumstances, different regionalized techniques are applied to develop synthetic unit hydrograph. Though it has various limitations, empirical equations require regional validity, which relate the salient hydrograph characteristics to basin characteristics. Moreover, it is strictly site specific, and cannot be considered as universal [10]. Kumar [11] pointed out limitations of regionalization: requires a large amount of rainfall-runoff data, inevitable heterogeneity of hydrological behavior of adjacent gauged catchments and periodical adjustment of model parameters that take care of unforeseen impacts of land use and climate change. The rational method based on the concept of hydrological zoning, according to Singh [7] is not only applicable for solving problems of water related design but also fails to generate complete information about river flow.

Dooge [12] developed a more complete conceptual model for the calculation of UH and showed that for rivers where there are no available hydrological observations, it is advisable to establish generalized UH. But, since the equation of UH was not easily solvable for complex problems, various simplifications were proposed. For example, the procedure for constructing a UH developed by Snyder [13] is based on the analysis of a large number of basins and single hydrographs in order to obtain a relationship between the shape of a UH and the physical and geographical characteristics of the catchment. In Snyder's approach, the coefficients of the equation associated with the physical and geographical characteristics of the basin vary significantly sometimes over a range of 10 times [14] leading to inaccurate estimates of floods. According to Pilgrim [14],

due to the empirical nature of Snyder's approach, its application should be limited to the region for which these coefficients were obtained.

To overcome the difficulties associated to the dependence of UH on the effective rainfall duration, instantaneous unit hydrograph (IUH) [7] that considers vanishingly small duration has been introduced since long time back. The IUH is the unit impulse response or characteristic response of a catchment. It is widely applied because it can reflect the characteristic of valley flow concentration [15] and much more important information about the basin characteristics can also be extracted. Numerous hydrological conceptual models have been proposed to develop IUH. These models consider a catchment as a system that converts the input effective rainfall into a flood. For example, a conceptual cascade of linear reservoirs was proposed [12, 16, 17] to simulate the process of transformation of precipitation into runoff. Nash [18] developed a general theory of the IUH which is represented by a linear scheme of river channels and reservoirs. However, the limitations in the application of these models for ungauged catchments are proven [19] due to the nonlinear nature of the relationship between precipitation and runoff. Moreover, conceptual models contain large numbers of parameters that cannot be related to physical watershed characteristics [4, 20]: hence, they must be estimated by calibration using observed data.

Under such circumstances, the use of geomorphologic instantaneous unit hydrograph (GIUH) approach [21], which is based upon the widespread use of laws of stream orders proposed by Horton [22] and later modified by Strahler [23], is required. Rodriguez-Iturbe and Valdes [21] developed a physical methodology for the derivation of IUH using the empirical laws of geomorphology and climate characteristics. Specifically, the GIUH approach has two specific advantages: no requirement of historical flow records and ability to develop IUH using only topographic maps or remote sensing data that can be done using freely available shuttle radar topography mission (SRTM) data in geographical information system (GIS) environment. Gupta and others [24] related the parameters (peak and time peak) of IUH with geomorphologic characteristics of the catchment with a varying dynamic velocity parameter. Difficulties arise in the estimation of dynamic velocity parameter that has different values for each flood event: hence, it requires intermittent evaluation. Later, it was rationalized as a function of the effective rainfall intensity and duration to produce a concept of GIUH [25]. In this concept, the governing equations become a function of the mean effective rainfall intensity, Manning's roughness coefficient, average width and slope of the highest order stream. Rosso [26] related the Horton's order ratios [22] to the parameters of Nash model through power regression. Yen and Lee [19, 27] developed a geomorphology and kinematic-wave and stream order laws based hydrograph derivation. As such, GIUH became more powerful technique than the parametric Clark model [16] and Nash model [18]. To avoid the limitation of parameter estimation due to scanty hydrometeorological data in ungauged catchments, coupling of models has become a common practice. The GIUH from the watershed geomorphologic characteristics was related to the Nash model parameters [28] and Clark model [11]. Recently, a new method to estimate the Nash model parameters on the basis of the concept of geomorphologic dispersion stemming from spatial heterogeneity of flow paths within a catchment [29] has been formulated. The reliability and accuracy of Nash model based GIUH as compared to other approaches are shown in the works of [6, 11, 28, 30]. Nonetheless, Guzha and others [31] argue that coupling of two or more models can result in inconsistencies because the individual models may describe the same processes in different ways. However, the recent works on the applicability of the GIUH-Nash based model for the derivation of UH [4] show the adequacy of the GIUH-Nash model for the derivation of UH suggesting for further research aiming at assessing the impact of the resolution and source of digital elevation model (DEM) on the direct runoff predictions. On the basis of this suggestion, this paper will investigate the efficacy of DEM and quantum geographic information system (QGIS)-based computational algorithms for obtaining river flow information based on the GIUH-Nash model.

A DEM is defined as any digital representation of a continuous change in elevation in space that can be derived from topographic maps and satellite imagery. It is the most important source of data on topography and catchment characteristics, which are widely used in numerous hydrological studies. Nonetheless, DEM data are often used in hydrological studies without quantifying the effects of errors that constitute uncertainty [32]. Areas related to the uncertainty of the DEM that affect its use for hydrological applications include: the DEM error, topographic parameters often derived from the DEM and related algorithms used to derive these parameters, the influence of the scale of the elevation matrix as determined by the resolution of the grid cell, the interpolation of the elevation matrix and the modification of the terrain surface used to create hydrologically viable elevation matrix surfaces. Each of these areas contributes to the uncertainty of the DEM and can potentially influence the results of hydrological models with distributed parameters that rely on the DEM to obtain model inputs. In modern hydrology, a significant amount of research has been carried out [32] to eliminate the uncertainty associated with errors in DEM and to use appropriate solutions to improve the input parameters of models. For example, Lawrence Hawker and others [9] have identified three approaches to correcting the DEM error: editing the DEM, new elevation matrices created using advanced sensing technologies and stochastic modeling of the elevation matrix.

In the works of Weschler [32, 33], the inadequate level of attention paid by users of DEM to the question of uncertainty of DEM and its influence on various topographic parameters often used in hydrological studies is presented. Moreover, not only the accuracy of DEM depends on resolution but also the quality of the primary

source in which the DEM is generated significantly affects the topographical parameters of the DEM [34]. Size and accuracy of DEM resolution has a direct impact on the forecast of hydrological information on models, for example, TOPMODEL [35] and SWAT [36, 37]. However, when it comes to the generation of topographical parameters from DEM, it appears that the higher resolution of DEM is not necessarily better than the lower resolution [37]. On the other hand, the efficiency of the rainfall-runoff models that depend on the river network characteristics are impacted by the resolution of the selected DEM and threshold values [38]. Therefore, understanding the implications of DEM and GIS-based algorithms on various parameters should be the first step in hydrological modelling.

Keeping view of aforesaid facts and considering unavailability of literatures that indicate how the DEM and algorithm selection affect runoff prediction based on GIUH-Nash model, the present study was intended to solve mainly the problem of quantitative assessment of runoff from ungauged catchments in the absence or insufficiency of hydrological information within the framework of the following specific tasks: (1) evaluation of the effectiveness of DEM in predicting direct surface runoff using the GIUH-Nash model, and (2) evaluation of the impact of stream network formation algorithms on the prediction of direct surface runoff using the GIUH-Nash model. To this end, various methods were employed and are explained in the ensuing section.

## 2. Methods

The subject of this study is to assess the effectiveness of digital elevation models and GIUH-Nash models in predicting surface runoff for the unexplored Mereb-Gash river Debarwa catchment in Eritrea.

This research is an applied research that intends to find a solution for some of the pressing practical problems in water resources development and management projects in Eritrea. Thus, the approach employed is primarily based on the widely known conceptual, linear, time-invariant Nash-model coupled with the geomorphologic, physical and geographical characteristics derived from open-source DEMs. QGIS software is intensively used to process, analyze and map the DEMs-based data. Apparently, GIUH-Nash model is purely an analytical method whose parameters can be determined explicitly with the exception of scale parameter,  $n$  which is determined implicitly. The computed outputs of the model are calibrated using five recorded storm events. The details of the adopted methods are presented in the ensuing sub-sections.

### 2.1. Study area

The object of the study is the Debarwa catchment area with its outlet near the town of Debarwa, located in the southern region of Eritrea. Its outlet is specifically located at 15°05'49" N latitude and 38°50'11" E longitude about 29 km south of the capital in the eastern part of the Mereb-Gash river basin (Figure 1). The drainage area is estimated to be 200 km<sup>2</sup> with its elevation varying between 1,905–2,550 m above mean sea level. The watershed comprises hilly and dissected mountains mainly covered with open and sparse shrubs and mild slope agricultural lands (Figure 2). As per the information obtained from the 30 m resolution SRTM-based DEM, average basin slope is equal to 13.325 %. The main channel is 37 km long with a longitudinal slope of 1.16 %. Drainage density and channel segment frequency are 0.64 km/km<sup>2</sup> and 0.21 streams per km<sup>2</sup>, respectively. According to the agro-ecological classification of Eritrea, the Debarwa catchment lies in moist highlands zone where temperature varies from 0 °C to 32 °C and an average annual rainfall of 547 mm. Climate in the catchment can be characterized as moderate with December-January being the coldest and March-April the hottest. Maximum precipitation occurs in the summer season, specifically in the months of July and August with a monthly mean rainfall of 185 mm and 175 mm, respectively.

### 2.2. Geomorphologic database

The physical characteristics of stream channels of a drainage basin can provide helpful information through the likely effects of the variation of hydraulic radius and roughness on average flow velocities [14]. The success of the GIUH-based model also completely relies upon the quality of stream channels formation. In this study, four frequently used open-source DEMs were considered for the extraction of geomorphological database of the catchment with the help of the freely available QGIS software. They are based on geo data of several global elevation matrices: level-1 with a resolution of 90 m (3-arc seconds) and level-2 data with a resolution of 30 m (1-arc second). Specifically, the DEMs include two shuttle radar topographic mission (SRTM 90 and SRTM 30), 30-m resolution data from the advanced space thermal emission and reflection radiometer (ASTER 30) and 30m resolution data from advanced land observing satellite - JAXA's Global ALOS 3D (ALOS 30). The georeferenced and QGIS compatible file format (GeoTiff) files of the four DEM-sources were imported to QGIS. Accordingly, the geomorphological database of the study area was established using two of the best known open-source QGIS packages: geographic resources analysis support system (GRASS) and system for automated geoscientific analyses (SAGA).

The geospatial data analysis library (GDAL) has been used to handle the raster geographic data formats of DEM. As such, multi-layered raster was created in the original virtual directory so as to delineate the catchment area. Using the gdalbuildvrt utility of the GDAL library, a virtual mosaic of the dataset (vrt) of the catchment was established from all GeoTiff input files. The mosaic from the original rasters meets the

following conditions: all images must be in the same coordinate system and have the same number of bands, but the resolution may be different and the rasters may overlap. The raster file of the mosaiced virtual dataset was reprojected by using an algorithm derived from the GDAL warp utility. The sinks in the output file were filled using the fill sinks function from SAGA to get filled DEM and flow directions. As such, Strahler order raster and channel network in vector form were produced from the channel network and drainage basin algorithm in SAGA. The raster of the catchment was delineated from the filled DEM input using the watershed basin analysis program in SAGA and appropriate value of the minimum size of exterior watershed basin criteria. The co-ordinates of the outlet for the watershed under consideration were identified using the co-ordinate capture plugin tool. Using the drainage direction as input in the watershed creation program in GRASS and the outlet co-ordinates, the required catchment was extracted. After converting the watershed in raster file into vector format, the GDAL extraction function was then used to clip raster DEM and area of interest is extracted. On top of this, the channels file was also clipped to the area of interest using the clip function in vector overlay tools. From these processes four DEM versions were obtained for the study area.

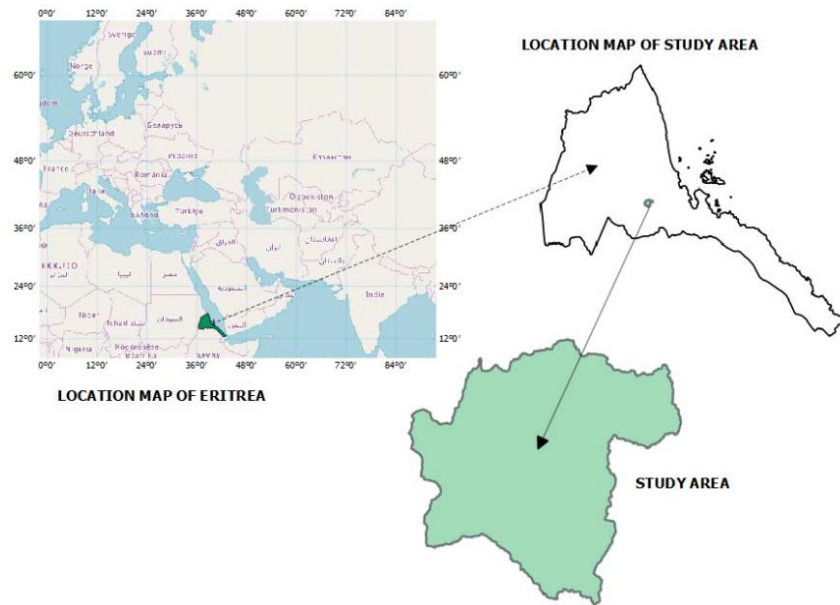


Figure 1. Location map of Eritrea and study area [4].

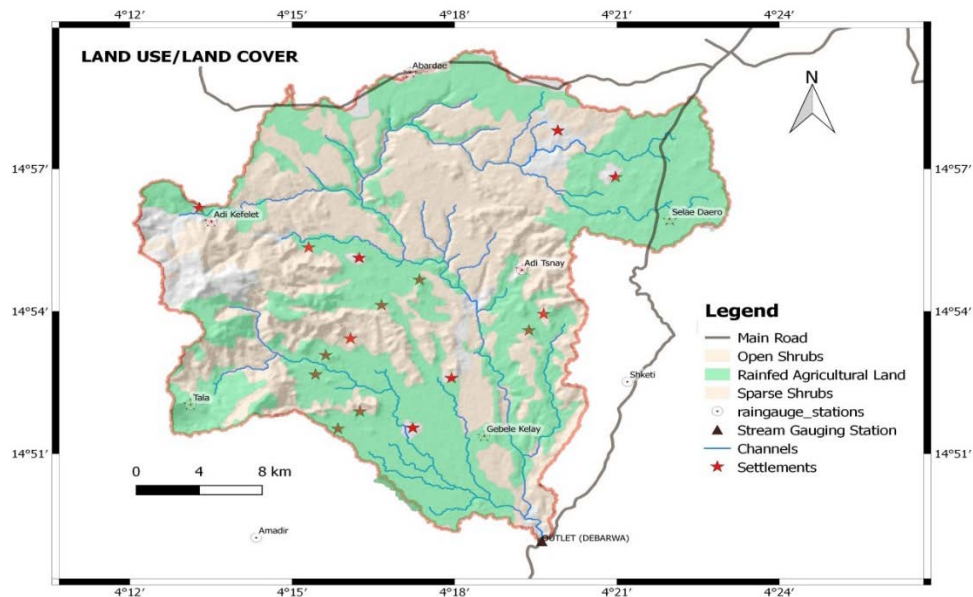


Figure 2. Land use/land cover map of Debarwa catchment [4].

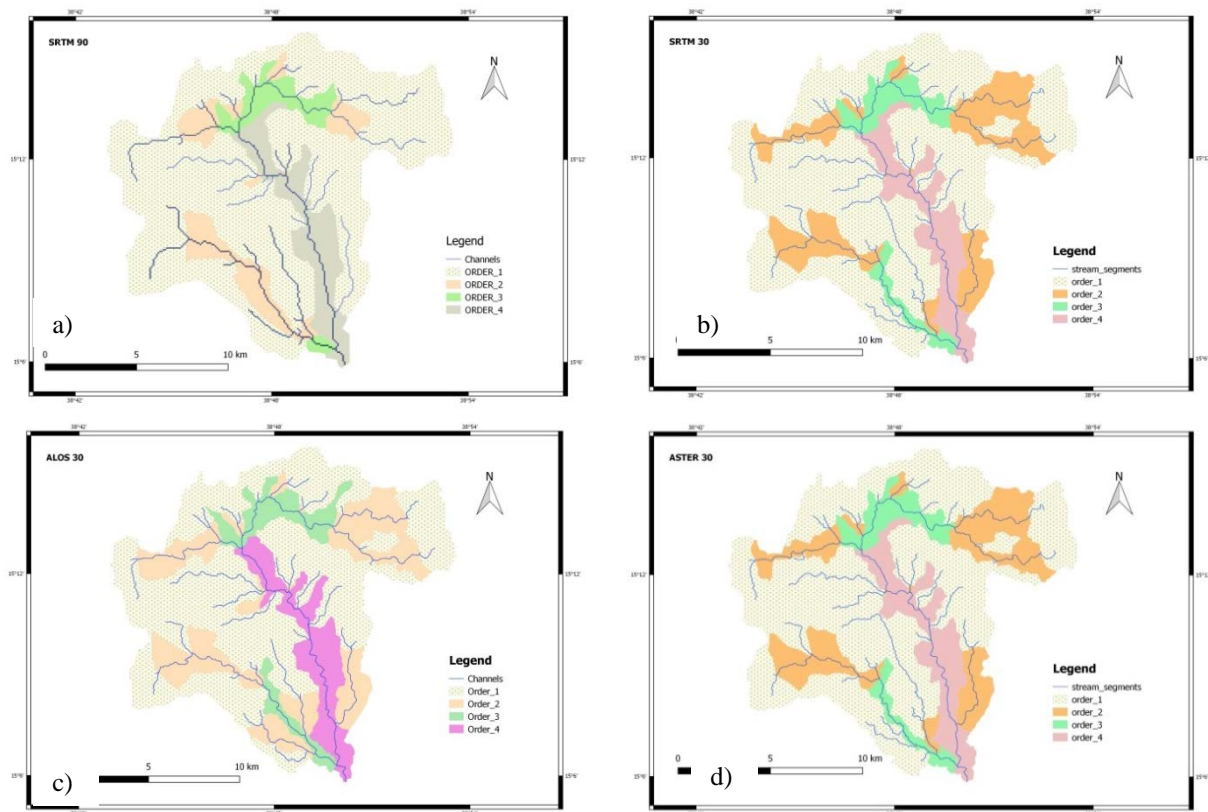
To study the implication of algorithms on virtual channel network creation and in the geomorphologic database preparation, watershed basin analysis program from GRASS and channel network and drainage basins from SAGA were used. Apparently, the noticeable difference among these two algorithms is the threshold value assignment. The former uses number of cells and the later uses stream orders. In the GRASS-algorithm, the values of minimum size of exterior watershed basin were intuitively chosen to be 1,500 cells for SRTM 30, ASTER 30 and ALOS 30 and 166 cells for SRTM 90, respectively. All of them produce a catchment with the same number of stream orders, the highest being fourth order (Figure 3). In the SAGA-



algorithm, threshold values of 6 and 4 for the 30 m and 90 m resolutions are applied, respectively (Figure 4). The overall patterns of the channel networks and the number of stream orders from both algorithms are relatively similar. Nevertheless, discrepancy in the lengths of the highest ordered channels are easily noticeable in the outputs from the 30 m resolution DEMs. The algorithm from GRASS produce longer fourth order channels (18436 m) than that of SAGA (1423 m). On the contrary, the 90 m resolutions DEMs generate nearly the same lengths of fourth ordered channels; 18621 m and 16484 m by GRASS and SAGA, respectively. To what extent would these and other unforeseen discrepancies affect the performance of the GIUH-Nash model-based runoff predictions?

To address the above question, four DEM-scenarios were considered for each algorithm obtained using the aforementioned procedures. In each case, stream lengths, elevations at the stream junctions, stream numbers and their orders and other attributes were processed and stored. The most tedious and time consuming part of the work was the on-screen digitization of the areas corresponding to the  $i^{th}$  stream order of the eight scenarios. Eventually, the bifurcation ratios ( $R_B$ ), length ratios ( $R_L$ ) and area ratios ( $R_A$ ) are calculated according to Horton's laws based on the following relationships: law of stream numbers  $R_B = N_\omega / N_{\omega+1}$ , law of stream lengths  $R_L = \bar{L}_\omega / \bar{L}_{\omega-1}$  and law of stream areas  $R_A = \bar{A}_\omega / \bar{A}_{\omega-1}$ ; where  $N_\omega$  is the number of streams,  $\bar{L}_\omega$  is the mean length of streams, and  $\bar{A}_\omega$  - the mean area of the basins of order,  $\omega$ . The ratios in nature are normally between 3 and 5 for  $R_B$ , between 1.5 and 3.5 for  $R_L$ , and between 3 and 6 for  $R_A$ , respectively [21].

The geomorphological parameters namely  $R_B$ ,  $R_L$  and  $R_A$  are computed graphically by plotting stream orders versus logarithm transformed stream numbers ( $N_s$ ), mean stream length ( $L_m$ ) and mean stream areas ( $A_m$ ), respectively so as to have a linear relationship among the variables. The actual values of the ratios (Figure 5) are obtained from the slopes of the best fit lines corresponding to bifurcation, length and area ratios, respectively. Some of the GRASS-based and SAGA-based geomorphological parameters for the study area are presented in Table 1 and Table 2, respectively.



**Figure 3. Channel systems and stream areas from GRASS [4]:  
a) SRTM 90 and b) SRTM 30 c) ALOS 30 and d) ASTER 30.**

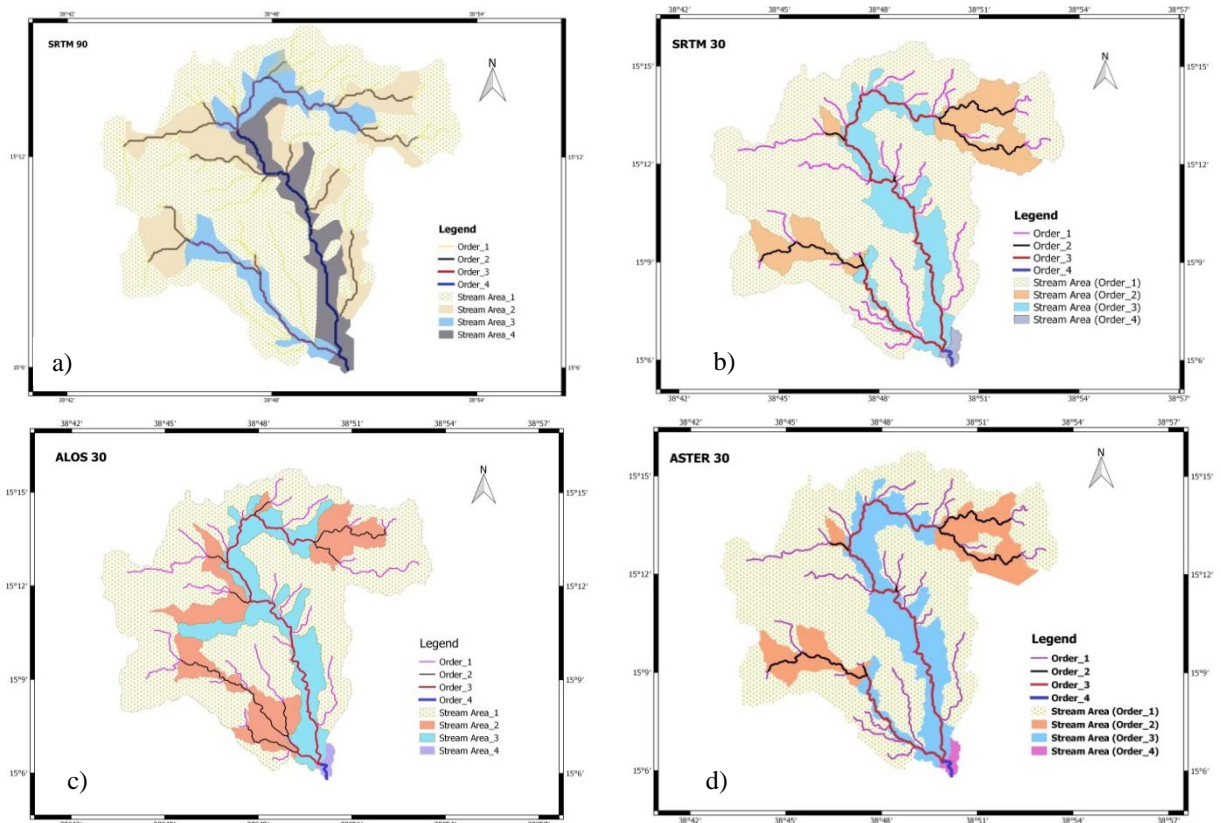


Figure 4. Channel systems and stream areas from SAGA [4]:  
a) SRTM 90 and b) SRTM 30 c) ALOS 30 and d) ASTER 30.

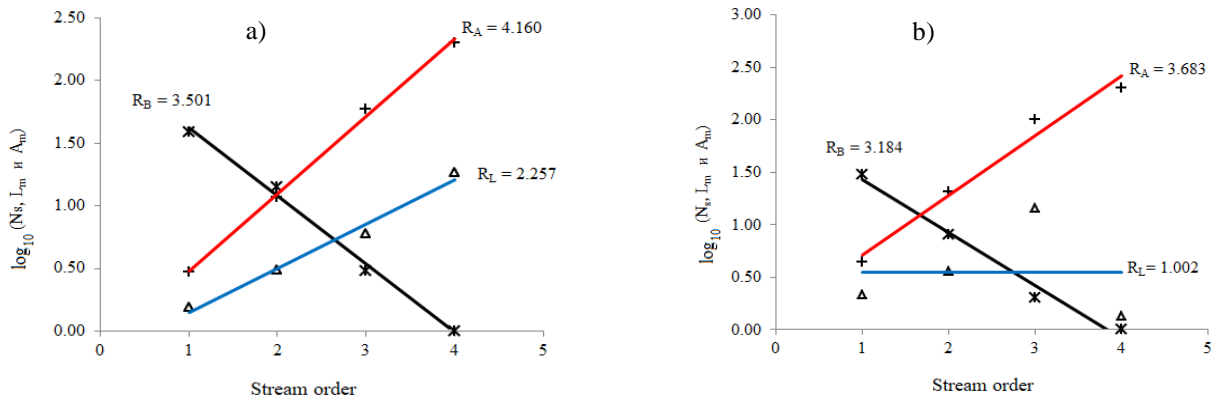


Figure 5. Examples of Horton's laws based ratios from ALOS 30: a) GRASS and b) SAGA.

Table 1. GRASS-based geomorphologic characteristics of Debarwa Catchment.

DEM	Stream Order ( $\omega$ )	No of streams ( $N_\omega$ )	stream length $L$ (km)	mean stream length $\bar{L}_\omega$ (km)	mean stream area $\bar{A}_\omega$ (km <sup>2</sup> )	$R_B$	$R_L$	$R_A$
ALOS 30	1	39	59.856	1.535	2.979	3.501	2.257	4.160
	2	14	43.303	3.093	11.670			
	3	3	17.987	5.996	59.596			
	4	1	18.572	18.572	200.262			
ASTER 30	1	40	68.252	1.706	3.104	3.474	2.183	4.039
	2	12	37.765	3.147	13.514			
	3	3	18.571	6.190	58.851			
	4	1	18.368	18.368	199.453			
SRTM 30	1	40	68.252	1.706	3.104	3.474	2.183	4.039
	2	12	37.765	3.147	13.514			
	3	3	18.571	6.190	58.851			
	4	1	18.368	18.368	199.453			
SRTM 90	1	34	67.141	1.975	4.088	3.383	2.113	3.794
	2	10	24.412	2.441	16.551			
	3	2	10.299	5.149	88.384			
	4	1	18.621	18.621	199.179			

**Table 2. SAGA-based geomorphologic characteristics of Debarwa catchment.**

DEM	Stream Order ( $\omega$ )	No of streams ( $N_\omega$ )	stream length $L$ (km)	mean stream length $\bar{L}_\omega$ (km)	mean stream area $\bar{A}_\omega$ (km <sup>2</sup> )	$R_B$	$R_L$	$R_A$
ALOS 30	1	30	64.140	2.138	4.382	3.184	1.002	3.683
	2	8	29.108	3.639	20.690			
	3	2	29.008	14.504	99.467			
	4	1	1.357	1.357	200.232			
ASTER 30	1	32	66.885	2.090	4.281	3.206	0.945	3.662
	2	7	22.919	3.274	23.394			
	3	2	34.158	17.079	99.401			
	4	1	1.456	1.456	200.066			
SRTM 30	1	32	66.868	2.090	4.215	3.157	1.042	3.597
	2	6	22.919	3.820	26.928			
	3	2	34.158	17.079	97.340			
	4	1	1.456	1.456	196.006			
SRTM 90	1	63	85.042	1.350	1.897	4.121	2.378	4.882
	2	17	41.936	2.467	9.399			
	3	3	23.558	7.853	60.626			
	4	1	16.484	16.484	201.120			

### 2.3. Development of the GIUH-Nash Model

#### 2.3.1. Nash model

One of well-known and widely used models is Nash cascade [18] which can be visualized as a sequence of  $n$  linear reservoirs in series, each of which has a time lag of  $K$ , during which individual precipitation is instantly superimposed on the upper reservoir. A linear reservoir is a reservoir for which there is a linear relationship between the storage of each tank and the output. An input of a unit of excess rainfall over the catchment is applied instantaneously to the first reservoir. The routed outflow from the first reservoir becomes the input to the second reservoir in series and the second reservoir output becomes the input to the third, and so on. Output from the last  $n^{th}$  reservoir is the output from the system representing an IUH for the catchment. The resulting mathematical form for the unit hydrograph  $q(t)$  is equivalent to the gamma distribution:

$$q(t) = \frac{1}{\Gamma(n)} \frac{1}{K} \left( \frac{t}{K} \right)^{n-1} e^{-t/K}, \quad (1)$$

where  $q(t)$  is the IUH of the Nash model;

$\Gamma(n)$  is the Gamma function;

$K$  is the storage coefficient in  $h$ .

The parameters,  $n$  and  $K$ , can be determined by a number of ways; the most widely used being the method of moments. Mathematically,  $n$  may take fractional values [6] so as to give a wider range of shapes in fitting the observed data. Direct determination of the above parameters requires reliable historical records of rainfall-runoff. In the absence of historical rainfall-runoff data, they are determined as described below.

#### 2.3.2. GIUH-Nash model

According to Beven [6], GIUH method is still widely used as a tool for predicting flood discharges in ungauged catchments: it has the advantage of using it in situations where there is insufficient amount of input information and is simple for practical application. The estimation of the GIUH for a given catchment allows the user to use this hydrograph for any case of precipitation in the catchment and therefore to assess its response.

The relationship between the peak discharge  $q_p$  and time peak  $t_p$  of the IUH as a function of the geomorphologic characteristics of the catchment [21] is given as follows,

$$q_p = 1.31 R_L^{0.43} (V / L_\Omega) \quad (2)$$

and

$$t_p = 0.44 \left( \frac{L_\Omega}{V} \right) \left( \frac{R_B}{R_A} \right)^{0.55} R_L^{-0.38}, \quad (3)$$

where  $\Omega$  is stream order of the catchment;

$L_{\Omega}$  is length of the highest order stream (km);

$V$  is dynamic velocity parameter ( $\text{ms}^{-1}$ ). The parameters  $q_p$  and  $t_p$  have units ( $\text{h}^{-1}$ ) and ( $\text{h}$ ), respectively. Multiplication of equations (2) and (3) that have units of time gives a non-dimensional term which is independent of the dynamic velocity and storm characteristics. It is purely a function of the geomorphologic characteristics:

$$q_p \times t_p = 0.5764 \left( \frac{R_B}{R_A} \right) 0.55 R_L^{0.05}, \quad (4)$$

The first derivative of (1) gives the time to peak as follows,

$$t_p = (n-1) \times K. \quad (5)$$

Substituting this value for  $t_p$  in (1), the peak discharge  $q_p$  of the IUH is obtained as,

$$q_p = \frac{(n-1)^{n-1}}{K \times \Gamma(n)} \times e^{-(n-1)}. \quad (6)$$

The product of (5) and (6) gives a function of the Nash-parameter,  $n$ . Thus,

$$q_p \times t_p = \frac{(n-1)^n}{\Gamma(n)} \times e^{-(n-1)}. \quad (7)$$

Equating (4) and (7), the following relationship is arrived at:

$$\frac{(n-1)^n}{\Gamma(n)} \times e^{-(n-1)} = 0.5764 \left( \frac{R_B}{R_A} \right)^{0.55} R_L^{0.05}. \quad (8)$$

The value of  $n$  in equation (8) can be solved by Newton-Rapson iteration or Matlab optimization tool. Rearranging (5) and substituting the right hand side of (3) for  $t_p$ , the value of  $K$  could be solved as,

$$K = \frac{0.44}{n-1} \times \left( \frac{L_{\Omega}}{V} \right) \left( \frac{R_B}{R_A} \right)^{0.55} R_L^{-0.38}. \quad (9)$$

The dynamic velocity proposed is the velocity corresponding to the peak runoff for a given rainfall-runoff event in the catchment. This velocity can be obtained with the help of Manning's equation [4, 10, 11].

$$V = \frac{1}{n_m} R^{2/3} S_m^{1/2}, \quad (10)$$

where  $n_m$  is Manning's roughness coefficient;

$R$  is hydraulic radius;

$S_m$  is slope of the main channel.

The value of the roughness coefficient is influenced by hydraulic flow elements (depth, slope), including those associated with changes in cross-section and river bed. For example, the values of  $n_m$  may decrease with increasing depth or flow to the level of water discharge to floodplain, when floods remain confined within the channel banks [14], which has been the case of the study area. It should be noted that in the Debarwa catchment, a permanent hydrometric gauging station is installed along one of the concrete walls of the Debarwa bridge with a rocky cobbles river bed. Given these boundary conditions and performing trial and error to obtain optimal prediction of the desired hydrograph,  $n_m$  was taken to be 0.022.  $S_m$  is computed using the «85-10» slope factor method [7].

Since Manning's coefficient  $n_m$  greatly affects the dynamic velocity  $V$  and time lag  $K$  in the GIUH-Nash model, its actual value must be studied before applying the model for hydrological modeling.

### 2.3.3. Direct surface runoff computation

The ultimate objective of GIUH development is to derive a UH of required duration which in turn can be used for computation of direct surface runoff. Thus, equation (11) is applied for this purpose. Pilgrim

recommends the use of a period longer than a quarter of the UH time peak may result in large errors, especially at the hydrograph peak. Accordingly, since the time peak in most of the derived UHs from the observed stream flows is one hour, 0.25 hour UH duration is used. The relationship between IUH [ $u(t)$ ] and D-hour UH [ $U(D, t)$ ], both of the same unit depth, are related by the formula:

$$U(D, t) = \frac{\int_0^t u(t) dt}{D}, \quad (11)$$

where  $D$  is the duration of the UH.

Eventually, the direct runoff hydrograph is estimated by convoluting the excess rainfall hyetograph with the UH obtained from equation (11) for all storm events corresponding to each DEM-scenario and algorithm. The predicted direct runoffs were compared with five single peaked storm events so as to evaluate the GIUH-Nash model. Various objective fit functions and statistical indices are also used for this purpose as presented in the ensuing sub-section.

### 2.3.4. Model evaluation

Since all models and their parameters are approximations to reality, comparing the computed results and observed data is a must in hydrologic modelling. To this end, several model evaluation techniques are employed for judging the fit of calculated to observed hydrograph. In this study, the differences between peak magnitudes, a measure of overall fit such as the sum of absolute values or squares of the differences of individual ordinates, or differences between lags or other time measures were used. Moreover, visual inspection of the shape and major characteristics of the hydrographs (time peak, peak discharge, and time base) for different storm events were applied. The standard regression and error indices used in the study are briefly explained in the ensuing paragraphs.

Nash-Sutcliffe efficiency (NSE): The efficiency of a hydrological model is measured by the NSE, which determines the relative magnitude of the residual variance compared to the measured data variance [39]. It indicates how well the plot of observed versus simulated data fits the 1:1 line given by:

$$NSE = 1 - \frac{\sum_{t=1}^N [Q_o(t) - Q_p(t)]^2}{\sum_{t=1}^N [Q_o(t) - \bar{Q}_o(t)]^2}. \quad (12)$$

Nash-Sutcliffe efficiency can range from  $-\infty$  to 1. An efficiency of 1 ( $NSE = 1$ ) corresponds to a perfect match of modelled discharge to the observed data. An efficiency of 0 ( $NSE = 0$ ) indicates that the model predictions are as accurate as the mean of the observed data, whereas an efficiency less than zero ( $NSE < 0$ ) occurs when the observed mean is a better predictor than the model or, in other words, when the residual variance (described by the numerator in the expression above), is larger than the data variance (described by the denominator). Essentially, the closer the model efficiency is to 1, the more accurate the model is.

Special correlation coefficient (SC): a goodness of fit between observed and predicted is also given by:

$$SC = \sqrt{\frac{2 \sum_{t=1}^N Q_o(t) Q_p(t) - \sum_{t=1}^N [Q_p(t)]^2}{\sum_{t=1}^N [Q_o(t)]^2}}. \quad (13)$$

Mean absolute error (MAE) and root mean square error (RMSE): These indices allow us to estimate how the values of the sets of observed and predicted values may differ from the average, which helps in the analysis of the results. The RMSE value is important for determining the plausibility of the phenomenon under study in comparison with the predicted value of the model: if the average value of measurements is very different from the predicted values of the model (a large value of the standard deviation), then the values obtained or the method of obtaining them should be rechecked. The value 0 indicates a perfect match between the model and nature. The MAE and RMSE values can be calculated from equations (14) and (15), respectively:

$$MAE = \frac{\sum_{t=1}^N |Q_o(t) - Q_p(t)|}{N}, \quad (14)$$



$$RMSE = \sqrt{\frac{\sum_{t=1}^N [Q_o(t) - Q_p(t)]^2}{N}}, \quad (15)$$

where  $Q_o(t)$  and  $Q_p(t)$  are observed and predicted direct runoff rates at time  $t$ , respectively,

$N$  is total number of ordinates of direct runoff hydrograph (DRH).

Indices of simulation of single-event allow us estimation of the accuracy of predicted hydrograph ordinates. For this purpose, we used three methods: error of the direct runoff volume (EV), the relative error at the peak (REP) and the uncertainty of the time occurrence of peak (ETP) [11].

$$EV = \frac{V_o - V_p}{V_o} \times 100, \quad (16)$$

$$REP = \frac{Q_o - Q_p}{Q_o} \times 100, \quad (17)$$

$$ETP = T_p - T_o, \quad (18)$$

where  $V_o$  and  $V_p$  are observed and predicted runoff volumes;

$Q_o$  and  $Q_p$  are observed and predicted peak runoff rates;

$T_o$  and  $T_p$  are time peak of observed and predicted runoffs, respectively.

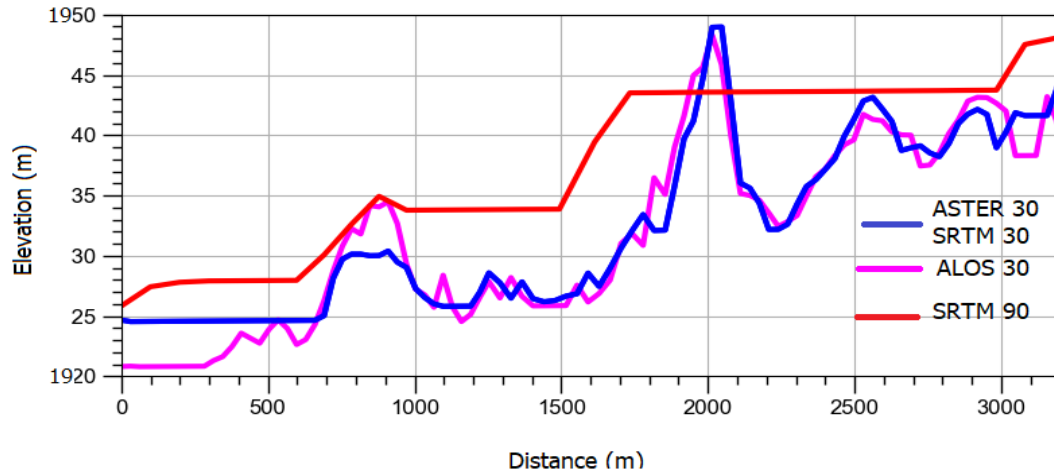
### 3. Results and Discussions

Prior to the application of the selected model, intensive analyses were carried out on various physical and geographical parameters so as to observe the discrepancies and uncertainties among the DEMs and, of course, to determine the parameters to be used in the model. Details of these parameters obtained from four DEMs are presented in Table 3. A noticeable discrepancies and uncertainties among them could be seen in some of these parameters. For example, the basin area obtained from ALOS 30, ASTER 30 and SRTM 90 are larger (~200 km<sup>2</sup>) than SRTM 30 (~196 km<sup>2</sup>) whereas the 30 m resolution DEMs produced higher basin slope (~13.4 %) as compared to the 90 m DEM (8.662 %). The vast majority of the physical and geographical parameters obtained from lower resolutions are higher than DEMs of higher resolution.

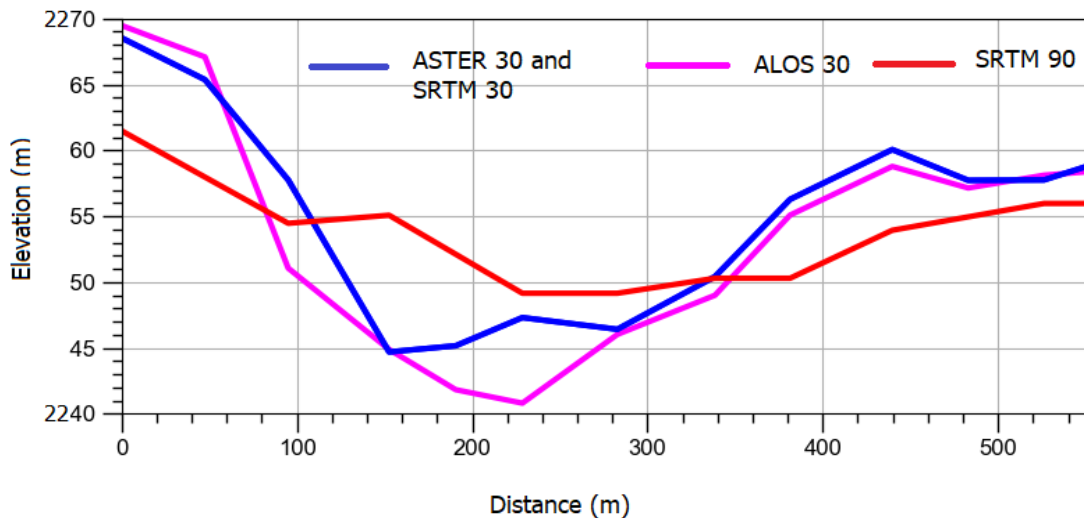
**Table 3. DEM-wise physiographic parameters of Debarwa catchment.**

Physiographic parameter	DEM-Scenarios			
	ALOS 30	ASTER 30	SRTM 30	SRTM 90
Average basin slope (%)	13.382	13.872	13.325	8.662
Basin area (km <sup>2</sup> )	200.232	200.066	196.006	201.120
Basin perimeter (km)	101.494	109.675	103.737	98.472
Basin relief (km)	0.673	0.617	0.643	0.639
Channel segment frequency (no. /km <sup>2</sup> )	0.205	0.210	0.209	0.418
Circularity ratio	0.244	0.209	0.229	0.261
Constant of channel maintenance (km <sup>2</sup> /km)	1.620	1.595	1.563	1.204
Drainage density (km/km <sup>2</sup> )	0.617	0.627	0.640	0.830
Elongation ratio	0.851	0.851	0.842	0.853
Fineness ratio	1.218	1.144	1.209	1.696
Form factor	0.569	0.569	0.557	0.572
Main channel length (km)	36.682	36.891	36.891	33.697
Main channel slope (%)	1.083	1.130	1.162	1.214
Maximum basin length (km)	18.757	18.757	18.757	18.757
Maximum elevation (m)	2575.694	2527.694	2549.139	2555.151
Minimum elevation (m)	1902.833	1902.833	1905.936	1916.185
Relief ratio	0.036	0.033	0.034	0.034
Ruggedness number	0.415	0.387	0.412	0.531
Shape factor	2.297	2.311	1.961	2.106
Unity shape factor	1.326	1.326	1.340	2.376

To further verify the uncertainties and discrepancies among the DEMs, longitudinal and transversal elevation profiles of the main channel length (MCL) were checked. For example, longitudinal profiles of DEMs taken near 10 % of MCL (Figure 6) and transversal profiles of DEMs taken at 85 % of MCL (Figure 7) are presented below. As pointed out in the methods section, 85 % and 10 % of MCL measured from the outlet are used for the determination of  $S_m$ . Graphical results of these profiles indicate absolute overlapping of SRTM 30 and ASTER 30 DEMs whereas significant elevation differences could be clearly observed among SRTM 90, ALOS 30 and SRTM 30–ASTER 30. Besides, in most cases, the elevations of SRTM 90 are significantly higher than other DEMs. Even though statistical verification of these variations could not be done on account of lack of ground control points, these elevation profiles and values of physiographic parameters comply with the conclusions of Wechsler [32].



**Figure 6. Longitudinal profiles of DEMs at 10 % of the main channel length (MCL).**



**Figure 7. Transversal profiles of DEMs at 85 % the main channel length (MCL).**

The Nash model parameters are calculated from equations (8) and (9), respectively. Nash parameters, peak runoff and time peak for various storm events obtained from the selected algorithms are presented in Table 5 and Table 6. The results of the calculations for the four DEM-scenarios indicate that values of  $n$  and  $K$  obtained from GRASS-based stream networks are higher, in most cases, than those of SAGA-based. The reason behind this disparity and their implications on the performance of the model was investigated and is discussed in the ensuing paragraphs.

**Table 4. GRASS-based dynamic velocity and scale parameter.**

Storm event	ALOS 30		ASTER 30		SRTM 30		SRTM 90	
	$V$ , m/s	$K$ , h	$V$ , m/s	$K$ , h	$V$ , m/s	$K$ , h	$V$ , m/s	$K$ , h
July 17, 2006	6.220	0.431	6.354	0.420	6.445	0.414	6.587	0.410
August 02, 2006	6.617	0.405	6.759	0.395	6.855	0.389	7.007	0.386
August 04, 2006	6.455	0.415	6.593	0.405	6.687	0.399	6.835	0.395
August 16, 2006	5.531	0.485	5.650	0.473	5.731	0.466	5.857	0.461
August 22, 2006	8.043	0.333	8.215	0.325	8.333	0.320	8.517	0.317

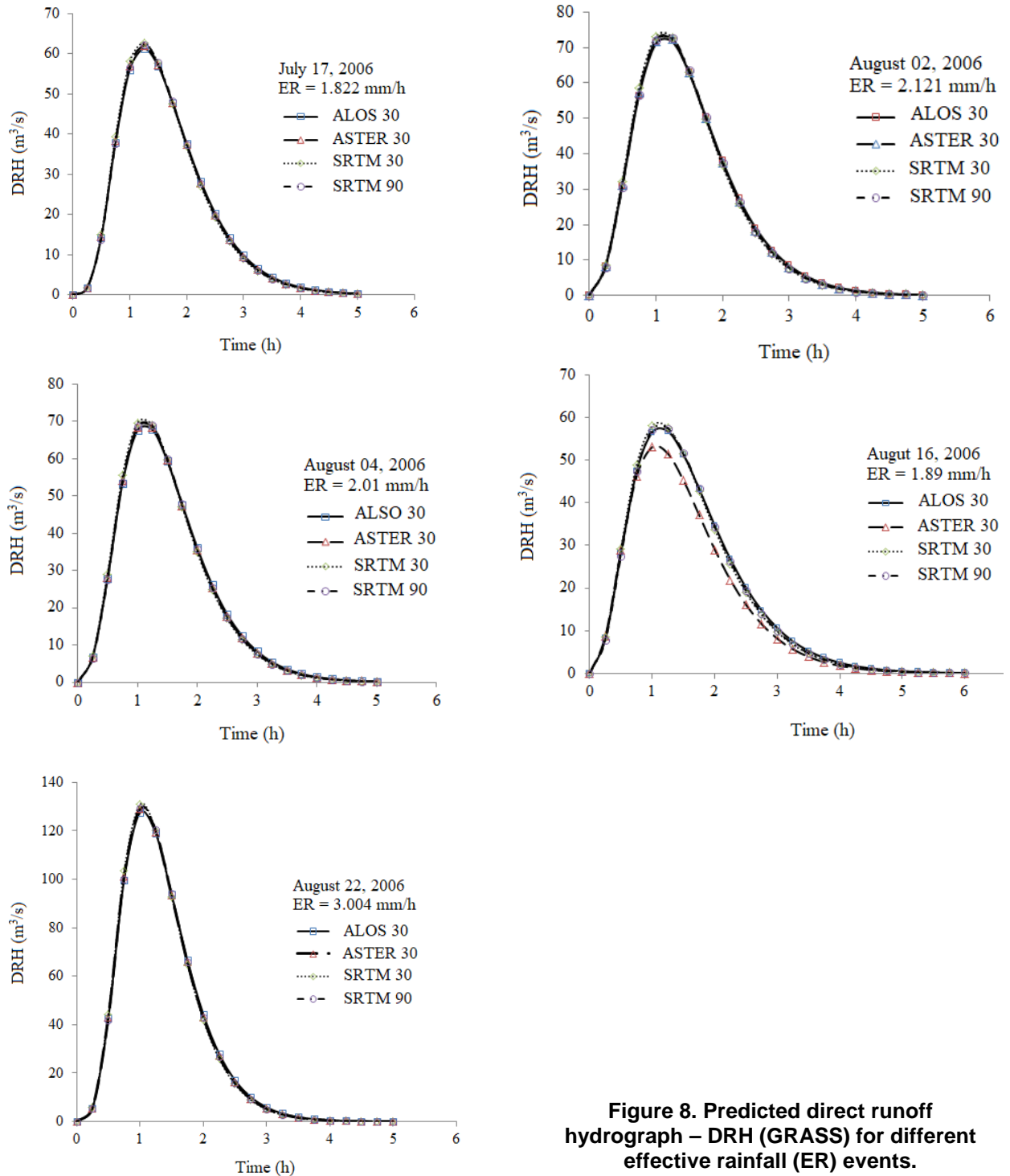
**Table 5. GRASS-based values of Nash parameters, peak runoff and time peak.**

Storm event	DEM	Nash parameters		Peak runoff			Time peak		
		$n$	$K$ , h	$Q_o$ , m <sup>3</sup> /s	$Q_p$ , m <sup>3</sup> /s	$Q_{avg}$ , m <sup>3</sup> /s	$T_o$ , h	$T_p$ , h	$T_{avg}$ , h
July 17, 2006	ALOS 30	3.035	0.431	61.921	61.299	62.137	0.50	1.25	1.25
	ASTER 30	3.071	0.420		62.039			1.25	
	SRTM 30	3.071	0.414		62.827			1.25	
	SRTM 90	3.142	0.410		62.382			1.25	
August 02, 2006	ALOS 30	3.035	0.405	66.860	71.627	72.360	1.00	1.25	1.25
	ASTER 30	3.071	0.395		72.245			1.25	
	SRTM 30	3.071	0.389		73.029			1.00	
	SRTM 90	3.142	0.386		72.737			1.25	
August 04, 2006	ALOS 30	3.035	0.415	73.301	67.837	68.657	1.00	1.25	1.00
	ASTER 30	3.071	0.405		68.573			1.00	
	SRTM 30	3.071	0.399		69.710			1.00	
	SRTM 90	3.142	0.395		68.968			1.25	
August 16, 2006	ALOS 30	3.035	0.485	44.585	56.801	56.250	1.00	1.25	1.00
	ASTER 30	3.071	0.473		53.105			1.00	
	SRTM 30	3.071	0.466		58.078			1.00	
	SRTM 90	3.142	0.461		57.526			1.25	
August 22, 2006	ALOS 30	3.035	0.333	118.000	127.476	129.249	1.00	1.00	1.00
	ASTER 30	3.071	0.325		129.070			1.00	
	SRTM 30	3.071	0.320		130.919			1.00	
	SRTM 90	3.142	0.317		129.531			1.00	

The dependence of IUH on velocity has serious implications in the estimation of the peak flow and time peak of storms when using the UH approach [10, 21]. This reality became clear in the direct runoff prediction process as a result of the dynamic velocity,  $V$  being extremely sensitive to small changes in  $n_m$ , which was also proven by others [4, 10, 28]: thereupon the GIUH-Nash model performance [11]. Thus, it seems that  $n_m$  representing the site under consideration must be obtained prior to the use of the selected model for practical applications. In the SAGA-based stream networks, two main channels having the same stream order converged near the outlet resulting in a smaller length,  $L_\Omega$  of higher orders as shown in Table 2. These values lead to poor correlation among the number of streams and the log-transformed mean stream length resulting  $R_L$  to be smaller than the minimum threshold values suggested by Rodriguez [21]. Eventually,  $K$  being a function of  $V$ ,  $L_\Omega$  and Horton's ratios, its results were also significantly affected. Conversely, GRASS-based Nash parameters are higher and Horton's ratios within the recommended ranges [21] due to higher,  $L_\Omega$ . Table 4 shows the dynamic velocity and scale parameter of the different storm sand DEMs. The values of the dynamic velocity, ranging between 5 to 9 ms<sup>-1</sup>, are high due to large main channel slopes (1.16 %) and mainly small value of  $n_m$ . Small value of  $K$  (< 0.5 h) is indicative of lower storage capacity of the catchment.

The quality of GIUH-Nash model-based runoff depends on the accuracy of the estimation of its parameters. Table 5 shows GRASS-based values of Nash parameters, peak runoff and time peak of different storms and DEMs. The implications of the adopted algorithms and corresponding Nash parameters on the predicted hydrographs were analyzed. Visual inspections of observed and predicted runoffs indicate that GRASS-based parameters give better results, as expected, than SAGA-based. The GRASS-based predicted hydrographs from all the DEM-scenarios are plotted in the same graph for visual comparison (Figure 8). The comparison reveals that the characteristics of the predicted hydrographs from the four DEM-scenarios are nearly in perfect match. Thus, we felt that there is no need to apply goodness of fit functions and statistical indices to each DEM-scenario. Rather, we opted to calculate predicted runoff averages ( $Q_{avg}$ ) of the four DEM-scenarios and compare them with the observed hydrographs (Figure 9). It can be observed that  $Q_{avg}$  is larger than  $Q_o$  in three storm events, smaller in one storm event and nearly the same for the remaining one event. The time peaks are small (~ 1.0 h) due to smaller values of scale parameter. The predicted peak runoff averages have a time lag of 0.25 h.

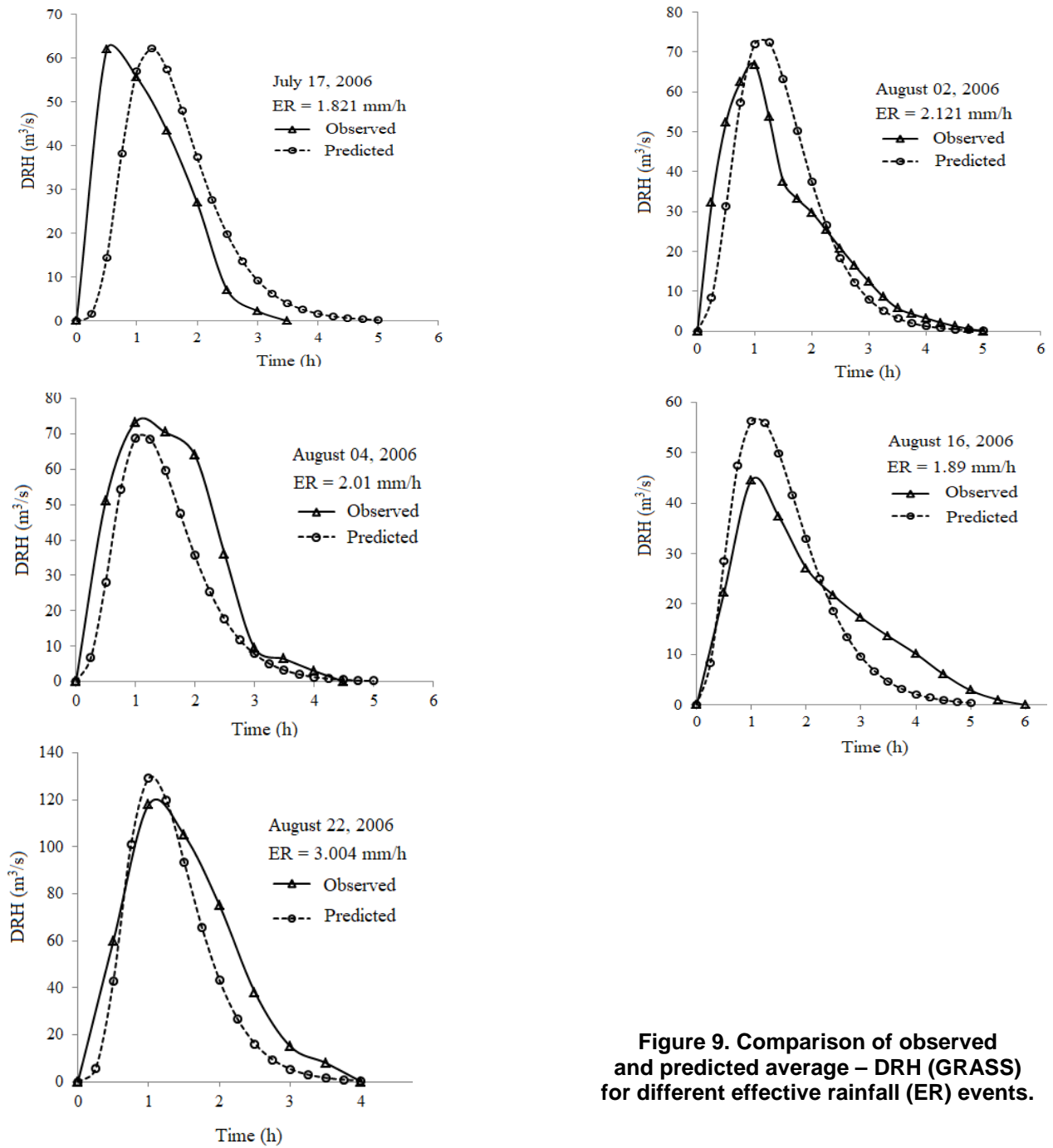
On the other hand, the SAGA-based predicted hydrographs reveal significant mismatch with the observed hydrographs. The effects of lower values of Nash parameters from this algorithm are clearly revealed on the outputs. Poor prediction was obtained from the lower resolution DEMs (Figure 10) and relatively better estimate was obtained from SRTM 90. Figure 10 shows inconsistencies among predicted runoffs from the same storm event: there are over-prediction and under-prediction of the hydrograph characteristics. The lower values of  $n$  and  $K$  in most DEM-scenarios produced a short time peak (0.5 h) and time base (1.0 h) with the exception of SRTM 90 m. Table 6 shows SAGA-based Nash parameters, peak runoff and time peak. The estimated predicted peak runoffs are found to be different for all the DEM-scenarios.



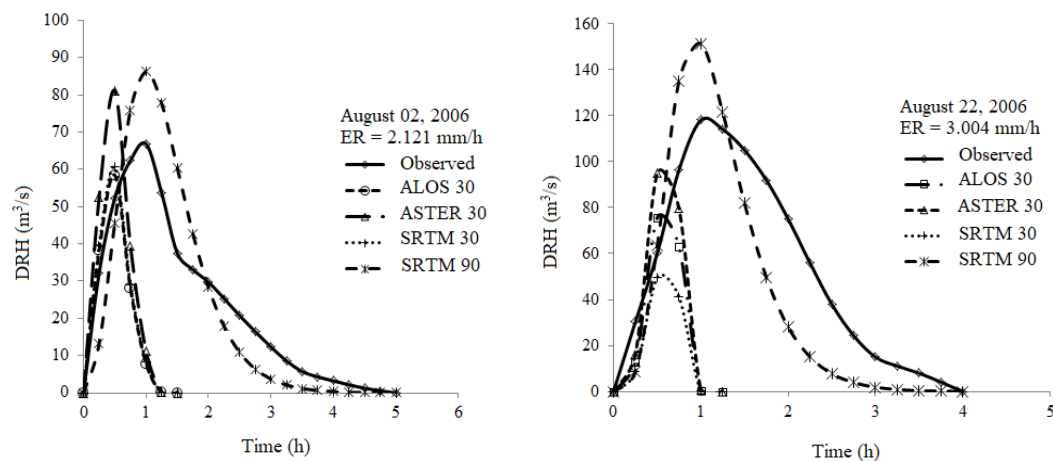
**Figure 8. Predicted direct runoff hydrograph – DRH (GRASS) for different effective rainfall (ER) events.**

The statistical measures of the selected model based on the two algorithms (Table 7 and Table 8) are obtained using equations 12–18. The various statistical analyses show GRASS-based approach is fitting better for the catchment under consideration than SAGA-based approach. For GRASS (Table 7), the minimum values of NSE and SC are 0.507 and 0.843, respectively, demonstrating the sufficiency of the GIUH-Nash model [39]. In general, the EV and ETP do not show significant variation among predicted and observed values. The negative values in REP, EV and ETP represent the predicted peak runoffs, volumes and corresponding time peaks are more than observed peak runoffs, volumes and time peaks. RMSE happens to be higher in some of the storm events.

On the other hand, the statistical indices of SAGA-based approach (Table 8) indicate that for the majority of the DEM-scenarios and storm events, the performance of GIUH-Nash is found to be unsatisfactory. The vast majority of NSE values are  $<0$ ; hence, the residual variance is greater than the variance of the observed data indicating unacceptable model performance [39]. The values of the other indices are also considerably higher than that of GRASS-based model. Hydrograph characteristics of the lower resolution DEM-based predictions are smaller than observed values. As pointed out earlier in the preceding discussions, the reason for this approach poor performance is mainly associated with the smaller lengths of the higher orders.



**Figure 9. Comparison of observed and predicted average – DRH (GRASS) for different effective rainfall (ER) events.**



**Figure 10. Examples of predicted and observed DRH (SAGA) comparisons.**



**Table 6. SAGA-based values of Nash parameters, peak runoff and time peak.**

Storm event	DEM	Nash parameters		Peak runoff		Time peak	
		$n$	$K, h$	$Q_0, m^3s^{-1}$	$Q_p, m^3s^{-1}$	$T_0, h$	$T_p, h$
July 17, 2006	ALOS 30	2.938	0.052	61.921	88.528	1.00	0.50
	ASTER 30	2.952	0.056		100.791		0.50
	SRTM 30	2.975	0.046		68.747		0.50
	SRTM 90	3.049	0.352		72.837		1.00
August 02, 2006	ALOS 30	2.938	0.043	66.860	58.453	1.00	0.50
	ASTER 30	2.952	0.052		81.101		0.50
	SRTM 30	2.975	0.043		60.583		0.50
	SRTM 90	3.049	0.331		86.277		0.50
August 04, 2006	ALOS 30	2.938	0.050	73.301	91.633	1.00	0.50
	ASTER 30	2.952	0.054		106.070		0.50
	SRTM 30	2.975	0.044		69.353		0.50
	SRTM 90	3.049	0.339		82.971		1.00
August 16, 2006	ALOS 30	2.938	0.051	44.585	92.258	1.00	0.50
	ASTER 30	2.952	0.063		129.356		0.50
	SRTM 30	2.975	0.052		94.357		0.50
	SRTM 90	3.049	0.396		43.720		0.50
August 22, 2006	ALOS 30	2.938	0.040	118.000	75.537	1.00	0.50
	ASTER 30	2.952	0.043		94.868		0.50
	SRTM 30	2.975	0.036		49.600		0.50
	SRTM 90	3.049	0.272		151.388		1.00

**Table 7. GRASS-based statistical measures of GIUH-Nash model.**

Storm event	REP (%)	RMSE	EV (%)	ETP(h)	MAE	NSE	SC
July 17, 2006	-0.349	16.237	0.742	0.75	10.375	0.507	0.843
August 02, 2006	-8.226	10.904	-0.372	0.25	7.122	0.740	0.856
August 04, 2006	6.335	14.013	30.101	0.00	10.132	0.759	0.948
August 16, 2006	-26.164	7.163	0.659	0.00	5.949	0.722	0.942
August 22, 2006	-1.498	16.561	21.501	-0.25	13.319	0.840	0.967

**Table 8. SAGA-based statistical measures of GIUH-Nash model.**

Storm event	DEM	REP (%)	RMSE	EV (%)	ETP	MAE	NSE	SC
July 17, 2006	ALOS 30	-42.969	24.530	55.278	0.00	16.450	-0.098	0.633
	ASTER 30	-62.773	25.670	48.541	0.00	17.539	-0.203	0.587
	SRTM 30	-11.024	23.850	65.675	0.00	14.769	-0.038	0.659
	SRTM 90	-17.629	15.118	-0.039	0.50	9.011	0.583	0.879
August 02, 2006	ALOS 30	12.574	24.523	71.676	-0.50	17.140	-0.316	0.608
	ASTER 30	-21.300	24.627	60.547	-0.50	18.189	-0.327	0.604
	SRTM 30	9.388	24.465	70.635	-0.50	17.241	-0.310	0.611
	SRTM 90	-29.041	11.095	-1.142	0.00	8.281	0.731	0.933
August 04, 2006	ALOS 30	-25.009	40.529	70.846	-0.50	29.911	-0.745	0.390
	ASTER 30	-44.705	41.371	66.076	-0.50	30.598	-0.818	0.342
	SRTM 30	5.386	39.958	78.058	-0.50	28.774	-0.696	0.420
	SRTM 90	-13.191	16.396	29.496	0.00	11.783	0.714	0.928
August 16, 2006	ALOS 30	-106.927	21.204	99.986	-0.50	16.264	-1.029	0.021
	ASTER 30	-190.133	21.171	99.890	-0.50	16.248	-1.023	0.059
	SRTM 30	-111.633	21.204	99.984	-0.50	16.263	-1.029	0.022
	SRTM 90	1.939	13.822	71.180	-0.50	11.578	0.138	0.758
August 22, 2006	ALOS 30	35.986	58.984	82.052	-0.50	42.710	-0.405	0.415
	ASTER 30	19.603	58.953	77.381	-0.50	42.658	-0.404	0.416
	SRTM 30	57.966	59.998	88.254	-0.50	43.973	-0.454	0.378
	SRTM 90	-28.295	25.457	20.932	0.00	20.186	0.738	0.920

## 4. Conclusions

Conclusions inferred from this study may be summarized in the following statements.

1. Despite in congruencies among physical and geographical parameters and elevation profiles derived from various DEMs, results of the study for the catchment Debarwa indicate that their implications on runoff predictions based on GIUH-Nash model are negligible unlike TOPMODEL [35] and SWAT [36, 37].

2. Algorithm selection affects the performance of the model in agreement with the works of [32, 33, 38]. GRASS algorithm generates hydrographs with reasonable accuracy to recorded hydrographs whereas SAGA-algorithm based model performance is found to be unsatisfactory. The authors conclude that care should be taken while selecting stream network generating algorithms for catchments similar to the Debarwa catchment, which have an outlet located near an upstream confluence of two major rivers.

3. Source and resolution of DEM insignificantly affects GIUH-Nash model performance as compared to algorithm selection. As such, GRASS-based runoff predictions are less influenced by source and resolution of DEM than SAGA-based. In this regard, lower resolution yields relatively consistent and acceptable performance than higher resolution which complies with the conclusions drawn by [37].

4. Considering the simplicity of the GIUH-Nash model development and application for practical purposes, ease of access to DEM and processing tools, good agreement of the theoretical and practical results from carefully chosen algorithms and consistency in the model outputs due to its inconsiderable dependence on source and resolution of DEM, the model has the potential to be a useful tool in resolving runoff prediction based difficulties in data scarce regions such as the Debarwa catchment in Eritrea.

5. Finally, in order to take a broad view of the findings of this study and promote the use of effective and appropriate runoff prediction approaches in ungauged catchments, future investigations should be undertaken in conjunction with available reference information systems. These investigations will include the GIUH-Nash model applicability and reliability in different agro-ecological zones, comparison of the selected model performance with other conventional and contemporary models and effects of DEM source and resolution and stream networks generating algorithm selection on the performance of various models in different catchment sin the territory of Eritrea.

## References

1. FAO. Review of Water Resources by Country water reports 23. Rome. 2003. 79 p. [Online] URL: [http://www.fao.org/nr/water/aquastat/countries\\_regions/ERI](http://www.fao.org/nr/water/aquastat/countries_regions/ERI)
2. Anghesom, A.G., Amlesom, S., Bovas, J.J.L. An overview of Eritrea's water resources. *International Journal of Engineering Research and Development*. 2017. Vol. 13. No. 3. Pp. 74–84.
3. Anghesom, A.G., Mathur B.S. Geomorphologic instantaneous unit hydrographs for rivers in Eritrea (East Africa). *Journal of Indian Water Resources Society*. 2014. Vol. 34. No. 1. Pp. 1–14.
4. Garry, L. Grabow, P., McCormick, G., James, R.G. Stream gauging of torrential rivers of eastern Eritrea. *Journal of Hydrologic Engineering*. 1998. Vol. 3. No. 3. Pp. 211–214.
5. Beven, K.J. *Rainfall-Runoff Modelling: The Primer*, John Wiley and sons Ltd. 2012. Pp. 25–49.
6. Singh, V.P. *Hydrologic Systems: Rainfall-Runoff Modeling vol. I*. Prentice-Hall, Englewood Cliffs. New Jersey. 1988.
7. Sherman, L.K. Streamflow from rainfall by unit-graph method. *Engineering news-Record*. 1932. Vol. 108. No. 4. Pp. 501–505.
8. Hawker, L., Bates, P., Neal, J., Rougier, J. Perspectives on digital elevation model (DEM) simulation for flood modeling in the absence of a high-accuracy open access global DEM. *Frontiers in Earth Science*. 2018. Vol. 6. No. 233. doi.org/10.3389/feart.2018.00233.
9. Sarkar, S., Goel, N.K., Mathur, B.S. Adequacy of Nakagami-m distribution function to derive GIUH. *Journal of Hydrologic Engineering*. 2009. Vol. 14. No. 10. Pp. 1070–1079.
10. Kumar, R., Chatterjee, C., Singh, R.D., Lohani, A.K., Kumar, S. Runoff estimation for ungauged catchments using GIUH. *Hydrologic Processes*. 2007. Vol. 21. No. 4. Pp. 1829–1840.
11. Dooge, J.C.I. A general theory of unit hydrograph. *Journal of Geophysical Research*. 1959. Vol. 64. No. 2. Pp. 241–256.
12. Snyder, F.F. Synthetic unit hydrographs. *Transactions of the American Geophysical Union*. 1938. Vol. 19. No. 1. Pp. 447–454.
13. Pilgrim, D.H., Cordery, I., Maidment, D.R. at al. Flood Runoff in Maidment D.R.(Eds.). *Handbook of Hydrology*. McGraw Hill. New York, 1993. 9.27 p.
14. Gupta, V.K., Waymire, E.C., Wang, C.T. A representation of an instantaneous unit hydrograph from geomorphology. *Water Resources Research*. 1980. Vol. 16. No. 5. Pp. 855–862.
15. Clark, C.O. Storage and the unit hydrograph. *Transactions. American Society of Civil Engineers*. 1945. Vol. 110. No. 1. Pp. 1419–1446.
16. Nash, J.E. Determining runoff from rainfall. *Proceedings of the institution of civil engineers*. Dublin. 1958. Vol. 10. Pp. 163–84.
17. Nash, J.E. The form of the instantaneous unit hydrograph. *International Association of Scientific Hydrology Publication*. 1957. Vol. 45. No. 3. Pp. 114–121.
18. Yen, B.C., Lee, K.T. Unit hydrograph derivation for ungauged watersheds by stream order laws. *Journal of Hydrologic Engineering*. 1997. Vol. 2. No. 1. Pp. 1–9.
19. Nourani, V., Singh, V.P., Delafrouz, D. Three geomorphological rainfall-runoff models based on the linear reservoir concept. *Journal of Catena*. 2008. Vol. 76. No. 3. Pp. 206–214.
20. Rodriguez-Iturbe, I., Valdes, J.B. The geomorphologic structure of hydrology response. *Water Resources Research*. 1979. Vol. 15. No. 6. Pp. 1409–1420.
21. Horton, R.E. Erosional development of streams and their drainage basins: hydrophysical approach to quantitative morphology. *Geological Society of America Bulletin*. 1945. Vol. 56. Pp. 275–370
22. Strahler, A.N. Quantitative analysis of watershed geomorphology. *Transactions American Geophysical Union*. 1957. Vol. 38. No. 6. Pp. 913–920.
23. Gupta, V.K., Waymire, E.C., Rodriguez-Iturbe, I. On scales gravity and network structure in basin runoff. In: Gupta, V.K., Rodriguez-Iturbe, I., Wood, E.F. (Eds.), *Scale Problems in Hydrology*. D. Reidel, Dordrecht, Holland. 1986. Pp. 159–184.
24. Rodriguez-Iturbe, I., Gonzalez-Sanabria, M., Bras, R.L. The geomorphoclimatic theory of the instantaneous unit hydrograph. *Water Resources Research*. 1982a. Vol. 18. No. 4. Pp. 877–886.
25. Rosso, R. Nash model relation to Horton order ratios. *Water Resources Research*. 1984. Vol. 20. No. 7. Pp. 914–920.
26. Lee, K.T., Yen, B.C. Geomorphology and kinematic-wave-based hydrograph derivation. *Journal of Hydraulic Engineering*. 1997. Vol. 123. No. 1. Pp. 73–80.

27. Bhaskar, N.R., Parida, B.P., Nayak, A.K. Flood estimation for ungauged catchments using the GIUH. *Journal of Water Resources Planning and Management*. 1997. Vol. 123. No. 4. Pp. 228–238.
28. Choi, Y.J., Lee, G., Kim J.C. Estimation of the Nash model parameters based on the concept of geomorphologic dispersion. *Journal of Hydrologic Engineering*. 2011. Vol. 16. No. 11. Pp. 806–817.
29. Zakizadeh, F., Malekinezhad, H. Comparison of methods for estimation of flood hydrograph characteristics. *Meteorology and Hydrology*. 2015. Vol. 40. No.12. Pp. 74–86. (rus)
30. Guzha, A.C., Hardy, T.B. Simulating streamflow and water table depth with a coupled hydrological model. *Water Science and Engineering*. 2010. Vol. 3. No. 3.Pp. 241–256.
31. Wechsler, S.P. Uncertainties associated with digital elevation models for hydrologic applications: a review. *Hydrology and Earth Systems Sciences Discussions, European Geosciences Union*. 2006, Vol. 3. No. 4. Pp. 2343–2384.
32. Wechsler, S.P. Perceptions by digital elevation model uncertainty by DEM users. *URISA Journal*. 2003. Vol. 15. No. 2. Pp. 57–64.
33. Bolstad, P., Stowe, T. An evaluation of DEM accuracy: elevation, slope, and aspect. *Photogrammetric Engineering and Remote Sensing*. 1994. Vol. 60. No. 11. Pp. 1327–1332.
34. Wolock, D., Price, C. Effect of digital elevation model map scale and data resolution on a topography-based watershed model. *Water Resources Research*. 1994. Vol. 30. No. 11. Pp. 3041–3052.
35. Chapplot, V. Impact of DEM mesh size and soil map scale on SWAT runoff, sediment, and NO<sub>3</sub>-N loads predictions. *Journal of Hydrology*. 2005. Vol. 312 No. 1–4. Pp. 207–222.
36. Reddy, S.A., Reddy, J.M. Evaluating the influence of spatial resolutions of DEM on watershed runoff and sediment yield using SWAT. *Journal of Earth System Science*. 2015. Vol. 124. No. 7. Pp. 1517–1529.
37. Azizian, A., Shokoohi, A. DEM resolution and stream delineation threshold effects on the results of geomorphologic-based rainfall runoff models. *Turkish Journal of Engineering and Environmental Sciences*. 2014. Vol. 38. Pp. 64–78.
38. Nash, J.E., Sutcliffe, J.V. River flow forecasting through conceptual models part I: a discussion of principles. *Journal of Hydrology*. 1970. Vol. 10. No. 3. Pp. 282–290.

### **Contacts:**

*Dmitry Kozlov, +79854813569; kozlovdv@mail.ru*

*Anghesom Alemngus Ghebrehiwot, +79851936320; bahghi2012@gmail.com*

© Kozlov, D.V., Ghebrehiwot, A.A., 2019



DOI: 10.18720/MCE.87.9

## Эффективность цифровых моделей рельефа и моделей Нэша в прогнозировании стока

**Д.В. Козлов\*, А.А. Гебрехиот,**

*Национальный исследовательский Московский государственный строительный университет,  
г. Москва, Россия*

*\* E-mail: kozlovdv@mail.ru*

**Ключевые слова:** цифровая модель рельефа, ГИС-алгоритм, модель GIUH-Nash, прямой поверхностный сток, гидрограф, водосбор, речная сеть, прогноз стока.

**Аннотация.** Цифровые модели рельефа (ЦМР) широко используются в гидрологическом моделировании и определении геоморфологических свойств водосборных бассейнов. В последнее время гидрологи проявляют интерес к изучению воздействия ЦМР из различных источников на моделируемые результаты. В рамках этих усилий данное исследование было направлено на оценку влияния различных ЦМР и выбора алгоритмов прогноза геоморфологических мгновенных единичных гидрографов (GIUH) прямого поверхностного стока на основе модели Нэша для неизученного речного водосбора Дебарва в Эритрее. Были применены четыре ЦМР с открытым исходным кодом и два алгоритма квантовой географической информационной системы (QGIS) (GRASS и SAGA), а соответствующие результаты были оценены с использованием пяти наблюдаемых паводковых событий. Эти два алгоритма привели к созданию речных сетей с одинаковыми порядками русел, но различными геоморфологическими характеристиками, такими как соотношение русел. Субъективная и объективная оценки результатов указали на то, что эффективность модели, основанной на SAGA, была неудовлетворительной, в то время как модель GIUH-Nash, основанная на алгоритме GRASS, была приемлемой для всех сценариев ЦМР, независимо от их источников и разрешений. В исследовании сделан вывод о том, что выбор ЦМР при расчете гидрографов стока для условий водосбора Дебарва мало влияет на прогнозы прямого поверхностного стока на основе модели GIUH-Nash. Однако при выборе алгоритмов генерации речной сети следует проявлять большую осторожность, особенно для водосборных бассейнов, выходы которых расположены вблизи слияния двух крупных рек.

### Литература

1. FAO. Review of Water Resources by Country water reports 23. Rome. 2003. 79 p. [Электронный ресурс] URL: [http://www.fao.org/nr/water/aquastat/countries\\_regions/ERI](http://www.fao.org/nr/water/aquastat/countries_regions/ERI)
2. Anghesom A.G., Amlesom S., Bovas J.J.L. An overview of Eritrea's water resources // International Journal of Engineering Research and Development. 2017. Vol. 13. № 3. Pp. 74–84.
3. Anghesom A.G., Mathur B.S. Geomorphologic instantaneous unit hydrographs for rivers in Eritrea (East Africa) // Journal of Indian Water Resources Society. 2014. Vol. 34. № 1. Pp. 1–14.
4. Garry L., Grabow P., McCormick G., James, R.G. Stream gauging of torrential rivers of eastern Eritrea // Journal of Hydrologic Engineering. 1998. Vol. 3. № 3. Pp. 211–214.
5. Beven K.J. Rainfall-Runoff Modelling: The Primer, John Wiley and sons Ltd. 2012. Pp. 25–49.
6. Singh V.P. Hydrologic Systems: Rainfall-Runoff Modeling vol. I. Prentice-Hall, Englewood Cliffs. New Jersey. 1988.
7. Sherman L.K. Streamflow from rainfall by unit-graph method // Engineering news-Record. 1932. Vol. 108. № 4. Pp. 501–505.
8. Hawker L., Bates P., Neal J., Rougier J. Perspectives on digital elevation model (DEM) simulation for flood modeling in the absence of a high-accuracy open access global DEM // Frontiers in Earth Science. 2018. Vol. 6. № 233. doi.org/10.3389/feart.2018.00233.
9. Sarkar S., Goel N.K., Mathur B.S. Adequacy of Nakagami-m distribution function to derive GIUH // Journal of Hydrologic Engineering. 2009. Vol. 14. № 10. Pp. 1070–1079.
10. Kumar R., Chatterjee C., Singh R.D., Lohani A.K., Kumar S. Runoff estimation for ungauged catchments using GIUH // Hydrologic Processes. 2007. Vol. 21. № 4. Pp. 1829–1840.
11. Dooge J.C.I. A general theory of unit hydrograph // Journal of Geophysical Research. 1959. Vol. 64. № 2. Pp. 241–256.
12. Snyder F.F. Synthetic unit hydrographs // Transactions of the American Geophysical Union. 1938. Vol. 19. № 1. Pp. 447–454.
13. Pilgrim D.H., Cordery I., Maidment D.R. et al. Flood Runoff in Maidment D.R. (Eds.). Handbook of Hydrology. McGraw Hill. New York, 1993. 9.27 p.

14. Gupta V.K., Waymire E.C., Wang C.T. A representation of an instantaneous unit hydrograph from geomorphology // *Water Resources Research*. 1980. Vol. 16. № 5. Pp. 855–862.
15. Clark C.O. Storage and the unit hydrograph. *Transactions // American Society of Civil Engineers*. 1945. Vol. 110. № 1. Pp. 1419–1446.
16. Nash J.E. Determining runoff from rainfall. *Proceedings of the institution of civil engineers*. Dublin. 1958. Vol. 10. Pp. 163–84.
17. Nash J.E. The form of the instantaneous unit hydrograph // *International Association of Scientific Hydrology Publication*. 1957. Vol. 45. № 3. Pp. 114–121.
18. Yen B.C., Lee K.T. Unit hydrograph derivation for ungauged watersheds by stream order laws // *Journal of Hydrologic Engineering*. 1997. Vol. 2. № 1. Pp. 1–9.
19. Nourani V., Singh V.P., Delafrouz D. Three geomorphological rainfall–runoff models based on the linear reservoir concept // *Journal of Catena*. 2008. Vol. 76. № 3. Pp. 206–214.
20. Rodriguez-Iturbe I., Valdes J.B. The geomorphologic structure of hydrology response. *Water Resources Research*. 1979. Vol. 15. № 6. Pp. 1409–1420.
21. Horton R.E. Erosional development of streams and their drainage basins: hydrophysical approach to quantitative morphology // *Geological Society of America Bulletin*. 1945. Vol. 56. Pp. 275–370
22. Strahler A.N. Quantitative analysis of watershed geomorphology // *Transactions American Geophysical Union*. 1957. Vol. 38. № 6. Pp. 913–920.
23. Gupta V.K., Waymire E.C., Rodriguez-Iturbe I. On scales gravity and network structure in basin runoff // Gupta V.K., Rodriguez-Iturbe I., Wood E.F. at al. *Scale Problems in Hydrology*. D. Reidel, Dordrecht, Holland. 1986. Pp. 159–184.
24. Rodriguez-Iturbe I., Gonzalez-Sanabria M., Bras R.L. The geomorphoclimatic theory of the instantaneous unit hydrograph // *Water Resources Research*. 1982a. Vol. 18. № 4. Pp. 877–886.
25. Rosso R. Nash model relation to Horton order ratios // *Water Resources Research*. 1984. Vol. 20. № 7. Pp. 914–920.
26. Lee K.T., Yen B.C. Geomorphology and kinematic-wave-based hydrograph derivation // *Journal of Hydraulic Engineering*. 1997. Vol. 123. № 1. Pp. 73–80.
27. Bhaskar N.R., Parida B.P., Nayak A.K. Flood estimation for ungauged catchments using the GIUH // *Journal of Water Resources Planning and Management*. 1997. Vol. 123. № 4. Pp. 228–238.
28. Choi Y.J., Lee G., Kim J.C. Estimation of the Nash model parameters based on the concept of geomorphologic dispersion // *Journal of Hydrologic Engineering*. 2011. Vol. 16. № 11. Pp. 806–817.
29. Zakizadeh F., Malekinezhad H. Comparison of methods for estimation of flood hydrograph characteristics // *Meteorology and Hydrology*. 2015. Vol. 40. №12. Pp. 74–86.
30. Guzha A.C., Hardy T.B. Simulating streamflow and water table depth with a coupled hydrological model // *Water Science and Engineering*. 2010. Vol. 3. № 3. Pp. 241–256.
31. Wechsler, S.P. Uncertainties associated with digital elevation models for hydrologic applications: a review. *Hydrology and Earth Systems Sciences Discussions, European Geosciences Union*. 2006, Vol. 3. № 4. Pp. 2343–2384.
32. Wechsler S.P. Perceptions by digital elevation model uncertainty by DEM users // *URISA Journal*. 2003. Vol. 15. № 2. Pp. 57–64.
33. Bolstad P., Stowe T. An evaluation of DEM accuracy: elevation, slope, and aspect // *Photogrammetric Engineering and Remote Sensing*. 1994. Vol. 60. № 11. Pp. 1327–1332.
34. Wolock D., Price C. Effect of digital elevation model map scale and data resolution on a topography-based watershed model // *Water Resources Research*. 1994. Vol. 30. № 11. Pp. 3041–3052.
35. Chapplot V. Impact of DEM mesh size and soil map scale on SWAT runoff, sediment, and NO<sub>3</sub>-N loads predictions // *Journal of Hydrology*. 2005. Vol. 312 № 1–4. Pp. 207–222.
36. Reddy S.A., Reddy J.M. Evaluating the influence of spatial resolutions of DEM on watershed runoff and sediment yield using SWAT // *Journal of Earth System Science*. 2015. Vol. 124. № 7. Pp. 1517–1529.
37. Azizian A., Shokoohi A. DEM resolution and stream delineation threshold effects on the results of geomorphologic-based rainfall runoff models. *Turkish Journal of Engineering and Environmental Sciences*. 2014. Vol. 38. Pp. 64–78.
38. Nash J.E., Sutcliffe J.V. River flow forecasting through conceptual models part I: a discussion of principles // *Journal of Hydrology*. 1970. Vol. 10. № 3. Pp. 282–290.

#### **Контактные данные:**

*Дмитрий Вячеславович Козлов, +79854813569; эл. почта: kozlovdv@mail.ru*  
*Ангхесом Алемнугс Гебрехивот, +79851936320; эл. почта: bahghi2012@gmail.com*

© Козлов Д.В., Гебрехивот А.А., 2019





DOI: 10.18720/MCE.87.10

## Numerical studies of long-wave processes in the reaches of hydrosystems and reservoirs

**D.R. Bazarov, D.A. Mavlyanova\***,

*Tashkent Institute of Irrigation and Agricultural Mechanization Engineers, Tashkent, Uzbekistan*

\* E-mail: [dildoramav@mail.ru](mailto:dildoramav@mail.ru)

**Keywords:** long-wave processes, breakthrough, the Saint-Venant equations of motion, mathematical modeling, numerical method.

**Abstract.** The problem of development of mathematical models and computer programs for calculation and forecast of various long-wave processes occurring in the reaches of reservoirs and hydro-systems is considered. The basic method to solve the problem is a mathematical modeling based on differential equations for the channel flow – the Saint-Venant equations using numerical methods. Conventional methods in hydraulics, methods for building mathematical models based on the laws of hydromechanics and their numerical calculations are also used. A mathematical and a computer program to carry out forecast calculations of long-wave processes occurring in the reaches of hydro-systems and reservoirs have been developed. The reliability of the results obtained is confirmed by rigorous mathematical statement, the use of well-known and tested equations and methods of hydraulics, and by the agreement of the results obtained in the work with the data obtained by other authors and available in literature.

### 1. Introduction

Broad-crested weirs are widely used in the practice of hydro-technical engineering; the flow through the weir can be considered as a long-wave process. These long-wave processes may be of natural origin due to freshets and floods; they may be the result of waves of release from overlying hydro-systems or they may be the breakthrough waves caused by hydrodynamic accidents. In this case, the role of a weir is played by a breakthrough in the dam body [1]. Breakthrough floods spread along the downstream at high speed and have an extremely high destructive force. The most severe consequences in the world practice of hydro-technical engineering have been caused by the breakthroughs of the pressure head of the dam banking up.

In solving practical problems of the hydraulics of open flows, one of the key points is the realization of the fact that two-dimensional unsteady Saint-Venant equations describe well enough both smoothly varying and sharply varying flows with the formation of breakthrough (circulation) zones. The derivation of the Saint-Venant equations without assumptions of smooth variability of the flow has been made by V.M. Lyatkher and A.N. Militeev in [2, 3], where it is shown that the pumping of energy into the circulation zone occurs due to pulsations at the border with the transit jet. Moreover, in numerical experiments, it is possible to obtain a spectrum of pulsations enriched by new harmonics when the computational grid is thickened, which, among other things, testifies to the high quality of the applied difference scheme.

There are a large number of publications devoted to the study of flow passage through a broad-crested weir. In [4], the influence of the Reynolds number on the coefficient of flow through the broad-crested weir is considered. It is shown that the coefficient of flow through the weir increases with increasing Reynolds number.

In [5] approach enabling the possibility to define the finite lifetime of a small earth dam is presented. The proposed approach does not require any variables monitoring. It is based on the definition of lifetime by assessing the water impact on the small earth dams by quantitative methods of system analysis.

Bazarov, D.R., Mavlyanova, D.A. Numerical studies of long-wave processes in the reaches of hydrosystems and reservoirs. Magazine of Civil Engineering. 2019. 87(3). Pp. 123–135. DOI: 10.18720/MCE.87.10.

Базаров Д.Р., Мавлянова Д.А. Численные исследования длинноволновых процессов в бьефах гидроузлов и водохранилищ // Инженерно-строительный журнал. 2019. № 3(87). С. 123–135. DOI: 10.18720/MCE.87.10



This open access article is licensed under CC BY 4.0 (<https://creativecommons.org/licenses/by/4.0/>)

In [6] there is theoretically shown that pressure is equal to half of flow depth at state of speed flow, i.e. it is equal to half of critical depth. Knowing it, authors offer a device that is designed to finding critical section and critical depth in open flows.

The study in [7] is devoted to the experimental investigation of a broad-crested weir. To determine the basic characteristics of the weir, generally accepted methods of hydraulic calculations are used. A refined correlation is obtained to determine the discharge coefficient of a broad-crested weir.

In [8], two mathematical models based on the Saint-Venant equations are considered for calculating unsteady flows in channels with floodplains. In the 1<sup>st</sup> model, the influence of the floodplain presence on the passage of flood or flush waves is taken into account through the morphometric and hydraulic characteristics, total for the channel and floodplain. In the 2<sup>nd</sup> model, based on the separation of the channel flow, the floodplain plays the role of a storage tank.

[9] is devoted to imitating the breakthrough of the Vakhdat dam (Iran) by integrating the ArcMap and HEC-RAS software and field observations. The Manning coefficient for the Geshlag River in the lower reaches of the dam is estimated using the Manning's ratio and field observations and measurements.

In [10], the problem of streamlining a weir crest of various designs is discussed. It is shown that when designing rectangular weirs without lateral compression, when no intake of atmospheric air under the jet from the downstream is provided, the flow measurement error may increase by 20–25 %. The best solution to this issue is, if possible, to project the weir with a small lateral compression, about 2–3 %.

In [11], a substantiation is given for choosing the optimal methods for organizing automated water flow accounting and collecting hydrological and climatic information for modeling the dynamics of water-balance elements, and to ensure adaptive land use and the needs of hydrological and geochemical monitoring.

In [12] is devoted to substantiating the conditions for the use of reserve weirs at hydro-systems with earth dams and to the development of the methods for calculating the basic parameters of such reserve weirs. As a result of research, it has been found that the advantages of the proposed structure compared to other weir structures are low construction costs, simplicity of the device, significantly lower total possible damage in the event of an accident at a dam, since the part of the excess flood will be discharged in advance through the reserve weir and will be distributed longer in time.

Stationary and non-stationary plane problems of hydromechanics for a semi-infinite fluid layer of finite depth are considered. Hydrodynamic pressure on the vertical upstream face of the dam under the horizontal seismic load with energy absorption on the reservoir bottom and a layer of sediment is determined in [13].

In [14] the methodology of the development of scenarios and the water overflow probability that is one of the basic causes of the emergency situations at the dams is given. The causes of the spillway failure and most frequent events leading to the failures or disturbances of the spillway structures are analyzed.

In [15] reliability problems for low pressure waterworks are considered. Earthen dams with long operational periods are shown to have substantial damage and are in unsatisfactory condition.

In [16] according to the proposed algorithm, a computer program was developed, and the calculation of the displacement of the crest of the dam Sayano-Shushenskaya HPP for 2001...2016 years (360 intervals). The estimation of accuracy of the received results is given.

In [17], mathematical problem of calculating the unsteady flow of water is considered when regulating concentrated water discharge releases in watercourses in downstream spillways. An algorithm for the analytical solution of the problem is compiled, based on a hydraulic calculation of the process of propagation and transformation of long waves described by the Saint-Venant equations.

In [18], the effect of soaking of the upstream side of rectangular broad-crested weirs on discharge coefficient and flow characteristics is investigated. Five weirs have been developed with tilt angles of 15, 30, 45, 60 and 90° and a flow rate coefficient, negative velocity along the dam crest and water surface profiles along the weir crest have been estimated in laboratory hydraulic trays. The results obtained by reducing the inclined side upstream, increase the discharge efficiency and discharge capacity of the weir.

In [19] it is shown that in wide rectangular channels of flows for which the Manning formula is applicable, at constant roughness of the bottom along the length of the water channel, analytical solutions of the Saint-Venant equations can be constructed in the form of rising waves propagating down the slope of the channel without changing the shape. Such waves are called monoclinal ones.

It should be noted that the construction of solutions of the Saint-Venant equations in the form of a monoclinal wave is a rather complicated and time-consuming task [19]. The fact of the possibility of constructing such solutions is proved in [19], but the solutions themselves are not given. In [20], it is noted that the construction of such solutions for the propagation of a monoclinal wave along the initially dry channel is much simpler than in the general case with a filled channel, since in this case the water velocity is constant throughout the flow region and is equal to the wave propagation velocity. This is so because in initially dry bed there is no water flow through the

body of the wave. In [20], an analytical solution is constructed for a monoclinal wave propagating in a dry channel at a constant value of the hydraulic friction coefficient. The obtained analytical solution is compared to the results of numerical solution of the Saint-Venant equations using an explicit finite-difference scheme and the finite element method [21–23], showing a satisfactory agreement.

In [24], a new method for controlling unsteady flow in open channels is presented. The equations are derived from the differential form of complete shallow water equations in one dimension.

In [25] regularized equations describing hydrodynamic flows in the two-layer shallow water approximation are constructed. A conditionally stable finite-difference scheme based on the finite-volume method is proposed for the numerical solution of these equations.

In real long-wave processes in prismatic channels with a constant slope and roughness, a more complex flow pattern arises in which a quiet flow below the downstream floor at initial period of release wave passage can differ quite strongly from a monoclinal wave, and only gradually throughout the whole quiet flow section does the wave flow approach to it [26, 27].

Based on the above, the aim of this work is defined, which consists in determining the numerical value of the coefficient of flow through the broad-crested weir, which was used in the numerical study of long-wave processes.

## 2. Methods

Here we present the methodology for the end-to-end calculation of spillway dams, taking into account flooding and the possibility of maintaining a given (fixed or variable) level in the upstream (US) [28]. Figure 1 shows a diagram of river section with a diverting dam, which shows water flow through a weir.

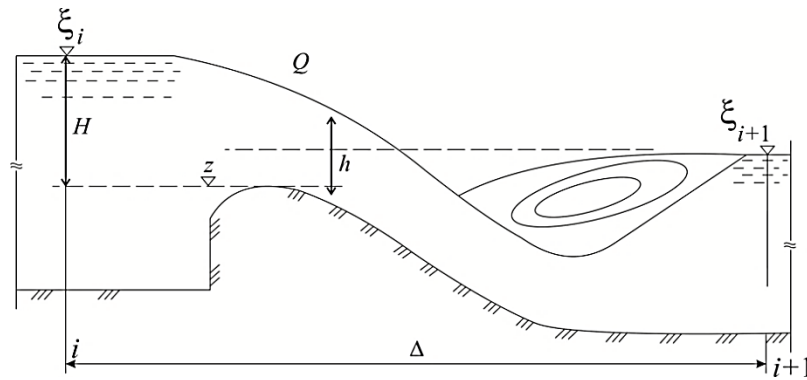


Figure 1. Pattern of water flow through the weir.

Here  $i, i + 1$  are the nodes of computational grid, where free surface levels are calculated  $\zeta_i, \zeta_{i+1}$ ;  $Q$  is the flow rate through the dam;  $z$  is the top mark of the weir;  $H = \zeta_i - z$  is the pressure over the crest of the weir;  $h = \zeta_{i+1} - z$  is the depth of flooding from the downstream (DS);  $\Delta$  is the distance between the nodes.

As a rule, a normal retaining level is maintained in the US by maneuvering dam shutters. However, as noted above, at high floods, accompanied by long-wave processes, the dam can be fully opened, and then there is a water flow through the weir, in conditions of flooding ( $h > 0$ ) as well. Thus, at given water flow rate, three flow modes are possible: with a fixed level of US, through non-submerged and submerged weirs. Obviously, in the latter case, the DS level has an impact on the US level. The Saint-Venant equations do not describe the water flow through the submerged weir, therefore we modify them so that along with the flow in natural channel, to calculate end-to-end all the listed modes of water supporting structure. To do this, to the equation of motion on the segment  $[i, i + 1]$  it is necessary to introduce an additional hydraulic resistance, similar to friction, which would provide the required water level difference at the dam, and to exclude convective terms. The equation of continuity does not change. Then, in the stationary case, the relationship of flow rates and levels is obtained in the form

$$g\omega \frac{\zeta_i - \zeta_{i+1}}{\Delta} = QF. \quad (1)$$

In the absence of a dam

$$F = F_0 = \frac{\lambda}{2} \frac{|Q|}{\omega R}, \quad (2)$$

where  $\lambda = 2gn^2 R^{-1/3}$  is the hydraulic friction coefficient, other designations are similar to those given earlier;

$\omega$  is flow cross section;

$R$  is hydraulic radius;

$g$  is gravity relative to unit mass.

In the presence of a weir from a known ratio

$$Q = m\sigma b\sqrt{2g}H^{3/2}, \quad (3)$$

where  $m$  is the coefficient of weir flow;

$\sigma$  is the flooding coefficient;

$b$  is the width of the weir; the following expression is obtained

$$H \equiv \zeta_i - z = \left( \frac{Q}{m\sigma b\sqrt{2g}} \right)^{2/3}, \quad (4)$$

which is converted to the form (1) if assume that

$$F = \frac{g\omega(1-\xi)}{\Delta(m\sigma b\sqrt{2g}Q)^{2/3}} \equiv F_1(1-\xi). \quad (5)$$

where  $\xi = \frac{h}{H} \equiv \frac{\zeta_{i+1} - z}{\zeta_i - z} \leq 1$  is the degree of flooding.

The expression for the flooding coefficient  $\sigma$  depends on the type of weir, and, for the weirs of practical profile can be taken in the form:

$$\sigma = \begin{cases} (1-\xi)^{0.3}, & 0 \leq \xi < 1; \\ 1, & \xi < 0. \end{cases} \quad (6)$$

Broad-crested weirs are widely used in the practice of hydraulic engineering, for example, in the inlet part of weir structures of dams with discharge facilities. One of the main hydrodynamic parameters of weirs are the flow carrying capacity, which can be determined using the calculation formula for broad-crest weirs in significantly narrowed channels, in dike dams, in the area of diverting dams, in narrow floodplains, in approaches to bridges, as well as in dams with partial passage of high floods on submerged floodplain. Since in various problems of computational hydrodynamics it is necessary to choose and adapt the above-mentioned computational formula, the identification of such an expression is the aim of this study.

Under conditions of sharp variability of hydrological processes, a large amount of water flow in a relatively short time, accompanied by long-wave processes, passes through rivers and canals. If these processes in the river beds have a natural origin (floods and freshets), then in hydro-systems and reservoirs they can be the flush waves from the overlying hydroelectric complex or the breakthrough waves caused by hydrodynamic accidents. In this case, the breakthrough in the dam body plays the role of a weir [29].

In numerical studies of long-wave processes, the inclusion to the program of an internal boundary condition that approximates a weir formula makes it very difficult. It should be noted that the calculation formula in a general form for a broad-crest weir can be obtained from the equation of the curve of free water surface in the channel, which is a special case of the Saint-Venant equation of motion for steady-state flow [29, 30]. It is easy to show from the equation of the curve of free surface that the transition of a steady-state river flow from quiet flow mode (where the Froude number and kinetic parameter is less than unity ( $Fr < 1$  or  $P_k < 1$ )) to a turbulent mode ( $Fr > 1$  or  $P_k > 1$ ) is possible on the sections of river where the channel first narrows and then widens. This property of the channel flow is similar to the property of pressure gas flows in Laval nozzles; it is a striking example of a hydraulic-gas-dynamic analogy found by the classics in hydro-dynamics – N.Ye. Zhukovsky and D.P. Ryabushinsky [31].

To obtain an improved calculation formula for a non-submerged broad-crest weir using the formula for the curve of water free surface directly, without using the Belange hypothesis, the mathematical model is used to predict long-wave processes in the reaches of hydroelectric complexes and reservoirs; this model consists of hydrodynamic equations of water flow, presented in the form:

$$\begin{cases} \frac{\partial \omega}{\partial t} + \frac{\partial Q}{\partial x} = 0, \\ \frac{\partial Q}{\partial t} + \frac{\partial(V^2\omega + gS)}{\partial x} - g \frac{\partial S}{\partial x} \Big|_{Z_{fs} = \text{const}} + \frac{\lambda}{2} V^2 \chi = 0, \end{cases} \quad (7)$$

where  $Z_{fs}$  is mark of free surface of flow.

Propagation velocity of waves of small amplitude along the channel, corresponding to (7) is

$$C = \sqrt{g \frac{\omega}{B}},$$

$$\omega \frac{\partial V}{\partial t} + V \frac{\partial \omega}{\partial t} + V \frac{\partial \omega V}{\partial x} + V \omega \frac{\partial V}{\partial x} + g \frac{\partial S}{\partial x} - g \frac{\partial S}{\partial x} \Big|_{Z_{fs} = \text{const}} + \frac{\lambda}{2} V^2 \chi = 0,$$

$$\frac{\partial V}{\partial t} + V \frac{\partial V}{\partial x} + \frac{g}{\omega} \left( \frac{\partial S}{\partial x} - \frac{\partial S}{\partial x} \Big|_{Z_{fs} = \text{const}} \right) + \frac{\lambda}{2} \frac{V^2}{R} = 0, \quad (8)$$

$$S = \int_{Z_{rb}}^{Z_{fs}} B(Z_{fs} - z) dz, .$$

where  $Z_{rb}$  is mark of the bottom of the channel.

To differentiate the static moment of the section, the formula known from mathematical analysis is used, where there is a function:

$$F(x) = \int_{\alpha(x)}^{\beta(x)} \Phi(x, y) dy; \quad \frac{dF}{dx} = \int_{\alpha}^{\beta} \frac{\partial \Phi}{\partial x} dy + \Phi|_{y=\beta} \frac{d\beta}{dx} - \Phi|_{y=\alpha} \frac{d\alpha}{dx};$$

$$\frac{\partial S}{\partial x} = \frac{\partial}{\partial x} \int_{Z_{rb}}^{Z_{fs}} (Z_{fs} - z) B dz = \int_{Z_{rb}}^{Z_{fs}} \frac{\partial (Z_{fs} - z) B}{\partial x} dz + (Z_{fs} - z) B \Big|_{z=Z_{fs}} \frac{\partial Z_{fs}}{\partial x} -$$

$$- (Z_{fs} - z) B \Big|_{z=Z_{rb}} \frac{\partial Z_{rb}}{\partial x} = \int_{Z_{rb}}^{Z_{fs}} \frac{\partial Z_{fs}}{\partial x} B dz + \int_{Z_{rb}}^{Z_{fs}} Z_{fs} \frac{\partial B}{\partial x} dz - HB \frac{\partial Z_{rb}}{\partial x} =$$

$$= \frac{\partial Z_{fs}}{\partial x} \int_{Z_{rb}}^{Z_{fs}} B dz + Z_{fs} \int_{Z_{rb}}^{Z_{fs}} \frac{\partial B}{\partial x} dz - HB \frac{\partial Z_{rb}}{\partial x} = \omega \frac{\partial Z_{fs}}{\partial x} + Z_{fs} \int_{Z_{rb}}^{Z_{fs}} \frac{\partial B}{\partial x} dz - HB \frac{\partial Z_{rb}}{\partial x};$$

$$\frac{\partial S}{\partial x} \Big|_{Z_{fs} = \text{const}} = Z_{fs} \int_{Z_{rb}}^{Z_{fs}} \frac{\partial B}{\partial x} dz - HB \frac{\partial Z_{rb}}{\partial x}.$$

So,

$$\frac{\partial S}{\partial x} - \frac{\partial S}{\partial x} \Big|_{Z_{fs} = \text{const}} = \omega \frac{\partial Z_{fs}}{\partial x}$$

and

$$\frac{\partial V}{\partial t} + V \frac{\partial V}{\partial x} + g \frac{\partial Z_{fs}}{\partial x} + \frac{\lambda}{2} \frac{V^2}{R} = 0 \quad (9)$$

hence

$$\frac{\partial V}{\partial t} + \frac{\partial (V^2 / 2 + g Z_{fs})}{\partial x} + \frac{\lambda}{2} \frac{V^2}{R} = 0. \quad (10)$$

Equation (10) at steady state flow, when  $\frac{\partial V}{\partial t} = 0$ , is the equation of curve of the free surface in the channel. When  $\lambda = 0$ , it turns into the Bernoulli equation

$$\frac{d(V^2 / 2 + g Z_{fs})}{dx} + \frac{\lambda}{2} \frac{V^2}{R} = 0. \quad (11)$$



Given the stationary nature of the flow in the computational domain, we get

$$\frac{d(Q^2 / 2\omega^2 + gh)}{dx} = gI - \frac{\lambda}{2} \frac{V^2}{R}. \quad (12)$$

If to take a channel of rectangular cross section, but with varying width and bottom level along the flow, that is, at each location  $\omega = Bh$ , where  $B$  and  $h$  can vary in  $x$ , then instead of (12) we get

$$\left( g - \frac{Q^2}{\omega^3} \frac{\partial \omega}{\partial h} \right) \frac{dh}{dx} - \frac{Q^2}{\omega^3} \frac{\partial \omega}{\partial B} \frac{dB}{dx} = gI - \frac{\lambda}{2} \frac{V^2}{R}. \quad (13)$$

Since  $\frac{\partial \omega}{\partial h} = B$ .

$$\left( g - \frac{V^2 B}{Bh} \right) \frac{dh}{dx} - \frac{V^2 h}{Bh} \frac{dB}{dx} = gI - \frac{\lambda}{2} \frac{V^2}{R},$$

$$\left( 1 - \frac{V^2}{gh} \right) \frac{dh}{dx} - \frac{V^2 h}{Bgh} \frac{dB}{dx} = gI - \frac{\lambda}{2} \frac{V^2}{hR},$$

$$R = Bh / (B + 2h).$$

As  $Fr = \frac{V^2}{gh}$ ,

$$(1 - Fr) \frac{dh}{dx} = I + Fr \frac{h}{B} \frac{dB}{dx} - \frac{\lambda}{2} \frac{V^2}{gR},$$

$$\frac{dh}{dx} = \frac{I + Fr \frac{h}{B} \frac{dB}{dx} - \frac{\lambda}{2} \frac{V^2}{gR}}{1 - Fr}. \quad (14)$$

In cases where the influence of friction is small, it follows from (14) that at the narrowing of channel section ( $I < 0$ ,  $\frac{dB}{dx} < 0$ ): in a quiet flow state ( $Fr < 1$ ,  $P_k < 1$ ), the depth decreases, an increase in the average flow velocity is observed; in a turbulent state of flow ( $Fr > 1$ ,  $P_k > 1$ ) the depth of the flow increases, and the average velocity decreases;

at the widening of channel section ( $I > 0$ ,  $\frac{dB}{dx} > 0$ ): in a quiet flow ( $Fr < 1$ ) the depth increases and the flow rate decreases, in a turbulent flow ( $Fr > 1$ ) the depth decreases and the speed increases.

According to the above statements, it can be stated that the Froude number in a quiet flow increases with narrowing of the channel and decreases with its widening, and in a turbulent flow, on the contrary, it decreases with narrowing of the channel, and increases with its widening. According to the above, the transition of the flow from a quiet flow mode to a turbulent one can occur only when the channel form changes from narrowing to widening one, and in the narrowest section of the channel the values of the Froude number and the kinetic parameter will be equal to  $Fr = P_k = 1.0$ .

Fundamental importance of the hydraulic-gas-dynamic analogy of hydrodynamics found by N.E. Zhukovsky and D.P. Ryabushinsky, similar to the theory of the Laval nozzle widely known in technical gas dynamics has already been noted. In accordance with this analogy, the depth of the flow is similar to gas density, the pressure forces for the channel flow and gas flow in a pipe are similar, the propagation velocity of waves of small amplitude in the channel is similar to the sound velocity in a gas. The analogue of the Froude number is the square of the Mach number. A detailed description of the hydraulic-gas-dynamic analogy and its use in engineering is given in literature [31].

Further, the minimum area in the dam location, in which the Froude number  $Fr = 1$ , will be called critical one, and the flow parameters – critical parameters; will mark it by an index with an asterisk. Naturally, the transition from the quiet mode of the flow of a channel stream to a turbulent mode is possible only under the condition that the critical depth of the flow is not flooded from the downstream.

So,

$$Fr = \frac{V_*^2}{gh_*} = 1. \quad (15)$$

These considerations have been carried out under the insignificant influence of hydraulic friction along the channel, where the basic conditions for the application of the Bernoulli equation are satisfied.

Suppose that the upstream channel becomes very broad (a reservoir is located there), so that the velocity pressure in that zone can be neglected; let the water depth in the reservoir above the bottom of the critical section of the channel be equal to  $N$ . Then the Bernoulli equation will look like:

$$H = h_* + \frac{V_*^2}{2g}, \quad (16)$$

or in accordance with (15),

$$V_*^2 = gh_*,$$

$$H = \frac{3}{2}h_*. \quad (17)$$

From the above follows the well-known in hydraulics formula of a broad-crested weir

$$Q = B_*h_*V_* = B_*h_*\sqrt{gh_*} = B_*\sqrt{gh_*^3} = B_*\sqrt{g}\left(\frac{2}{3}H\right)^{3/2} = mB_*\sqrt{2g}H^{3/2}, \quad (18)$$

where  $m$  is the discharge coefficient to determine the flow rate of water through a non-submerged broad-crested weir (18); it is a result of some mathematical transformations of equation (11) directly, without using the Belange hypothesis.

$$m = 2/3^{3/2} \approx 0.385. \quad (19)$$

It should be noted that the well-known formula of Saint-Venant-Wanzel [31] is an analogue of formula (18) for pressure flows, which allows determining the flow rate of gas flowing out of a pressure tank through nozzles (assuming the process is adiabatic); it is widely used in engineering.

A numerical experiment has been conducted on flow passage through a non-submerged broad-crested weir. The A.N. Militeev explicit finite-difference scheme, adapted for channels of arbitrary shape, was used [32]. In the experiment, the channel of a rectangular cross section without a slope and friction has been suddenly narrowed 100 times, and then suddenly widened 100 times. On the finite-difference grid, the weir was modeled by two narrowing locations. As a boundary condition at the inlet to computational domain, the flow rate was set, at the outlet – the Froude number  $Fr$ . Generally speaking, it could be set greater than 1, but in the study the Froude number was taken as  $Fr = 0.12$ . As an initial condition, the water flow over the entire area was assumed to be 0, a depth was set above the narrowed area, and below – the depth corresponding to the inlet flow rate and the Froude number at the outlet from the area.

In a numerical experiment, after a certain period, a flow mode was established in which the depth in the upstream significantly exceeded the depth in the downstream; below the narrowed zone, a turbulent flow area, a hydraulic jump and a quiet flow area appeared. In the absence of friction with the bottom, the problem of numerical simulation of the section of displacement of hydraulic jump is impossible, but this was not the subject

of this experiment. Figure 2 presents a graph of the value  $m = \frac{Q}{B_*\sqrt{2g}H^{3/2}}$  obtained in numerical experiment, which, in a steady mode is the weir coefficient. As a result of the experiment found that  $m \approx 0.394$ , it slightly differs from the theoretical value of  $m \approx 0.385$ .

When setting the hydraulic friction on the section of narrowing, the coefficient of weir flow drops. According to the above, it can be concluded that the equation of curve of water free surface is a result of the Saint-Venant equations; and in numerical calculations of flows on broad-crested weirs (and polygonal weirs of a spread out profile) it is possible to use them directly, end-to-end, without inserting the formula of weir as an internal boundary condition. Naturally, this does not apply to calculations of weirs of practical profile or the ones with a thin wall, in which there is a greater curvature of jets and the pressure distribution over the depth differs greatly from the hydrostatic one; this excludes the use of the Saint-Venant equations. For flows with

small curvature of jets the Saint-Venant equations are suitable, the flow coefficient  $m = 2/3^{3/2}$  is a maximum and suits only in the absence of any additional hydraulic losses in the inlet section.

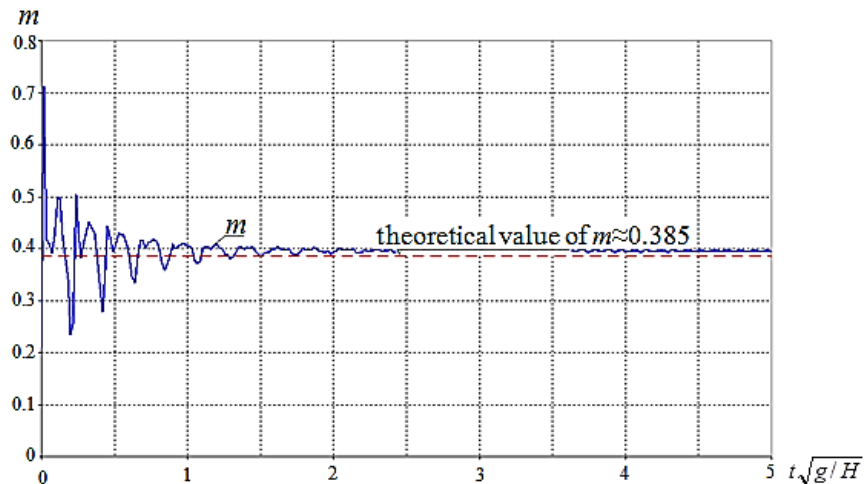


Figure 2. Change of value  $m = \frac{Q}{B_* \sqrt{2gH^{3/2}}}$  in time obtained in numerical experiment  
(in the steady state,  $m$  is the coefficient of weir flow).

### 3. Results and Discussion

To study the course of the long-wave process in the reaches of hydro-systems and reservoirs, take the river basin to the plain part of the region with real hydrological, hydraulic and morphometric parameters. In the considered section of the river basin, there is a cascade with several reservoirs for irrigation and hydropower purposes. An example of a cascade accident on a river in a plain terrain is shown in Figure 3.

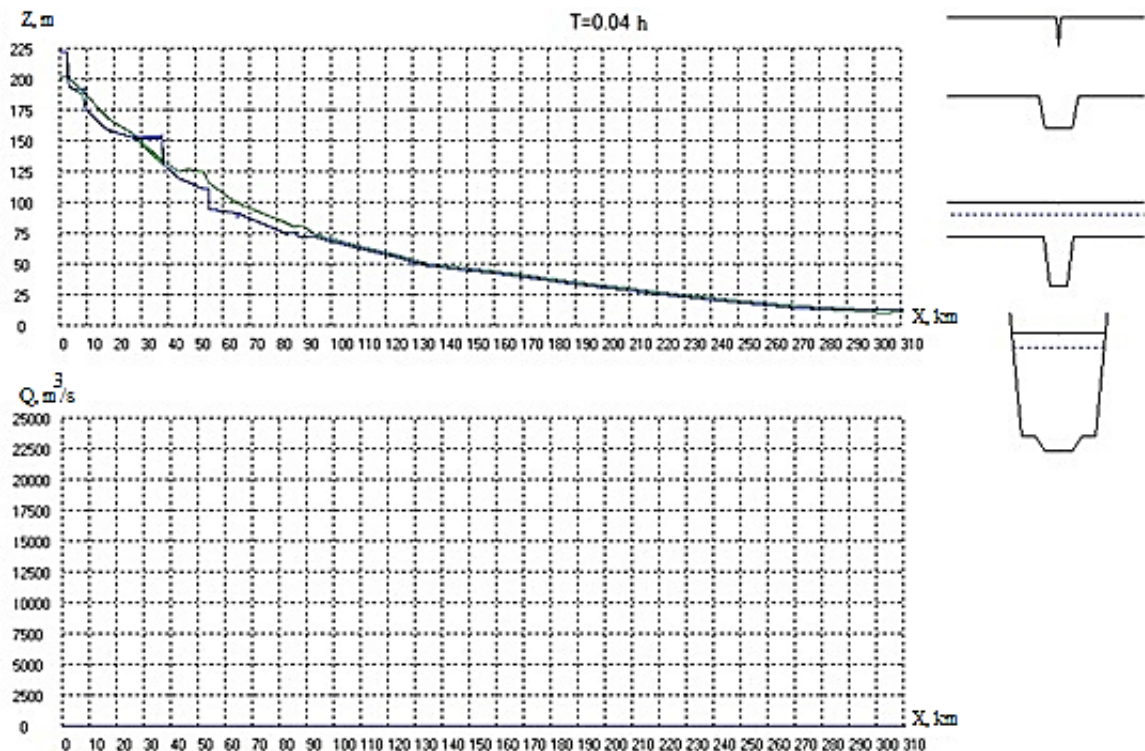
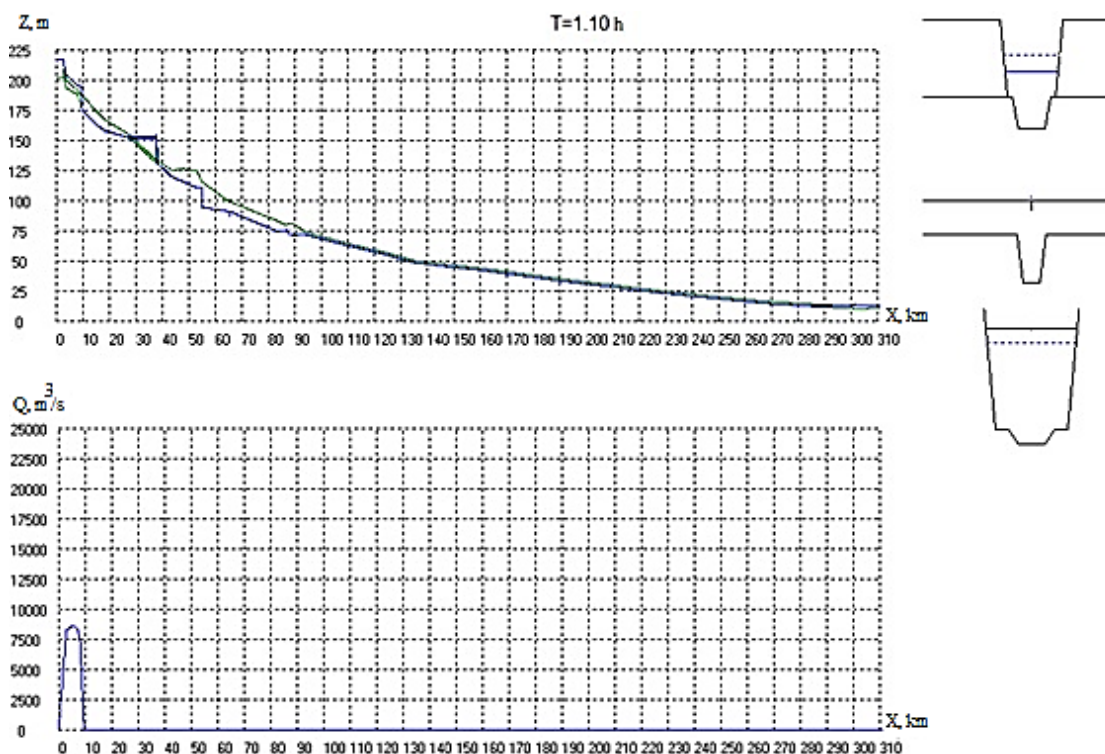


Figure 3. Beginning of a numerical study of a cascade of structures in a plain river with three reservoirs over a length of 300 km.

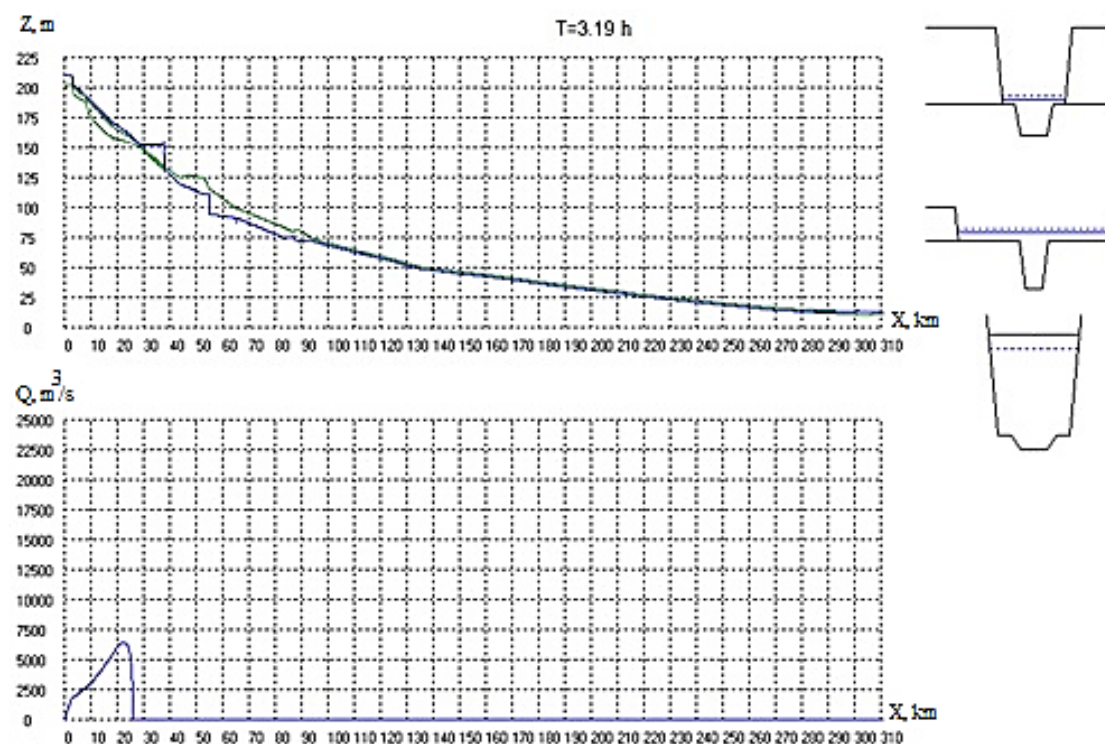
A cascade consists of 3 relatively small reservoirs (upper one – 100 million  $m^3$ , medium – 4 million  $m^3$ , lower – 100 million  $m^3$ ). With a sharp increase in water volume in the first reservoir, the long-wave process begins with the passage of a large flow of water through the dam. According to the course of calculation, the long-wave flow destroys at high velocity the first dam and makes sharply varying movements in the form of a wave after  $t = 1.1h$  of the estimated time, reaches the dam of the second reservoir (Figure 4).

The dynamics of water level in the river basin and of the flow of water with characteristic cross sections in the locations of the cascade reservoirs are presented.



**Figure 4. Results of numerical calculation of sharply varying flow after  $t = 1.10$  h.**

The intensively filled second reservoir almost instantly transmits a long wave in the downstream of the cascade reservoir. As the calculation results show, it is possible to hold the accident for a certain time, about 3 hours, when a breakthrough wave reaches the lower reservoir (Figure 5).



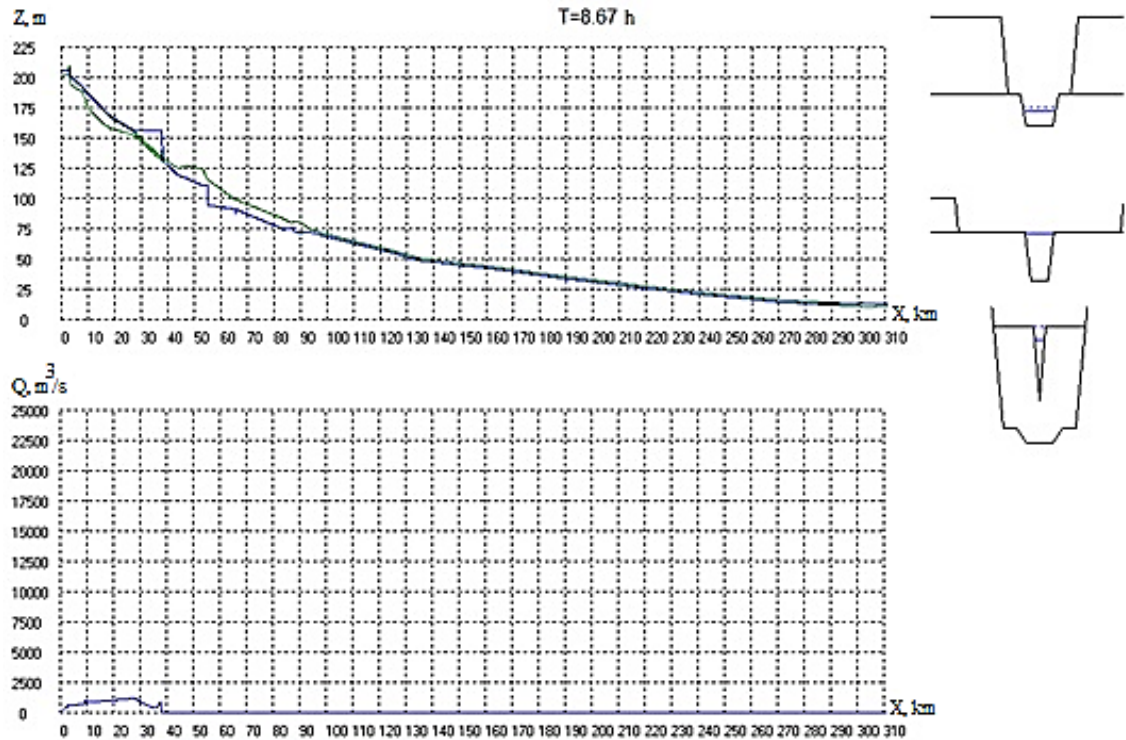
**Figure 5. Results of numerical calculation of sharply varying flow in a cascade after  $t = 3.19$  hours.**

The dynamics of the water level in the river basin and of the flow of water with characteristic cross sections in the locations of the cascade reservoirs are presented.

According to the results of numerical study of the developed model, after 8 hours, the third reservoir overflows and a breakthrough occurs, accompanied by long waves, and the throughput capacity of the water



discharge and weir structures of the last hydro-system turns out to be insufficient to prevent a hydrodynamic accident during large floods (Figure 6).



**Figure 6. Results of numerical calculation of sharply varying flow in a cascade after  $t = 8$  h.**

The dynamics of the water level in the river basin and the flow of water with characteristic cross sections in the locations of the cascade reservoirs are presented. Beginning of the fourth process of long waves propagation through the dam of the third reservoir.

Further, the breakthrough wave, gradually weakening (but for a small river remaining catastrophic along the entire length of the river), spreads downstream till the place where the river flows into a large lake.

The result of calculation allows us to determine the characteristic of the flow dynamics in the river bed and in floodplain and flooding zone of the adjacent territories of the studied river basin. These data can be used in determining the extent of possible damage and the losses resulting from the passage of flood flows, accompanied by long-wave processes. The description of the dynamics of hydrodynamic parameters of the flow and the morphometry of the riverbed in the developed model is the next step in numerical studies of the current investigation. A cascade of hydro-technical structures on the Chirchik river basin has been chosen for the numerical study.

#### 4. Conclusions

1. Using the vector flow equation and the scalar equation of continuity, a system of equations describing the flow of water is obtained.
2. The value of the coefficient of flow is calculated, where the input part of overflow to the broad-crested weir is taken.
3. Numerical studies of the passage of long waves through the dams of the reservoirs of the Chirchik river basin have been carried out.
4. Numerical studies of the passage of long waves through the dam of a real object have been carried out.

#### References

1. Istorik, B.L., Lyatkher, V.M. Propagation of a flush wave in a prismatic channel. *Fluid Dynamics*. 1975. Vol. 10. No. 1. Pp. 31–35.
2. Lyatkher, V.M., Militeev, A.N. *Gidravlicheskiye issledovaniya chislennymi metodami* [Hydraulic Studies by Numerical Methods]. Water Resources. 1981. No. 3. Pp. 60–79. (rus)
3. Lyatkher, V.M., Militeev, A.N., Togunova, N.P. Investigation of the distribution of currents in the lower pools of hydraulic structures by numerical methods. *Hydrotechnical Construction*. 1978. Vol. 12. No. 6. Pp. 585–593.
4. Medzveliia, M.L., Pipiya, V.V. Discharge ratio of the broad-crested weir flow in the low head area. *Vestnik MGSU*. 2013. No. 4. Pp. 167–171. (rus)



5. Titova, T.S., Longobardi, A., Akhtyamov, R.G., Nasyrova, E.S. Lifetime of earth dams. Magazine of Civil Engineering. 2017. 69(1). Pp. 34–43. doi: 10.18720/MCE.69.3
6. Yerzhanova, N.K., Mussin, Zh.A., Dzholdasov, S.K., Altynbekova, A.D. Critical section and critical depth in open flows finding device. Magazine of Civil Engineering. 2017. 76(8). Pp. 106–114. doi: 10.18720/MCE.76.10
7. Kosichenko, Yu.M., Mikhailov, E.D., Baev, O.A. Eksperimentalnyye issledovaniya vodosliva s shirokim porogom rezervnogo vodosplosa [An experimental research of a spillway with a wide threshold of a reserve water outlet]. Vestnik SGASU. Town planning and architecture. 2015. No. 3(20). Pp. 73–81. (rus)
8. Voevodin, A.F., Nikiforovskaya, V.S., Ostapenko, V.V. Mathematical Modeling of Transformation of Flood Waves in Stream Channels with Floodplains. Russian Meteorology and Hydrology. 2008. Vol. 33. No. 3. Pp. 193–198.
9. Amini, A., Arya, A., Eghbalzadeh, A., Javan, M. Peak Flood Assessment and Over-watering Conditions at Vahdat Dam, Kurdistan Iran. Arabian Journal of Geosciences. 2017. Vol. 10. No. 6. Pp. 127.
10. Yegorov, N.L., Loitsker, O.D. On the flow characteristic of a measuring weir of unconventional profile. Water Supply and Sanitary Technique. 2015. No. 4. Pp. 63–67. (rus)
11. Kopysov, S.G., Yarlykov, R.V. Experience in organization of hydrological and climatic observations at small model catchments of West Siberia. Bulletin of the Tomsk Polytechnic University. Geo Assets Engineering. 2015. Vol. 326. No. 12. Pp. 115–121.
12. Kosichenko, Yu.M., Mikhaylov, Ye.D. Method for calculating the parameters of reserve spillway with scoured insert. Scientific Journal of Russian Scientific Research Institute of Land Improvement Problems. 2014. No. 4(16). Pp. 176–189. (rus)
13. Kaufman, B.D. Accounting for the impact of uncertain factors on the determination of the hydrodynamic pressure on the dam. Magazine of Civil Engineering. 2012. 35(9). Pp. 59–69. (rus) doi: 10.5862/MCE.35.8
14. Stefanyshyn, D.V., Shtilman, V.B. Towards assessing the probability of water overflow across the dam crest. Magazine of Civil Engineering. 2012. 35(9). Pp. 70–78. (rus) doi: 10.5862/MCE.35.9
15. Mikhasek, A.A., Rodionov, M.V. Reliability of low pressure waterworks with earthen dams. Construction of Unique Buildings and Structures. 2013. 12(7). Pp. 20–29. (rus)
16. Bednaruk, S.E., Chukanov, V.V., Klenov, E.M., Kozlov, D.V. Model displacements of the dam crest reservoir Sayano-Shushenskaya HPP. Construction of Unique Buildings and Structures. 2018. 66(3). Pp. 60–69. (rus)
17. Mikheev, P.A., Ivanenko, Yu.G., Tkachev, A.A., Gurin, K.G., Ivanenko, D.Yu. Regulation of concentrated releases of water discharges on stream flows in lower tails of spillway waterworks. Scientific Journal of KubSAU. 2017. No. 132. Pp. 1374–1388. (rus)
18. Kiumars, Badr, Dariush, Mowla. Development of Rectangular Broad-crested Weirs for Flow Characteristics and Discharge Measurement. KSCE Journal of Civil Engineering. 2015. Vol. 19. No. 1. Pp. 136–141.
19. Stoker, J.J. Water Waves: The Mathematical Theory with Applications. New York: Interscience Publishers, 1957. 609 p.
20. Bazarov, D.R., Shkolnikov, S.Y., Mavlyanova, D.A., Rayimova, I.D. The form of a monoclinic wave propagating along an initially dry riverbed. Construction of Unique Buildings and Structures. 2018. 64(1). Pp. 7–19. (rus)
21. Drutsa, A.B. A Finite Difference Method for Solving a Nonlinear Shallow Water Equations on Unstructured Grids. Numerical Methods and Programming. 2012. Vol. 13. Pp. 511–516. (rus)
22. Delis, A.I., Katsaounis, Th. Numerical Solution of the Two-dimensional Shallow Water Equations by Application of the Relaxation Methods. Applied Mathematical Modelling. 2005. Vol. 29. No. 8. Pp. 754–783.
23. Liang, Shin-Jye, Hsu, Tai-Wen. Least-squares Finite-element Method for Shallow-water Equations with Source Terms. Acta Mechanica Sinica. 2009. Vol. 25. No. 5. Pp. 597–610.
24. Sanders, B.F., Katopodes, N.D. Control of canal flow by adjoint sensitivity method. Journal of Irrigation and Drainage Engineering. 1999. Vol. 125. No. 5. Pp. 287–297.
25. Elizarova, T.G., Ivanov, A.V. Regularized equations for numerical simulation of flows in the two-layer shallow water approximation. Computational Mathematics and Mathematical Physics. 2018. Vol. 58. No. 5. Pp. 714–734.
26. Atanov, G.A., Evseeva, E.G., Meselhe, E.A. Estimation of Roughness Profile in Trapezoidal Open Channels. Journal of Hydraulic Engineering. 1999. Vol. 125. No. 3. Pp. 309–312.
27. Gessese, A., Wa, K.M., Sellier, M. Bathymetry Reconstruction Based on the Zero-inertia Shallow Water Approximation. Theoretical and Computational Fluid Dynamics. 2013. Vol. 27. No. 5. Pp. 721–732.
28. Belikov, V.V., Zaitsev, A.A., Militeev, A.N. Mathematical Modeling of Complex Reaches of Large River Channels. Water Resources. 2002. Vol. 29. No. 6. Pp. 643–650.
29. Le Mehaute, B. An Introduction to Hydrodynamics and Water Waves. Springer-Verlag, New York, 1976. 323 p.
30. Belikov, V.V., Norin, S.V., Shkolnikov, S.Ya. O proryve damb polderov [On the Breakthrough of Polder Dams]. Hydrotechnical Construction. 2014. No. 12. Pp. 25–34. (rus)
31. Vinogradov, R.I., Zhukovsky, M.I., Yakubov, I.R. Gazogidravlicheskaya analogiya i yeye prakticheskoye primeneniye [Gas-hydraulic Analogy and its Practical Application]. M.: Mashinostroenie, 1978. 152 p. (rus)
32. Militeev, A.N. Resheniye zadach gidravliki melkikh vodoyemov i byefov gidrouzlov s primeneniyem chislennykh metodov [Solving Problems of Hydraulics of Small Reservoirs and Reaches of Hydro-systems Using Numerical Methods]. Abstract of doctoral tech. science thesis. M.: 1982. 307 p. (rus)

### Contacts:

*Dilshod Bazarov*, +7(871)2371989; *dbazarov61@mail.ru*

*Dildora Mavlyanova*, +7(371)2371926; *dildoramav@mail.ru*



# Инженерно-строительный журнал

ISSN  
2071-  
0305

сайт журнала: <http://engstroy.spbstu.ru/>

DOI: 10.18720/MCE.87.10

## Численные исследования длинноволновых процессов в бьефах гидроузлов и водохранилищ

**Д.Р. Базаров, Д.А. Мавлянова\***,

*Ташкентский институт инженеров ирригации и механизации сельского хозяйства,*

*г. Ташкент, Узбекистан*

*\* E-mail: dildoramav@mail.ru*

**Ключевые слова:** длинноволновые процессы, проран, уравнения движения Сен-Венана, математическое моделирование, численный метод.

**Аннотация.** Рассматривается проблема разработки математических моделей и компьютерных программ для расчетов и прогнозов различных длинноволновых процессов, происходящих в бьефах водохранилищ и гидроузлов. Основным методом решения задач является математическое моделирование на основе дифференциальных уравнений для руслового потока – уравнений Сен-Венана, с использованием численных методов. Также используются общепринятые методы в гидравлике, методы составления математических моделей на основе законов гидромеханики и их численных расчетов. Разработана математическая модель и компьютерная программа для проведения прогнозных расчетов длинноволновых процессов происходящих в бьефах гидроузлов и водохранилищ. Достоверность полученных результатов подтверждается достаточно строгой математической постановкой, применением известных и апробированных уравнений и методов гидравлики, а также соответствием полученных в работе результатов с имеющимися в литературе данными других авторов.

### Литература

1. Историк Б.Л., Лятхер В.М. Распространение волн прорыва в призматическом русле // Известия АН СССР. Механика жидкости и газа. 1975. № 1. С. 39–44.
2. Лятхер В.М., Милитеев А.Н. Гидравлические исследования численными методами // Водные ресурсы. 1981. № 3. С. 60–79.
3. Лятхер В.М., Милитеев А.Н., Тогунова Н.П. Исследование плана течений в нижнем бьефе гидротехнических сооружений численными методами // Гидротехническое строительство. 1978. № 6. С. 27–32.
4. Медзвелья М.Л., Пипия В.В. Коэффициент расхода водослива с широким порогом в области малых напоров // Вестник МГСУ. 2013. № 4. С. 167–171.
5. Титова Т.С., Лонгобарди А., Ахтямов Р.Г., Насырова Э.С. Срок эксплуатации грунтовых плотин // Инженерно-строительный журнал. 2017. № 1(69). С. 34–43. doi: 10.18720/MCE.69.3
6. Ержанова Н.К., Мусин Ж.А., Джолдасов С.К., Алтынбекова А.Д. Устройство для нахождения критического сечения и критической глубины в открытых потоках // Инженерно-строительный журнал. 2017. № 8(76). С. 106–114. doi: 10.18720/MCE.76.10
7. Косиченко Ю.М., Михайлов Е.Д., Баев О.А. Экспериментальные исследования водослива с широким порогом резервного водосброса // Вестник СГАСУ. Градостроительство и архитектура. 2015. № 3(20). С. 73–81.
8. Воеводин А.Ф., Никифоровская В.С., Остапенко В.В. Математическое моделирование трансформации волн паводков в руслах с поймами // Метеорология и гидрология. 2008. № 3. С. 88–95.
9. Amini A., Arya A., Eghbalzadeh A., Javan M. Peak flood estimation under overtopping and piping conditions at Vahdat Dam, Kurdistan Iran // Arabian Journal of Geosciences. 2017. Vol. 10. Issue 6. Pp. 127.
10. Егоров Н.Л., Лойцкер О.Д. К вопросу о расходной характеристике измерительного водослива нетипового профиля // Водоснабжение и санитарная техника. 2015. № 4. С. 63–67.
11. Копысов С.Г., Ярлыков Р.В. Опыт организации гидролого-климатических наблюдений на малых модельных водосборах Западной Сибири // Известия Томского политехнического университета. Инжиниринг георесурсов. 2015. Т. 326. № 12. С. 115–121.
12. Косиченко Ю.М., Михайлов Е.Д. Методика расчета параметров резервного водосброса с размываемой вставкой // Научный журнал Российского НИИ проблем мелиорации. 2014. № 4(16). С. 176–189.
13. Кауфман Б.Д. Учет влияния неопределенных факторов при определении гидродинамического давления на плотину // Инженерно-строительный журнал. 2012. № 9(35). С. 59–69. doi: 10.5862/MCE.35.8

14. Стефанишин Д.В., Штильман В.Б. К оценке вероятности перелива воды через гребень плотины // Инженерно-строительный журнал. 2012. № 9(35). С. 70–78. doi: 10.5862/MCE.35.9
15. Михасек А.А., Родионов М.В. Надежность низконапорных гидроузлов с грунтовыми плотинами // Строительство уникальных зданий и сооружений. 2013. № 7(12). С. 20–29.
16. Беднарук С.Е., Чуканов В.В., Кленов Е.М., Козлов Д.В. Модель перемещений гребня плотины водохранилища Саяно-Шушенской ГЭС // Строительство уникальных зданий и сооружений. 2018. № 3(66). С. 60–69.
17. Михеев П.А., Иваненко Ю.Г., Ткачев А.А., Гурин К.Г., Иваненко Д.Ю. Регулирование сосредоточенных попусков расходов воды на водотоках в нижних бьефах водосбросных гидроузлов // Научный журнал КубГАУ. 2017. № 132. С. 1374–1388.
18. Kiumars Badr, Dariush Mowla. Development of rectangular broad-crested weirs for flow characteristics and discharge measurement // KSCE Journal of Civil Engineering. 2015. Vol. 19. Issue 1. Pp. 136–141.
19. Стокер Дж.Дж. Волны на воде. Математическая теория и приложения. М.: Изд-во иностранной литературы, 1959. 618 с.
20. Базаров Д.Р., Школьников С.Я., Мавлянова Д.А., Райимова И.Д. Форма моноклиальной волны, распространяющейся по первоначально сухому руслу // Строительство уникальных зданий и сооружений. 2018. № 1 (64). С. 7–19.
21. Друца А.В. Конечно-разностный метод для решения нелинейной системы уравнений динамики мелкой воды на неструктурированной сетке // Вычислительные методы и программирование. 2012. Т. 13. С. 511–516.
22. Delis A.I., Katsaounis Th. Numerical solution of the two-dimensional shallow water equations by the application of relaxation methods // Applied Mathematical Modelling. 2005. Vol. 29. Issue 8. Pp. 754–783.
23. Liang Shin-Jye, Hsu Tai-Wen. Least-squares finite-element method for shallow-water equations with source terms // Acta Mechanica Sinica. 2009. Vol. 25. Issue 5. Pp. 597–610.
24. Sanders B.F., Katopodes N.D. Control of canal flow by adjoint sensitivity method // Journal of Irrigation and Drainage Engineering. 1999. Vol. 125. Issue 5. Pp. 287–297.
25. Елизарова Т.Г., Иванов А.В. Регуляризованные уравнения для численного моделирования течений в приближении двухслойной мелкой воды // Журнал вычислительной математики и математической физики. 2018. Т. 58. № 5. С. 741–761.
26. Atanov G.A., Evseeva E.G., Meselhe E.A. Estimation of roughness profile in trapezoidal open channels // Journal of Hydraulic Engineering. 1999. Vol. 125. Issue 3. Pp. 309–312.
27. Gessese A., Wa K.M., Sellier M. Bathymetry reconstruction based on the zero-inertia shallow water approximation // Theoretical and Computational Fluid Dynamics. 2013. Vol. 27. Issue 5. Pp. 721–732.
28. Беликов В.В., Зайцев А.А., Милитеев А.Н. Математическое моделирование сложных участков русел крупных рек // Водные ресурсы. 2002. Т. 29. № 6. С. 698–705.
29. Ле Меоте Б. Введение в гидродинамику и теорию волн на воде. Л.: Гидрометеиздат, 1974. 368 с.
30. Беликов В.В., Норин С.В., Школьников С.Я. О прорыве дамб польдеров // Гидротехническое строительство. 2014. № 12. С. 25–34.
31. Виноградов Р.И., Жуковский М.И., Якубов И.Р. Газогидравлическая аналогия и ее практическое применение. М.: Машиностроение, 1978. 152 с.
32. Милитеев А.Н. Решение задач гидравлики мелких водоемов и бьефов гидроузлов с применением численных методов. Дисс. на соиск. ученой степени д.т.н. М., 1982. 307 с.

#### **Контактные данные:**

*Дилшод Райимович Базаров, +7(871)2371989; эл. почта: dbazarov61@mail.ru*

*Дилдора Абдурашидовна Мавлянова, +7(371)2371926; эл. почта: dildoramav@mail.ru*



**ПОЛИТЕХ**

Санкт-Петербургский  
политехнический университет  
Петра Великого

Инженерно-строительный институт  
Центр дополнительных профессиональных программ

195251, г. Санкт-Петербург, Политехническая ул., 29,  
тел/факс: 552-94-60, [www.stroikursi.spbstu.ru](http://www.stroikursi.spbstu.ru),  
[stroikursi@mail.ru](mailto:stroikursi@mail.ru)

**Приглашает специалистов проектных и строительных организаций,  
не имеющих базового профильного высшего образования  
на курсы профессиональной переподготовки (от 500 часов)  
по направлению «Строительство» по программам:**

**П-01 «Промышленное и гражданское строительство»**

Программа включает учебные разделы:

- Основы строительного дела
- Инженерное оборудование зданий и сооружений
- Технология и контроль качества строительства
- Основы проектирования зданий и сооружений
- Автоматизация проектных работ с использованием AutoCAD
- Автоматизация сметного дела в строительстве
- Управление строительной организацией
- Управление инвестиционно-строительными проектами. Выполнение функций технического заказчика

**П-02 «Экономика и управление в строительстве»**

Программа включает учебные разделы:

- Основы строительного дела
- Инженерное оборудование зданий и сооружений
- Технология и контроль качества строительства
- Управление инвестиционно-строительными проектами. Выполнение функций технического заказчика и генерального подрядчика
- Управление строительной организацией
- Экономика и ценообразование в строительстве
- Управление строительной организацией
- Организация, управление и планирование в строительстве
- Автоматизация сметного дела в строительстве

**П-03 «Инженерные системы зданий и сооружений»**

Программа включает учебные разделы:

- Основы механики жидкости и газа
- Инженерное оборудование зданий и сооружений
- Проектирование, монтаж и эксплуатация систем вентиляции и кондиционирования
- Проектирование, монтаж и эксплуатация систем отопления и теплоснабжения
- Проектирование, монтаж и эксплуатация систем водоснабжения и водоотведения
- Автоматизация проектных работ с использованием AutoCAD
- Электроснабжение и электрооборудование объектов

**П-04 «Проектирование и конструирование зданий и сооружений»**

Программа включает учебные разделы:

- Основы сопротивления материалов и механики стержневых систем
- Проектирование и расчет оснований и фундаментов зданий и сооружений
- Проектирование и расчет железобетонных конструкций
- Проектирование и расчет металлических конструкций
- Проектирование зданий и сооружений с использованием AutoCAD
- Расчет строительных конструкций с использованием SCAD Office

**П-05 «Контроль качества строительства»**

Программа включает учебные разделы:

- Основы строительного дела
- Инженерное оборудование зданий и сооружений
- Технология и контроль качества строительства
- Проектирование и расчет железобетонных конструкций
- Проектирование и расчет металлических конструкций
- Обследование строительных конструкций зданий и сооружений
- Выполнение функций технического заказчика и генерального подрядчика

По окончании курса слушателю выдается диплом о профессиональной переподготовке  
установленного образца, дающий право на ведение профессиональной деятельности



